Modélisation numérique du magnétisme solaire et stellaire

Raphaël Raynaud

To cite this version:

Raphaël Raynaud. Modélisation numérique du magnétisme solaire et stellaire. Physique [physics]. Observatoire de Paris, 2015. Français. NNT : . tel-01196516

OBSERVATOIRE DE PARIS

ÉCOLE DOCTORALE
ASTRONOMIE ET ASTROPHYSIQUE D'ÎLE-DE-FRANCE

Doctorat
ASTRONOMIE ET ASTROPHYSIQUE

Raphaël Raynaud

Modélisation numérique du magnétisme solaire et stellaire

Thèse dirigée par Emmanuel Dormy et Ludovic Petitdemange

Soutenue le 26 juin 2015

Jury

Claude Catala	Président
Thierry Alboussière	Rapporteur
Michel Rieutord	Rapporteur
Jacques Le Bourlot	Examinateur
Gilles Chabrier	Examinateur
Ulrich R. Christensen	Examinateur
Emmanuel Dormy	Directeur de thèse
Ludovic Petitdemange	Directeur de thèse

Ever tried. Ever failed.
No matter.
Try again. Fail again.
Fail better.

Samuel Beckett, *Worstward Ho*, 1982.

Remerciements

En général, j'ai remarqué qu'il fallait remercier les hommes le moins possible, parce que, la reconnaissance qu'on leur témoigne les persuade aisément qu'ils en font trop !

Constant (1895)

Je souhaite d'abord adresser mes remerciements à mes directeurs de thèse, Emmanuel Dormy et Ludovic Petitdemange, pour leur grande disponibilité, leur soutien amical, et leur confiance — inébranlable.

J'ai également à cœur de remercier en particulier Stéphan Fauve, qui, de la Licence au Master, m'aura suivi tout au long de mes tortueuses années d'études à l'ENS, et sans qui je n'aurais probablement pas entrepris de me lancer dans cette (deuxième) thèse.

Il m'est tout aussi nécessaire de remercier sincèrement ses collègues du Laboratoire de Physique Statistique, Christophe Gissinger et François Pétrélis, dont les conseils avisés — parfois enrobés d'un humour caustique — me furent toujours précieux.

Je tiens ensuite à exprimer ma reconnaissance à tous les membres du Laboratoire de Radioastronomie qui m'ont accueilli au cours de ces trois années, ainsi qu'au personnel administratif et technique du LERMA et de l'ENS qui a participé au bon déroulement de cette thèse dans des conditions parfois difficiles, entre gravats et marteaux-piqueurs... Je souhaite aussi faire part de ma gratitude envers Michel Pérault pour son soutien actif à ma candidature en post-doctorat.

Mes remerciements vont également à mes rapporteurs, Thierry Alboussière et Michel Rieutord, pour l'intérêt qu'ils ont porté à mon travail, sans oublier les autres membres du jury : Claude Catala, Jacques Le Bourlot, Gilles Chabrier et Ulrich R. Christensen.

En outre, je remercie Steve M. Tobias qui m'a généreusement accueilli lors de mon passage à l'Université de Leeds, ainsi que Toby Wood qui a fait de même à l'Université de Newcastle. À leur contact, ma virée anglaise me fut extrêmement profitable.

Bien sûr, je n'oublierai pas de remercier chaleureusement Martin Schrinner qui m'a beaucoup aidé lors de mon premier stage au Laboratoire de Radioastronomie. De plus, je tiens à préciser que cette thèse représente en partie la continuation des recherches qu'il a menées au sein du laboratoire sur l'approximation anélastique.

Enfin, je remercie Sarah Najand pour toutes les minutieuses relectures apportées à ce manuscrit et son aide dans l'organisation de la soutenance.

Résumé

Cette thèse traite de la génération d'un champ magnétique par l'écoulement d'un fluide conducteur de l'électricité, connu sous le nom d'effet dynamo. De nombreuses études numériques ont ainsi cherché à comprendre l'origine du champ magnétique terrestre par l'analyse des champs magnétiques engendrés par les mouvements de convection d'un fluide conducteur contenu dans une coquille sphérique en rotation. La plupart de ces modèles simplifiés du noyau externe de fer liquide font communément usage de l'approximation dite de Boussinesq ; cette approximation n'est cependant pas adaptée pour décrire la convection dans des systèmes fortement stratifiés tels que les intérieurs stellaires, dont la zone convective est potentiellement mieux modélisée en ayant recours à l'approximation anélastique qui considère la convection comme une perturbation par rapport à un état de référence stratifié adiabatiquement. À l'aide de simulations numériques directes, nous étudions l'influence de la stratification en densité du système sur les propriétés des champs magnétiques engendrés par effet dynamo. Nos analyses tendent à souligner la robustesse des résultats de géodynamo sur la structure et l'intensité du champ magnétique, lesquels semblent ainsi rester pertinents dans le cadre de l'étude des dynamos stellaires.

Mots-clefs : convection – dynamo – magnétohydrodynamique (MHD) – approximation anélastique – simulations numériques – étoiles : champ magnétique

Cette thèse a été réalisée au sein du LERMA (Laboratoire d'Études du Rayonnement et de la Matière en Astrophysique et Atmosphères), UMR 8112, sur le site du Laboratoire de Radioastronomie de l'École normale supérieure, situé au numéro 24 de la rue Lhomond, dans le 5^{e} arrondissement de Paris.

Abstract

Dynamo action, i.e. the self-amplification of a magnetic field by the flow of an electrically conducting fluid, is considered to be the main mechanism for the generation of the magnetic fields of stars and planets. Intensive and systematic parameter studies by direct numerical simulations using the Boussinesq approximation revealed fundamental properties of these models. However, this approximation considers an incompressible conducting fluid, and is therefore not adequate to describe convection in highly stratified systems like stars or gas giants. A common approach to overcome this difficulty is then to use the anelastic approximation, that allows for a reference density profile while filtering out sound waves for a faster numerical integration. Through a systematic parameter study of spherical anelastic dynamo models, we investigate the influence of the stratification on the dynamo mechanisms, and compare them with previous results obtained in the Boussinesq approximation. We discuss the influence of the density stratification on the field geometry and the field strength. Our results are in overall agreeement with the previous geodynamo studies, and thus the main established results seem to be still relevant to the study of stellar dynamos.

Title: Numerical modelling of the solar and stellar magnetism

Key words: convection – dynamo – magnetohydrodynamics (MHD) – anelastic approximation – numerical simulations – stars: magnetic field

Sommaire

Remerciements **iii**

Résumé **v**

Abstract **vii**

Sommaire **xi**

Liste des tableaux **xiii**

Quelques notations **xv**

1 Introduction **1**
- 1.1 Du magnétisme à la théorie dynamo 1
- 1.2 Le champ magnétique solaire 4
  - 1.2.1 Le cycle solaire 4
  - 1.2.2 Une étoile parmi d'autres 8
- 1.3 Activités magnétiques stellaires 16
- 1.4 L'approche numérique 19
  - 1.4.1 La géodynamo 19
  - 1.4.2 Limitations 21
  - 1.4.3 De la Terre aux étoiles 23

2 Modélisation **27**
- 2.1 L'équation d'induction 27
- 2.2 Différentes approximations pour la convection 28
  - 2.2.1 Modèle compressible 29
  - 2.2.2 Modèle anélastique 32
  - 2.2.3 Modèle Boussinesq 35
- 2.3 Le système magnétohydrodynamique 36
- 2.4 Approximation numérique 38
  - 2.4.1 Présentation du code PARODY 39

2.4.2 Implémentation des équations anélastiques 41

3 Dynamos anélastiques 47
3.1 Topologie du champ magnétique 47
3.1.1 Paramètres de sortie 47
3.1.2 Dynamos dipolaires et multipolaires 48
3.1.3 Dipôle équatorial 51
3.1.4 Discussion 53
3.2 Influence de la distribution de masse 55
3.2.1 Bifurcations entre branches dynamos 56
3.2.2 Dipôle équatorial 58
3.3 Dynamos dipolaires et stratification 63
3.3.1 Bistabilité 63
3.3.2 Seuil du dipôle 64
3.3.3 Perte du dipôle 66
3.3.4 Mécanismes dynamos 70
3.4 Lois d'échelle 71
3.4.1 Scaling du champ magnétique 73
3.4.2 Scaling du champ de vitesse 74
3.4.3 Scaling du temps de dissipation ohmique 75
3.4.4 Scaling du Nusselt 76
3.4.5 Discussion 77

4 Intermittence 79
4.1 *On-off* : notion de bruit multiplicatif 80
4.1.1 Un modèle simple 80
4.1.2 Propriétés caractéristiques 81
4.1.3 Influence du spectre du bruit 83
4.1.4 Bilan 83
4.2 Dynamos de Couette sphérique 83
4.2.1 Contexte et motivations 83
4.2.2 Équations 84
4.2.3 Simulations numériques directes 87
4.2.4 Discussion 91
4.3 Dynamos stellaires : symétries et modulations 97
4.3.1 Contexte 97
4.3.2 Résultats 98
4.3.3 Bilan 101

5 Conclusion **103**
5.1 Bilan général 103
5.2 Perspectives 105

A Validation du code **109**

B Publications **111**
B.1 *Intermittency in spherical Couette dynamos* 111
B.2 *Anelastic dynamo simulations* 118
B.3 *Influence of the mass distribution* 132
B.4 *Dipolar dynamos in stratified systems* 142

C Prépublications **155**
C.1 *High order semi-Lagrangian advective schemes* 155
C.2 *Stellar dynamos : symmetries and modulations* 178

D Comptes rendus de conférences **189**
D.1 Journées de la SF2A 2014 189
D.2 18e Rencontre du Non-Linéaire 189

Bibliographie **191**

Liste des tableaux

1.1 Caractéristiques du Soleil 10
1.2 Quelques propriétés des étoiles de la séquence principale 10
1.3 Paramètres typiques des modèles de géodynamo 22
1.4 Quelques ordres de grandeur pour le Soleil 22

3.1 Lois d'échelle pour les modèles Boussinesq et anélastiques 77

A.1 Benchmark hydrodynamique 109
A.2 Benchmark dynamo stationnaire 110
A.3 Benchmark dynamo non stationnaire 110

Quelques notations

Vecteurs unitaires cartésiens	$\mathbf{e}_x$, $\mathbf{e}_y$, $\mathbf{e}_z$
Vecteurs unitaires sphériques	$\mathbf{e}_r$, $\mathbf{e}_\theta$, $\mathbf{e}_\varphi$
Perméabilité magnétique du vide	μ_0
Vitesse de la lumière	c
Constante de Boltzman	k_B
Constante de radiation	a
Unité de masse atomique unifiée	m_u
Constante universelle de gravitation	G
Rayons des sphères interne et externe	r_i, r_o
Taille de la zone convective	$d = r_\mathrm{o} - r_\mathrm{i}$
Facteur de forme de la coquille sphérique	$\chi = r_\mathrm{i}/r_\mathrm{o}$
Conductivité électrique	σ
Diffusivité magnétique	η
Cœfficient de dilatation	α
Chaleur spécifique à pression constante	c_p
Conductivité thermique	k
Diffusivité thermique	κ
Diffusivité turbulente d'entropie	κ_s
Index polytropique	n
Masse volumique	ϱ
Pression	p
Température	T
Entropie	s
Viscosité dynamique	ν
Vitesse	U,$\mathbf{u}$
Vitesse angulaire	Ω

Chapitre 1

Introduction

> *Ecco finalmente scoperto in quella parte del Cielo, che meritamente la più pura, e sincera stimar si deve, dico in faccia del Sole stesso, prodursi continuamente, ed in brevi tempi dissolversi innumerabile moltitudine di materie oscure, dense, e caliginose; eccoci una vicissitudine di produzioni, e disfacimenti, che non finirà in tempi brevi; ma, durando in tutti i futuri secoli, darà tempo a gl'ingegni umani di osservare quanto lor piacerà, e di apprendere quelle dottrine, che del sito loro gli possa rendere sicuri.*
>
> Galileo (1613)

1.1 Du magnétisme à la théorie dynamo

LA QUESTION de l'origine des champs magnétiques observés aujourd'hui dans l'Univers, aussi bien au niveau des planètes, des étoiles, que des galaxies, n'admet pas encore de réponse unanime. Si la première référence littéraire [1] connue du magnétisme est chinoise et remonte au IVe siècle av. J.-C., la première mention d'un instrument d'orientation reposant sur le magnétisme date de la publication, en 1044, du *Wujing Zongyao*, littéralement « Collection des plus importantes techniques militaires » [2]. En 1600, William Gilbert, médecin de la reine Élisabeth Ire, assimile pour la première fois la Terre à un gros aimant, grâce à une série d'expériences réalisées avec une *terrella*, modèle de petite Terre constitué d'un aimant dipolaire sphérique (cf. figure 1.1). En comparaison, la première détection du champ magnétique d'une étoile date seulement du début du XXe siècle : elle est due à George Ellery Hale qui sut interpréter la polarisation des raies spectrales dans les taches solaires à partir de l'effet Zeeman (1897), et l'attribua ainsi à un champ magnétique de l'ordre de 3 kG (cf. figure 1.2).

---

[1] Wang Zu, *Livre du maître de la vallée du diable*.

[2] Sur l'histoire du magnétisme terrestre, voir Dormy (1997, ch. 1) et Le Mouël & Poirier (2013).

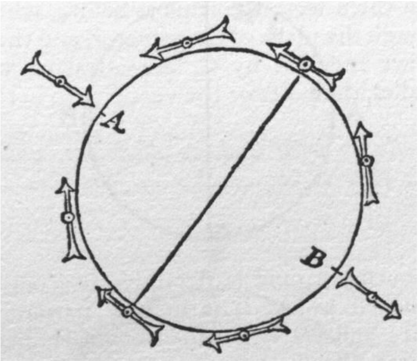

Figure 1.1 – *Terrella* (Gilbert 1600).

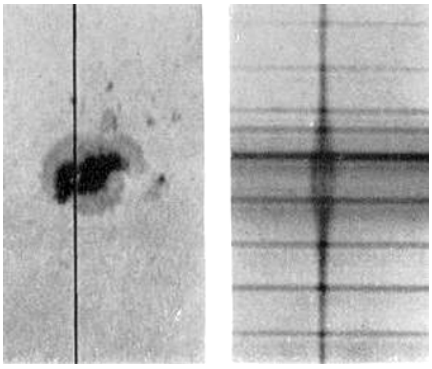

Figure 1.2 – Effet Zeeman (Hale *et al.* 1919).

> Thanks to Zeeman's discovery of the effect of magnetism on radiation it appeared that the detection of such a magnetic field should offer no great difficulty, provided it were sufficiently intense. When a luminous vapor is placed between the poles of a powerful magnet the lines of its spectrum, if observed along the lines force, appear in most cases as doublets, having components circularly polarized in opposite directions. The distance between the components of a given doublet is directly proportional to the strength of the field. As different lines in the spectrum of the same element are affected in different degree, it follows that in a field of moderate strength many of the lines may be simply widened, while others, which are exceptionally sensitive, may be separated into doublets. Hale (1908)

Historiquement, c'est avant tout pour rendre compte du champ magnétique solaire que la théorie de la dynamo auto-excitée sera proposée une dizaine d'années plus tard.

En l'absence de source, le champ magnétique d'un corps conducteur de taille caractéristique l décroît sur une durée de l'ordre de quelques temps de diffusion magnétique $\tau_\eta = l^2/\eta$, où la diffusivité magnétique η est donnée par $\eta = 1/(\mu_0\sigma)$, σ étant la conductivité électrique et μ_0 la perméabilité magnétique du vide. Dans le cas de la Terre, une estimation[3] conduit à un temps magnétique τ_η de l'ordre de 200 000 ans, en prenant pour taille caractéristique le rayon du noyau $l = 3{,}48 \times 10^6$ m et une conductivité de l'ordre de 4×10^{-5} S m^{-1}. Il n'est donc pas possible d'avoir recours à un champ magnétique fossile pour expliquer l'origine du champ magnétique terrestre. En revanche, la nécessité d'avoir un mécanisme capable de régénérer le champ magnétique pourrait, de prime abord, paraître moins évidente dans le cas de systèmes de plus grande taille : une estimation naïve de τ_η

---

[3] Les ordres de grandeur sont tirés de Proctor & Gilbert (1994, ch. 1).

pour le Soleil donne un résultat de l'ordre de 10^{12} ans, soit un temps supérieur à l'âge de l'Univers. Même si cette estimation peut dans certains cas être réduite de plusieurs ordres de grandeur en estimant des diffusivités turbulentes (Chabrier & Küker 2006), la théorie du champ fossile constitue une explication plausible du magnétisme de certaines étoiles comme les étoiles de type A ; les plus fortes intensités de champs magnétiques de grande échelle observées — quelques Teslas pour les étoiles A, de l'ordre de 10^5 T pour les naines blanches, et jusqu'à 10^{11} T pour une étoile à neutrons — semblent en effet compatibles avec l'amplification du champ par conservation du flux lors de la formation de l'étoile par contraction (Charbonneau 2013). Toutefois, cette théorie peut difficilement rendre compte de la dynamique éventuelle du champ magnétique qui se manifeste parfois par des inversions de polarité, ou renversements, survenant par exemple de manière périodique à la surface du Soleil.

En 1919, Sir Joseph Larmor, physicien irlandais, proposa trois hypothèses pour expliquer le champ magnétique des taches solaires, dont celle qui allait donner naissance à la théorie de la dynamo auto-excitée.

> In the case of the sun, surface phenomena point to the existence of a residual internal circulation mainly in meridian planes. Such internal motion induces an electric field acting on the moving matter : and if any conducting path around the solar axis happens to be open, an electric current will flow round it, which may in turn increase the inducing magnetic field. In this way it is possible for the internal cyclic motion to act after the manner of the cycle of a self-exciting dynamo, and maintain a permanent magnetic field from insignificant beginnings, at the expense of some of the energy of the internal circulation.
>
> Larmor (1919)

En outre, Larmor nota que cette hypothèse permettrait également d'expliquer l'origine du champ magnétique terrestre, sous réserve que l'intérieur de la Terre fût fluide... ce qui sera effectivement établi à la fin des années trente (Gutenberg 1939), conduisant ainsi les scientifiques à repenser la théorie du magnétisme terrestre :

> To any given magnetic field at a given instant a fluid motion can be found which amplifies or de-amplifies this field at a prescribed rate, and continues to amplify or de-amplify it over a finite length of time.
>
> Elsasser (1946)

La théorie de l'effet dynamo vise donc à décrire les processus par lesquels un fluide conducteur en mouvement agit afin de maintenir un champ magnétique (Moffatt 1978). Le déplacement d'un fluide conducteur soumis à un champ magnétique crée un déplacement de charges à l'intérieur du fluide. Dans certains cas, le courant électrique engendré par ce phénomène d'induction électromagnétique peut donner naissance à un nouveau champ magnétique qui vient renforcer le premier. Cette création de champ magnétique s'oppose à la dissipation ohmique des courants électriques. Ce rapport est mesuré qualitativement par le nombre de Reynolds magnétique

$$\mathrm{Rm} = \mu_0 \sigma U L = \frac{UL}{\eta}, \tag{1.1}$$

où L et U représentent respectivement l'échelle et la vitesse typiques de l'écoulement. Le nombre de Reynolds magnétique est relié au nombre de Reynolds usuel $\mathrm{Re} = UL/\nu$ faisant intervenir la viscosité cinématique du fluide ν par la relation

$$\mathrm{Rm} = \mathrm{Re}\,\mathrm{Pm} \qquad \text{avec} \qquad \mathrm{Pm} = \frac{\nu}{\eta}. \tag{1.2}$$

Un champ magnétique ne pourra être auto-amplifié que si les processus d'induction sont plus importants que la dissipation ohmique, ce qui implique donc que Rm soit au minimum de l'ordre de l'unité au seuil de l'instabilité dynamo. Celle-ci se manifeste par la croissance exponentielle d'un champ magnétique à partir d'une perturbation infinitésimale. En pratique, ce phénomène est souvent observé pour des écoulements turbulents de fluides caractérisés par de faibles valeurs du nombre de Prandtl magnétique Pm. Lorsque le champ magnétique engendré devient suffisamment fort, il agit en retour sur le fluide via la force de Lorentz, et l'instabilité sature généralement dans un état d'équilibre. D'un point de vue énergétique, l'effet dynamo peut être vu comme une conversion partielle d'énergie cinétique en énergie magnétique par l'intermédiaire de courants électriques.

1.2 Le champ magnétique solaire

1.2.1 Le cycle solaire

La découverte de Hale a permis d'établir l'origine magnétique des taches solaires vers lesquelles s'étaient tournées les premières lunettes astronomiques au début du XVII$^{\text{e}}$ siècle[4]. Comme on peut le voir sur les figures 1.3(a) et 1.3(b), le disque solaire apparaît parsemé, dans le domaine visible, de taches sombres dont le diamètre varie de 7 000 km à plus de 60 000 km, les taches étant alors visibles à l'œil nu. Le fort champ magnétique présent au niveau des taches solaires tend à inhiber le flux de chaleur transporté par convection et conduit ainsi à une diminution de la température de surface. Localement, le rayonnement émis est donc moins intense, et ces zones nous apparaissent sous la forme de taches sombres (cf. figures 1.3(b) et 1.3(c)).

---

[4] Pour une introduction historique sur les taches solaires, voir Thomas & Weiss (2008, ch. 2). Pour une présentation plus générale des dynamos stellaires, voir Charbonneau (2013).

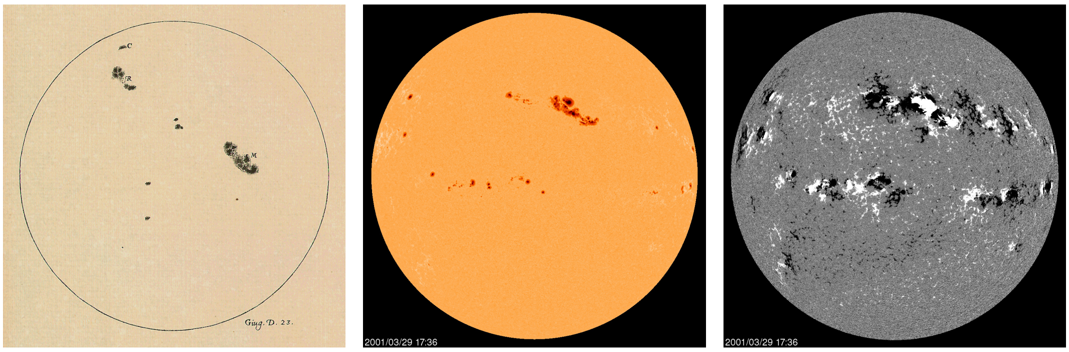

(a) Galilée (23 juin 1613). (b) SOHO (29 mars 2001). (c) Magnétogramme.

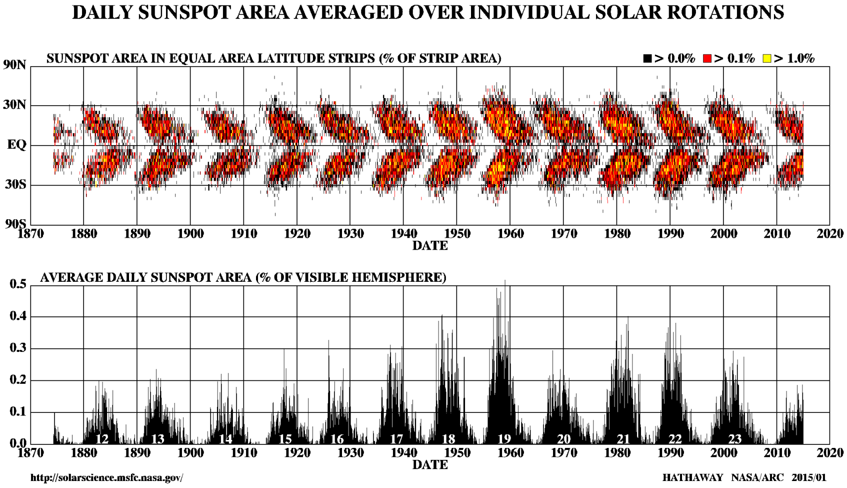

(d) Évolution de la position et du nombre de taches en fonction du temps.

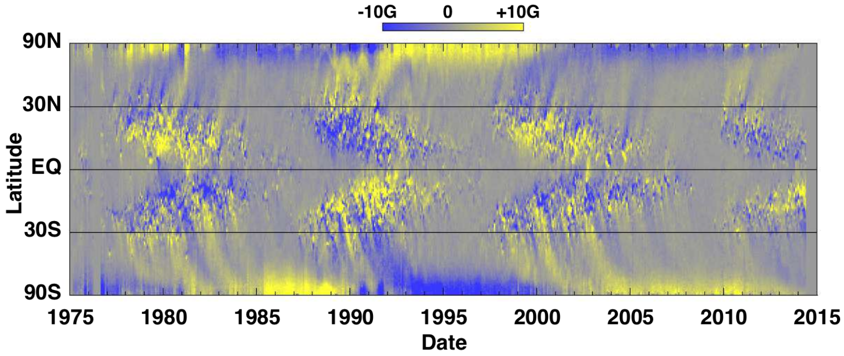

(e) Diagramme papillon magnétique reconstruit à partir du champ magnétique radial moyenné en longitude (obtenu à partir des données de Kitt Peak et SOHO).

Figure 1.3 – Taches et cycle solaires. (Sources : (a) galileo.rice.edu, (b,c) sohowww.nascom.nasa.gov, (d) solarscience.msfc.nasa.gov et (e) Hathaway (2015).)

Au XIXe siècle — soit plus de deux siècles après leur découverte — des observations systématiques ont révélé que le nombre et la position des taches solaires variaient au cours du temps. Bien que déjà détectable dans des données du XVIIIe siècle (dont celles de Herschel), le cycle solaire fut ainsi découvert par Heinrich Schwabe, pharmacien astronome qui observa systématiquement le Soleil pendant plus de quarante ans à la recherche d'une planète à l'intérieur de l'orbite de Mercure… La première mention qu'il fit d'une possible périodicité dans les variations du nombres des taches solaires passa d'ailleurs relativement inaperçue (Schwabe 1844), et cette découverte ne retiendra vraiment l'attention qu'avec la publication du troisième volume du *Kosmos* de Humboldt.

> The numbers contained in the following table leave no room to doubt that at least from the year 1826 to 1850 the solar spots have shown a period of about ten years with maxima in 1828, 1837, and 1848, and minima in 1833 and 1843. I have had no opportunity of becoming acquainted with any continuous series of earlier observations, but I readily admit that the period may be a variable one.
>
> Schwabe, in Humboldt (1852)

La variation des taches solaires présente en effet une remarquable périodicité, laquelle donne leur aspect caractéristique aux diagrammes papillons dont la première construction a été établie quelques années avant la découverte du champ magnétique solaire par le couple Annie et Edward Walter Maunder (1904). Comme on le voit figure 1.3(d), ces diagrammes représentent l'évolution temporelle de la latitude moyenne des taches solaires et mettent clairement en évidence leur migration vers l'équateur, découverte par Carrington (1863). Le diagramme papillon de la figure 1.3(e) montre que ces motifs sont en fait la signature du cycle magnétique de l'étoile, dont le champ connaît une inversion de polarité tous les 11 ans (Babcock 1961). Le champ magnétique solaire présente ainsi un comportement temporel semblable à celui d'une onde dont la période est de 22 ans.

Toutefois, sur une échelle de 80 ans environ, l'amplitude du cycle n'apparaît pas constante mais modulée de manière apériodique, selon le cycle de Gleissberg (1939, 1971). De plus, l'analyse des taches solaires révèle des périodes d'activité réduite pendant lesquelles les taches peuvent presque entièrement disparaître de la surface du Soleil (cf. figure 1.4). Cependant, l'abondance de certains isotopes tels que le ^{10}Be contenu dans les calottes polaires — dont la production est modulée par la fréquences des éruptions solaires et la force du champ magnétique de l'héliosphère[5] — semble suivre les mêmes variations périodiques pendant le minimum de Maunder à la fin du XVIIe siècle (Eddy 1976) ; cela suggère que l'activité magnétique connaît seulement une baisse d'intensité (cf. figure 1.4(a)). Par

---

[5] Aussi appelé champ magnétique interplanétaire (CMI).

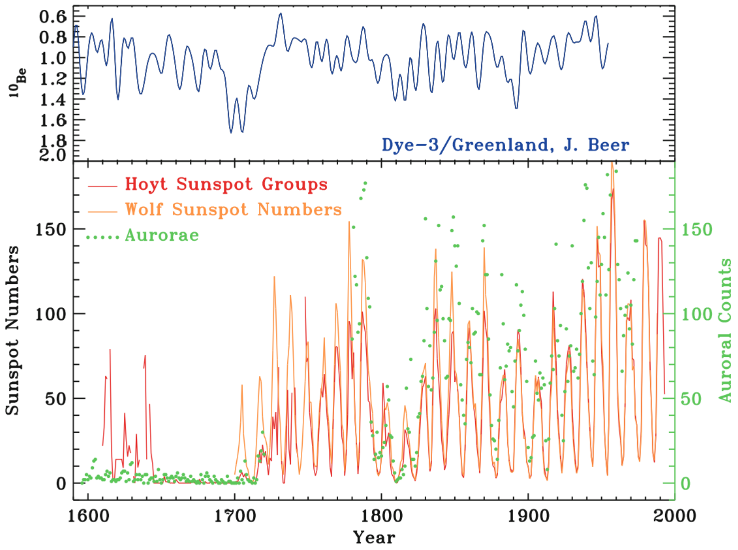

(a) Minimums de Maunder (1645–1715) et de Dalton (1790–1830), tels qu'ils ressortent des données du ^{10}Be (*haut*) ou du nombre de taches solaires et d'aurores (*bas*). Tiré de Charbonneau (2013).

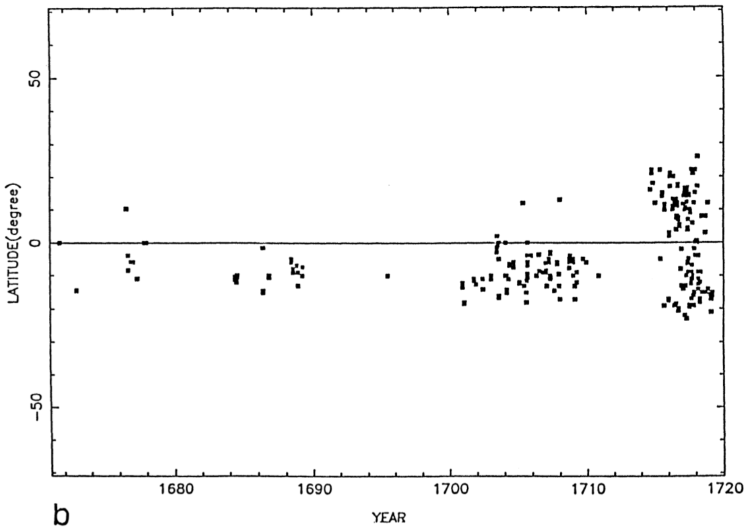

(b) Répartition des taches solaires à la fin du minimum de Maunder. Tiré de Sokoloff & Nesme-Ribes (1994).

Figure 1.4 – Modulations du cycle solaire.

ailleurs, ainsi que l'avait remarqué l'astronome allemand Gustav Spoerer (1889) [6], la répartition des taches solaires n'a pas toujours été symétrique par rapport à l'équateur : sur la figure 1.4(b), les taches solaires apparaissent essentiellement localisées dans l'hémisphère sud pendant le minimum de Maunder. Une telle localisation hémisphérique du champ magnétique est également observée à la surface de la planète Mars — dont la dynamo n'est plus active — (Langlais & Quesnel 2008) et pourrait résulter d'une interaction entre modes de différentes parités par rapport à la symétrie équatoriale (Gallet & Pétrélis 2009).

Enfin, l'analyse de l'abondance du ^{14}C présent dans les cernes des arbres a permis de retracer les variations de l'activité magnétique solaire sur les 11 000 dernières années et a révélé la présence de 27 grands minimums espacés de manière irrégulière à des intervalles de 200–300 ans, parmi lesquels on distingue les minimums « courts » d'une durée de 30 à 90 ans — semblables à celui de Maunder —, et les minimums « longs » d'une durée supérieure à 110 ans — semblables à celui de Spörer (Usoskin *et al.* 2007). La variation de l'activité solaire basée sur la mesure du ^{14}C est illustrée figure 1.5. Ces modulations de l'amplitude du cycle solaire sont susceptibles d'avoir un impact sur l'évolution du climat terrestre, les minimums de Maunder et de Spörer coïncidant avec des périodes de refroidissement (Eddy 1976, Lockwood *et al.* 2010). Aussi de nombreuses études ont-elles tenté de prédire ces variations, dont l'origine pourrait être liée aux effets de fluctuations stochastiques (Schmitt *et al.* 1996, Choudhuri & Karak 2012, Hazra *et al.* 2014) ou de chaos déterministe, étant donnée le caractère intrinsèquement non-linéaire du système (ch. 6, Dormy & Soward 2007, Weiss 2011).

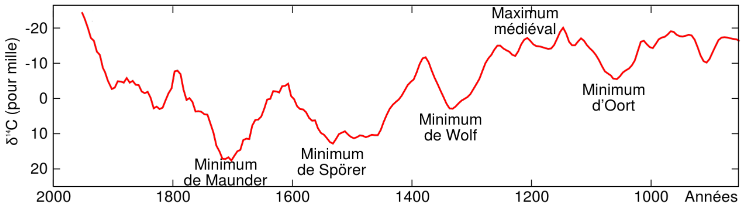

Figure 1.5 – Variation de l'activité solaire basée sur la mesure du ^{14}C jusqu'en 1950 environ. (Source : d'après Wikipédia).

1.2.2 Une étoile parmi d'autres

Caractéristiques du Soleil et classification

Étoile la plus proche de la Terre et donc la mieux observée, le Soleil est naturellement devenu la pierre de touche de toutes les théories relatives aux étoiles [7]. Il

---

[6] Il lui revient également la découverte du minimum dit de Maunder entre 1645 et 1715.

[7] Pour une introduction détaillée, voir Schatzman & Praderie (1990) ou Christensen-Dalsgaard (2008).

n'en reste pas moins une étoile naine banale dont les principales caractéristiques sont résumées table 1.1. Au début du XX^e siècle, les astronomes de Harvard ont classé les étoiles en fonction de leur type spectral, désigné par la séquence O B A F G K M. Cette séquence repose sur la modification de l'aspect des raies d'absorption et décrit des populations d'étoiles dont la masse et la température de surface vont décroissant, comme indiqué table 1.2. Chaque type spectral est subdivisé en dix sous-catégories (G0,G1…G9) classées par ordre de température de surface décroissante. De plus, une étoile est aussi caractérisée par sa classe de luminosité, qui comprend cinq catégories principales : supergéantes (I), géantes lumineuses (II), géantes (III), sous-géantes (IV) et étoiles de la séquence principale, également appelées naines (V). Cette classification spectrale à deux dimensions constitue une grille de référence permettant une première reconnaissance des propriétés d'une étoile et se présente, la plupart du temps, sous la forme d'un diagramme de Hertzsprung-Russel, dont un exemple est donné figure 1.6.

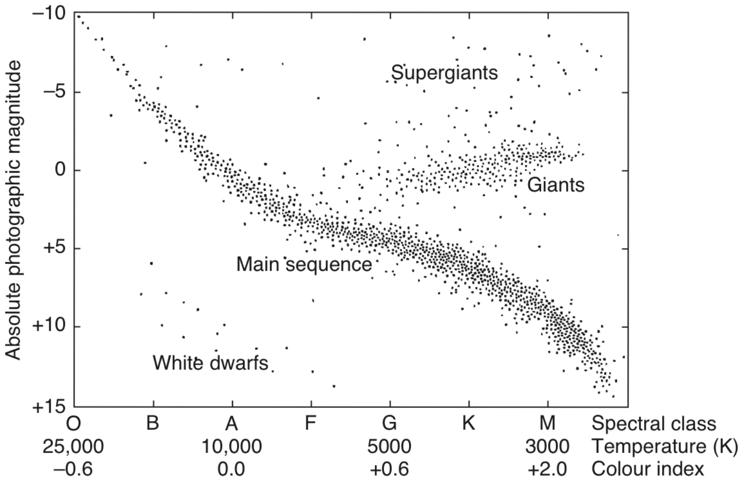

Figure 1.6 – Diagramme de Hertzsprung-Russel. D'après Abel (1964).

Structure interne

La structure interne du Soleil est généralement subdivisée en trois zones, comme on le voit dans la partie supérieure de la figure 1.7. L'énergie rayonnée par l'étoile est générée au niveau du cœur par réactions nucléaires ; elle est transférée vers l'extérieur, d'abord par radiation jusqu'à environ 0,7 $R_\odot$, puis par convection jusqu'à la surface. La signature de la convection thermique se traduit en surface par un motif caractéristique dit de granulation, visible en périphérie sur la figure 1.8. Ce motif est constitué de granules clairs correspondant à du plasma chaud arrivant

Table 1.1 – Caractéristiques du Soleil. D'après Dormy & Soward (2007, p. 286) et Thomas & Weiss (2008).

Grandeur	Valeur	Unité
type spectral	G2 V	
âge	$4{,}57 \times 10^9$	an
rayon ($R_\odot$)	$6{,}96 \times 10^8$	m
masse ($M_\odot$)	$1{,}99 \times 10^{30}$	kg
luminosité ($L_\odot$)	$3{,}84 \times 10^{26}$	W
température centrale	$15{,}6 \times 10^6$	K
température de surface	$5{,}78 \times 10^3$	K
masse volumique centrale	$1{,}5 \times 10^5$	$\mathrm{kg\,m^{-3}}$
masse volumique de surface	$2{,}0 \times 10^{-4}$	$\mathrm{kg\,m^{-3}}$
diamètre de la granulation de surface	10^3	km
champ magnétique de grande échelle	5×10^4	nT (0,5 G)
champ magnétique des taches solaires	0,3	T (3 000 G)
période de rotation à l'équateur	25	jour
période de rotation à 60° de latitude	29	jour
distance Terre-Soleil	$1{,}5 \times 10^{11}$	m

Table 1.2 – Quelques propriétés des étoiles de la séquence principale. D'après Thomas & Weiss (2008).

Type spectral	Masse $M/M_\odot$	Rayon $R/R_\odot$	Luminosité $L/L_\odot$	T_{eff} K
O5	58	14	800 000	46 000
B0	16	5,7	16 000	29 000
B5	5,4	3,7	750	15 200
A0	2,6	2,3	63	9 600
A5	1,9	1,8	24	8 700
F0	1,6	1,5	9,0	7 200
F5	1,35	1,2	4,0	6 400
G0	1,08	1,05	1,45	6 000
G2	1,0	1,0	1,0	5 780
G5	0,95	0,98	0,70	5 500
K0	0,83	0,89	0,36	5 150
K5	0,62	0,75	0,18	4 450
M0	0,47	0,64	0,075	3 850
M5	0,25	0,36	0,013	3 200

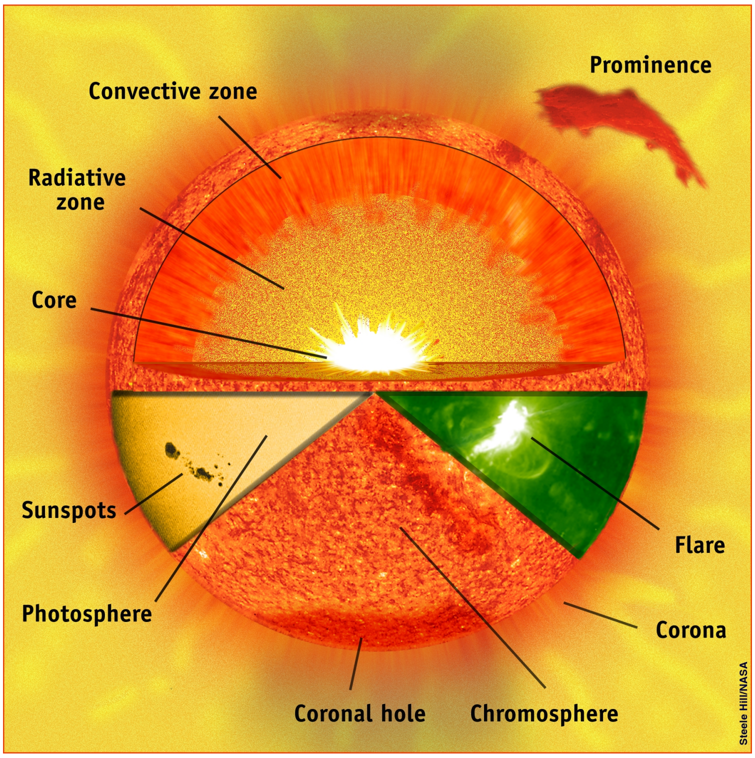

Figure 1.7 – Vue schématique du Soleil et de sa structure interne. (sohowww.nascom.nasa.gov)

en surface, cernés de filaments plus sombres correspondant à des écoulements descendants légèrement plus froids (la différence de température est de l'ordre de 400 K). Un granule a une taille caractéristique de l'ordre de 1 000 km et une durée de vie de 8 à 20 minutes. L'écoulement du plasma à l'intérieur des granules peut atteindre des vitesses supersoniques de plus de 7 km s^{-1}. En plus de ce réseau d'écoulements ascendants et descendants, des motifs convectifs de plus grande échelle ont également été détectés (cf. Rieutord & Rincon 2010).

Dès le XIX^{e} siècle, les observations directes ont révélé la rotation différentielle de la surface du Soleil dont les pôles tournent moins vite que l'équateur (Carrington 1863), mais ne permettent pas de sonder l'intérieur de l'étoile. Celui-ci a toutefois pu être révélé à partir des années 1980 (Brown *et al.* 1989) par l'étude des modes de vibration de la surface du Soleil[8], ou héliosismologie[9], qui a connu un important essor grâce aux données fournies par les instruments GOLF et MDI embarqués à bord du satellite SOHO (en service depuis le 2 décembre 1995). Comme le montre la figure 1.9, la rotation différentielle du Soleil présente les particularités suivantes :

— une accélération équatoriale de l'ordre de 23 % à la surface ;

— la rotation en bloc de la zone radiative.

---

[8] Les oscillations de l'étoile résultent la fois de la présence d'ondes sonores (modes p) et d'ondes de gravité (modes g).

[9] Revues sur le sujet : Miesch (2005), Gizon & Birch (2005), Howe (2009).

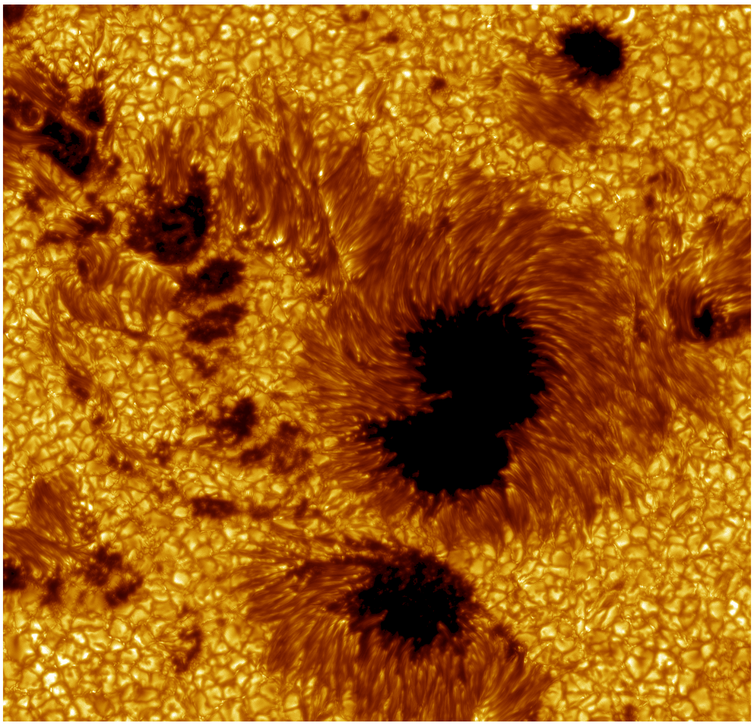

Figure 1.8 – Photographie de taches solaires prise le 15 juillet 2002 à une longueur d'onde de 487,7 nm, mettant en évidence la pénombre entourant les plus grosses taches. La granulation de la surface est visible en arrière plan. (www.solarphysics.kva.se)

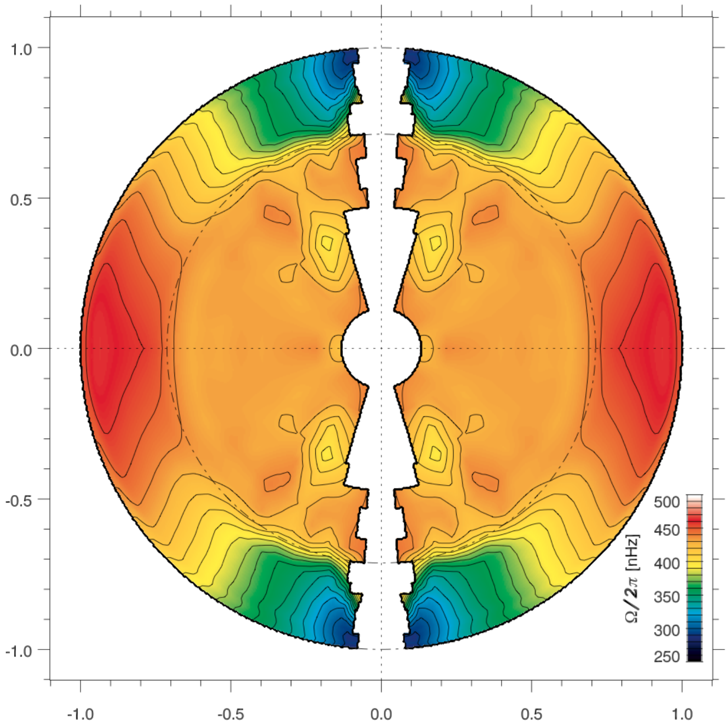

Figure 1.9 – Vitesse angulaire du Soleil en fonction de la profondeur et de la latitude. Ces données mettent en évidence la rotation différentielle entre les pôles et l'équateur s'étendant à l'intérieur de la zone convective, ainsi que la rotation en bloc de la zone radiative. Tiré de Korzennik & Eff-Darwich (2011).

La transition de la rotation différentielle à la rotation en bloc est remarquablement rapide puisqu'elle se fait dans une fine couche à la base de la zone convective : la tachocline (ainsi nommée par Spiegel & Zahn 1992) s'étend en effet sur moins de 4 % du rayon de l'étoile. Cette zone présente un important cisaillement de grande échelle ; aussi de nombreuses études lui attribuent-elles un rôle fondamental dans la génération du champ magnétique solaire (cf. Charbonneau 2010, 2013). Enfin, notons que les caractéristiques de la rotation différentielle sont susceptibles d'avoir été différentes par le passé, notamment pendant le minimum de Maunder où l'activité magnétique du Soleil était réduite (Ribes & Nesme-Ribes 1993).

Localisation de la zone convective

Dans la plupart des modèles de dynamos numériques, la convection thermique est toujours considérée comme étant la principale source de mise en mouvement du fluide conducteur, et ce, indépendamment du fait que l'objet premier d'étude soit la génération du champ magnétique terrestre ou solaire. Pour la Terre, le noyau de fer liquide est modélisé par une coquille sphérique de facteur de forme $\chi = 0{,}35$. En revanche, dans le cas du Soleil, la zone convective est localisée sous la surface dans une coquille sphérique relativement fine, et ne représente ainsi que 2 % de la masse totale du Soleil. Cependant, il n'en va pas de même pour toutes les étoiles : comme le montre la figure 1.10, les étoiles de type B possèdent un cœur convectif dont la taille s'étend à 30 % du rayon ; les étoiles de plus faible masse ont au contraire une zone convective localisée sous la surface dont l'épaisseur croît jusqu'à occuper la totalité de l'étoile pour les étoiles les plus légères.

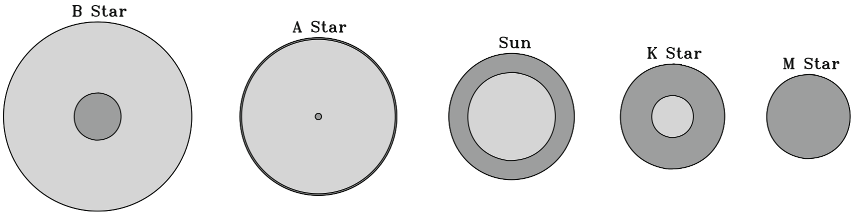

Figure 1.10 – Représentation schématique des zones radiatives (gris clair) et convectives (gris foncé) pour des étoiles de la séquence principale. La finesse de la zone convective externe pour une étoile de type A est volontairement exagérée car à cette échelle elle ne dépasserait pas l'épaisseur du trait délimitant la surface. Les tailles relatives de chaque type d'étoile ne sont pas non plus à l'échelle (cf. table 1.2). Tiré de Charbonneau (2013).

La condition de stabilité de l'équilibre mécanique d'un fluide, autrement dit l'absence de convection, est en général donnée par le critère de Schwarzschild (Lebovitz 1966, Kaniel & Kovetz 1967). Nous reprenons ici une présentation simplifiée où l'on néglige les effets de la viscosité et de la diffusion thermique (Landau

& Lifchitz 1971). Le raisonnement consiste à considérer un élément de fluide de masse volumique $\varrho(p,s)$, où p et s désignent la pression et l'entropie d'équilibre à l'altitude z, dans un champ de gravité $\mathbf{g} = -g\mathbf{e}_z$. Si cet élément de fluide subit une petite translation adiabatique de ξ vers le haut, sa masse volumique devient $\varrho(p',s)$, p' étant la pression à la hauteur $z+\xi$. L'équilibre du fluide est stable si l'élément en question tend à redescendre à sa position initiale, ce qui est le cas s'il est plus lourd que l'élément de fluide de masse volumique $\varrho(p',s')$ auquel il s'est substitué, s' étant l'entropie d'équilibre à la hauteur $z+\xi$. La condition de stabilité se traduit donc par l'inégalité sur les volumes spécifiques $V = 1/\varrho$

$$V(p',s') - V(p',s) > 0 . \tag{1.3}$$

En développant $s' = s + \xi \frac{\mathrm{d}s}{\mathrm{d}z}$, on obtient

$$\left(\frac{\partial V}{\partial s}\right)_p \frac{\mathrm{d}s}{\mathrm{d}z} > 0 , \tag{1.4}$$

qui se réduit en fait à l'inégalité

$$\frac{\mathrm{d}s}{\mathrm{d}z} > 0 . \tag{1.5}$$

En effet, en introduisant la chaleur spécifique à pression constante c_p et le cœfficient de dilatation α — supposé positif — définis par

$$c_p = T\left(\frac{\partial s}{\partial T}\right)_p > 0 , \tag{1.6}$$

$$\alpha = \frac{1}{V}\left(\frac{\partial V}{\partial T}\right)_p , \tag{1.7}$$

on constate que

$$\left(\frac{\partial V}{\partial s}\right)_p = \frac{T}{c_p}\left(\frac{\partial V}{\partial T}\right)_p > 0 . \tag{1.8}$$

De plus, en considérant l'entropie comme fonction de la température et de la pression, et en utilisant l'équilibre hydrostatique

$$\frac{\mathrm{d}p}{\mathrm{d}z} = -\varrho g , \tag{1.9}$$

sans oublier la relation de Maxwell $\left(\frac{\partial s}{\partial p}\right)_T = -\left(\frac{\partial V}{\partial T}\right)_p$, l'équation (1.5) peut se ramener à une condition de stabilité sur le gradient de température,

$$\frac{\mathrm{d}T}{\mathrm{d}z} > -\frac{g}{c_p}\alpha T . \tag{1.10}$$

On considérera par la suite le cas d'un gaz parfait pour lequel $\alpha = 1/T$, ce qui simplifie le membre de droite de l'équation (1.10).

Enfin, toujours d'après l'équation (1.5), on voit que la condition de stabilité marginale se traduit par une condition d'isentropie qui définit également le gradient adiabatique

$$\nabla s_a = 0 \iff \nabla T_a = \frac{\mathbf{g}}{c_p}. \tag{1.11}$$

La stabilité du fluide par rapport à la convection thermique va donc être déterminée par l'écart au gradient adiabatique (un gradient de température suradiabatique étant instable). En outre, si la vitesse caractéristique des mouvements convectifs est largement subsonique, il est raisonnable de faire l'hypothèse que l'écart au gradient adiabatique reste faible. Les modèles d'intérieurs stellaires (ou planétaires) confirment d'ailleurs que le gradient de température dans la zone convective n'est que légèrement au-dessus du gradient adiabatique. Une telle situation justifie donc une approche perturbative consistant à traiter la convection comme une perturbation par rapport à un état de référence isentropique. Ceci constitue l'hypothèse de base dans la dérivation de l'approximation anélastique que nous détaillerons dans le chapitre suivant, et dont les prémices remontent aux années cinquante (Batchelor 1953).

Enfin, ce raisonnement permet de comprendre qualitativement l'évolution de la zone convective des étoiles de la séquence principale en examinant la stabilité d'un modèle pour lequel le transport d'énergie se ferait uniquement par radiation. Sans rentrer dans les détails de calcul, on peut montrer dans ce cas que le gradient de température prend la forme (Christensen-Dalsgaard 2008, ch. 5 et 6)

$$\frac{\mathrm{d}T}{\mathrm{d}r} = -\frac{3\tilde{\kappa}\varrho L(r)}{16\pi a c r^2 T^3}, \tag{1.12}$$

où $\tilde{\kappa}$, a, c et $L(r)$ représente respectivement l'opacité[10], la constante de radiation, la vitesse de la lumière et la luminosité. À l'aide de l'équilibre hydrostatique $\frac{\mathrm{d}p}{\mathrm{d}r} = -Gm\varrho/r^2$ et de l'équation d'état du gaz parfait écrite sous la forme $p = \varrho T k_\mathrm{B}/(\mu m_\mathrm{u})$, l'équation (1.12) est en général réécrite sous la forme

$$\frac{\mathrm{d}\ln T}{\mathrm{d}\ln p} = \frac{3k_\mathrm{B}}{16\pi a c G m_\mathrm{u}} \frac{\tilde{\kappa}}{\mu} \frac{L(r)}{m(r)} \frac{\varrho}{T^3}. \tag{1.13}$$

L'instabilité convective apparaît lorsque le gradient de température radiatif excède le gradient adiabatique, ce qui tend à advenir préférentiellement dans les conditions suivantes :

— $\tilde{\kappa} \gg 1$. D'après la loi de Kramers, $\tilde{\kappa} \propto \varrho T^{-7/2}$, cette condition tend à être vérifiée dans les couches externes des étoiles de faible masse de la séquence

---

[10] L'opacité est définie à partir du libre parcours moyen λ par $\tilde{\kappa} = 1/(\lambda\varrho)$.

principale, ou plus généralement pour les étoiles dont la température de surface est faible ;

— $\varrho / T^3 \gg 1$, ce qui est aussi typiquement vérifié pour les couches externes des étoiles relativement froides ;

— $L(r)/m(r) \gg 1$, ce qui est typiquement vérifié pour les étoiles dont la masse est supérieure à 1,2 $\mathrm{M}_\odot$, pour lesquelles la fusion de l'hydrogène se fait principalement par le cycle CNO (Bethe 1939). Le taux de génération d'énergie croît alors rapidement avec la température et est donc fortement concentré au centre de l'étoile, favorisant ainsi l'apparition de cœurs convectifs.

Précisons qu'au cours de cette thèse nous n'avons jamais cherché en priorité à reproduire des modèles de dynamo « solaire » car nous considérerons le plus souvent des zones convectives relativement larges, dans les proportions du noyau externe terrestre. D'une part, la parallélisation du code que nous utilisons est plus efficace dans cette géométrie ; d'autre part, ce choix présente surtout l'avantage de faire plus facilement le lien avec les études de géodynamo précédentes qui ont naturellement servi de guide tout au long de nos travaux.

1.3 Activités magnétiques stellaires

Les progrès des techniques observationnelles ont non seulement révélé que le Soleil était loin d'être la seule étoile présentant une activité magnétique, mais ont aussi montré qu'il existe une très grande diversité des champs magnétiques stellaires. Ces champs magnétiques diffèrent en effet les uns des autres aussi bien par leur intensité ou par leurs structures spatiales, que du point de vue de leurs dynamiques temporelles.

Observations directes

Bien que le champ magnétique ne soit pas directement visible, on qualifie de directes les méthodes qui reposent sur l'effet Zeeman [11]. La méthode de détection la plus directe repose alors sur la mesure de la division des raies spectrales dont une illustration schématique est donnée figure 1.11. Toutefois, l'élargissement des raies spectrales ne résulte pas exclusivement de la présence d'un champ magnétique mais dépend également d'autres facteurs tels que la rotation, ce qui peut rendre délicate l'interprétation des données.

Un second moyen de détecter les champs magnétiques consiste à mesurer la polarisation de la lumière dans les raies spectrales due à l'effet Zeeman. La spectropolarimétrie, qui donne en plus des informations sur la géométrie du champ

---

[11] Revues sur le sujet : Donati & Landstreet (2009), Reiners (2012).

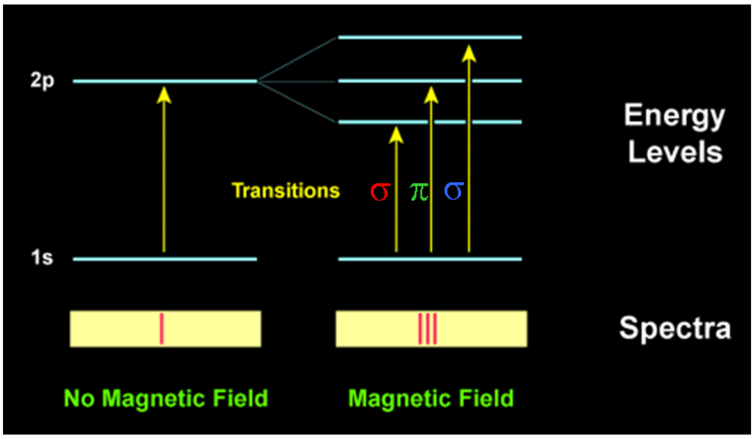

Figure 1.11 – Vue schématique de l'effet Zeeman. Tiré de Reiners (2012).

magnétique, connaît un essor depuis le début du XXI^{e} siècle avec le développement des spectropolarimètres tels que

- ESPaDOnS[12], développé à l'Observatoire Midi-Pyrénées (OMP) et installé au Canada-France-Hawaii Telescope (CFHT) à Hawaii depuis 2004 ;
- NARVAL[13], copie d'ESPaDOnS installée au Télescope Bernard Lyot à l'Observatoire du Pic du Midi depuis 2006 ;
- HARPSpol[14] installé dans l'hémisphère sud au télescope de 3,6 m de l'ESO (European Southern Observatory) depuis 2010 ;
- SPIRou[15], dont la mise en service au CFHT est prévue pour 2017.

La figure 1.12 illustre la diversité de la géométrie des champs magnétiques des étoiles de faible masse. Il n'est pas facile de déterminer quels paramètres gouvernent cette géométrie, qui peut notamment varier entre des étoiles dont la masse et la période de rotation sont pourtant similaires. Toutefois, Donati & Landstreet (2009) notent les tendances suivantes :

- lorsque $Ro \simeq 1$, les étoiles de plus de 0,5 $M_{\odot}$ ont tendance à générer des champs magnétiques avec une forte composante toroïdale et dont la composante poloïdale est principalement non axisymétrique ;
- les étoiles de moins de 0,5 $M_{\odot}$ présentent souvent de forts champs magnétiques de grande échelle, principalement poloïdaux et axisymétriques.

Observations indirectes

Les méthodes de détection du champ magnétique dites indirectes reposent sur la mesure d'émissions induites par le champ magnétique. La source de ces

---

[12] www.ast.obs-mip.fr/projets/espadons/espadons.html

[13] www.ast.obs-mip.fr/projets/narval/v1

[14] www.astro.uu.se/ piskunov/RESEARCH/INSTRUMENTS/HARPSpol

[15] www.cfht.hawaii.edu/en/projects/SPIRou/index.php

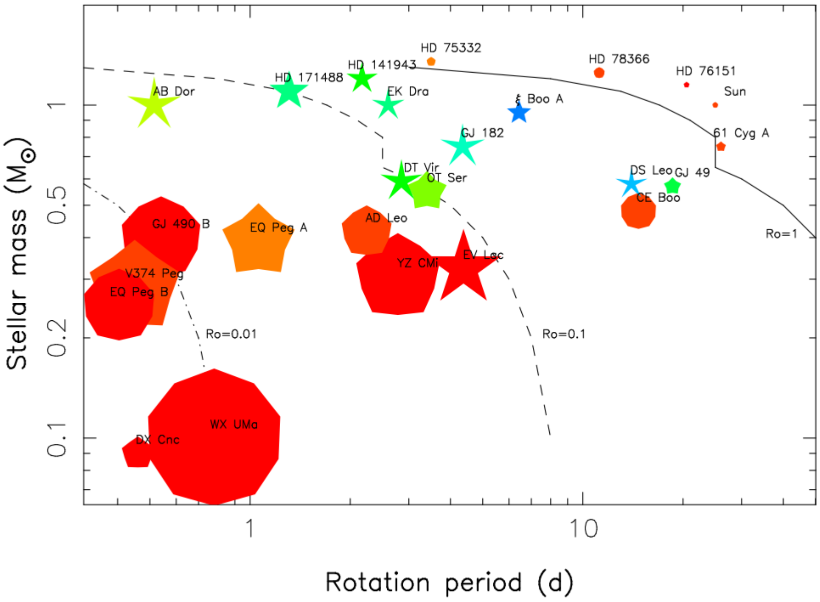

Figure 1.12 – Propriétés topologiques des champs magnétiques de grande échelle, d'après Donati & Landstreet (2009). La taille des symboles est proportionnelle à la densité d'énergie, la couleur indique la géométrie du champ magnétique (bleu/rouge pour un champ purement poloïdal/toroïdal), et la forme des symboles renvoie au degré d'axisymétrie de la composante poloïdale.

émissions est en général située au niveau de la chromosphère (Hall 2008). Plus accessibles que les mesures directes de la polarisation magnétique, elles ont pu fournir des informations sur les champs d'une large population d'étoiles ; ces observations tendent en effet à indiquer la présence de champ magnétique sur toutes les étoiles de la séquence principale de type F, G, K, M (*cool, late-type stars*).

Parmi ces méthodes, nous mentionnons tout particulièrement les émissions des raies H et K du Calcium ionisé CaII (respectivement à 396,8 et 393,4 nm) dont l'intensité n'est pas reliée à une augmentation de la température par radiation mais s'avère en réalité proportionnelle à la densité de flux magnétique. Schrijver *et al.* (1989) proposent la relation suivante, $(I_c - 0,13)/I_W = 0,008\,\langle fB\rangle^{0,6}$, où I_c et I_W désignent respectivement l'intensité du cœur et des ailes de la raie. La figure 1.13 montre qu'il existe bien une relation entre le rayonnement de CaII et l'intensité du champ magnétique à la surface du Soleil.

En 1966, Olin C. Wilson entreprit de mesurer à l'Observatoire du Mont Wilson les émissions de CaII H+K d'un échantillon d'étoiles de type solaire pour répondre à la question suivante, *Does the chromospheric activity of main-sequence stars vary with time, and if so, how ?* (Wilson 1978). De grande envergure, le HK Project a ainsi permis d'enregistrer les variations de l'activité chromosphérique de plus

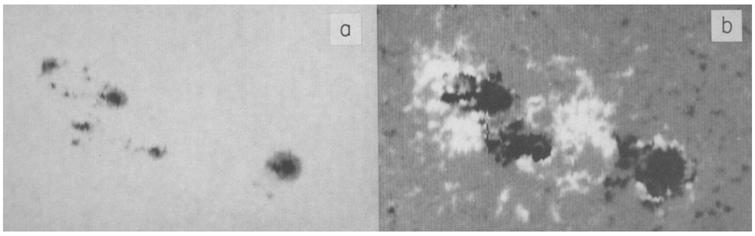

Figure 1.13 – Émission de la raie CaII K (a) et magnétogramme (b) d'une région active à la date du 22 octobre 1985. Tiré de Schrijver *et al.* (1989).

d'une centaine d'étoiles de types spectraux allant de F2 à M2, pendant plus de quarante ans (Baliunas *et al.* 1995, Oláh *et al.* 2009). La figure 1.14 illustre, grâce à trois exemples, les différents types de séries temporelles observées : certaines émissions sont constantes, d'autres plus ou moins chaotiques, mais l'on observe également des activités cycliques semblables à l'activité magnétique solaire. Des constatations empiriques indiquent d'une part que l'activité magnétique tend à augmenter lorsque la période de rotation diminue, et d'autre part que, dans le cas d'une activité cyclique, la période du cycle augmente avec la période de rotation de l'étoile (Charbonneau 2013, p. 199).

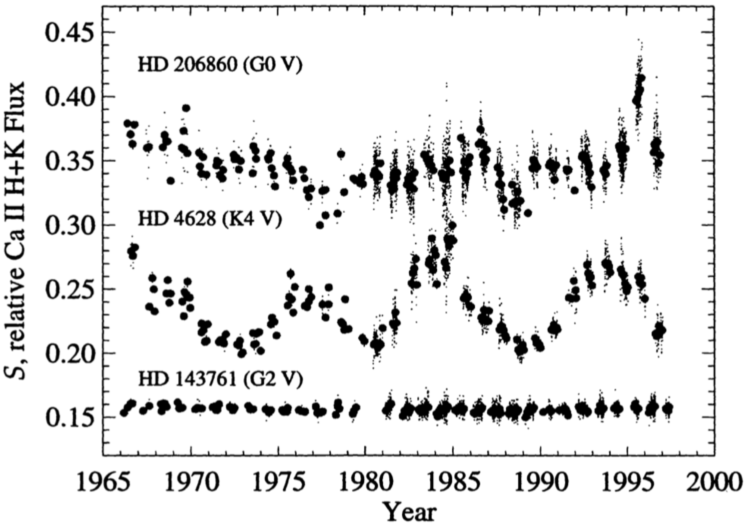

Figure 1.14 – Exemples de séries temporelles du flux de CaII H+K illustrant différents types de comportements : variable (HD 206860), cyclique (HD 4628) ou constant (HD 143761). Tiré de Baliunas *et al.* (1998).

1.4 L'approche numérique

1.4.1 La géodynamo

L'augmentation de la puissance des calculateurs a rendu possible l'intégration numérique du jeu complet des équations de la magnétohydrodynamique à partir des années 1990, alors qu'auparavant les études numériques étaient limitées à des

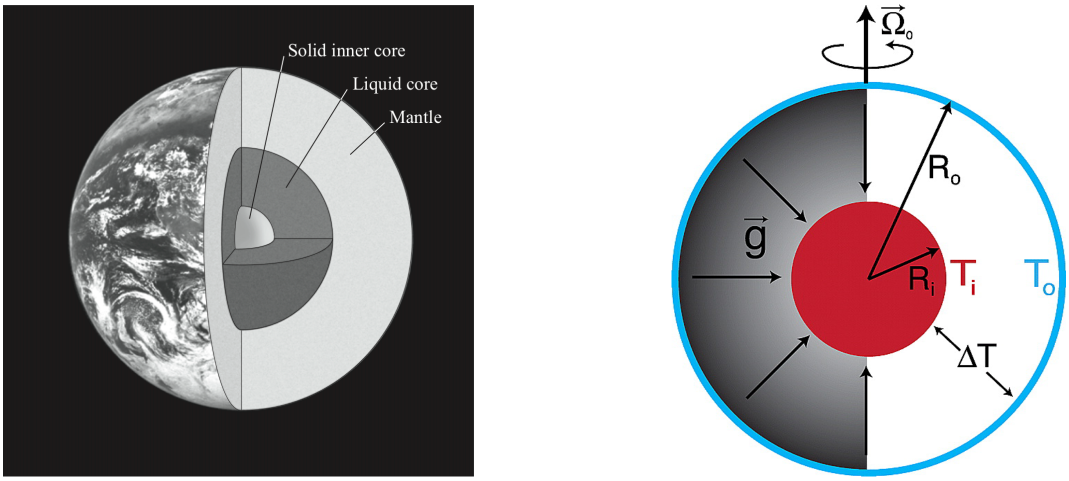

(a) Structure interne de la Terre.

(b) Modèle du noyau.

Figure 1.15 – Schémas des modèles de géodynamo. Tirés respectivement de Dormy & Soward (2007, p. 203) et King *et al.* (2010).

modèles dits de champ moyen[16]. À la suite de Glatzmaier & Roberts (1995), les simulations numériques directes ont connu un essor considérable, qui contraste d'autant plus avec le nombre restreint de dynamos expérimentales obtenues à ce jour : citons par exemple la dynamo de Karlsruhe (Stieglitz & Müller 2001) — inspirée de l'écoulement de G. O. Roberts (1970) —, la dynamo de Riga (Gailitis *et al.* 2000) — inspirée du modèle de Ponomarenko (1973) — et enfin la première dynamo fluide obtenue dans l'expérience VKS (Monchaux *et al.* 2007).

Dans les modèles numériques de géodynamo, seul le noyau externe de fer liquide est généralement pris en compte. Comme le montre la figure 1.15, il est simplement modélisé par une coquille sphérique de largeur $d = r_{\rm o} - r_{\rm i}$ en rotation à la vitesse angulaire $\mathbf{\Omega} = \Omega \mathbf{e}_z$. Le fluide conducteur contenu à l'intérieur a d'abord été décrit dans le cadre de l'approximation Boussinesq qui présente, entre autres, l'avantage de filtrer les ondes sonores. Enfin, la convection du fluide peut être simplement engendrée par une différence de température ΔT imposée entre la sphère interne et la sphère externe[17]. Les autres conditions aux limites sont les suivantes :

— non glissement aux parois pour le champ de vitesse ($\mathbf{u} = 0$) ; ce choix implique en général d'utiliser de hautes résolutions spatiales pour résoudre numériquement les couches limites qui se forment aux bords lorsque la viscosité s'équilibre avec la force de Coriolis et dont la taille caractéristique

---

[16] cf. Moffatt (1978, ch. 7) ou le chapitre rédigé par Rädler dans Molokov *et al.* (2007, p. 55).

[17] Pour une discussion des différents modes de chauffage possibles, voir Dormy (1997, ch. 4).

vérifie $\delta \sim (\nu/\Omega)^{1/2}$;

— raccord continu à un champ potentiel pour le champ magnétique,

$$\mathbf{B} = -\nabla\Phi \qquad \text{avec} \qquad \nabla^2\Phi = 0\,. \tag{1.14}$$

Quelques études choisissent parfois de considérer la graine comme un conducteur dont les propriétés magnétiques sont identiques à celles du fluide, ce qui implique alors de résoudre l'équation d'induction pour le champ magnétique dans la graine.

Les champs magnétiques obtenus avec ces modèles ont été répartis selon une classification binaire qui distingue les dynamos dipolaires dominées par un dipôle axial — à l'image du champ magnétique terrestre — des autres configurations magnétiques, désignées sous le terme générique de dynamos multipolaires. Christensen & Aubert (2006) ont montré que la transition d'une branche à l'autre semble être gouvernée par l'importance du terme inertiel $(\mathbf{u}\cdot\nabla)\mathbf{u}$ dans l'équation de Navier-Stokes. Cet équilibre est estimé par le calcul d'un nombre de Rossby local $Ro_\ell = U/(\Omega l)$, dans lequel l'échelle de longueur l ne correspond pas à la taille de la zone convective mais à une échelle caractéristique de l'écoulement (estimée en pratique à partir des spectres de l'énergie cinétique). Indépendamment de la manière dont on fait varier les paramètres de contrôle, on constate que la solution dipolaire est perdue lorsque l'inertie devient importante ; cela se traduit empiriquement par $Ro_\ell \gtrsim 0{,}1$.

1.4.2 Limitations

Malgré l'existence de similarités *a priori* encourageantes entre les dynamos numériques et certains champs magnétiques observés, la puissance des calculateurs est encore loin de permettre de résoudre les équations de la MHD dans des régimes de paramètres réalistes ; cela demanderait de résoudre une trop large gamme d'échelles spatiales et temporelles (contraignant ainsi drastiquement le pas de temps d'intégration et la résolution spatiale) [18]. Comme le montre la table 1.3, ces limitations se traduisent par un fossé de plusieurs ordres de grandeur entre les valeurs de paramètres accessibles numériquement et leur estimation pour le noyau terrestre. Il est donc délicat de savoir dans quelle mesure les modèles de dynamos numériques sont susceptibles de mettre en évidence des mécanismes génériques suffisamment robustes pour s'appliquer avec pertinence aux objets réels, ou si au contraire les similarités obtenues ne sont qu'apparentes et fortuites.

Face à cette difficulté, différentes stratégies peuvent être adoptées : essayer de comprendre la génération du champ magnétique dans l'espace de paramètres

---

[18] Au rythme actuel, il faudrait au moins un siècle avant de pouvoir réaliser des simulations numériques directes dans le « bon » régime de paramètres (Spruit 2011).

Table 1.3 – Paramètres typiques des modèles de géodynamo. D'après Roberts & King (2013).

Paramètre	Définition	Noyau	Simulations
Paramètres de contrôle			
E	$\nu/(2\Omega L^2)$	10^{-15}	$10^{-3}-10^{-5}$
Ra	$\alpha g L \Delta T/(2\Omega\kappa)$	10^{9}	$10^{5}-10^{7}$
Pr	ν/κ	10^{-1}	$10^{-1}-10^{1}$
Pm	ν/η	10^{-6}	$10^{-1}-10^{1}$
Paramètres de sortie			
Re	UL/ν	10^{9}	$40-10^{2}$
Rm	UL/η	10^{3}	$10^{1}-10^{3}$
Ro	$U/(2\Omega L)$	10^{-6}	$10^{-3}-10^{0}$
Λ	$B^2/(2\Omega\eta\mu_0\varrho)$	10^{0}	$10^{-1}-10^{1}$

Table 1.4 – Quelques ordres de grandeur pour le Soleil. D'après Dormy & Soward (2007, p. 286).

Paramètre	Définition	Zone convective (bas)	Photosphère
E	$\nu/(\Omega L^2)$	10^{-15}	10^{-17}
Ra	$gd^4(\nabla-\nabla_{\mathrm{ad}})/(\nu\kappa)$	10^{20}	10^{16}
Pr	ν/κ	10^{-6}	10^{-13}
Pm	ν/η	10^{-1}	10^{-7}
Re	UL/ν	10^{13}	10^{13}
Rm	UL/η	10^{11}	10^{6}
Ro	$U/(\Omega L)$	10^{-2}	10^{3}

accessible par simulations numériques directes, ou bien se rapprocher des conditions réelles en modélisant les petites échelles impossibles à résoudre (*large eddy simulations*). Cela revient la plupart du temps à supposer l'existence d'une séparation d'échelle et à dériver un jeu d'équations décrivant uniquement la dynamique des grandes échelles. On se retrouve alors face à un problème de fermeture, lequel est en général levé en faisant appel à une modélisation simple de la turbulence (et donc facilement critiquable). Nos travaux, ainsi que les études avec lesquelles nous tenterons de faire le lien, s'inscrivent dans la première approche, même si l'approximation que nous utilisons repose en partie sur des arguments de turbulence pour modéliser le flux de chaleur. Notons qu'à la suite du développement des théories de champ moyen dans les années cinquante, les modèles de dynamos convectives sont progressivement devenus l'approche la plus répandue pour comprendre la génération des champs magnétiques :

> Convection has become such an integral part of thinking about dynamos in stars that the subject of "stellar magnetic fields" has been almost synonymous with "convective dynamos" for decades.
>
> Spruit (2011)

1.4.3 De la Terre aux étoiles

Toute tentative de simulation directe de la convection solaire se heurte inévitablement à une difficulté inhérente aux valeurs des paramètres de contrôle : la table 1.4 donne une estimation de ces paramètres respectivement à la base et au sommet de la zone convective (photosphère). Indépendamment de ce problème, la question reste de savoir, d'une part, dans quelle mesure les résultats de géodynamo peuvent être pertinents pour l'étude des dynamos stellaires, et, d'autre part, comment le modèle développé pour le noyau terrestre peut être simplement adapté à la zone convective d'une étoile, en dépit des différences extrêmes entre ces corps. La réponse à cette question n'est sûrement pas unique, et nous mentionnerons seulement quelques tentatives dans cette direction dont nos travaux constituent en quelque sorte le prolongement.

Taille de la zone convective

De ce point de vue, une première différence notable entre la Terre et le Soleil réside au niveau des facteurs de forme de la zone convective, beaucoup plus fine dans le cas du Soleil. Goudard & Dormy (2008) ont ainsi montré que ce facteur purement géométrique pouvait être responsable d'une transition d'un dipôle à une solution oscillante.

Les conditions aux limites

Une autre modification relativement simple consiste à remplacer les conditions d'adhérence aux parois par des conditions de glissement, lesquelles ont été aussi proposées dans un premier temps pour les intérieurs planétaires (Simitev & Busse 2009). Schrinner *et al.* (2012) ont ainsi généralisé le critère de Christensen & Aubert (2006) séparant les différentes branches dynamos. Le principal changement dû à l'utilisation des conditions aux limites de glissement est l'apparition d'une transition hystérétique entre les branches dynamos. La saturation de la dynamo devient en effet sensible aux conditions initiales et l'on observe ainsi une zone bistable entre dipôles et multipôles : si le champ magnétique initial est faible, un fort vent zonal se développe du fait des conditions aux limites, ce qui favorise les dynamos multipolaires. En revanche, si le champ initial est un dipôle de forte amplitude, la rotation différentielle reste contrôlée par le champ magnétique ; le dipôle est donc une solution également stable.

Le profil de gravité

Dans les modèles de géodynamo, le noyau est assimilé à un corps homogène à symétrie sphérique, de telle sorte que le champ gravitationnel est de la forme $\mathbf{g} = g(r)\mathbf{e}_r$. Le théorème de Gauss appliqué à une sphère de rayon $r \in [r_\mathrm{i}, r_\mathrm{o}]$ s'écrit

$$\int_{S_r} \mathbf{g}\cdot\mathbf{n}\,\mathrm{d}S = -4\pi G \int_{V_r} \varrho\,\mathrm{d}V\,, \tag{1.15}$$

où G représente la constante de gravitation universelle et $\mathbf{n}$ le vecteur normal sortant à la sphère. On obtient donc

$$g4\pi r^2 = 4\pi G\varrho\frac{4}{3}\pi r^3 \implies g \propto r\,. \tag{1.16}$$

La variation linéaire de la gravité dans le noyau est en bon accord avec les modèles d'intérieur terrestre (modèle PREM, Dziewonski & Anderson 1981).

En revanche, on peut également considérer que la masse totale M est entièrement contenue dans la sphère interne, ce qui est une hypothèse raisonnable dans le cas du Soleil où la masse de la zone convective est de l'ordre de 0,02 $\mathrm{M}_\odot$. On obtient alors toujours avec le théorème de Gauss

$$g = -\frac{GM}{r^2}\,. \tag{1.17}$$

Les profils de gravité (1.16) et (1.17) sont, évidemment, des cas limites idéalisés. Le cas plus complexe auto-gravitant [19] dans lequel $\mathbf{g}$ peut varier à cause des mouvements convectifs n'est pas pris en compte, de même que la non sphéricité de l'objet

---

[19] En ce qui concerne l'équilibre d'une masse fluide en rotation, voir Poincaré (1885, 1892).

ou la force d'inertie d'entraînement due à la rotation. L'estimation de l'oblicité[20] du Soleil due à la rotation est de l'ordre de 0,001 %. En pratique, les déviations mesurées sont légèrement plus importantes et révèlent une corrélation avec les variations du champ magnétique solaire (Fivian *et al.* 2008). Par la suite, nous adopterons toujours l'hypothèse simplificatrice d'une distribution de masse centrale, indépendamment de la taille de la zone convective.

L'approximation convective

Enfin, la compressibilité d'un gaz n'étant pas comparable à celle d'un métal liquide, les zones convectives stellaires se présentent donc comme des milieux dans lesquels la stratification du fluide sous son propre poids est *a priori* moins négligeable que dans le noyau terrestre. Comme l'indique la table 1.1 page 10, la masse volumique du plasma solaire varie en effet de plusieurs ordres de grandeur entre le bas de la zone convective et la surface. En conséquence, la contrainte d'incompressibilité qui découle de l'approximation Boussinesq ne peut être satisfaite dans un tel système.

D'une manière plus générale, si les propriétés du fluide diffèrent significativement d'une extrémité à l'autre de la zone convective, il est légitime de s'attendre à une asymétrie entre les écoulements ascendants et descendants, telle qu'on l'observe par exemple au niveau de la granulation solaire, mais aussi dans des expériences de laboratoire (Dubois *et al.* 1978). Cette asymétrie ne peut être capturée par l'approximation de Boussinesq, laquelle revient à négliger les variations de la densité, *except in so far as they modify the action of gravity* (Rayleigh 1916), autrement dit, partout à l'exception du terme de poussée d'Archimède. Spiegel & Veronis (1960) ont montré que cette approximation permettait également de décrire, sous certaines conditions, la convection d'un gaz parfait.

> It has been shown that the equations governing convection in a perfect gas are formally equivalent to those for an incompressible fluid if the static temperature gradient is replaced by its excess over the adiabatic, c_v is replaced by c_p, and the following approximations are valid: (a) the vertical dimension of the fluid is much less than any scale height, and (b) the motion-induced fluctuations in density and pressure do not exceed, in order of magnitude, the total static variations of the quantities. Spiegel & Veronis (1960)

L'approximation de Boussinesq présente un double avantage : d'une part, d'un point de vue théorique, elle permet de simplifier les équations de manière à capturer le mécanisme d'instabilité avec une complexité minimale ; d'autre part, d'un point de vue pratique, le jeu d'équations est plus simple à intégrer car il filtre les

---

[20] L'oblicité désigne la différence de rayon entre les pôles et l'équateur.

ondes sonores, qui ne sont *a priori* pas essentielles pour comprendre la dynamique d'un écoulement pour lequel la vitesse du fluide est nettement inférieure à la vitesse du son.

Aussi l'un des enjeux consistait-t-il à dériver une autre approximation capable de décrire les écoulements convectifs à faible nombre de Mach dans des systèmes stratifiés. C'est ainsi que l'approximation anélastique a été développée en premier lieu pour décrire la convection atmosphérique (Ogura & Phillips 1962, Gough 1969) et a été reprise, par la suite, dans un modèle de convection thermo-compositionnelle du noyau terrestre (Braginsky & Roberts 1995). Lantz & Fan (1999) ont redérivé un modèle semblable pour les zones convectives solaires et stellaires. Jones *et al.* (2011) ont ensuite définis des cas tests numériques à partir de ce même modèle qui est parfois désigné dans la littérature sous le terme de *LBR anelastic approximation* (d'après les noms de Lantz, Branginsky et Roberts), afin de le distinguer d'autres variantes de l'approximation anélastique (Gilman & Glatzmaier 1981, Drew *et al.* 1995, Brun *et al.* 2004).

Dans cette thèse, nous étudierons les effets sur la génération du champ magnétique induits par le passage de l'approximation Boussinesq à l'approximation anélastique. Cela se traduit principalement par les conséquences suivantes :

- le choix d'une distribution de masse centrale ;
- l'introduction d'un profil de référence stratifié.

L'approximation anélastique et son implémentation numérique sont décrites dans le chapitre 2 et les résultats obtenus sont présentés au chapitre 3. Enfin, le chapitre 4 traite de l'apparition de différentes formes d'intermittence dans la dynamique temporelle de différents modèles de dynamos.

◆

Chapitre 2

Modélisation

> *On a former occasion I have shewn, that we have great reason to look upon the sun as a most magnificent habitable globe; and, from the observations which will be related in this Paper, it will now be seen, that all the arguments we have used before are not only confirmed, but that we are encouraged to go a considerable step farther, in the investigation of the physical and planetary construction of the sun. [...] But, if the Egyptians could avail themselves of the indications of a good Nilometer, what should inder us from drawing as profitable consequences from solar observations ?*
>
> Herschel (1801)

DANS CE CHAPITRE, nous introduisons le système d'équations que nous avons utilisé pour modéliser la génération du champ magnétique par la convection stellaire. Ce système est naturellement composé du couplage de l'équation d'induction et de l'équation de Navier-Stokes dans le régime de l'approximation anélastique. Nous discuterons les points qui nous semblent les plus importants, sans procéder à une dérivation mathématique exhaustive de ces modèles, dérivation que l'on peut retrouver dans les ouvrages de référence.

2.1 L'équation d'induction

L'équation décrivant l'évolution du champ magnétique **B** dérive des équations de Maxwell (Maxwell 1865, Jackson 1975)

$$\nabla \cdot \mathbf{E} = \frac{\varrho_\mathrm{e}}{\varepsilon_0}, \qquad \nabla \times \mathbf{E} = -\frac{\partial \mathbf{B}}{\partial t}, \tag{2.1a}$$

$$\nabla \cdot \mathbf{B} = 0, \qquad \nabla \times \mathbf{B} = \mu_0 \mathbf{j} + \frac{1}{c^2}\frac{\partial \mathbf{E}}{\partial t}, \tag{2.1b}$$

où **E**, **j**, ϱ_e, ε_0 et μ_0 désignent respectivement le champ électrique, la densité de courant, la densité de charge, la permittivité diélectrique et la perméabilité magnétique du vide. En magnétohydrodynamique classique, on fait l'hypothèse que les vitesses typiques sont faibles devant la vitesse de la lumière c ; l'équation de Maxwell-Ampère est alors simplifiée en

$$\nabla \times \mathbf{B} = \mu_0 \mathbf{j}. \tag{2.2}$$

eDans le même ordre d'approximation, la loi d'Ohm s'écrit, pour un conducteur en mouvement à une vitesse non relativiste **u**,

$$\mathbf{j} = \sigma \left(\mathbf{E} + \mathbf{u} \times \mathbf{B} \right), \tag{2.3}$$

où σ représente la conductivité électrique du fluide qui, pour simplifier, sera considérée comme constante. En combinant ces équations et en définissant la diffusivité magnétique $\eta = 1/(\mu_0 \sigma)$, nous obtenons l'équation d'induction

$$\frac{\partial \mathbf{B}}{\partial t} = \nabla \times (\mathbf{u} \times \mathbf{B}) + \eta \nabla^2 \mathbf{B}. \tag{2.4}$$

En l'absence de sources extérieures, cette équation décrit l'évolution du champ magnétique dans un fluide conducteur globalement neutre en mouvement, avec la contrainte $\nabla \cdot \mathbf{B} = 0$. La possibilité de définir une conductivité électrique suppose que le temps moyen séparant deux collisions entres électrons et ions soit court par rapport au temps caractéristique des mouvements du fluide. En outre, il faut que la trajectoire des électrons entre deux collisions successives soit faiblement modifiée par le champ magnétique pour que l'on puisse considérer la conductivité comme indépendante du champ magnétique. Le taux de collision des électrons doit donc également être plus élevé que la fréquence de Larmor eB/m_e, où e et m_e représentent respectivement la charge élémentaire et la masse d'un électron. Cette hypothèse est à l'origine de l'invariance de l'équation (2.4) sous la transformation $\mathbf{B} \to -\mathbf{B}$ et revient à négliger l'effet Hall qui apparaîtrait comme un terme non linéaire proportionnel à $\mathbf{j} \times \mathbf{B}$ dans la loi d'Ohm (Pétrélis 2011).

2.2 Différentes approximations pour la convection

La modélisation retenue considère que les mouvements du fluide résultent du transfert de chaleur vers l'extérieur par convection thermique. La description mathématique d'un tel système fait donc intervenir un système de plusieurs équations couplées : l'équation de conservation de la masse, l'équation de Navier-Stokes et l'équation de transfert thermique. Dans un premier temps, nous décrivons les différentes approximations de ce système dans un référentiel galiléen sans champ magnétique. Nous introduisons la notation suivante pour la dérivée lagrangienne

$$\frac{D}{Dt} = \frac{\partial}{\partial t} + (\mathbf{u} \cdot \nabla) \, . \tag{2.5}$$

2.2.1 Modèle compressible

La dérivation de ce système d'équations repose sur des lois de conservation, détaillées dans des ouvrages de référence tels que Batchelor (1967), Landau & Lifchitz (1971) ou Tritton (1988). Si l'on ne prend en compte que la viscosité et la poussée d'Archimède dans le bilan des forces, les équations reliant la masse volumique ϱ, la vitesse $\mathbf{u}$, la pression p, la température T et l'entropie massique s peuvent s'écrire sous la forme

$$\frac{\partial \varrho}{\partial t} + \nabla \cdot \left(\varrho \mathbf{u}\right) = 0 \, , \tag{2.6}$$

$$\varrho \frac{D\mathbf{u}}{Dt} = -\nabla p + \varrho \mathbf{g} + \mathbf{F}^{v} \, , \tag{2.7}$$

$$\varrho T \frac{Ds}{Dt} = -\nabla \cdot \mathbf{I}^{q} + Q^{v} \, . \tag{2.8}$$

La force visqueuse $\mathbf{F}^{v}$ dans l'équation de Navier-Stokes s'exprime comme la divergence du tenseur visqueux des contraintes d'un fluide newtonien, soit en notation tensorielle

$$F_i^{v} = \frac{\partial}{\partial x_j} \sigma'_{ij} \, , \tag{2.9}$$

avec

$$\sigma'_{ij} = 2\mu \left(e_{ij} - \frac{1}{3} e_{kk} \delta_{ij} \right) + \mu'' \delta_{ij} e_{kk} \, , \tag{2.10}$$

$$e_{ij} = \frac{1}{2} \left(\frac{\partial u_i}{\partial x_j} + \frac{\partial u_j}{\partial x_i} \right) . \tag{2.11}$$

La loi de comportement (2.10) faisant intervenir deux cœfficients de viscosité μ et μ'', on la simplifie, le plus souvent en faisant l'hypothèse dite de Stokes qui consiste à décomposer le tenseur des contraintes σ_{ij} en une composante de trace nulle σ'_{ij} (avec $\mu'' = 0$) et une composante isotrope $-p\delta_{ij}$. La pression est ainsi définie comme la moyenne des contraintes normales, $p = -\sigma_{ii}/3$. Notons que cette hypothèse supplémentaire n'est toutefois pas nécessaire si le fluide est incompressible, en vertu de l'égalité $\nabla \cdot \mathbf{u} = e_{kk} = 0$. Ces considérations posent en réalité le problème du sens des grandeurs thermodynamiques dans le système d'équations (2.6)–(2.8), et notamment du lien entre la pression thermodynamique et la pression « mécanique » définie ci-dessus. Si l'on suppose que l'on peut définir l'énergie interne massique du fluide ε à chaque instant, il devient alors possible de calculer une pression p_e à partir d'une équation d'état caractérisant en principe l'équilibre du fluide $p_e = f(\varrho, \varepsilon)$. Ensuite, le raisonnement consiste à supposer que l'écart entre la pression d'équilibre et la pression mécanique dépend linéairement des gradients de vitesse locaux

$$p - p_e = A_{ij} \frac{\partial u_i}{\partial x_j}. \tag{2.12}$$

Les arguments permettant d'aboutir à la loi de comportement (2.10) conduisent à la relation

$$p - p_e = -\zeta \nabla \cdot \mathbf{u}. \tag{2.13}$$

Le cœfficient de proportionnalité ζ est parfois appelé viscosité de compression et n'a *a priori* aucune raison d'être nul. Contrairement à la pression d'équilibre, la pression mécanique peut, en effet, dépendre des propriétés moléculaires du fluide. Il semble toutefois raisonnable de négliger ce cœfficient si l'on considère le modèle du gaz parfait monoatomique. Des observations de l'atténuation des ondes sonores à haute fréquence dans des gaz diatomiques ont permis de vérifier la relation (2.13) et tendent à indiquer que $\mu \sim \zeta$; quant à la viscosité de compression des liquides, elle reste peu connue (Batchelor 1967, Gad-el-Hak 1995).

Dans l'équation de transfert thermique (2.8), le terme Q^v correspond à la dissipation visqueuse

$$Q^v = \frac{\partial u_i}{\partial x_j} \sigma'_{ij} = 2\mu \left[e_{ij} - \frac{1}{3} e_{kk} \delta_{ij} \right]^2. \tag{2.14}$$

La forme de l'équation (2.8) présuppose, par ailleurs, qu'il n'y a pas d'autres termes sources de chaleur en volume.

Enfin, la fermeture du système d'équations requiert une relation phénoménologique qui permet d'exprimer le flux de chaleur $\mathbf{I}^q$ en fonction des variables du problème (De Groot & Mazur 1984). C'est ce que permet la loi de Fourier

$$\mathbf{I}^q = -k \nabla T, \tag{2.15}$$

où la conductivité thermique k se réduit à un scalaire — qui dépend en général de la température et de la pression — puisque l'on considère un milieu isotrope.

Le système d'équations (2.6)–(2.8) est cohérent avec le bilan énergétique

$$\frac{\partial E^{\text{tot}}}{\partial t} + \nabla \cdot \mathbf{I}^{\text{tot}} = 0, \tag{2.16}$$

en définissant l'énergie totale et son flux

$$E^{\text{tot}} = \varrho \left(\varepsilon + \varepsilon^c + \Phi\right), \tag{2.17}$$

$$\mathbf{I}^{\text{tot}} = \varrho \left(\varepsilon^c + h + \Phi\right) \mathbf{u} + \mathbf{I}^q + \mathbf{I}^v, \tag{2.18}$$

où $\varepsilon^c = \mathbf{u}^2/2$ représente la densité d'énergie cinétique, Φ le potentiel gravitationnel tel que $\mathbf{g} = -\nabla\Phi$, $h = \varepsilon + p/\varrho$ l'enthalpie massique, et $\mathbf{I}^v$ le flux d'énergie associé à la viscosité $I_i^v = -u_j \sigma'_{ji}$ tel que

$$\mathbf{u} \cdot \mathbf{F}^v = -\nabla \cdot \mathbf{I}^v - Q^v. \tag{2.19}$$

Cette cohérence reflète le respect du premier principe de la thermodynamique, en tant que principe de conservation. Le second principe de la thermodynamique est au contraire un principe d'évolution : une petite variation de l'entropie du système peut être décomposée sous la forme

$$\mathrm{d}S = \mathrm{d_e}S + \mathrm{d_i}S, \tag{2.20}$$

où $\mathrm{d_e}S$ désigne l'entropie échangée avec l'environnement et $\mathrm{d_i}S$ l'entropie créée à l'intérieur du système, soumise à la contrainte

$$\mathrm{d_i}S \geq 0. \tag{2.21}$$

Dans le cas d'un fluide, on écrit

$$S = \int_V \varrho s \,\mathrm{d}V, \tag{2.22}$$

$$\frac{D\,\mathrm{d_e}S}{Dt} = -\int_S \mathbf{I}^S \cdot \mathbf{n} \,\mathrm{d}S, \tag{2.23}$$

$$\frac{D\,\mathrm{d_i}S}{Dt} = \int_V \sigma \,\mathrm{d}V, \tag{2.24}$$

où $\mathbf{I}^S$ désigne le flux total d'entropie massique par unité de temps et σ le taux de création d'entropie. Ainsi, la décomposition (2.20) se réécrit sous la forme

$$\int_V \left(\frac{\partial \varrho s}{\partial t} + \nabla \cdot \mathbf{I}^S - \sigma\right) \mathrm{d}V = 0, \tag{2.25}$$

ce qui implique donc les deux relations suivantes

$$\frac{\partial \varrho s}{\partial t} + \nabla \cdot \mathbf{I}^S - \sigma = 0, \tag{2.26}$$

$$\sigma \geq 0. \tag{2.27}$$

À partir des équations (2.6) et (2.8), on obtient par identification

$$\mathbf{I}^S = \varrho s \mathbf{u} + \frac{\mathbf{I}^q}{T}, \tag{2.28}$$

$$\sigma = \mathbf{I}^q \cdot \nabla T^{-1} + \frac{Q^v}{T}. \tag{2.29}$$

On constate donc que la création d'entropie résulte bien de la présence des processus irréversibles de diffusion thermique et de dissipation visqueuse. En outre, le second principe contraint la positivité du cœfficient de viscosité dynamique μ, étant donné l'expression du chauffage visqueux (2.14). De même, la création d'entropie due à la diffusion thermique σ^k s'écrit en utilisant la loi de Fourier (2.15),

$$\sigma^k = k \frac{(\nabla T)^2}{T^2} \geq 0 \implies k \geq 0. \tag{2.30}$$

En revanche, le choix d'une autre relation phénoménologique pour modéliser le flux de chaleur peut ne plus garantir le respect du second principe. En anticipant sur la section suivante, on peut déjà constater que c'est, par exemple, le cas de la relation $\mathbf{I}^q \propto \nabla s$ qui est utilisée dans les modèles anélastiques, puisque le signe de $\sigma^k \propto \nabla T \cdot \nabla s$ est désormais quelconque.

2.2.2 Modèle anélastique

Comme nous l'avons déjà signalé, l'approximation anélastique est une approximation du système d'équations (2.6)–(2.8) qui cherche à décrire plus simplement des écoulements convectifs à bas nombre de Mach, notamment en filtrant les ondes sonores. Une dérivation détaillée de cette approximation se trouve dans les travaux de Braginsky & Roberts (1995, 2003, 2007). La même formulation a également été obtenue indépendamment par Lantz & Fan (1999) puis popularisée par Jones *et al.* (2011). L'idée à la base de ce modèle consiste à considérer la convection comme une perturbation par rapport à un état de référence stationnaire correspondant à un gaz parfait stratifié adiabatiquement à l'équilibre hydrostatique. On décompose donc la pression p, la densité ϱ et la température T sous la forme

$$f = f_a + f_c, \tag{2.31}$$

où $f_a = f_a(z)$ désigne la composante correspondant à l'état de référence et f_c la perturbation due à la convection telle que $f_c/f_a = O(\epsilon)$, où $\epsilon \ll 1$ mesure l'écart à l'état de référence adiabatique. On peut, par exemple, prendre pour définition $\epsilon = \frac{d}{c_p}\nabla s_a$. Le système anélastique peut être obtenu par un développement en puissances de ϵ et prend alors la forme

$$\nabla\cdot\left(\varrho_a \mathbf{u}\right) = 0\,, \tag{2.32}$$

$$\frac{D\mathbf{u}}{Dt} = -\nabla\left(\frac{p_c}{\varrho_a}\right) - \frac{s}{c_p}\mathbf{g} + \frac{\mathbf{F}^v}{\varrho_a}\,, \tag{2.33}$$

$$\varrho_a T_a \frac{Ds}{Dt} = -\nabla\cdot\mathbf{I}^q + Q^v\,. \tag{2.34}$$

Le premier point important à noter à propos de ce système concerne le terme de poussée d'Archimède qui se trouve simplement exprimé en fonction de l'entropie, mais dont l'expression naturelle serait

$$-\frac{1}{\varrho_a}\nabla p_c + \frac{\varrho_c}{\varrho_a}\mathbf{g}. \tag{2.35}$$

Cependant, en utilisant les relations thermodynamiques (1.6) et (1.7) et l'équilibre hydrostatique (1.9), on peut réexprimer les fluctuations de densité en fonction de l'entropie et de la pression,

$$\varrho_c = \left(\frac{\partial \varrho_a}{\partial s}\right)_p s + \left(\frac{\partial \varrho_a}{\partial p}\right)_s p_c = -\frac{\varrho_a}{c_p} s - \frac{1}{\varrho_a g}\frac{\partial \varrho_a}{\partial z} p_c\,. \tag{2.36}$$

La poussée d'Archimède peut donc s'écrire sans approximation supplémentaire

$$\frac{\varrho_c}{\varrho_a}\mathbf{g} = -\frac{s}{c_p}\mathbf{g} - \frac{p_c}{\varrho_a^2}\nabla\varrho_a\,, \tag{2.37}$$

conduisant ainsi à l'expression de Navier-Stokes (2.33). On voit notamment apparaître une pression réduite p_c/ϱ_a, dont le gradient joue le même rôle que le gradient de pression dans l'approximation de Boussinesq, à savoir celui d'un multiplicateur de Lagrange permettant de satisfaire la contrainte (2.32). Cette importante simplification caractérise la variante LBR du système anélastique et justifie, *a posteriori*, d'utiliser la formulation entropique de l'équation du transfert de chaleur (2.8) comme point de départ dans la dérivation de l'approximation anélastique (de préférence à une formulation équivalente basée sur la température, par exemple). Brown *et al.* (2012) ont montré que d'autres variantes de l'approximation anélastique ne conservent pas l'énergie. Leur approche repose sur l'étude des ondes de gravité dans un fluide stablement stratifié en négligeant les termes dissipatifs. En général, ces équations diffèrent de l'approximation LBR, soit par l'utilisation des fluctuations de température pour exprimer la poussée d'Archimède (Rogers & Glatzmaier 2005), soit par la prise en compte de termes proportionnels à ∇s_a, par essence négligeables dans l'hypothèse d'un état de référence adiabatique.

Une autre difficulté réside dans l'incorporation de la diffusion thermique, car l'approximation anélastique proprement dite ne présuppose aucune condition sur le traitement du flux de chaleur. Néanmoins, une utilisation naïve de la loi de Fourier habituelle conduirait à des incohérences. En effet, l'état de référence serait alors surdéterminé entre, d'une part l'hypothèse d'adiabaticité, et d'autre part, la condition de stationnarité qui aboutirait à la contradiction $\nabla \cdot \left(-k\mathbf{g}/c_p\right) = 0$. Cette difficulté peut être éludée en faisant l'hypothèse que le transport de chaleur sera principalement assuré par la turbulence, de telle sorte que l'on pourra négliger la contribution du flux de Fourier. Autrement dit, on utilise en réalité une équation de champ moyen qui repose nécessairement sur une relation de fermeture censée modéliser les petites échelles de la turbulence. Soit s^t le terme représentant les fluctuations turbulentes d'entropie tel que

$$\langle s^t \rangle = 0\,, \tag{2.38}$$

où les crochets $\langle\rangle$ désignent une procédure de moyenne permettant de définir l'entropie de grande échelle S ; le flux recherché va donc venir des corrélations entre ce terme s^t et le champ de vitesse turbulent $\mathbf{u}^t$, corrélations que l'on modélise en fonction du gradient de l'entropie moyenne,

$$I_i^{St} = \langle \varrho_a s^t \mathbf{u}^t \rangle_i = -\varrho_a \kappa_{ij} \frac{\partial S}{\partial x_j}\,. \tag{2.39}$$

L'hypothèse supplémentaire d'isotropie — certes discutable — permet de simplifier le cœfficient de proportionnalité $\kappa_{ij} = \kappa_s \delta_{ij}$. En outre, pour obtenir une équation de conservation, il est nécessaire d'introduire « à la main » un terme source d'entropie σ^t correspondant au flux $\mathbf{I}^{St}$,

$$\sigma^t = \mathbf{I}^{St} \cdot \nabla T_a^{-1} \ngeq 0\,. \tag{2.40}$$

C'est à ce prix qu'on obtient alors l'équation de transfert de chaleur telle qu'elle est utilisée,

$$\varrho_a T_a \frac{DS}{Dt} = -\nabla \cdot \left(\varrho_a T_a \kappa_s \nabla S\right) + Q^v\,. \tag{2.41}$$

Notons que si l'on utilise l'approximation anélastique pour modéliser une zone stablement stratifiée, comme c'est parfois le cas, on s'attend à ce que $\nabla S \cdot \nabla T \leq 0$, auquel cas ce système d'équation se trouve en contradiction avec le second principe de la thermodynamique. De plus, il convient d'ajouter que les arguments permettant d'arriver à cette équation deviennent d'autant plus douteux que l'on se trouve proche du seuil de convection. Les équations anélastiques ne sont alors plus nécessairement une bonne approximation du système compressible (Calkins *et al.* 2014, 2015).

Cependant, cette formulation présente aussi plusieurs avantages, ce qui explique sans doute pourquoi elle s'est finalement imposée dans la communauté scientifique. On constate ainsi que la température n'est plus une variable dynamique du problème. Il n'est donc pas nécessaire de calculer p_c, ϱ_c et T_c pour déterminer l'évolution temporelle du système, et le nombre d'inconnues est en fait le même que dans l'approximation Boussinesq (l'entropie ayant remplacé la température). De plus, on retrouve asymptotiquement l'approximation de Boussinesq dans la limite d'un état de référence faiblement stratifié (Jones *et al.* 2009). Nous ne serons d'ailleurs pas les premiers à faire preuve d'un certain pragmatisme :

> This simplification, which we hope is only mildly false, compensate for its deficiencies with enormous computational advantages.
>
> Depassier & Spiegel (1981)

2.2.3 Modèle Boussinesq

La convection thermique d'un fluide est le plus souvent étudiée avec le système suivant

$$\nabla \cdot \mathbf{u} = 0\,, \tag{2.42}$$

$$\frac{D\mathbf{u}}{Dt} = -\nabla\Pi - \alpha T_1 \mathbf{g} + \nu \nabla^2 \mathbf{u}\,, \tag{2.43}$$

$$\frac{DT_1}{Dt} = \kappa \nabla^2 T_1\,, \tag{2.44}$$

où $\kappa = k/(\varrho_0 c_p)$ désigne la diffusivité thermique du fluide. Cette approximation fut historiquement attribuée par Rayleigh à Joseph Boussinesq (Rayleigh 1916), lequel avait remarqué

> [...] la possibilité de négliger les variations de la densité, là où elles ne sont pas multipliées par la gravité g, tout en conservant, dans les calculs, leur produit par celle-ci. Grâce aux simplifications alors obtenues, la question, encore très difficile et presque toujours rebelle à l'intégration, n'est plus inabordable. Boussinesq (1903)

En effet, dans cette approximation, les variations des propriétés du fluide sont négligées, tout comme la chaleur engendrée par la dissipation visqueuse. Seules sont prises en compte les fluctuations de densité dans le terme de poussée d'Archimède, exprimées à partir d'une équation d'état simplifiée $\varrho = \varrho_0\,(1 - \alpha\,(T - T_0))$. Historiquement, cette approximation a d'abord été dérivée pour des liquides dont la densité ϱ et la température T restent proche de constantes ϱ_0 et T_0, et tels que la perturbation de densité $\varrho_1 = \varrho - \varrho_0$ ne dépend que de la perturbation de température $T_1 = T - T_0$. Étant donné que l'on néglige les perturbations de pression, la température et l'entropie deviennent équivalentes dans l'approximation

Boussinesq, puisque la relation thermodynamique

$$\mathrm{d}s = \frac{c_p}{T}\,\mathrm{d}T - \frac{\alpha}{\varrho}\,\mathrm{d}P\,, \tag{2.45}$$

nous donne $T_0 s_1 = c_p T_1$.

Formellement, l'approximation Boussinesq peut être dérivée de manière analogue à l'approximation anélastique, sous l'hypothèse que la taille caractéristique du domaine d est petite devant l'échelle de longueur caractéristique du fluide $g/(c_p T_r)$, où T_r désigne une température de référence. On peut en effet définir un paramètre d'expansion supplémentaire $\epsilon' = gd/(c_p T_r)$, et retrouver l'approximation Boussinesq dans la limite $\epsilon' \ll 1$, pour laquelle l'état de référence devient uniforme (Malkus 1964, Dormy & Soward 2007, ch. 1).

Cette approximation est souvent utilisée pour décrire des expériences de laboratoire dans lesquelles la stratification du fluide sous son propre poids peut être raisonnablement négligée ; étant donnée sa simplicité, elle a également servi de point de départ à la modélisation des dynamos naturelles.

2.3 Le système magnétohydrodynamique

Nous utilisons l'approximation anélastique LBR pour modéliser un fluide stratifié conducteur qui est en convection dans une coquille sphérique de largeur $d = r_\mathrm{o} - r_\mathrm{i}$ et de facteur de forme $\chi = r_\mathrm{i}/r_\mathrm{o}$, elle-même étant en rotation à la vitesse angulaire $\Omega\mathbf{e}_z$ (cf. figure 1.15(b) page 20). Le fluide est assimilé à un gaz parfait caractérisé par ses cœfficients de viscosité cinématique ν, de diffusivité turbulente d'entropie κ_s, de chaleur spécifique c_p et de diffusivité magnétique η, tous supposés constants. La convection est engendrée par une différence d'entropie ΔS imposée entre la sphère interne et la sphère externe. Si l'on suppose que le champ de gravité résulte d'une distribution de masse centrale, $\mathbf{g} = -GM\mathbf{e}_r/r^2$ avec G la constante de gravitation et M la masse contenue dans la sphère interne, alors l'état de référence polytropique donné par l'équilibre du système anélastique prend la forme

$$p_a = p_r\, w^{n+1}, \quad \varrho_a = \varrho_r\, w^n, \quad T_a = T_r\, w, \quad w = c_0 + \frac{c_1 d}{r}, \tag{2.46}$$

avec

$$c_0 = \frac{2w_\mathrm{o} - \chi - 1}{1-\chi}, \qquad c_1 = \frac{(1+\chi)(1-w_\mathrm{o})}{(1-\chi)^2}, \tag{2.47}$$

$$w_\mathrm{o} = \frac{\chi + 1}{\chi\exp(N_\varrho/n) + 1}, \qquad w_\mathrm{i} = \frac{1+\chi-w_\mathrm{o}}{\chi}, \tag{2.48}$$

où l'index polytropique n est relié à l'exposant adiabatique $\gamma = c_p/c_v$ par la relation $\gamma = (n+1)/n$, et où $N_\varrho = \ln\left[\varrho_a(r_\mathrm{i})/\varrho_a(r_\mathrm{o})\right]$ mesure le contraste de densité.

Les valeurs p_r, ϱ_r et T_r désignent respectivement la pression, la densité et la température de référence évaluées à mi-chemin entre la sphère interne et la sphère externe et servent d'unité pour les variables correspondantes. Les autres variables sont adimensionnées en utilisant les unités suivantes : d est pris comme unité de longueur, d^2/η comme unité de temps, ΔS comme unité d'entropie et $\sqrt{\Omega\varrho_c\mu_0\eta}$ comme unité de champ magnétique. Les équations MHD anélastiques s'écrivent alors (Jones *et al.* 2011)

$$\frac{\partial\mathbf{B}}{\partial t} = \nabla\times(\mathbf{u}\times\mathbf{B}) + \nabla^2\mathbf{B}, \tag{2.49}$$

$$\frac{D\mathbf{u}}{Dt} = \mathrm{Pm}\left[-\frac{1}{\mathrm{E}}\nabla\left(\frac{p_c}{w^n}\right) + \frac{\mathrm{Pm}}{\mathrm{Pr}}\mathrm{Ra}\frac{S}{r^2}\mathbf{e}_r - \frac{2}{\mathrm{E}}\mathbf{e}_z\times\mathbf{u} + \mathbf{F}^* + \frac{1}{\mathrm{E}\,w^n}(\nabla\times\mathbf{B})\times\mathbf{B}\right], \tag{2.50}$$

$$\frac{DS}{Dt} = w^{-n-1}\frac{\mathrm{Pm}}{\mathrm{Pr}}\nabla\cdot\left(w^{n+1}\nabla S\right) + \frac{\mathrm{Di}}{w}\left[\mathrm{E}^{-1}w^{-n}(\nabla\times\mathbf{B})^2 + Q^*\right], \tag{2.51}$$

avec les contraintes

$$\nabla\cdot\mathbf{B} = 0, \tag{2.52}$$

$$\nabla\cdot\left(w^n\mathbf{u}\right) = 0. \tag{2.53}$$

En supposant la viscosité cinématique $\nu = \mu/\varrho_a$ constante, la force visqueuse $\mathbf{F}^*$ devient

$$F_i^* = w^{-n}\frac{\partial}{\partial j}\left(2w^n e_{ij}\right) - \frac{2}{3}w^{-n}\frac{\partial}{\partial i}\left(w^n\nabla\cdot\mathbf{u}\right). \tag{2.54}$$

Le paramètre de dissipation Di et le chauffage visqueux Q^* dans (2.51) ont pour expression

$$\mathrm{Di} = \frac{c_1\mathrm{Pr}}{\mathrm{PmRa}}, \tag{2.55}$$

$$Q^* = 2\left[e_{ij}e_{ij} - \frac{1}{3}(\nabla\cdot\mathbf{u})^2\right]. \tag{2.56}$$

Ce système d'équations est contrôlé par sept nombres sans dimension :

$$\begin{gathered}\mathrm{Ra} = \frac{GMd\Delta S}{\nu\kappa_s c_p},\quad \mathrm{Pr} = \frac{\nu}{\kappa_s},\quad \mathrm{Pm} = \frac{\nu}{\eta},\quad \mathrm{E} = \frac{\nu}{\Omega d^2},\\ N_\varrho = \ln\left(\frac{\varrho_\mathrm{i}}{\varrho_\mathrm{o}}\right),\qquad \chi = \frac{r_\mathrm{i}}{r_\mathrm{o}},\qquad n,\end{gathered} \tag{2.57}$$

où Ra est le nombre de Rayleigh, Pr le nombre de Prandtl, Pm le nombre de Prandlt magnétique et E le nombre d'Ekman.

Les nouveaux termes qui apparaissent dans l'équation de Navier-Stokes (2.50) sont respectivement la force de Coriolis $\mathbf{f}_\Omega = -2\varrho_a\mathbf{\Omega}\times\mathbf{u}$ et la force de Lorentz $\mathbf{f}_B =$

$\mathbf{j} \times \mathbf{B}$ qui traduit la rétroaction du champ magnétique sur l'écoulement. Le couplage de l'équation d'induction au système hydrodynamique s'accompagne également de la prise en compte du terme de dissipation Joule $Q_j = \eta \mu_0 \mathbf{j}^2$ dans l'équation de transfert de chaleur (2.51).

Enfin, les conditions aux limites sont les suivantes : le champ magnétique se raccorde à un champ potentiel (1.14) et on suppose par ailleurs la nullité des contraintes tangentielles, $\sigma'_{r\theta} = \sigma'_{r\varphi} = 0$, de telle sorte que le fluide glisse au contact des parois. De plus, la conservation de la masse impose $\mathbf{u} \cdot \mathbf{n} = 0$. Dans le cas d'un système de coordonnées sphériques, on obtient les conditions aux limites suivantes pour le champ de vitesse

$$u_r = 0\,, \tag{2.58a}$$

$$\frac{\partial}{\partial r}\frac{u_\theta}{r} = 0\,, \tag{2.58b}$$

$$\frac{\partial}{\partial r}\frac{u_\varphi}{r} = 0\,. \tag{2.58c}$$

La principale différence liée à l'approximation anélastique vient des conditions aux limites sur l'entropie

$$S(r = r_\mathrm{i}) = \Delta S\,, \tag{2.59a}$$

$$S(r = r_\mathrm{o}) = 0\,. \tag{2.59b}$$

qui remplacent les conditions aux limites habituelles sur la température, étant donné l'expression du flux de chaleur dans l'équation (2.41).

2.4 Approximation numérique

Nos résultats ont été obtenus à l'aide du code numérique PARODY, initialement développé par Emmanuel Dormy (1997), puis parallélisé en collaboration avec Vincent Morin et Julien Aubert. À l'origine, ce code permet de résoudre les équations de la magnétohydrodynamique dans une coquille sphérique en rotation pour un fluide Boussinesq. Les développements ultérieurs entrepris par Martin Schrinner et auxquels nous avons également pris part ont permis d'implémenter les équations anélastiques dans PARODY (Schrinner *et al.* 2014). La version anélastique de ce code numérique a été validée par la reproduction des cas tests proposés par Jones *et al.* (2011), dont les résultats numériques sont donnés dans l'annexe A page 109. En outre, nous avons aussi adapté ce même code pour simuler des écoulements magnétohydrodynamiques de Couette sphérique (cf. section 4.2 page 83).

2.4.1 Présentation du code PARODY

Les équations vectorielles sont d'abord projetées sur une base de deux potentiels scalaires qui présente l'avantage de garantir mathématiquement le caractère solénoïdal des champs de vecteurs. Dans la mesure où la pression est une variable implicite servant à satisfaire la contrainte solénoïdale du fluide, cette décomposition permet par la même occasion d'éliminer le gradient de pression du système. La coquille sphérique est ensuite discrétisée sous forme de sphères concentriques, reliées par un schéma aux différences finies. À un rayon donné, chaque champ scalaire est alors projeté sur une base de fonctions harmoniques. Seuls les termes non-linéaires sont, quant à eux, calculés dans l'espace physique. Une telle structure se prête naturellement à une parallélisation par domaines radiaux. À partir d'une condition initiale donnée, le système d'équations est intégré temporellement par un schéma aux différences finies de type semi-implicite Crank-Nicholson, pour la diffusion, et Adams-Bashford, pour les termes non-linéaires, les termes de couplage et la force de Coriolis.

Décomposition poloïdale-toroïdale

Tout champ vectoriel $\mathbf{V}$ solénoïdal peut s'écrire comme la somme d'une composante poloïdale et d'une composante toroïdale, $\mathbf{V} = \mathbf{V}_\mathrm{P} + \mathbf{V}_\mathrm{T}$, avec

$$\mathbf{V}_\mathrm{P} = \nabla \times \nabla \times (\mathbf{r} V_\mathrm{P}) \, , \tag{2.60a}$$

$$\mathbf{V}_\mathrm{T} = \nabla \times (\mathbf{r} V_\mathrm{T}) \, , \tag{2.60b}$$

où V_P et V_T sont deux scalaires qui représentent respectivement les composantes poloïdale et toroïdale. Exprimée dans la base de coordonnées sphériques $\left(\mathbf{e}_\mathrm{r}, \mathbf{e}_\theta, \mathbf{e}_\varphi\right)$, cette décomposition — aussi appelée décomposition de Mie — s'écrit

$$\mathbf{V} = \begin{pmatrix} \dfrac{1}{r} \mathrm{L}_2(V_\mathrm{P}) \\ \dfrac{\partial}{\partial \theta}\left(\dfrac{1}{r}\dfrac{\partial}{\partial r}(r V_\mathrm{P})\right) + \dfrac{1}{\sin\theta}\dfrac{\partial V_\mathrm{T}}{\partial \varphi} \\ \dfrac{1}{\sin\theta}\dfrac{\partial}{\partial \varphi}\left(\dfrac{1}{r}\dfrac{\partial}{\partial r}(r V_\mathrm{P})\right) - \dfrac{\partial V_\mathrm{T}}{\partial \theta} \end{pmatrix} , \tag{2.61}$$

où l'opérateur L_2 est le laplacien de Beltrami défini par

$$\mathrm{L}_2 = -\frac{1}{\sin\theta}\frac{\partial}{\partial\theta}\left(\sin\theta\frac{\partial}{\partial\theta}\right) - \frac{1}{\sin^2\theta}\frac{\partial^2}{\partial\varphi^2} \, . \tag{2.62}$$

Il correspond aux composantes angulaires de l'opérateur laplacien

$$\nabla^{\mathbf{2}} = \frac{\partial^2}{\partial r^2} + \frac{2}{r}\frac{\partial}{\partial r} - \frac{1}{r^2}\mathrm{L}_2 \, . \tag{2.63}$$

Chaque équation vectorielle peut donc être transformée en deux équations scalaires équivalentes en prenant les composantes radiales du rotationnel et du double rotationnel de l'équation en question [1]. Les relations suivantes s'avèrent particulièrement utiles pour mener à bien les calculs,

$$\mathbf{V}\cdot\mathbf{r} = \mathrm{L}_2(V_\mathrm{P})\,, \tag{2.64a}$$

$$(\nabla\times\mathbf{V})\cdot\mathbf{r} = \mathrm{L}_2(V_\mathrm{T})\,. \tag{2.64b}$$

Harmoniques sphériques

Les harmoniques sphériques $Y_l^m(\theta,\varphi)$ sont des fonctions complexes définies sur la sphère par

$$\begin{gathered} Y_l^m(\theta,\varphi) = \sqrt{(2-\delta_{m0})(2l+1)\frac{(l-m)!}{(l+m)!}}\, P_l^m(\cos\theta)\, e^{\mathrm{i}m\varphi}\,, \\ \text{avec} \quad \begin{cases} l = 0,1,2,\dots,+\infty \\ m = 0,1,\dots,l \end{cases} , \end{gathered} \tag{2.65}$$

où δ_{ij} est le symbole de Kronecker et P_l^m le polynôme de Legendre de degré l et d'ordre m (Cohen-Tannoudji *et al.* 1973, Dormy 1997). À titre d'exemple, nous avons $Y_0^0 = 1$, $Y_1^0 = \sqrt{3}\cos\theta$, $Y_1^1 = -\sqrt{3}\sin\theta e^{\mathrm{i}\varphi}$, ...

Les harmoniques sphériques sont les fonctions propres de l'opérateur L_2 et satisfont la relation

$$\mathrm{L}_2\, Y_l^m = l\,(l+1)\, Y_l^m\,. \tag{2.66}$$

Ainsi définies, elles forment une base orthonormée et nous pouvons donc écrire toute fonction F continue sur la sphère comme

$$F(\theta,\varphi) = \sum_{l=0}^{+\infty}\sum_{m=0}^{l} f_l^m Y_l^m(\theta,\varphi) \quad + \quad \text{c. c.}, \tag{2.67}$$

où l'abréviation c. c. désigne le complexe conjugué du terme qui la précède. Les décompositions en harmoniques sphériques sont l'équivalent, en géométrie sphériques, des transformées de Fourier.

À titre d'exemple, nous pouvons donc écrire les composantes poloïdale et toroïdale du champ magnétique ainsi,

$$B_\mathrm{P}(r,\theta,\varphi) = \sum_{l=0}^{+\infty}\sum_{m=0}^{l} {B_\mathrm{P}}_l^m(r)\, Y_l^m(\theta,\varphi) \quad + \quad \text{c. c.}, \tag{2.68a}$$

$$B_\mathrm{T}(r,\theta,\varphi) = \sum_{l=0}^{+\infty}\sum_{m=0}^{l} {B_\mathrm{T}}_l^m(r)\, Y_l^m(\theta,\varphi) \quad + \quad \text{c. c.}. \tag{2.68b}$$

---

[1] C'est ainsi que le gradient de pression dans l'équation de Navier-Stokes est éliminé.

Il est intéressant de noter que cette décomposition peut nous renseigner immédiatement sur les symétries équatoriale et axiale du champ magnétique. En effet, si la composante poloïdale présente des cœfficients dominants ${B_{\mathrm{P}}}_l^m$ tels que la somme $l+m$ est paire (impaire), nous dirons que le champ magnétique présente une symétrie dipolaire (quadrupolaire). Inversement, si l'on se concentre sur la composante toroïdale, un dipôle (quadrupôle) sera caractérisé par des cœfficients dominants ${B_{\mathrm{T}}}_l^m$ tels que la somme $l+m$ est impaire (paire). Enfin, si le spectre en m est principalement dominé par la composante $m=0$, alors le champ est globalement axisymétrique.

2.4.2 Implémentation des équations anélastiques

Nous donnons dans cette section le détail de l'implémentation des équations anélastiques dans PARODY. Comme l'équation d'induction est inchangée, nous n'expliciterons que l'équation de Navier-Stokes et l'équation de transfert thermique. L'équation de Navier-Stokes (2.50) est réécrite sous la forme

$$\frac{\partial \mathbf{u}}{\partial t}+\frac{\mathrm{Pm}}{\bar{\varrho}}\nabla\times\left(\nabla\times\bar{\varrho}\mathbf{u}\right)=-\nabla\left(\frac{p_c}{\bar{\varrho}}+\frac{\mathbf{u}^2}{2}\right)+\mathbf{N}, \tag{2.69}$$

avec

$$\mathbf{N}=\mathbf{u}\times\boldsymbol{\omega}+\mathrm{Pm}\left[\mathbf{F}^\dagger+\frac{\mathrm{Pm}}{\mathrm{Pr}}\mathrm{Ra}\frac{S}{r^2}\mathbf{e}_r-\frac{2}{\mathrm{E}}\mathbf{e}_z\times\mathbf{u}+\frac{1}{\mathrm{E}\bar{\varrho}}\left(\nabla\times\mathbf{B}\right)\times\mathbf{B}\right], \tag{2.70}$$

$$\mathbf{F}^\dagger=\mathbf{F}^*+\frac{1}{\bar{\varrho}}\nabla\times\left(\nabla\times\bar{\varrho}\mathbf{u}\right), \tag{2.71}$$

où $\boldsymbol{\omega}=\nabla\times\mathbf{u}$ désigne la vorticité et $\bar{\varrho}=w^n$ la densité adimensionnée de l'état de référence. Le développement de $\mathbf{F}^\dagger$ donne

$$\mathbf{F}^\dagger=\frac{1}{3}\nabla\left(\nabla\cdot\mathbf{u}\right)+\frac{1}{\bar{\varrho}}\left(\nabla\bar{\varrho}\times\boldsymbol{\omega}\right)-\frac{\mathbf{u}}{\bar{\varrho}}\nabla^2\bar{\varrho}+\frac{2}{3}\frac{1}{\bar{\varrho}^2}\left(\frac{\mathrm{d}\bar{\varrho}}{\mathrm{d}r}\right)^2\mathbf{e}_r\cdot\mathbf{u}. \tag{2.72}$$

Pour alléger les notations, on notera par la suite

$$\xi=\frac{1}{\bar{\varrho}}\frac{\mathrm{d}\bar{\varrho}}{\mathrm{d}r}, \tag{2.73}$$

de telle sorte que les termes de l'équation (2.72) se réécrivent

$$\frac{1}{\bar{\varrho}}\left(\nabla\bar{\varrho}\times\boldsymbol{\omega}\right)=-\xi\omega_\varphi\mathbf{e}_\theta+\xi\omega_\theta\mathbf{e}_\varphi, \tag{2.74}$$

$$\frac{\mathbf{u}}{\bar{\varrho}}\nabla^2\bar{\varrho}=\mathbf{u}\left(\frac{2}{r}\xi+\frac{\mathrm{d}\xi}{\mathrm{d}r}+\xi^2\right). \tag{2.75}$$

Lors du passage de l'approximation de Boussinesq à l'approximation anélastique, la contrainte $\nabla \cdot \mathbf{u} = 0$ devient $\nabla \cdot \left(\bar{\varrho}\mathbf{u}\right) = 0$. En conséquence, pour préserver le caractère solénoidal, non plus de la vitesse mais de la quantité de mouvement $\mathbf{m} = \bar{\varrho}\mathbf{u}$, les composantes poloïdale et toroïdale du champ de vitesse sont redéfinies comme suit

$$\mathbf{m} = \bar{\varrho}\mathbf{u} = \sum_{l,m} \nabla \times \nabla \times u_{\mathrm{P}l}^{\;m} Y_l^m \mathbf{r} + \nabla \times u_{\mathrm{T}l}^{\;m} Y_l^m \mathbf{r}. \tag{2.76}$$

La dépendance radiale de $\bar{\varrho} = \bar{\varrho}(r)$ de l'état de référence est une des sources principales de complication dans l'implémentation numérique du système anélastique, puisque la décomposition poloïdale-toroïdale des équations implique de réécrire le champ de vitesse sous la forme $\mathbf{u} = \mathbf{m}/\bar{\varrho}$.

Équation de la vitesse poloïdale

L'équation du scalaire poloïdal de la vitesse $u_{\mathrm{P}l}^{\;m}$ est obtenue en prenant la composante radiale du double rotationnel de l'équation de Navier-Stokes. On obtient alors

$$\begin{aligned}
\frac{\partial}{\partial t}\left(\nabla^2 u_{\mathrm{P}l}^{\;m} - \frac{\xi}{r}\frac{\partial}{\partial r} r\, u_{\mathrm{P}l}^{\;m}\right) = \mathrm{Pm}\Bigg[& \nabla^2\nabla^2 u_{\mathrm{P}l}^{\;m} - \frac{\xi}{r}\nabla^2 u_{\mathrm{P}l}^{\;m} - \frac{\xi}{r}\frac{\partial}{\partial r}\nabla^2 u_{\mathrm{P}l}^{\;m} \\
& + \left(\xi^2 - \frac{\xi}{r}\right)\nabla^2 u_{\mathrm{P}l}^{\;m} - \xi\frac{\partial}{\partial r}\nabla^2 u_{\mathrm{P}l}^{\;m} - \frac{\mathrm{d}\xi}{\mathrm{d}r}\nabla^2 u_{\mathrm{P}l}^{\;m} \\
& + \left(2\frac{\mathrm{d}\xi}{\mathrm{d}r} - \xi^3\right)\frac{\partial}{\partial r} u_{\mathrm{P}l}^{\;m} \\
& + \frac{1}{r}\left(2\frac{\mathrm{d}\xi}{\mathrm{d}r} - \xi^3\right) u_{\mathrm{P}l}^{\;m} + \xi^2\left(\frac{\partial^2}{\partial r^2} u_{\mathrm{P}l}^{\;m} + \frac{2}{r}\frac{\partial}{\partial r} u_{\mathrm{P}l}^{\;m}\right) \\
& - \left(\frac{2}{r}\xi + \frac{\mathrm{d}\xi}{\mathrm{d}r} + \xi^2\right)\nabla^2 u_{\mathrm{P}l}^{\;m} \\
& - \left(-\frac{2}{r^2}\xi + \frac{2}{r}\frac{\mathrm{d}\xi}{\mathrm{d}r} + \frac{\mathrm{d}^2\xi}{\mathrm{d}r^2} - \frac{2}{r}\xi^2 - \xi^3\right)\left(\frac{u_{\mathrm{P}l}^{\;m}}{r} + \frac{\partial}{\partial r} u_{\mathrm{P}l}^{\;m}\right) \\
& - \frac{2}{3}\frac{\xi^2}{r^2} l(l+1)\, u_{\mathrm{P}l}^{\;m} \\
& + \frac{2}{\mathrm{E}}\frac{1}{l(l+1)}\left(Q_3 u_{\mathrm{T}l}^{\;m} + \mathrm{i}m u_{\mathrm{T}l}^{\;m}\right) \\
& + \frac{2}{\mathrm{E}}\frac{\xi}{l(l+1)}\left(\hat{Q}_3 u_{\mathrm{T}l}^{\;m} - \mathrm{i}m\frac{l(l+1)}{r} u_{\mathrm{P}l}^{\;m} - \mathrm{i}m\frac{1}{r}\frac{\partial}{\partial r} r\, u_{\mathrm{P}l}^{\;m}\right) \\
& - \frac{\mathrm{Pm}}{\mathrm{Pr}}\mathrm{Ra}\bar{\varrho}\frac{s_l^m}{r^3}\Bigg] \\
& - \frac{\bar{\varrho}}{l(l+1)}\mathbf{r}\cdot\nabla\times\nabla\times\left(\left(\mathbf{u}\cdot\nabla\right)\mathbf{u} - \frac{1}{\mathrm{E}\bar{\varrho}}\left(\mathbf{B}\cdot\nabla\right)\mathbf{B}\right)\Bigg|_{Y_l^m}.
\end{aligned} \tag{2.77}$$

Dans le fichier source `parody.f90`, les termes linéaires de l'équation (2.77) sont implémentés dans les tableaux `A2LU` et `adams2`. L'opérateur Q_3 est défini par

$$\begin{aligned} Q_3 {u_{\mathrm{T}l}}^m = &\left(K_{11}(l,m)\frac{1}{r}u_{\mathrm{T}l-1}^m\right)+\left(K_{12}(l,m)\frac{\mathrm{d}}{\mathrm{d}r}u_{\mathrm{T}l-1}^m\right)+ \\ &\left(K_{21}(l,m)\frac{1}{r}u_{\mathrm{T}l+1}^m\right)+\left(K_{22}(l,m)\frac{\mathrm{d}}{\mathrm{d}r}u_{\mathrm{T}l+1}^m\right), \end{aligned} \tag{2.78}$$

avec

$$K_{11}(l,m) = (l+1)(l-1)^2\sqrt{\frac{(l-m)(l+m)}{(2l-1)(2l+1)}}, \tag{2.79a}$$

$$K_{12}(l,m) = -(l-1)(l+1)\sqrt{\frac{(l-m)(l+m)}{(2l-1)(2l+1)}}, \tag{2.79b}$$

$$K_{21}(l,m) = -l(l+2)^2\sqrt{\frac{(l+1+m)(l+1-m)}{(2l+3)(2l+1)}}, \tag{2.79c}$$

$$K_{22}(l,m) = -l(l+2)\sqrt{\frac{(l+1+m)(l+1-m)}{(2l+3)(2l+1)}}. \tag{2.79d}$$

L'opérateur $\hat{Q}_3$ est défini par

$$\begin{aligned} \hat{Q}_3 {u_{\mathrm{T}l}}^m = &\left(\hat{K}_{11}(l,m)+\hat{K}_{12}(l,m)\right)u_{\mathrm{T}l-1}^m+ \\ &\left(\hat{K}_{22}(l,m)+\hat{K}_{21}(l,m)\right)u_{\mathrm{T}l+1}^m, \end{aligned} \tag{2.80}$$

avec

$$\hat{K}_{11}(l,m) = (l-1)\sqrt{\frac{l^2-m^2}{(2l+1)(2l-1)}}, \tag{2.81a}$$

$$\hat{K}_{12}(l,m) = l(l-1)\sqrt{\frac{l^2-m^2}{(2l+1)(2l-1)}}, \tag{2.81b}$$

$$\hat{K}_{22}(l,m) = -(l+2)\sqrt{\frac{(l-m+1)(l+m+1)}{(2l+1)(2l+3)}}, \tag{2.81c}$$

$$\hat{K}_{21}(l,m) = (l+1)(l+2)\sqrt{\frac{(l-m+1)(l+m+1)}{(2l+1)(2l+3)}}. \tag{2.81d}$$

Les indices des cœfficients K_{ij} donnés ci-dessus correspondent à l'implémentation numérique dans PARODY. Ils diffèrent de ceux que l'on trouve dans la thèse d'Emmanuel Dormy (1997) car on a exprimé ici la contribution des modes $l-1$ et $l+1$ au mode l, et non la contribution du mode l aux modes $l-1$ et $l+1$; aussi avons-nous redonné les expressions de ces cœfficients dans ce document.

Équation de la vitesse toroïdale

L'équation du scalaire poloïdal de la vitesse $u_{\mathrm{T}l}^{m}$ est obtenue en prenant la composante radiale du rotationnel de l'équation de Navier-Stokes. On obtient

$$\begin{aligned}\frac{\partial}{\partial t}u_{\mathrm{T}l}^{m} = \mathrm{Pm}\Big[\nabla^{\mathbf{2}}u_{\mathrm{T}l}^{m} &+ \left(\xi^2-\frac{\xi}{r}\right)u_{\mathrm{T}l}^{m} - \xi\frac{\partial}{\partial r}u_{\mathrm{T}l}^{m} - \left(\frac{2}{r}\xi+\frac{\mathrm{d}\xi}{\mathrm{d}r}+\xi^2\right)u_{\mathrm{T}l}^{m} \\ &+ \frac{2}{\mathrm{E}}\frac{1}{l(l+1)}\left(\mathrm{i}mu_{\mathrm{T}l}^{m} - Q_3 u_{\mathrm{P}l}^{m}\right)\Big] \\ &- \frac{\bar{\varrho}}{l(l+1)}\mathbf{r}\cdot\nabla\times\left((\mathbf{u}\cdot\nabla)\,\mathbf{u}-\frac{1}{\mathrm{E}\bar{\varrho}}(\mathbf{B}\cdot\nabla)\,\mathbf{B}\right)\bigg|_{Y_l^m}.\end{aligned} \tag{2.82}$$

Les termes linéaires de cette équation sont implémentés dans les tableaux `A1LU` et `adams1` dans le fichier `parody.f90`.

Équation de transfert thermique

Enfin, l'équation du transfert thermique (2.51) prend la forme

$$\begin{aligned}\frac{\partial}{\partial t}s_l^m = \frac{\mathrm{Pm}}{\mathrm{Pr}}&\left[\nabla^{\mathbf{2}}s_l^m + \left(\xi+\frac{\xi}{n}\right)\frac{\partial}{\partial r}s_l^m\right] \\ &-(\mathbf{u}\cdot\nabla s)|_{Y_l^m} + \frac{\mathrm{Di}}{w}\left(\frac{1}{\bar{\varrho}\mathrm{E}}(\nabla\times\mathbf{B})^2 + Q^{\nu}\right)\bigg|_{Y_l^m}.\end{aligned} \tag{2.83}$$

Les termes linéaires de cette équation sont implémentés dans les tableaux `A3` et `adams3` dans le fichier `parody.f90`.

Conditions aux limites

Pour le champ magnétique, le raccord à un champ potentiel se traduit à la sphère interne par

$$\frac{\partial}{\partial r}B_{\mathrm{P}l}^{m} = \frac{l}{r}B_{\mathrm{P}l}^{m}, \tag{2.84a}$$

$$B_{\mathrm{T}l}^{m} = 0, \tag{2.84b}$$

et à la sphère externe par

$$\frac{\partial}{\partial r}B_{\mathrm{P}l}^{m} = -\frac{l+1}{r}B_{\mathrm{P}l}^{m}, \tag{2.85a}$$

$$B_{\mathrm{T}l}^{m} = 0. \tag{2.85b}$$

Pour le champ de vitesse, les conditions de glissement au bord (2.58) deviennent

$$u_{\mathrm{P}l}^{\ m} = 0\,, \tag{2.86a}$$

$$\frac{\partial^2}{\partial r^2} u_{\mathrm{P}l}^{\ m} = \xi \frac{\partial}{\partial r} u_{\mathrm{P}l}^{\ m}\,, \tag{2.86b}$$

$$\frac{\partial}{\partial r} u_{\mathrm{T}l}^{\ m} = \left(\xi + \frac{1}{r}\right) u_{\mathrm{T}l}^{\ m}\,. \tag{2.86c}$$

⁂

Chapitre 3

Dynamos anélastiques

Theorem:
Given Cowling, ∃ no theoretical astrophysics.

attribué à Chandrasekhar par Paul H. Roberts
(*in* Molokov *et al.* 2007)

CE CHAPITRE présente les résultats obtenus à l'aide du modèle anélastique détaillé dans la section 2.3 et reprend, en anglais, l'essentiel des publications faites sur ce sujet. Les articles en question sont reproduits en intégralité dans les annexes B.2, B.3 et B.4. Notre approche s'inscrit dans la continuité des études de géodynamo : nous avons donc réalisé plusieurs études systématiques en variant différents paramètres de contrôle (2.57), sans chercher à reproduire les caractéristiques d'un astre donné. Ainsi avons-nous essayé de dégager des tendances génériques, caractéristiques du modèle utilisé.

3.1 Magnetic field topology

3.1.1 Output parameters

To characterize our numerical dynamo models, we use a number of non-dimensional output parameters which are mostly based on the kinetic and magnetic energy densities,

$$E_k = \frac{1}{2V}\int_V w^n \mathbf{u}^2\,\mathrm{d}V \qquad \text{and} \qquad E_b = \frac{1}{2V}\frac{\mathrm{Pm}}{\mathrm{E}}\int_V \mathbf{B}^2\,\mathrm{d}V, \tag{3.1}$$

where the integrals are taken over the volume of the fluid shell V. A non-dimensional measure for the velocity amplitude is then the magnetic Reynolds number, $\mathrm{Rm} = \sqrt{2E_k}$, or the Rossby number, $Ro = \mathrm{Rm}\mathrm{E}/\mathrm{Pm}$. A measure of the mean zonal flow is the zonal Rossby number Ro_z, whose definition is based on the averaged toroidal axisymmetric kinetic energy density. The amplitude of the average magnetic field is measured in terms of the Lorentz number, $Lo = \sqrt{2E_b}\mathrm{E}/\mathrm{Pm}$, and its dipolarity is characterized by the relative dipole field strength f_{dip}, originally defined as the time-average ratio on the outer shell boundary S_{o} of the dipole field strength to the total field strength,

$$f_{\mathrm{dip}} = \left\langle \sqrt{\frac{\int_{S_o} \mathbf{B}^2{}_{\ell=1}^{m=\{0,1\}} \sin\theta \,\mathrm{d}\theta \,\mathrm{d}\varphi}{\int_{S_o} \mathbf{B}^2 \sin\theta \,\mathrm{d}\theta \,\mathrm{d}\varphi}} \right\rangle_t . \tag{3.2}$$

We also define a relative *axial* dipole field strength filtering out non-axisymmetric contributions

$$f_{\mathrm{dip}_{\mathrm{ax}}} = \left\langle \sqrt{\frac{\int_{S_{\mathrm{o}}} \mathbf{B}^2{}_{\ell=1}^{m=0} \sin\theta \,\mathrm{d}\theta \,\mathrm{d}\varphi}{\int_{S_o} \mathbf{B}^2 \sin\theta \,\mathrm{d}\theta \,\mathrm{d}\varphi}} \right\rangle_t . \tag{3.3}$$

This definition of $f_{\mathrm{dip}_{\mathrm{ax}}}$ is similar to the relative dipole field strength used by Gastine *et al.* (2012), except for the square root, which explains the lower values for the dipolarity found in Gastine *et al.* (2012).

3.1.2 Dipolar and multipolar dynamos

Parameter studies for Boussinesq simulations revealed two distinct classes of dynamo models. They can be distinguished by their field geometry and are therefore referred to as "dipolar" and "multipolar" models (Kutzner & Christensen 2002, Christensen & Aubert 2006). The spatial variability of multipolar dynamos is a direct consequence of dynamo action in a turbulent environment and has to be expected. The class of dipolar dynamos, however, is more peculiar. Schrinner *et al.* (2011b) showed that these models are single-mode dynamos, that is except for the fundamental mode, all more structured magnetic eigenmodes are highly damped. The single-mode property leads to further characteristic differences between both classes of dynamos, apart from their different field geometries. Whereas the dipole axis is stable for models with a dominant axial dipole field , multipolar models show frequent polarity reversals (Kutzner & Christensen 2002) or oscillations (Goudard & Dormy 2008, Schrinner *et al.* 2012). A third fundamental difference between dipolar and multipolar models is related to their saturation mechanism. If a magnetic tracer field is advanced kinematically with the velocity field stemming from the full dynamo simulation, the tracer field grows exponentially for multipolar but not for dipolar models. Dipolar dynamos are "kinematically stable" and in this numerical experiment, the tracer field becomes aligned with the actual, self-consistent magnetic field after some initial transition period (Schrinner *et al.* 2010). Finally, dipolar and multipolar dynamos follow slightly different scaling laws for the magnetic field (Christensen 2010, Schrinner *et al.* 2012, Yadav *et al.* 2013a). This aspect will be further discussed in section 3.4.

Figure 3.1 – The relative dipole field-strength versus the local Rossby number for our sample of models. Filled symbols stand for dipolar, open symbols for multipolar dynamos. The symbol shape indicates the number of density scale heights: N_ϱ = 0.5: circle; $N_\varrho = 1$: upward triangle; $N_\varrho = 1.5$: downward triangle; N_ϱ = 2: diamond; N_ϱ = 2.5: square; $N_\varrho = 3, 3.5, 4$: star. A cross inscribed in some open symbols means that the field of these models exhibits a strong equatorial dipole component.

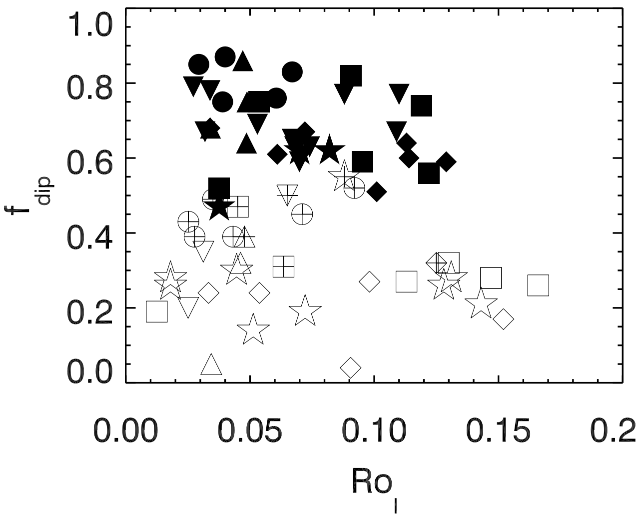

Christensen & Aubert (2006) proposed a criterion based on a local Rossby number to separate dipolar from multipolar dynamos. It says that dipolar dynamos may be found if the typical length scale of convection l, is at least an order of magnitude larger than the Rossby radius, or $Ro_\ell = U/(\Omega l) < 0.12$ (in which U is a typical rms velocity). In the following, we will use the definition of the local Rossby number $Ro_\ell = Ro_c \ell_c/\pi$ introduced by Schrinner *et al.* (2012), which is adapted from Christensen & Aubert (2006) since it is entirely based on convection and not influenced by the mean zonal flow. The typical convective length scale is computed from the mean harmonic degree ℓ_c of the velocity component $\mathbf{v}_c$ from which the mean zonal flow has been subtracted,

$$\ell_c = \sum_\ell \ell \frac{< w^n (\mathbf{u}_c)_\ell \cdot (\mathbf{u}_c)_\ell >}{< w^n \mathbf{u}_c \cdot \mathbf{u}_c >}. \tag{3.4}$$

where the brackets denote an average of time and radii. Consistently, the contribution of the mean zonal flow is removed for calculating Ro_c. This helped to generalize the Rossby number rule to models with different aspect ratios and mechanical boundary conditions (see Schrinner *et al.* 2012, App. A). Moreover, our reinterpretation assumes that the magnetic field is generated only by convection and therefore explains why the Rossby number criterion is not applicable to models for which differential rotation plays an essential role.

Figure 3.1 shows the relative dipole field strength versus the local Rossby number for all anelastic models considered here. [1] As for Boussinesq simulations, only multipolar models are found for $Ro_\ell > 0.12$ (Christensen & Aubert 2006), and the

---

[1] The list of these models can be found in the article in Appendix B.2 on page 118.

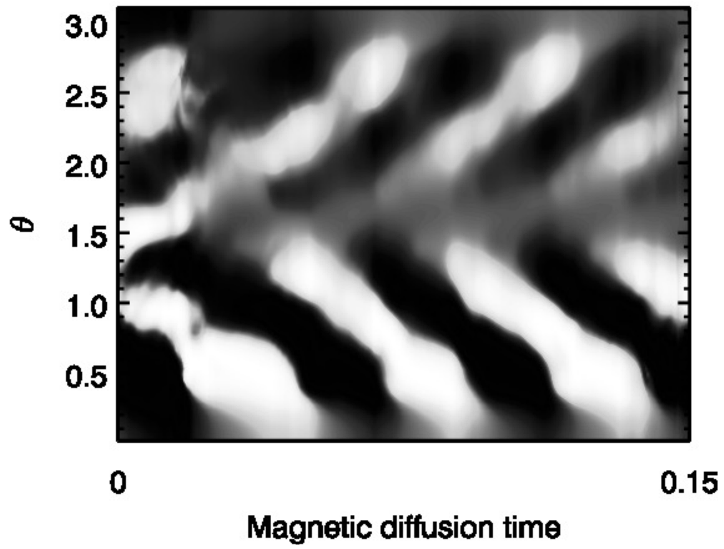

Figure 3.2 – Contour plot of the azimuthally averaged radial magnetic field of model3m versus time and colatitude. The contour plot was normalised by the maximum absolute value at each time step. The grey-scale coding ranges from -1, white, to +1, black.

multipolar branch extends into the dipolar regime in the form of a bistable region where both solutions are possible depending on the initial conditions (Schrinner *et al.* 2012). However, in contrast to comparable parameter studies of Boussinesq models (Christensen & Aubert 2006, Schrinner *et al.* 2012), dipolar and multipolar dynamos are hardly distinguishable from each other in terms of their relative dipole field strength. Contrary to previous results, models with an intermediate dipolarity ($f_{\mathrm{dip}} \approx 0.5$) lead to a fairly smooth transition of f_{dip} in Fig. 3.1. These are in particular those models with a high equatorial dipole contribution denoted by a cross inscribed in the plotting symbol. Because the dipole field strength alone is not conclusive to classify our models in Fig. 3.1, their time-dependence, their kinematic stability, and their scaling behaviour were additionally considered to assign them to one of both classes. The branches are also more easily identified by continuing simulations performed with other parameters, for which the dipolar/multipolar characteristic was previously established.

As in the case of Boussinesq simulations, only multipolar models were found to exhibit polarity reversals or oscillatory dynamo solutions. An example of a coherent dynamo wave for model3m[2] ($N_\varrho = 3$) is given in Fig. 3.2. The period of these oscillatory dynamo modes and the poleward propagation direction of the resulting wave can be surprisingly well explained by Parker's plane layer formalism (Parker 1955, Busse & Simitev 2006, Goudard & Dormy 2008, Schrinner *et al.* 2011a, Gastine *et al.* 2012). However, the recent claim that dynamo waves could migrate towards the equator if there is a considerable density stratification (Käpylä *et al.* 2013) was not confirmed by our simulations.

---

[2] model3m: $\mathrm{E} = 10^{-4}$, $\mathrm{Ra} = 5 \times 10^{6}$, $\mathrm{Pm} = 4$, $\mathrm{Pr} = 2$, $\chi = 0.35$, $N_\varrho = 3$.

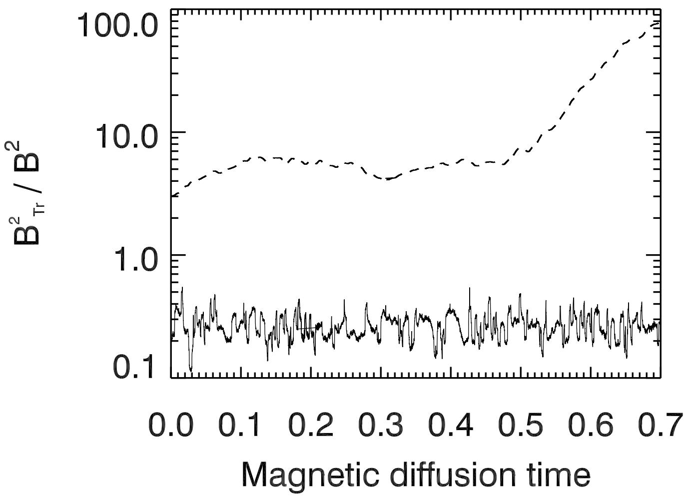

Figure 3.3 – Evolution of the energy of the tracer field normalised by the energy of the actual magnetic field for model2m (dashed line) and model54d (solid line).

Moreover, we tested some arbitrarily chosen models for kinematic stability and found the dipolar models to be kinematically stable, whereas all multipolar models considered exhibited at least periods of instability. Figure 3.3 shows as an example the evolution of the kinematically advanced tracer field for model2m[3] and model54d.[4] For the first, the tracer field grows exponentially but it stays stable for the latter although it has been permanently perturbed during the simulation.

A transition from the dipolar to the multipolar regime can be triggered by a decrease in the rotation rate or the dynamical length scale (possibly associated with a change in the aspect ratio), or an increase in the velocity amplitude. These three quantities influence the local Rossby number directly. In Fig. 3.4, we show that a transition towards the multipolar regime may also be forced by increasing N_ϱ. A higher density stratification with all the other parameters fixed causes smaller length scales and larger velocity amplitudes. This leads to an increase of Ro_ℓ and to a decrease of f_{dip} at $Ro_\ell \approx 0.12$ in Fig. 3.4.

3.1.3 Equatorial dipole

An example of a model strongly influenced by an equatorial dipole mode is presented in Fig. 3.5. A strong mean zonal flow often present in these models seems to be in conflict with the generation of non-axisymmetric fields. Figure 3.6 demonstrates that the strong equatorial dipole mode of model5m[5] is indeed maintained and rebuilt by the columnar convection and damped by the differential

---

[3] model2m: $E = 10^{-4}$, $Ra = 5 \times 10^6$, $Pm = 3$, $Pr = 2$, $\chi = 0.35$, $N_\varrho = 3$.

[4] model54d: $E = 10^{-3}$, $Ra = 3 \times 10^5$, $Pm = 3$, $Pr = 1$, $\chi = 0.35$, $N_\varrho = 2.5$.

[5] model5m: $E = 10^{-4}$, $Ra = 2 \times 10^6$, $Pm = 1$, $Pr = 1$, $\chi = 0.35$, $N_\varrho = 0.5$.

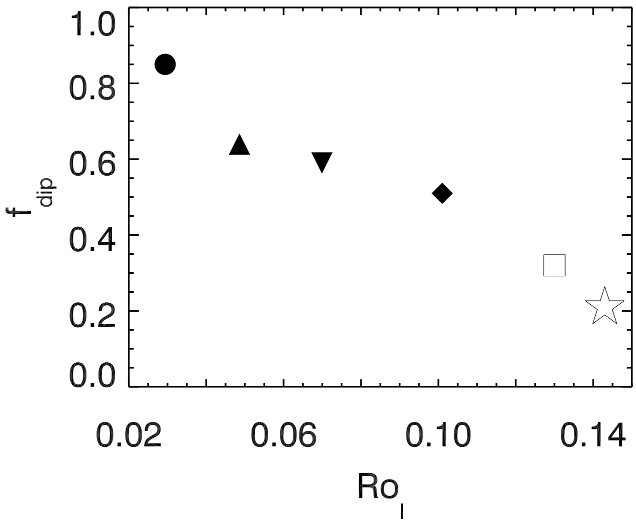

Figure 3.4 – Relative dipole field strength versus Ro_ℓ for a sequence of models with $\mathrm{E} = 3 \times 10^{-4}$, $\mathrm{Ra} = 4\mathrm{Ra_c}$, $\mathrm{Pm} = 3$, and $\mathrm{Pr} = 1$. The meaning of the symbols is as defined in the caption of Fig. 3.1.

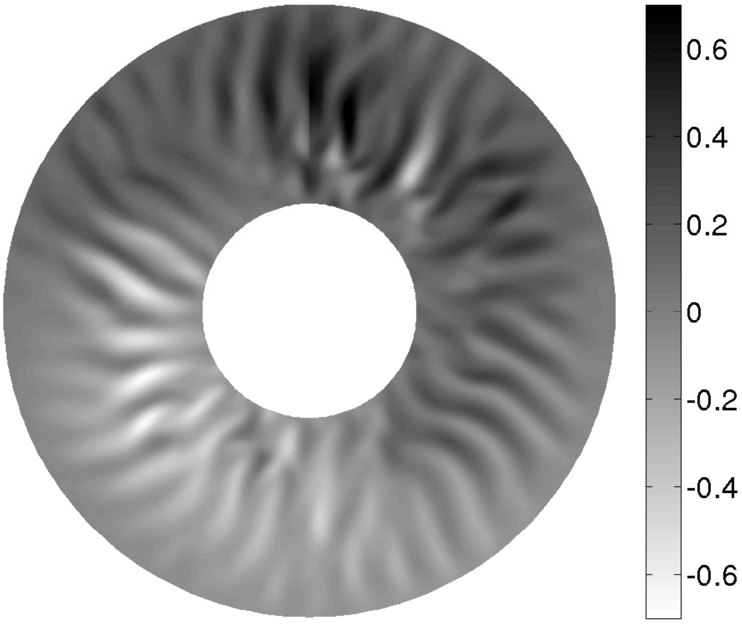

Figure 3.5 – Contour plot (equatorial cut) of the radial magnetic field of model2m at a given time.

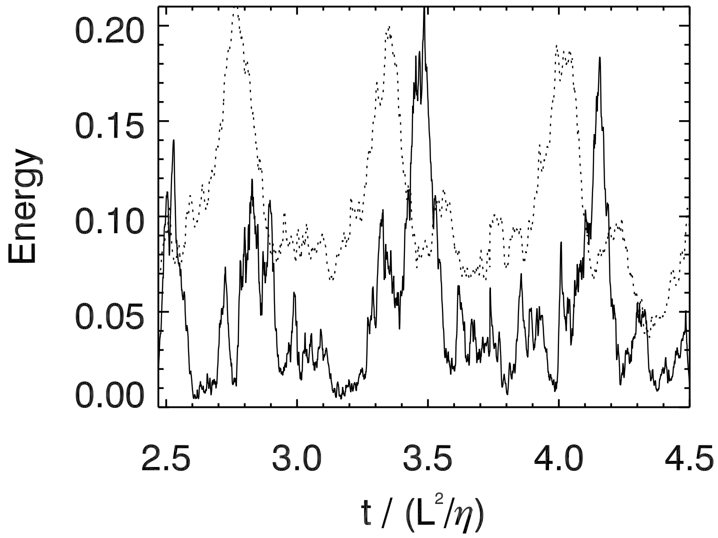

Figure 3.6 – Dotted line: axisymmetric kinetic energy of model5m normalised by an arbitrary value; solid line: ratio of axisymmetric to total magnetic energy.

rotation. In Fig. 3.6 the mean zonal kinetic energy normalised by an arbitrary value (dotted line) and the ratio of the axisymmetric magnetic energy to the total magnetic energy (solid line) are displayed. The action of the mean zonal flow, or more precisely the differential rotation, tends to damp non-axisymmetric components of the magnetic field. Thus, a burst of the mean zonal kinetic energy is followed by a maximum of the axisymmetric and a dip in the non-axisymmetric magnetic energy. Subsequently, the mean zonal flow is quenched by the axisymmetric field, the axisymmetric field decays and the non-axisymmetric field is rebuilt. The interaction between the mean zonal flow and the magnetic field observed in this model is still fairly weak, although the mean zonal flow contributes already 58% to the total kinetic energy. Therefore, the magnetic field of model5m stays on average highly non-axisymmetric. We note that this is very different from the Sun, for instance, where probably an even more efficient differential rotation causes a predominantly axisymmetric large-scale magnetic field (Charbonneau 2010), but also non-axisymmetric stellar magnetic fields were reported (Donati & Landstreet 2009).

3.1.4 Discussion

The fundamental cause of the high dipolarity of dynamo models in the low Rossby number regime is an outstanding question. Schrinner *et al.* (2012) argued for Boussinesq models that cylindrical convection in a spherical fluid domain leads to a characteristic pattern of the axisymmetric toroidal field which eventually results in the clear preference of only one, dipolar eigenmode. The argument relies on the idea that a line of fluid elements moving towards the outer spherical boundary has to shorten and causes a converging flow towards the equatorial plane. The toroidal field is then advected and markedly shaped by this flow component (see also Olson *et al.* 1999). This advection process could be rigorously identified and quantified as a strong γ-effect in a corresponding mean-field description (Schrinner *et al.* 2007, 2012). In addition, the recent finding that the dichotomy of dipolar and multipolar dynamos seems to be absent in convective dynamo simulations in Cartesian geometry (Tilgner 2012) is consistent with this argument and points again to the significance of the underlying symmetry constraints. What has been said about Boussinesq models largely applies to anelastic models, too. However, geometrical constraints are somewhat relaxed for a compressible fluid. Therefore, compressibility might damp the advection of the mean toroidal field towards the equatorial plane (γ-effect), which might result in the two differences that seem at first sight specific to anelastic dynamo models.

First, depending on the density contrast applied, it is more difficult to obtain dipolar solutions for anelastic than for Boussinesq models, even if $Ro_\ell < 0.12$. However, unlike Gastine *et al.* (2012), we did not find that dipolar solutions become impossible if N_ϱ exceeds a certain threshold. Instead, we observe that for a given N_ϱ, Ekman and Prandtl number, there seems to exist a critical magnetic Prandtl number for dipolar dynamos. For $\mathrm{E} = 10^{-4}$ and $\mathrm{Pr} = 1$, and $N_\varrho \geq 1.5$, we found $\mathrm{Pm_c} = 2N_\varrho - 2$, as apparent from Fig. 3.7. We emphasize again that the results of Fig. 3.7 depend of course on E and Pr; the data of our numerical study indicate that decreasing E and increasing Pr is favorable to dipolar dynamo models. We will study in more detail the influence of the density stratification of the stability domain of the dipolar branch in the section 3.3.

Second, magnetic field configurations dominated by an equatorial dipole seem to be more easily realized in anelastic than in Boussinesq simulations. For the latter, only a few examples under very specific conditions were reported (Aubert & Wicht 2004, Gissinger *et al.* 2012). The preference of non-axisymmetric modes is well known from dynamo models based on columnar convection (e.g. Ruediger 1980, Tilgner 1997), it is also the case of the Karlsruhe dynamo experiment (Müller & Stieglitz 2002). This agrees with our reasoning on the importance of the γ-effect in the axial dipole generation mechanisms (see also Schrinner *et al.* 2012). Indeed, the γ-effect vanishes in the above examples, as the geometrical constraints are relaxed. However, we show in the next section that this configuration is also characteristics of models with a very low stratification. Actually, we discuss in the next section how the gravity profile may also affect indirectly the magnetic field topology.

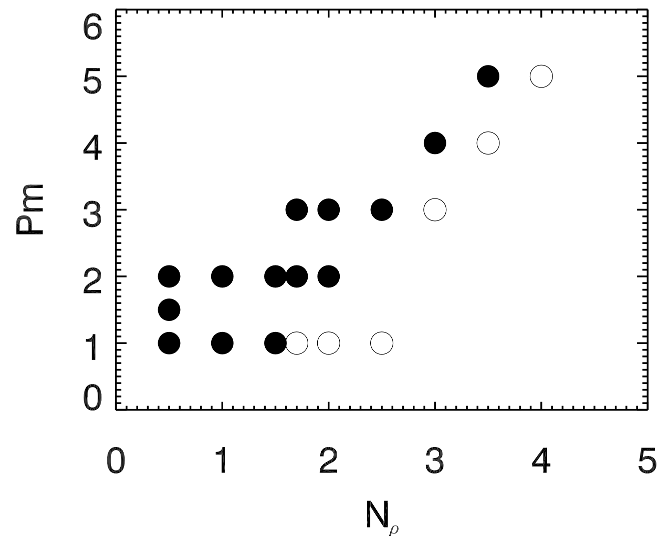

Figure 3.7 – Magnetic Prandtl number versus N_ϱ for models with $E = 10^{-4}$ and $Pr = 1$ and variable Rayleigh numbers. Filled circles stand for parameters for which dipolar solutions were obtained.

3.2 Influence of the mass distribution

In this section, we aim to clarify the reasons likely for the emergence of an equatorial dipole contribution when measuring the dipole field strength at the surface of numerical models. Since our approach closely follows previous methodology for studying the link with Boussinesq results, we decided to focus in more detail on one important change that comes with the anelastic approximation as formulated by Jones *et al.* (2011), assuming that all mass is concentrated inside the inner sphere to determine the gravity profile. In contrast, as proposed by the Boussinesq dynamo benchmark (Christensen *et al.* 2001), it was common for geodynamo studies to assume that the density is homogeneously distributed. This leads to different gravity profiles, the first being proportional to $1/r^2$, whereas the second is proportional to r. According to Duarte *et al.* (2013), Gastine *et al.* (2012) show that both gravity profiles lead to very similar results. Contrary to this statement, we show that the choice of the gravity profile may have strong consequences on the dynamo-generated field topology. To that end, we now restrict our investigation of the parameter space keeping for all simulations

$$E = 10^{-4}, \quad Pr = 1, \quad \chi = 0.35, \quad \text{and} \quad n = 2. \tag{3.5}$$

The polytropic index value was originally motivated by models of Jupiter's atmosphere (Jones *et al.* 2009). Furthermore, to differentiate the effects related to the change in the gravity profile from those related to the anelastic approximation, we perform low N_ϱ simulations so that we can assume that stratification no longer influences the dynamo process. In practice, we chose $N_\varrho = 0.1$, which means that the density contrast between the inner and outer spheres is only 1.1, and the simulations are thus very close to the Boussinesq limit. To further ensure the lack of stratification effects, we also checked in a few cases that the results do not differ from purely Boussinesq simulations.

3.2.1 Bifurcations between dynamo branches

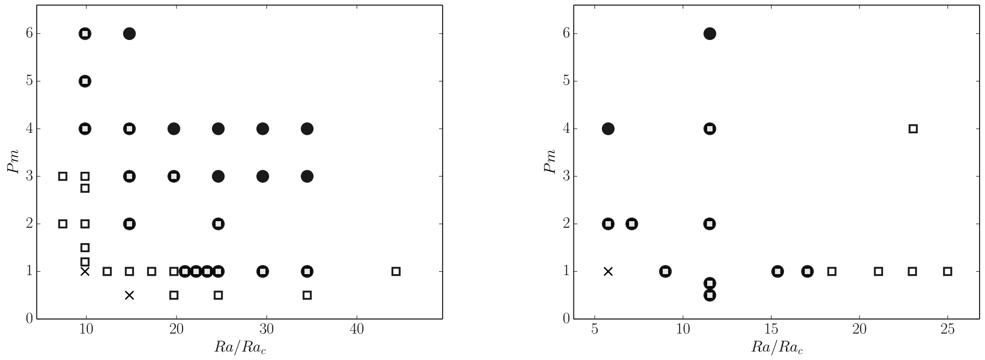

(a) $g \propto 1/r^2$ (b) $g \propto r$

Figure 3.8 – Dipolar (black circles) and multipolar (white squares) dynamos as a function of $\mathrm{Ra}/\mathrm{Ra_c}$ and Pm, for a central mass (a) and a uniform mass distribution (b). Crosses indicate the absence of a self-sustained dynamo.

Figure 3.8(a) shows the regime diagram we obtained, as a function of the Rayleigh and magnetic Prandtl numbers. For comparison, we use the data from Schrinner *et al.* (2012) and show in Fig. 3.8(b) the same regime diagram obtained for Boussinesq models with a uniform mass distribution. For Pm = 1, the transition from the dipolar to the multipolar branch can be triggered by an increase in Ra. In that case, the transition is due to the increasing role of inertia as revealed by Ro_ℓ. Alternatively, the transition from multipolar to dipolar dynamo can be triggered by increasing Pm. Then, the multipolar branch is lost when the saturated amplitude of the mean zonal flow becomes too small to prevent the growth of the dipolar solution (see Schrinner *et al.* 2012). It is worth noting that the two branches overlap for a restricted parameter range for which dipolar and multipolar dynamos may coexist. In that case, the observed solution strongly depends of the initial magnetic field, so we tested both weak and strong field initial conditions for all our models to delimit the extent of the bi-stable zone with greater accuracy. Actually, multipolar dynamos are favoured by the stronger zonal wind that may develop with stress-free boundary conditions, allowing for this hysteretic transition (Schrinner *et al.* 2012).

Finally, we see that the dynamo threshold is lower for multipolar models, which allows the multipolar branch to extend below the dipolar branch at low Rayleigh and magnetic Prandtl numbers. We see in Fig. 3.8(b) that this is different from Boussinesq models with a uniform mass distribution.

To investigate the different transitions between the different dynamo branches, we plot the Elsasser number $\Lambda = B_{\mathrm{rms}}^2/(\Omega \varrho_r \mu_0 \eta)$ in Fig. 3.9(a) (related to the Lorentz number by $\Lambda = Lo^2 \mathrm{Pm}/\mathrm{E}$) as a function of the distance to the threshold for models at Pm = 1 and Pm = 3. We see in Fig. 3.9(b) that the bifurcation for multipolar branch is supercritical. When decreasing the Rayleigh number, the dipolar branch loses its stability for $\mathrm{Ra}/\mathrm{Ra_c} \sim 20$, when the magnetic field strength becomes too weak.

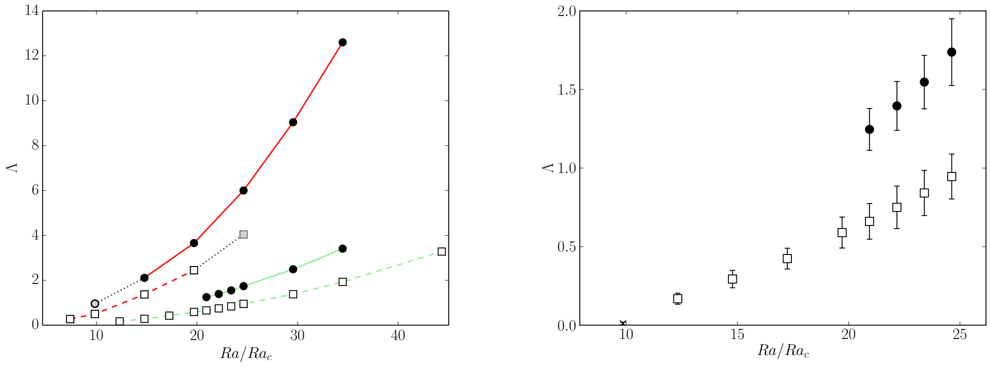

(a)

(b)

Figure 3.9 – (a): Elsasser number Λ as a function of $\mathrm{Ra}/\mathrm{Ra_c}$, for Pm = 1 (green) and Pm = 3 (red). The meaning of the symbol shapes is defined in the caption of Fig. 3.8. A grey marker indicates that the solution loses its stability. (b): Detail of the bifurcation close to the dynamo threshold for Pm = 1. Error bars represent the standard deviations.

For higher magnetic Prandtl numbers, the bifurcation of the multipolar branch still seems to be supercritical. Interestingly, one notes in Fig. 3.9(a) for Pm = 3 that the multipolar branch loses its stability when increasing the Rayleigh number. A physical explanation for this behaviour is that the mean zonal flow does not grow fast enough as the field strength increases, and the dynamo switches to the dipolar solution. This simple physical scenario can be illustrated by comparing the variation in the field strength of the dipolar branch, as measured by Λ^{dip}, and the zonal shear of the multipolar branch, as measured by Ro_z^{mul}. Indeed, we see in Fig. 3.10 that the higher the magnetic Prandtl number, the faster the growth of the ratio between Λ^{dip} and Ro_z^{mul}. This explains why the multipolar branch destabilizes at large forcing for larger Pm (Pm = 3, red dashed line in Fig. 3.9(a)), while it remains stable at smaller Pm ($Pm = 1$, green dashed line in Fig. 3.9(a)).

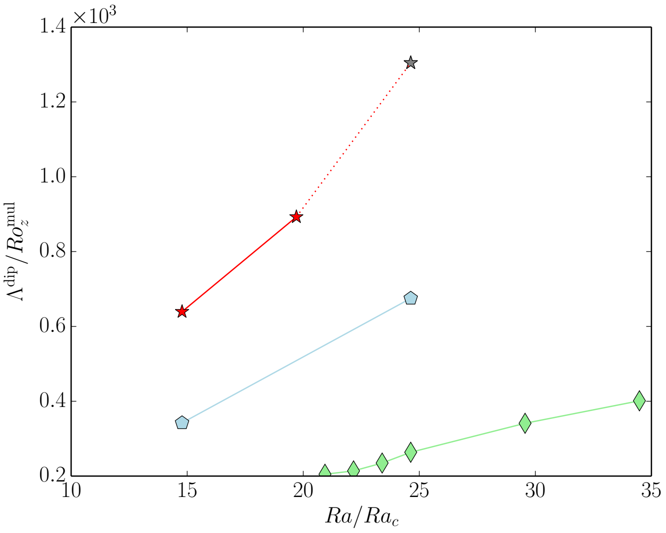

Figure 3.10 – Ratio $\Lambda^{\text{dip}}/Ro_z^{\text{mul}}$ as a function of $\text{Ra}/\text{Ra}_\text{c}$, for $\text{Pm} = 1$ (green diamonds), $\text{Pm} = 2$ (blue pentagons) and $\text{Pm} = 3$ (red stars). The point marked with the grey star has been computed with the model corresponding to the grey square in Fig. 3.9.

Because of computational limitations, we were not able to find for $\text{Pm} > 1$ the Rayleigh numbers for which the dipolar branch should disappear.

3.2.2 Equatorial dipole

We have shown in the previous section that dipolar and multipolar dynamos in anelastic simulations were no longer distinguishable from each other in terms of f_{dip}, contrary to Boussinesq models. This smoother transition has been attributed to the presence of dynamos with a high equatorial dipole contribution, which leads to intermediate values for f_{dip}.

However, Fig. 3.11(a) shows that this tendency already exits at low N_ϱ, and thus cannot be accounted for only in terms of anelastic effects. Furthermore, when the equatorial dipole component is removed to compute the relative dipole field strength, we recover a more abrupt transition, as we can see in Fig. 3.11(b) which shows the relative axial dipole field strength $f_{\text{dip}_{\text{ax}}}$. Dipolar dynamos are left unchanged by this new definition, whereas multipolar dynamos of intermediate dipolarity are no longer observed, which confirms that the increase in f_{dip} is due to a significant equatorial dipole component. The quantity $f_{\text{dip}_{\text{ax}}}$ therefore provides a robust criterion to distinguish the dipolar and the multipolar branches.

To further characterize the emergence of multipolar dynamos with a significant equatorial dipole contribution, we plot in Fig. 3.12(a) the values of the modified tilt angle θ, defined by

$$\theta = \frac{2}{\pi}\left\langle \sqrt{\left(\Theta(t) - \frac{\pi}{2}\right)^2} \right\rangle_t , \qquad (3.6)$$

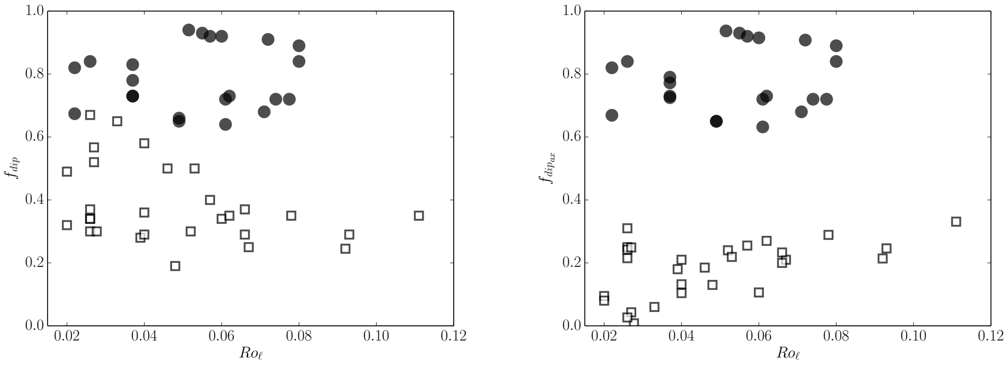

(a) $f_{\rm dip}$ (b) $f_{{\rm dip}_{\rm ax}}$

Figure 3.11 – (a): The relative dipole field strength $f_{\rm dip}$ versus the local Rossby number. (b): The relative axial dipole field strength $f_{{\rm dip}_{\rm ax}}$ versus the local Rossby number. The meaning of the symbol shapes is defined in the caption of Fig. 3.8.

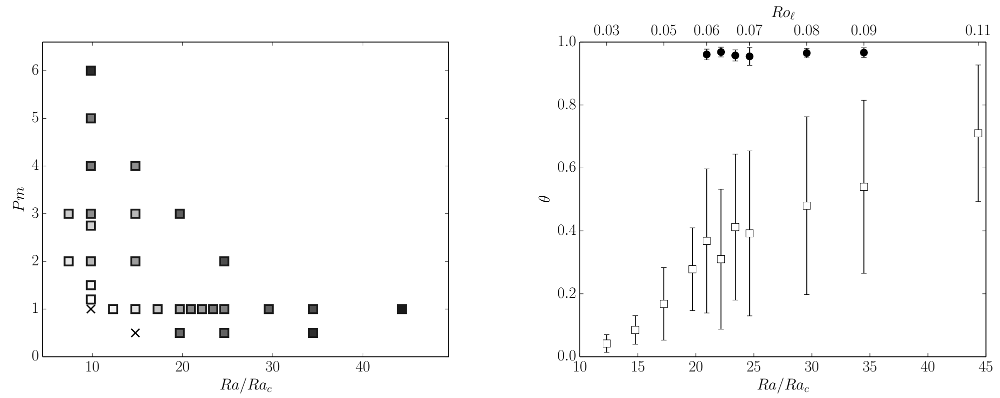

(a) (b)

Figure 3.12 – (a): Evolution of the modified tilt angle θ for multipolar dynamos as a function of $\mathrm{Ra/Ra_c}$ and Pm. Colour scale ranges from white ($\theta = 0$) to black ($\theta = 0.7$). (b): θ as a function of $\mathrm{Ra/Ra_c}$ for $\mathrm{Pm} = 1$. Upper x axis corresponds to the values of Ro_ℓ for the multipolar branch. The meaning of the symbol shapes is defined in the caption of Fig. 3.8. Error bars represent the standard deviations.

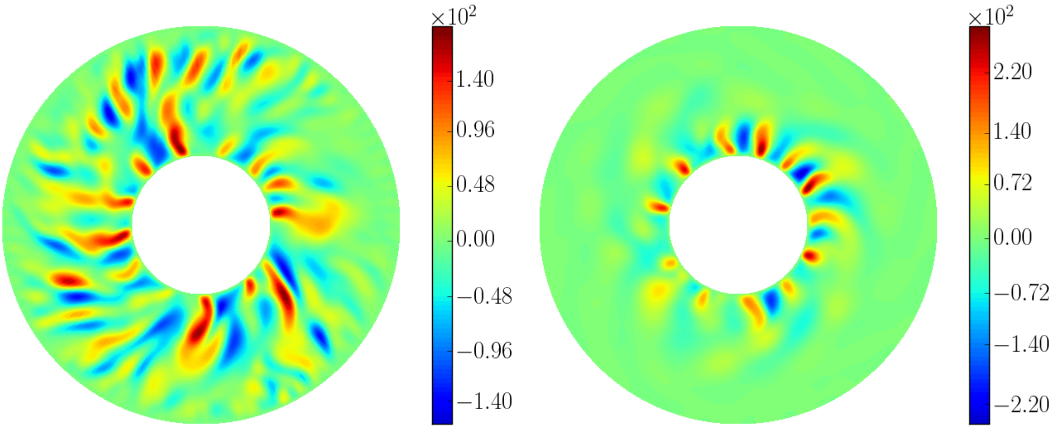

(a) $g \propto r$ (b) $g \propto 1/r^2$

Figure 3.13 – v_r equatorial cross sections, with $\mathrm{E} = 10^{-4}$, $\mathrm{Pr} = 1$. (a): $g \propto r$ and $\mathrm{Ra}/\mathrm{Ra_c} = 9.0$, $Pm = 1$. (b): $g \propto 1/r^2$ and $\mathrm{Ra}/\mathrm{Ra_c} = 9.9$, $Pm = 1.2$.

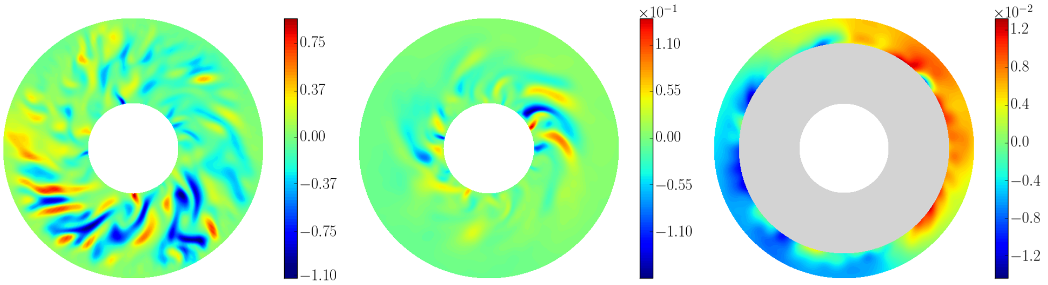

(a) $g \propto r$ (b) $g \propto 1/r^2$ (c) $g \propto 1/r^2$

Figure 3.14 – B_r equatorial cross sections, with $\mathrm{E} = 10^{-4}$, $\mathrm{Pr} = 1$. (a): $g \propto r$ and $\mathrm{Ra}/\mathrm{Ra_c} = 9.0$, $Pm = 1$. (b),(c): $g \propto 1/r^2$ and $\mathrm{Ra}/\mathrm{Ra_c} = 9.9$, $Pm = 1.2$. Colour in figure (c) has been rescaled to highlight the emergence of a $m = 1$ mode at the outer sphere.

Low values of θ are characteristic of an equatorial dipole on the surface of the outer sphere and they appear to be preferably localized close to the dynamo threshold of the multipolar branch, at low Rayleigh and magnetic Prandtl numbers. In our case, dynamos with a stronger equatorial dipole component belong to the class of multipolar dynamos, but since they are always close to the threshold, fewer modes are likely to be excited. As the Rayleigh number or the magnetic Prandtl number is increased, the dipole axis is not stable anymore but fluctuates in the interval $[0,\pi]$, which is typical of polarity reversals for multipolar dynamos (Kutzner & Christensen 2002). This evolution is illustrated in Fig. 3.12(b) for dynamos at $\mathrm{Pm}=1$. For this subset of models, we computed the percentage of the non-axisymmetric magnetic energy density with respect to the total magnetic energy density E_m and saw that it tends to increase from 85% on average for multipolar dynamos up to 93% as the Rayleigh number is decreased.

Part of the changes we reported about anelastic dynamos simulations do not seem to come from the stratified reference density profile, but from the choice of a gravity profile proportional to $1/r^2$. This profile differs from the gravity profile proportional to r that was used for Boussinesq simulations and is actually the only significant difference between previous studies and our low N_ϱ simulations. As a consequence, convection cells form and stay closer to the inner sphere, as we can see in Fig. 3.13. We compare here equatorial cuts of the radial component of the velocity for both choices of gravity profile. This strong difference in the flow reflects on the localization of the active dynamo regions, as we can see in the corresponding cuts of the radial component of the magnetic field in Fig. 3.14. With a gravity profile proportional to $1/r^2$, the magnetic field is mainly generated close to the inner sphere where the convection cells form. Consequently, our measure of the dipole field strength f_dip at the surface of the outer sphere appears to be biased, since it will essentially be sensitive to the less diffusive large scale modes. This filter effect is likely to be responsible for the increase in f_dip we reported in some anelastic dynamo models. However, for higher density stratification $N_\varrho=3$ and Prandtl numbers $\mathrm{Pr}=2$ and $\mathrm{Pm}=4$, we identify equatorial dipole dynamos with a $m=1$ component that is not localized on the outer sphere (see Fig. 3.5), and for which the present mechanism will not be relevant.

Besides, this study naturally constitutes an appropriate reference basis from which a detailed understanding of the role of the density stratification in anelastic dynamo models can be achieved. In the next section, we will focus on the influence of the density stratification on dipolar dynamos.

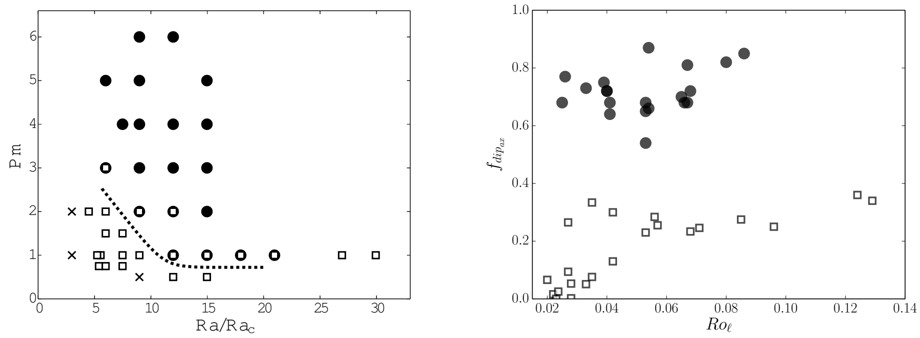

(a) $N_\varrho = 0.5$ (b) $N_\varrho = 0.5$

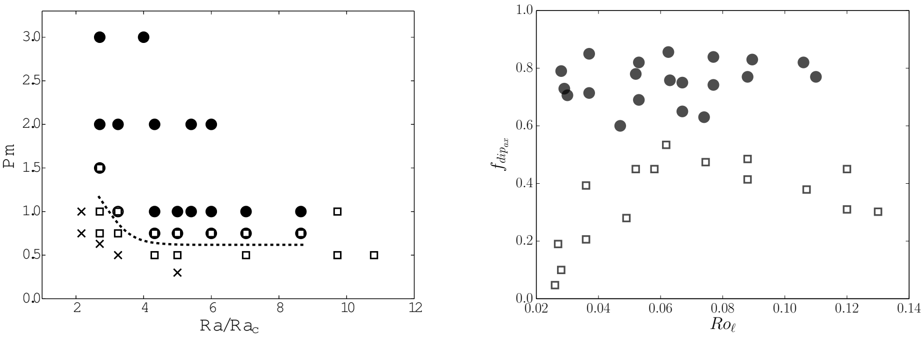

(c) $N_\varrho = 1.5$ (d) $N_\varrho = 1.5$

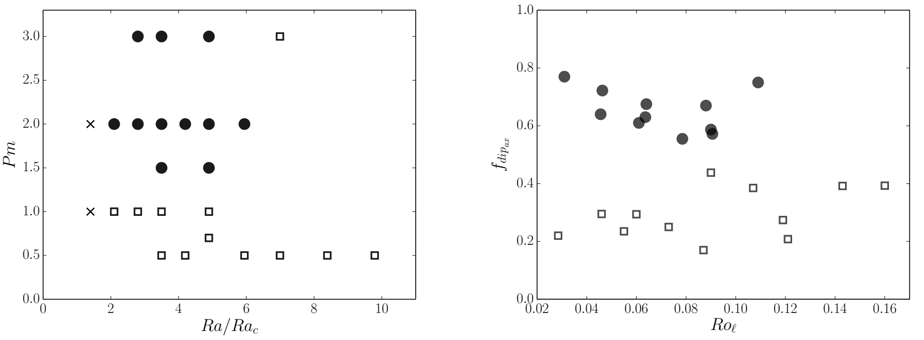

(e) $N_\varrho = 2.0$ (f) $N_\varrho = 2.0$

Figure 3.15 – Left: dipolar (black circles) and multipolar (white squares) dynamos as a function of Ra/Ra$_c$ and Pm, for $N_\varrho = 0.5$ (a), $N_\varrho = 1.5$ (c) and $N_\varrho = 2.0$ (e). A cross indicates the absence of a self-sustained dynamo. Right: the relative axial dipole field strength $f_{\text{dip}_{\text{ax}}}$ versus the local Rossby number for $N_\varrho = 0.5$ (b), $N_\varrho = 1.5$ (d) and $N_\varrho = 2.0$ (f).

3.3 Dipolar dynamos and stratification

We have already mentioned in the section 3.1 that for a given N_ϱ, E and Pr, there seems to exist a critical magnetic Prandtl number $\mathrm{Pm_c}$ below which the dipolar solution is not stable, and the higher the density stratification, the higher this critical magnetic Prandtl number (see Fig. 3.7 on page 55). To clarify the general statement that dipolar solutions seem more difficult to obtain as soon as substantial stratifications are considered (Gastine *et al.* 2012, Jones 2014), we will investigate in more detail the evolution of the stability domain of the dipolar branch as the density stratification is increased. To that end, we rely on a subset of 119 models characterised by the parameters (3.5) with increasing density contrasts.

3.3.1 Bistability

Figure 3.15 shows the distribution of dipolar and multipolar dynamos in the parameter space ($\mathrm{Ra}/\mathrm{Ra_c}$, Pm) (left-hand panels), together with the corresponding dipolarities (right-hand panels), for increasing density stratifications from top to bottom. One can see that several examples of bistable pairs are displayed. Bistability is commonly known for Boussinesq and anelastic models, and is related to the use of stress-free boundary conditions that allows for the growth of stronger zonal winds (Sasaki *et al.* 2011, Schrinner *et al.* 2012, Gastine *et al.* 2012). For $N_\varrho = 0.5$, the regime diagram in Fig. 3.15(a) does not qualitatively differ from what we can observe in the Boussinesq regime. As we found in Raynaud *et al.* (2014), the multipolar branch undergoes a supercritical bifurcation as Ra is increased, whereas the dipolar one still loses its stability in favour of the multipolar branch at low Rayleigh and magnetic Prandtl numbers. When increasing the density contrast N_ϱ to 1.5, one can note in Fig. 3.15(c) that the overlap between the two branches shrinks. At $N_\varrho = 2$, we do not observe a bistable case. More generally, for all models of our sample with a density stratification $N_\varrho \geq 2$, the saturated field of the dynamo is not anymore sensitive to the amplitude of the initial magnetic field. To understand this evolution from Boussinesq models to anelastic models with moderate stratification ($N_\varrho \leq 1.5$), it is worth stressing that the transition process from the multipolar to the dipolar branch triggered by the increase of Pm still applies to our sample of models (see Schrinner *et al.* 2012). Figure 3.16(a) illustrates on a few cases the progressive merging of the multipolar branch which is indeed lost when its zonal Rossby number becomes comparable to the zonal Rossby number of the dipolar branch. For a given Rayleigh number, the fact that the mean zonal flow of the multipolar branch decreases with Pm (and eventually becomes too small to prevent the growth of the axial dipole) is actually the limiting factor of the upper extent of the multipolar branch in the left-hand panels of Fig. 3.15. This also emphasizes the essential role played by differential rotation in the dynamo

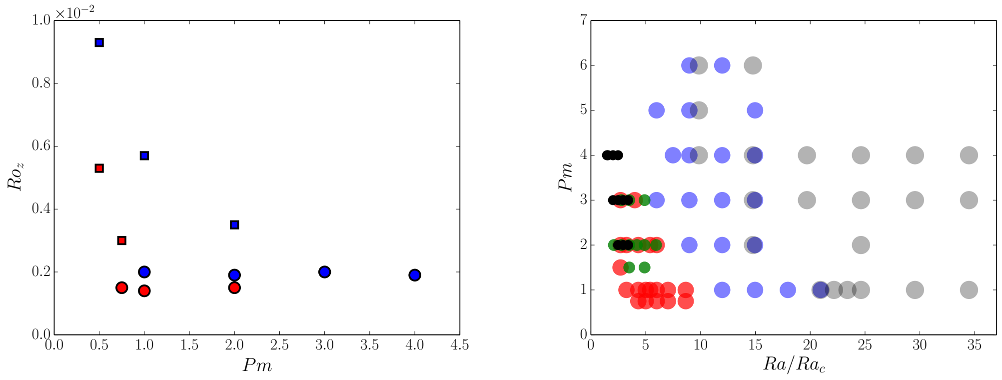

(a) (b)

Figure 3.16 – (a): Evolution of the zonal Rossby number as a function of Pm for a dynamo models with Ra = 4×10^6, at $N_\varrho = 0.5$ (blue) and $N_\varrho = 1.5$ (red). Circles (squares) stands for dipolar (multipolar) dynamos. (b): Dipolar dynamos in the parameter space ($\mathrm{Ra}/\mathrm{Ra}_c$, Pm), for increasing density stratifications: $N_\varrho = 0.1$ (grey), $N_\varrho = 0.5$ (blue) $N_\varrho = 1.5$ (red), $N_\varrho = 2.0$ (green) and $N_\varrho = 2.5$ (black).

mechanism of the multipolar branch, often accounted for in terms of Ω-effect.

Interestingly, the zonal Rossby number for multipolar dynamos substantially decreases between $N_\varrho = 0.5$ and 1.5 (see the blue and red squares in Fig. 3.16(a)), while it remains of the same order for dipolar dynamos. Hence, the available range of Pm for the multipolar solution is reduced, which therefore explains the relative shrinking of the bistable region when comparing Figs 3.15(a) and 3.15(c). The simplest argument to understand this downtrend is given by the comparison of the x-axis in Fig. 3.15, which reveals that the dynamo onset moves closer to the onset of convection when the density stratification is increased, as mentioned by Gastine *et al.* (2012). Indeed, despite changing the value of N_ϱ, we found that the Rayleigh numbers we had to consider always stay of the order of 10^6. At the same time, the critical Rayleigh number for the linear onset of convection monotonically increases with N_ϱ : we have in our case the following values of 3.34×10^5, 9.25×10^5 and finally 1.43×10^6 for the sequence of density stratifications $N_\varrho = 0.5$, 1.5 and 2.0, respectively.

3.3.2 Dipole onset

The density stratification strongly impacts on the stability domain of the dipolar branch, as we clearly see in Fig. 3.16(b). In this figure, we included data from Raynaud *et al.* (2014) in order to better highlight the differences with Boussinesq simulations. For moderate values of N_ϱ at a fixed Pm, the critical value of $\mathrm{Ra}/\mathrm{Ra}_c$

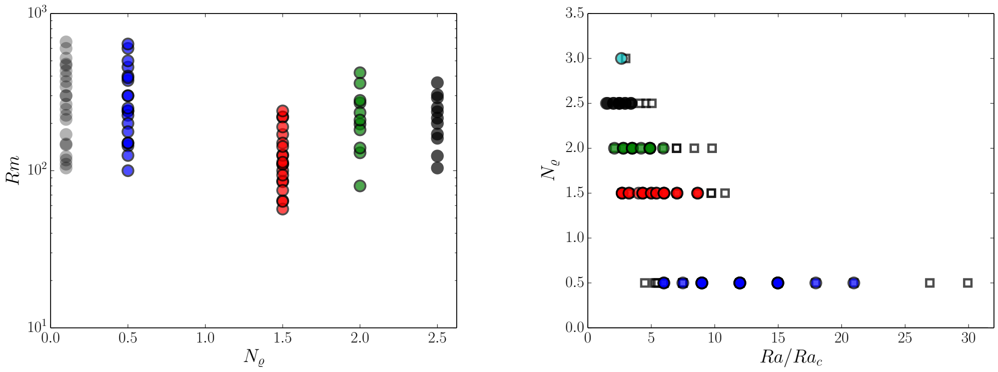

(a) (b)

Figure 3.17 – (a): Magnetic Reynolds number as a function of N_ϱ for dipolar dynamos. (b): Our sample of dipolar (circles) and multipolar (squares) dynamos in the parameter space $(\mathrm{Ra}/\mathrm{Ra}_c, N_\varrho)$.

at which it is possible to sustain a dipolar dynamo rapidly falls off (up to a factor of 4 if we consider the line $\mathrm{Pm} = 1$). However, this tendency hardly persists once we reach $\mathrm{Ra}/\mathrm{Ra}_c \sim 5$ for $N_\varrho = 1.5$, and the further increase of N_ϱ mainly affects the critical magnetic Prandtl number Pm_c below which it is not possible to sustain a dipolar dynamo. In our sample of models, the increase of Pm_c becomes effective for $N_\varrho \geq 2$, but we already reported it as a general tendency in Schrinner *et al.* (2014). Figure 3.15(c) enables us to conclude that $0.5 < \mathrm{Pm}_c \leq 0.75$ for $N_\varrho = 1.5$, whereas from Fig. 3.15(e), it is clear that $\mathrm{Pm}_c > 1$ for $N_\varrho = 2$.

The fact that dipolar dynamos are found closer to the convection threshold as N_ϱ increases can be more or less readily understood if one notices that, despite the increase of the density stratification, the critical magnetic Reynolds number Rm_c of the dipolar branch does not significantly vary, but stays in first approximation of the order of 10^2, as shown in Fig. 3.17(a). Then, if we take this as a necessary condition to obtain a dipolar solution, and given the fact that for a constant value of $\mathrm{Ra}/\mathrm{Ra}_c$ the flow amplitude increases with N_ϱ (Gastine *et al.* 2012), it explains why the dipolar branch can be found closer to the onset of convection when the stratification increases. However, we will see in the next subsection that, as N_ϱ is further increased, not only does the dipolar branch occur closer to the onset of convection, but also higher magnetic Prandtl numbers have to be considered to maintain a sufficiently high Rm while preventing the collapse of the dipole.

3.3.3 Dipole collapse

Another striking feature that arises when investigating the stability domain of the dipolar branch is that the range of Rayleigh numbers over which it extends becomes smaller and smaller as N_ϱ is increased. This is clearly visible in Fig. 3.17(b) that shows for different N_ϱ the transition from the dipolar to the multipolar branch resulting from the increase of Ra. In other words, at this moderate value of the Ekman number, dipolar dynamos are confined in a narrower and narrower window of Rayleigh numbers, which explains why dipolar solutions may seem more difficult to obtain at higher N_ϱ, despite comparable critical magnetic Reynolds numbers. As for the modification of the dynamo onset, this can be related to the fact that for a given value of $\mathrm{Ra}/\mathrm{Ra_c}$, the Rossby number Ro increases with N_ϱ. The transition from a dipolar to a multipolar solution triggered by an increase of Ra is related to the fact that inertia becomes significant in the force balance. We know from Christensen & Aubert (2006) that this transition can be measured by a local Rossby number Ro_ℓ based on a characteristic length-scale of the flow. We find that the collapse of the dipole still occurs for $Ro_\ell \sim 0.1$ when $N_\varrho \leq 2$, which is consistent with the results in Gastine *et al.* (2012). This is illustrated by Figures 3.15(b), 3.15(d) and 3.15(f) which show the relative axial dipole field strength $f_{\mathrm{dip_{ax}}}$ computed at the outer sphere, as a function of Ro_ℓ. In Fig. 3.15(b), the very low values of $f_{\mathrm{dip_{ax}}}$ at low Ro_ℓ are characteristics of multipolar dynamos dominated by an equatorial dipole component. We showed in Raynaud *et al.* (2014) that this magnetic configuration arises close to the dynamo onset and when convective cells are localized close to the inner sphere. However, we know from hydrodynamic studies that the convection cells move towards the outer shell when the stratification is increased (Jones *et al.* 2009, Gastine & Wicht 2012), which explains why this feature tends to disappear in Figs 3.15(d) and 3.15(f). Besides, we see in Fig. 3.18 that the values of $f_{\mathrm{dip_{ax}}}$ tend to decrease with N_ϱ, which is also clear if we focus for instance on the dipolar branch in Fig. 3.15(f) for which $f_{\mathrm{dip_{ax}}} < 0.8$. As expected, this indicates that the small magnetic scales at the outer surface are favoured with the increase of the stratification. This is also clearly confirmed by the comparison of the radial magnetic fields at the outer surface of the model, as shown in the left-hand panels of Figs 3.19 and 3.20. Finally, we also report the existence of multipolar dynamos whose dipolarity displays strong variations in time. This leads to averaged values of $f_{\mathrm{dip_{ax}}} \sim 0.5$, as one can notice in Fig. 3.15(d). These dynamos usually exhibit a relatively strong axial dipole component which undergoes reversals during which the value of $f_{\mathrm{dip_{ax}}}$ decreases drastically. Duarte *et al.* (2013) also reported similar behaviour for dynamo models with a variable electrical conductivity.

For $N_\varrho > 2.0$, we found that the dipole collapse tends to occur at values of Ro_ℓ lower than 0.1. However, it is likely that a volume-averaged quantity becomes less relevant when applied to models with a substantial stratification. For instance, we

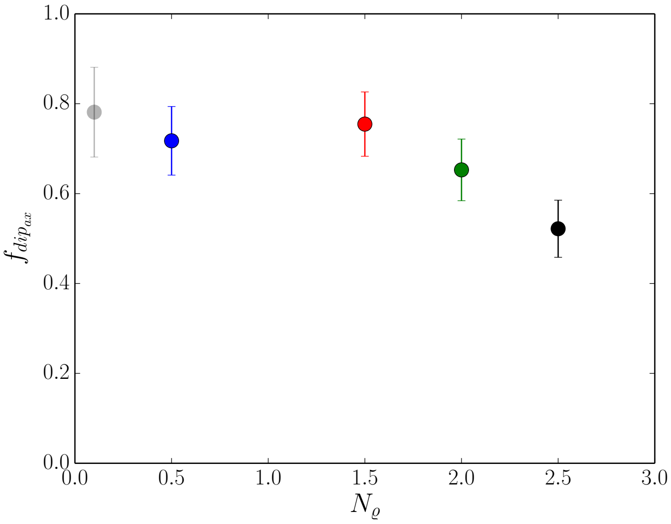

Figure 3.18 – Average values of $f_{\mathrm{dip}_{\mathrm{ax}}}$ for dipolar dynamos as a function of N_ϱ. Error bars represent the standard deviation. The average is done with 11 models for $N_\varrho = 2.5$.

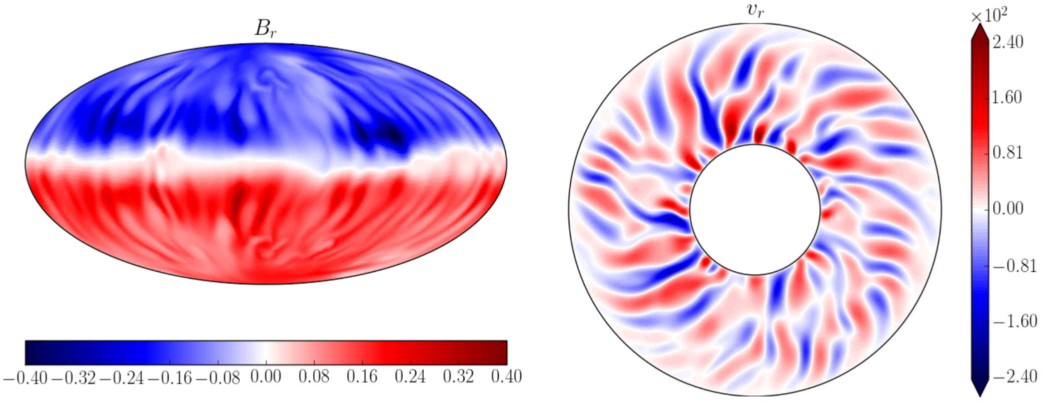

(a) $N_\varrho = 1.5$ (b) $N_\varrho = 1.5$

Figure 3.19 – Snapshot of B_r ($r = r_o$) (a) and equatorial cut of v_r (b) for a dipolar dynamo with $N_\varrho = 1.5$, Pm = 0.75, Ra = $4.625 \times 10^6 = 5\mathrm{Ra_c}$.

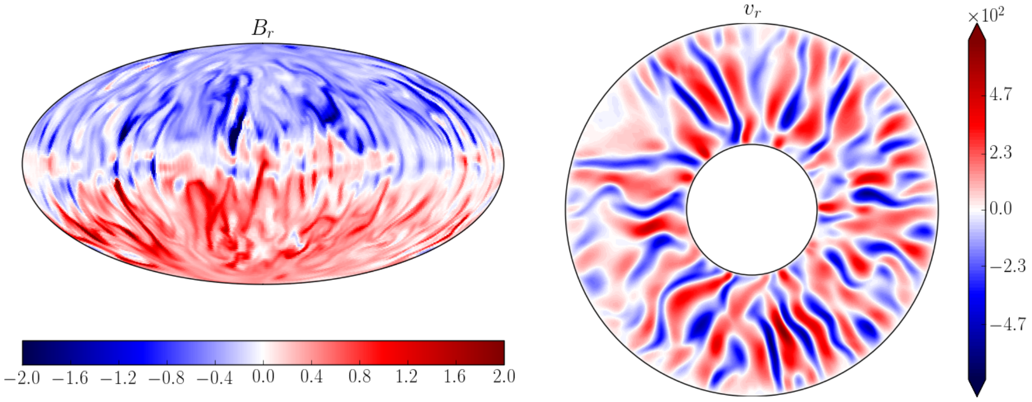

(a) $N_\varrho = 2.5$ (b) $N_\varrho = 2.5$

Figure 3.20 – Snapshot of B_r ($r = r_o$) (a) and equatorial cut of v_r (b) for a dipolar dynamo with $N_\varrho = 2.5$, $\mathrm{Pm} = 2$, $\mathrm{Ra} = 7.40 \times 10^6 = 3.4\mathrm{Ra_c}$.

see in Figs 3.19(b) and 3.20(b) that the smaller structures that develop at $N_\varrho = 2.5$ are confined close to the outer boundary, whereas there are no significant differences in the radial flow at mid-depth. Thus, it turns out that it is useful to examine the variations with depth of the local Rossby number, defined in such a way that $Ro_\ell = \int_{r_i}^{r_o} Ro_\ell(r) r^2 \, \mathrm{d}r$. We found that it is more suitable to slightly adapt our initial definition and investigate the radial dependence of $Ro_\ell^\star(r)$, which differs from $Ro_\ell(r)$ in so far as the velocity is not weighted by the reference density profile w^n. We also checked that, in our range of N_ϱ, both estimates of a characteristic velocity do not make a qualitative difference on the volume-averaged quantities. For instance, the difference between the values of the magnetic Reynolds number $\mathrm{Rm} = Ro\mathrm{Pm}/\mathrm{E}$ is about 1 per cent at $N_\varrho = 0.5$. Of course, it increases with N_ϱ: energy-based estimates lead to lower values about 7 and 10 per cent for $N_\varrho = 2.0$ and $N_\varrho = 2.5$, respectively. However, this does not change our conclusions, and that is why we do not adapt our definition for volume-averaged quantities. We examined the radial dependence of the different components of the local Rossby number $Ro_l^\star$, which is computed as the product of two terms: a convective Rossby number based on the velocity field $\mathbf{u}_c$ from which the mean zonal flow has been subtracted (see Fig. 3.21(a)) and a characteristic length-scale based on the mean harmonic degree of $\mathbf{u}_c$ (see Fig. 3.21(b)). We find that the monotonicity of $Ro_l^\star$ changes as N_ϱ is increased. Indeed, for low stratifications, $Ro_l^\star(r)$ mainly decreases with radius, whereas for $N_\varrho \geq 2.5$ it becomes an increasing function of r that steepens slightly close to the outer surface. Figure 3.21(c) shows the evolution of $Ro_l^\star(r)$ for increasing Rayleigh numbers up to the loss of the dipolar solution, at $N_\varrho = 2.5$ and 3.0. When the transition to the multipolar branch is reached, we see that $Ro_\ell^\star$

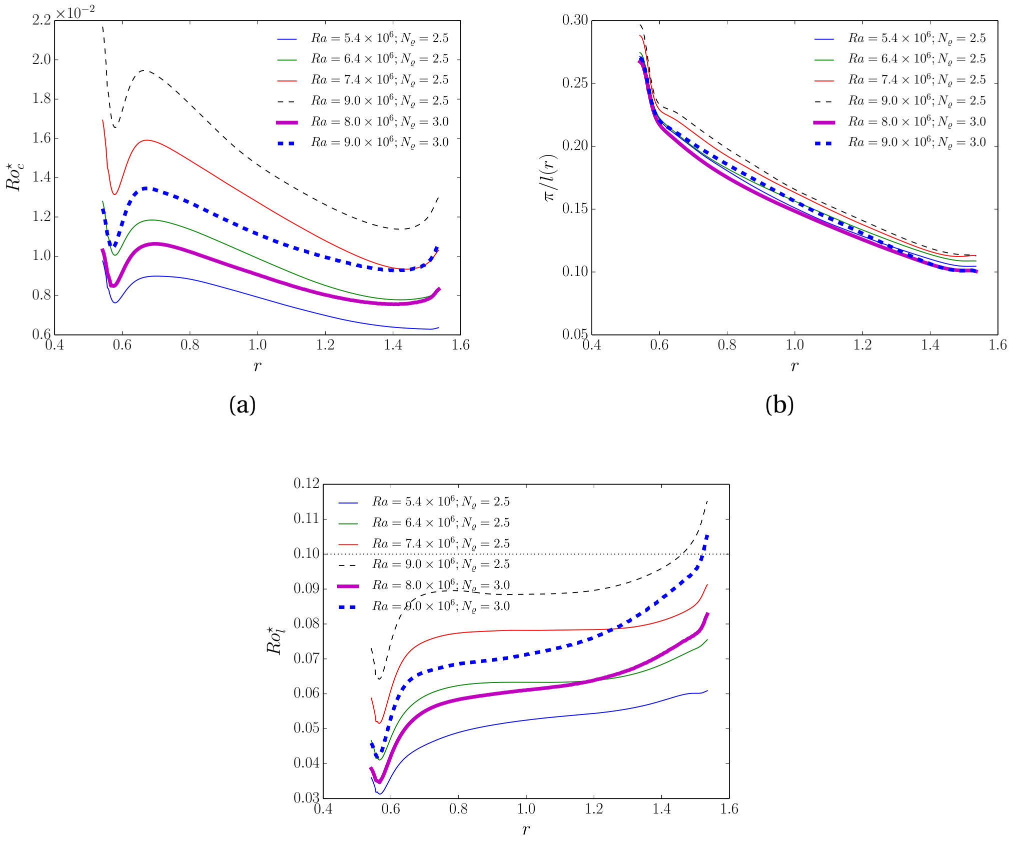

(a)

(b)

(c)

Figure 3.21 – The convective Rossby number (a), the convective length-scale (b) and the local Rossby number (c) as a function of radius for dipolar (solid lines) and multipolar (dashed lines) dynamos at ($N_\varrho = 2.5$, Pm = 2) (thin lines) and ($N_\varrho = 3$, Pm = 4) (thick lines).

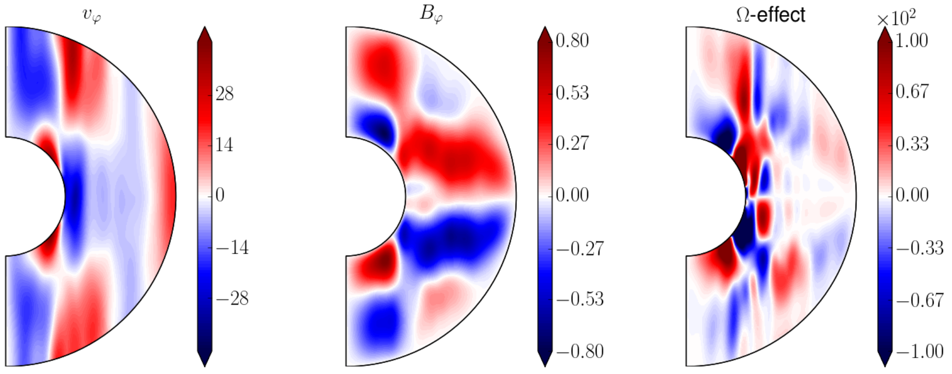

(a) $N_\varrho = 1.5$ (b) $N_\varrho = 1.5$ (c) $N_\varrho = 1.5$

Figure 3.22 – Time-averaged axisymmetric component of the azimuthal velocity field (a) and magnetic field (b) for a dipolar dynamo with $N_\varrho = 1.5$, $\mathrm{Ra} = 4.625 \times 10^6$, $\mathrm{Pm} = 0.75$.

tends to increase faster close to the outer surface, while the volume-averaged value can stay below the critical value of 0.1. Thus, it seems that inertia still causes the collapse of the dipolar branch, despite the fact that the usual local Rossby number criterion is not appropriate to separate the two dynamo branches for significant density stratifications.

3.3.4 Dynamo mechanisms

Finally, we try to investigate whether the dynamo mechanisms at work on the dipolar branch are modified when the stratification is increased. We see in Fig. 3.22 that the axisymmetric azimuthal magnetic field we observe at $N_\varrho = 1.5$ is strongly reminiscent of the magnetic structures that can be observed with Boussinesq models, which are usually interpreted in terms of α^2 dynamos (Olson *et al.* 1999, Schrinner *et al.* 2007, 2011a, 2012). Inside the tangent cylinder, the azimuthal magnetic field is mainly produced by the Ω-effect,

$$r\overline{\mathbf{B}}_r\partial\left(r^{-1}\overline{\mathbf{V}}_\varphi\right)/\partial r + r^{-1}\sin\theta\,\overline{\mathbf{B}}_\theta\partial\left(\sin\theta^{-1}\overline{\mathbf{V}}_\varphi\right)/\partial\theta\,, \tag{3.7}$$

which correlates inside the tangent cylinder with the axisymmetric azimuthal magnetic field, when comparing Figs 3.22(b) and 3.22(c). However, outside the tangent cylinder, the most part of the mean azimuthal field does not seem to be the result of the Ω-effect, and it is thus likely that the essential regeneration of the poloidal field is achieved by α-effect, leading to the emergence of characteristic equatorial patches of opposite polarity (see e.g. Christensen 2011, Schrinner *et al.* 2012).

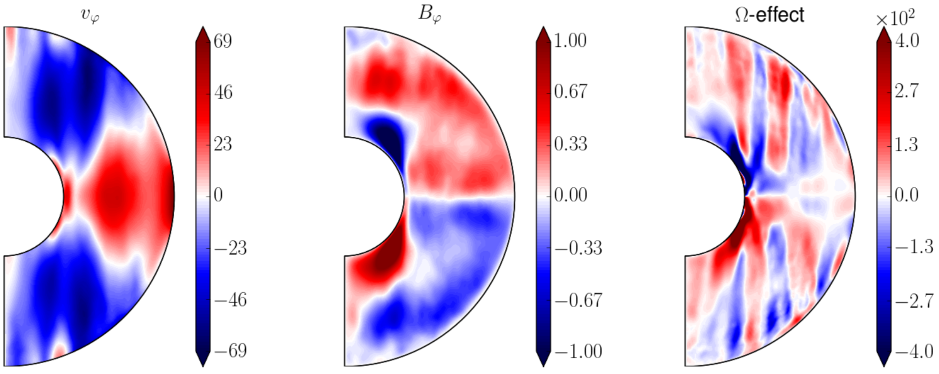

(a) $N_\varrho = 2.5$ (b) $N_\varrho = 2.5$ (c) $N_\varrho = 2.5$

Figure 3.23 – Time-averaged axisymmetric component of the azimuthal velocity field (a) and magnetic field (b) for a dipolar dynamo with $N_\varrho = 2.5$, $\mathrm{Ra} = 7.40 \times 10^6$, $\mathrm{Pm} = 2$.

We did not find in our sample of models tangible evidence that would invalidate this scenario at higher N_ϱ. For instance, at $N_\varrho = 2.5$, we see in Fig. 3.23 that the major differences lie in the stronger axisymmetric azimuthal velocity (compare Figs 3.22(a) and 3.23(a)). Nevertheless, the axisymmetric azimuthal magnetic field shown in Fig. 3.23(b) seems only modified about a colatitude $\theta \sim \pi/4$ close to the outer surface, and keeps now the same polarity in each hemisphere outside the tangent cylinder. This change can be correlated to the modifications of the axisymmetric azimuthal velocity, which in turn affect the Ω-effect (compare Figs 3.22(c) and 3.23(c)). Of course, we are for now limited to the observation of correlations, but it would be interesting to have a further insight into the dynamo mechanism in anelastic simulations using a test field method, in the spirit of the Boussinesq study by Schrinner *et al.* (2012).

3.4 Scaling laws

Because of computational limitations, very small length scales and time scales associated with extreme parameter values relevant for planets and stars cannot be resolved in global direct numerical dynamo simulations. Therefore, numerical models are in general not directly comparable to planetary or stellar dynamos. Instead, scaling laws, in particular for the field strength, have been derived from theory and simulations and then extrapolated to realistic parameter regimes (see Christensen 2010, and references therein). Subsequently, their predictions may be compared with planetary or stellar magnetic field data obtained from observations

(Christensen *et al.* 2009, Christensen 2010, Davidson 2013). By this consistency test, scaling laws may provide some evidence about the reliability of numerical dynamo models.

Moreover, different scaling laws could typically represent different force balances or dynamo mechanisms and their investigation might enable us to better distinguish between different types of dynamo models. It is in particular this second aspect which is of interest in the following. We adopt here the approach by Christensen & Aubert (2006) and test scaling laws for the field strength, the velocity, the magnetic dissipation time, and the convective heat transport and compare them with previous results from Boussinesq simulations. A similar study was recently published by Yadav *et al.* (2013b) based on a somewhat different sample of models. Similarities and differences with their findings will be discussed.

Most of the proposed scaling laws are independent of diffusivities, which are thought to be negligible under astrophysical conditions (Christensen 2010). However, present, global dynamo simulations run in parameter regimes where diffusivities still influence the overall dynamics and weak dependencies on the magnetic Prandtl number seem to persist in purely empirically derived scalings (Christensen & Tilgner 2004, Christensen & Aubert 2006, Christensen 2010, Yadav *et al.* 2013a, Stelzer & Jackson 2013). In this study we do not attempt to resolve this secondary dependence on Pm because the magnetic Prandtl number varies only between 1 and 5 in our sample of models.

To study the different scaling laws in our anelastic models, we need to introduce the following parameters. The Nusselt number, evaluated for instance at the inner sphere,

$$Nu_{\text{bot}} = -\frac{(\exp(N_\varrho)-1)\, w_{\text{i}} r_{\text{i}}^2}{4\pi n c_1} \int_{S_{\text{i}}} \frac{\partial s}{\partial r} \sin\theta \, \mathrm{d}\theta \, \mathrm{d}\varphi, \tag{3.8}$$

quantifies the total amount of heat transported in and out the fluid shell relative to the conductive heat flux. The constants in Eq. (3.8) are defined in Eqs (2.47) and (2.48), and the non-dimensionnal expression of r_{i} is given by $r_{\text{i}} = \chi/(1+\chi)$. We also introduce a Nusselt number based on the advective heat flux alone,

$$Nu^\star = (Nu_{\text{bot}} - 1)\,\frac{\mathrm{E}}{\mathrm{Pr}}, \tag{3.9}$$

and accordingly a quantity usually referred as the flux based Rayleigh number,

$$Ra_Q = (Nu_{\text{bot}} - 1)\,\frac{\mathrm{Ra}\,\mathrm{E}^3}{r_{\text{o}}^2\,\mathrm{Pr}^2}. \tag{3.10}$$

The energy balance plays a crucial role in the classical derivation of scaling laws for the saturation level of the magnetic field. In particular, the fraction of ohmic to total dissipation, $f_{\text{ohm}} = D/P$, is introduced because it determines the available

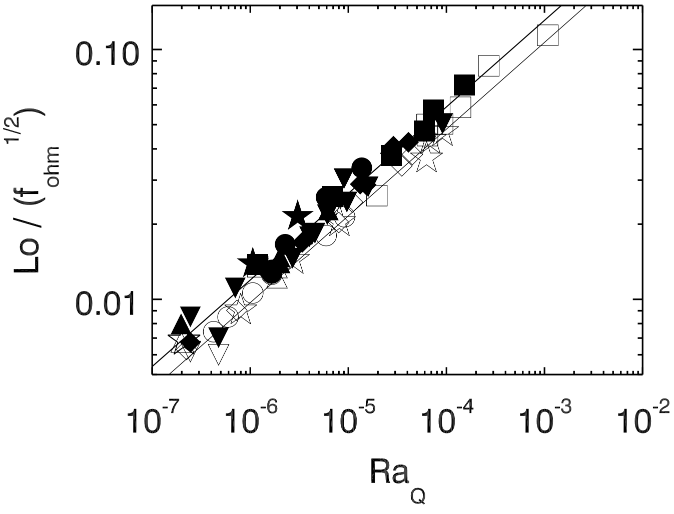

Figure 3.24 – $Lo/f_{\text{ohm}}^{1/2}$ as a function of Ra_Q. The symbols are explained in the caption of Fig. 3.1.

power used for the magnetic field generation. In an equilibrium state, the total dissipation equals the power released by buoyancy,

$$P = \frac{\mathrm{Ra}\,\mathrm{E}^3}{\mathrm{Pr}\,\mathrm{Pm}} \int_V w^n u_r S \,\mathrm{d}V, \tag{3.11}$$

and the ohmic dissipation is given by

$$D = \left(\frac{\mathrm{E}}{\mathrm{Pm}}\right)^2 \int_V (\nabla \times \mathbf{B})^2 \,\mathrm{d}V. \tag{3.12}$$

In Eqs (3.11) and (3.12), we scaled P and D by $\varrho_r \Omega^3 d^5$.

3.4.1 Magnetic field scaling

The magnetic field strength measured in terms of the Lorentz number scales with the available energy flux to the power of approximately 1/3. We find for the dipolar dynamos of our sample

$$\frac{Lo}{f_{\text{ohm}}^{1/2}} \simeq 1.58\, Ra_Q^{0.35}, \tag{3.13a}$$

and for the multipolar models

$$\frac{Lo}{f_{\text{ohm}}^{1/2}} \simeq 1.19\, Ra_Q^{0.34}. \tag{3.13b}$$

Except for somewhat larger exponential prefactors, this is in good agreement with previous results from Boussinesq simulations (Christensen 2010, Schrinner *et al.*

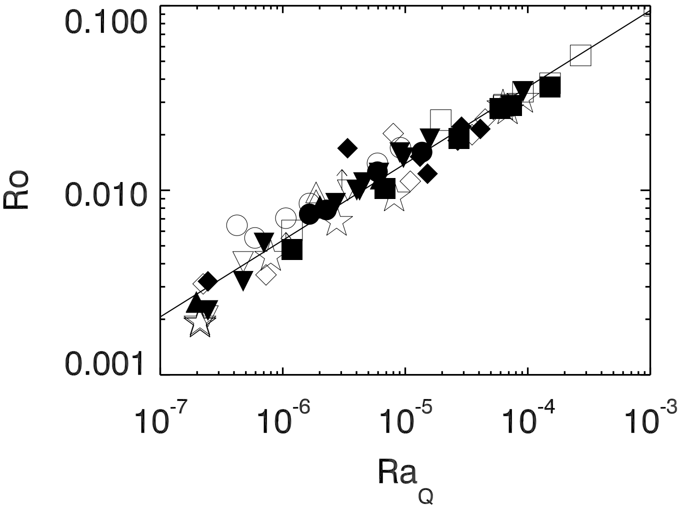

Figure 3.25 – Ro as a function of Ra_Q.

2012, Yadav *et al.* 2013a) and very similar to the magnetic field scaling given by Yadav *et al.* (2013b). We note however, that unlike Yadav *et al.* (2013b), we scale the Lorentz number with the flux based Rayleigh number Ra_Q and not directly with the power released by buoyancy forces. Of course, both should be closely related to each other. The same remark applies for the velocity scaling discussed below.

Models on the multipolar branch exhibit lower field strengths compared to their dipolar counterparts. This is not only apparent by the smaller prefactor in the multipolar scaling, but also the dynamo efficiency f_{ohm} for multipolar models is systematically lower than for the corresponding dipolar ones. The latter indicates that the bistable behaviour for models at $Ro_\ell \leq 0.12$ is caused by different dynamo mechanisms. This was already seen in Boussinesq simulations (Schrinner *et al.* 2012) and later confirmed by Gastine *et al.* (2012) for anelastic models.

Apart from a few exceptions, the shift between the two scalings in Fig. 3.24 may serve to separate dipolar from multipolar dynamos. In agreement with Yadav *et al.* (2013b), we obtained several models with dipole field strengths up to $f_{\mathrm{dip}} \approx 0.5$ which nevertheless clearly follow the multipolar scaling and belong to the multipolar class of dynamos.

3.4.2 Velocity scaling

There is an ongoing discussion about the velocity scaling in dynamo models (Christensen 2010, Davidson 2013, Yadav *et al.* 2013b). It is probably not surprising that the velocity measured in terms of the Rossby number scales with the flux based Rayleigh number, but the correct exponent and its theoretical justification is debated. The lower bound is set by the assumption of a balance between inertia

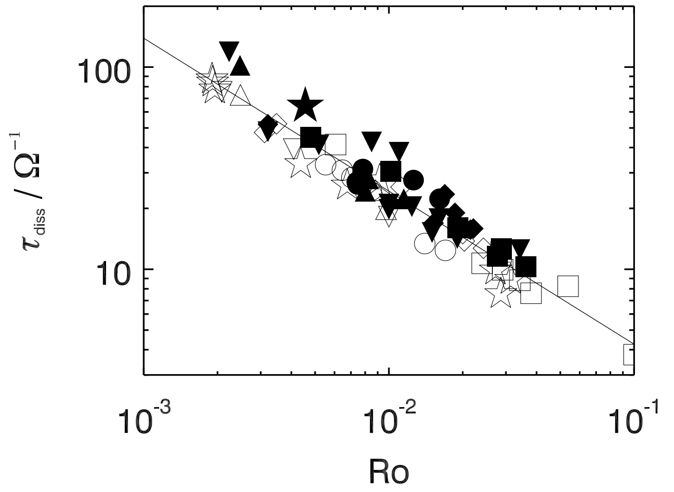

Figure 3.26 – Ohmic dissipation time versus Rossby number.

and buoyancy forces (mixing length balance), which leads to an exponent of 1/3 (Christensen 2010). If however, the predominant force balance is assumed to be between the Lorentz force, the buoyancy and the Coriolis force (MAC-balance) the exponent is closer to 1/2 (Christensen 2010, Davidson 2013). As most previous studies (Christensen & Aubert 2006, Christensen 2010, Yadav *et al.* 2013a, Stelzer & Jackson 2013, Yadav *et al.* 2013b) we obtained for our sample of models an exponent in between these two values,

$$Ro = 1.66\, Ra_Q^{0.42}. \tag{3.14}$$

The scatter in Fig. 3.25 is considerable, but the standard error is of the same order as for Boussinesq models with stress-free mechanical boundary conditions (Yadav *et al.* 2013a). Compressible effects do not seem to deteriorate the scaling.

However, as in Yadav *et al.* (2013b), we are not able to distinguish between dipolar and multipolar models in our velocity scaling contrary to what has been previously reported by Yadav *et al.* (2013a) for Boussinesq models.

3.4.3 Scaling of Ohmic dissipation time

The scaling of magnetic dissipation time,

$$\tau_{\rm diss} = E_M/D = \ell_B^2/\eta, \tag{3.15}$$

is used to evaluate the characteristic length scale ℓ_B of the magnetic field. Christensen & Tilgner (2004) originally identified a linear dependence of $\tau_{\rm diss}$ on the inverse Rossby number provided that time is measured in units of Ω^{-1}. Their

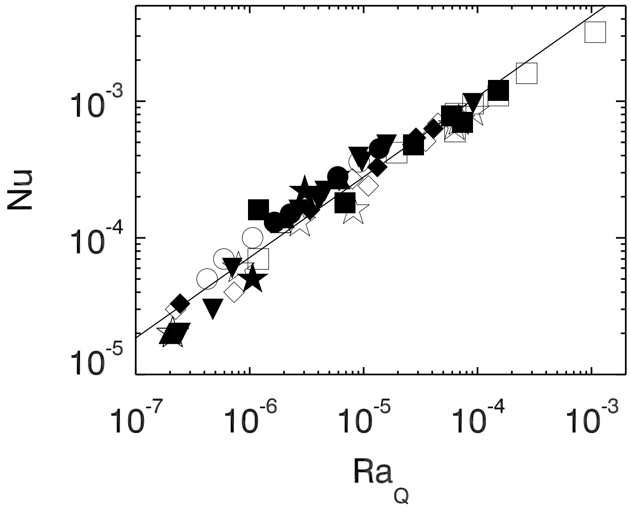

Figure 3.27 – $Nu^\star$ as a function of Ra_Q.

finding was supported by dipole-dominated Boussinesq models with no-slip mechanical boundary conditions and the evaluation of the Ohmic dissipation time in the Karlsruhe dynamo experiment. The best fit for our data points in Fig. 3.26, however, gives an exponent with a significantly lower absolute value,

$$\tau_{\text{diss}} = 0.75\, Ro^{-0.76}. \tag{3.16}$$

An almost identical result was found by Yadav *et al.* (2013b) from their somewhat more diverse and scattered data set. Apparently, the application of stress-free boundary conditions and maybe also compressible effects flatten the slope of τ_{diss} as a function of the Rossby number. Moreover, it would seem plausible that τ_{diss} followed different scaling relations for dipolar and multipolar models. Indeed, for bistable pairs, the dissipation time is systematically larger for dipolar than for multipolar models. However, separate least square fits for all dipolar and all multipolar models of our sample lead to very similar results.

3.4.4 Nusselt number scaling

The convective heat transport in dynamo models is very sensitive to rotation and depends to a much lower degree on the magnetic field, boundary conditions or the geometry of the fluid domain (Christensen 2002, Christensen & Aubert 2006, Aurnou 2007, Schmitz & Tilgner 2009, Busse & Simitev 2011, Gastine & Wicht 2012, Yadav *et al.* 2013a, Stelzer & Jackson 2013). The power law for the Nusselt number inferred from Fig. 3.27,

$$Nu^\star = 0.25\, Ra_Q^{0.59}, \tag{3.17}$$

is consistent with previous results and confirms this finding also for anelastic dynamo models; the exponent of 0.59 is very close to the value of 5/9 established by the above mentioned references. However, the scaling is somewhat more scattered than for Boussinesq models (Yadav *et al.* 2013a). We excluded in a test all models for which convection is only marginaly above the onset ($Nu^{\star} < 2$), but this reselection of models did not improve the quality of the fit.

3.4.5 Discussion

In an overall view, the scaling relations for Boussinesq and anelastic models are very similar (see Table 3.1). Beyond that, there is no obvious effect of compressibility on the scaling results and they might be even considered as consistent irrespective of the density stratification of the underlying models (Yadav *et al.* 2013b). However, the reason for the good agreement could be that the flux-based scaling laws are insensitive to different physical conditions. Using the example of the magnetic field scaling, we argue in the following that differences in the dynamo processes might not be visible in the scaling relation and some caution is needed in generalizing results from Boussinesq simulations.

Table 3.1 – Scaling laws for anelastic and Boussinesq models. Results for Boussinesq models were taken from Yadav *et al.* (2013a) (see also Schrinner *et al.* 2012). Yadav *et al.* (2013a) distinguished between dipolar and multipolar dynamos for their Rossby number scaling, whereas we derived a single power law for both classes of dynamo models.

Scaling	Anelastic			Boussinesq		
	c	x	σ	c	x	σ
$Lo/f_{\mathrm{ohm}}^{1/2} = c\,Ra_Q^x$	$1.58^{\dagger}$	$0.35^{\dagger}$	$0.017^{\dagger}$	$1.08^{\dagger}$	$0.37^{\dagger}$	$0.017^{\dagger}$
	$1.19^{\ddagger}$	$0.34^{\ddagger}$	$0.067^{\ddagger}$	$0.65^{\ddagger}$	$0.35^{\ddagger}$	$0.006^{\ddagger}$
$Ro = c\,Ra_Q^x$	1.66	0.42	0.025	$0.73^{\dagger}$	$0.39^{\dagger}$	$0.013^{\dagger}$
				$1.79^{\ddagger}$	$0.44^{\ddagger}$	$0.010^{\ddagger}$
$\tau_{\mathrm{diss}} = c\,Ro^{-x}$	0.75	0.76	0.024	–	0.8	–
$Nu^{\star} = c\,Ra_Q^x$	0.25	0.59	0.032	0.06	0.52	0.004

Notes. †Dipolar models. ‡Multipolar models.

If the magnetic energy density follows a simple power law in terms of the convective energy flux an exponent of 2/3 is already required for dimensional reasons (e.g. Christensen 2010). Moreover, the flux-based scaling law for the magnetic field is composed of the scalings for the velocity and the magnetic dissipation time. By definition, we have $E_M \sim f_{\text{ohm}} \tau_{\text{diss}} P$ and with $Ro \sim P^{\alpha}$ and $\tau_{\text{diss}} \sim Ro^{\beta}$, we find $E_M \sim f_{\text{ohm}} P P^{\alpha\beta}$. Dimensional arguments require $\alpha\beta = -1/3$ which establishes relations (3.13a) and (3.13b). Whereas the exponent in the flux-based scaling law for the magnetic field is fix, α and β are to some extend variable and may change according to the specific physical conditions. This reflects the outcome of more and more extended parameter studies: The exponent of 1/3 in the magnetic-field scaling is reliably reproduced but the values for α and β seem to be less certain and are under debate.

In addition, scaling relations (3.13a) and (3.13b) require that the field strength, measured by Lo, is compensated by the square root of f_{ohm} (interpreted as dynamo efficiency in Schrinner 2013). However, the parameter f_{ohm} probably is a complicated function of several control parameters and might depend strongly on the specific physical conditions. The often made assumption that $f_{\text{ohm}} \to 1$ for $\text{Pm} \ll 1$ (e.g. Davidson 2013) is probably too simple. For example, Schrinner (2013) demonstrated recently that f_{ohm} in dynamo models might depend strongly on the rotation rate. The dynamo efficiency dropped by two orders of magnitude as the rotation rate of these models was decreased. A further counterexample could be the solar dynamo. An independent estimate from dynamic flux-transport solar dynamo models result in $f_{\text{ohm}} \sim O(10^{-3})$ (Rempel 2006) although the magnetic Prandtl number is thought to be much smaller than one in the solar interior. In other words, the flux based scaling laws probably do not discriminate between different types of dynamos because differences in the field strength are absorbed by changes in f_{ohm}.

§

Chapitre 4

Intermittence

> *L'« inflation expérimentale » n'est pas moins pernicieuse que l'inflation économique : on a des instruments, on les utilise massivement et on en tire une masse infinie de données desquelles, à la fin, on ne sait rien tirer. Les données emplissent des bibliothèques entières, dorment ensuite dans des archives poussiéreuses et personne ne s'en occupe plus.*
>
> Thom (1983)

LES OBSERVATIONS ont révélé que la dynamique des dynamos naturelles peut être sujette à de fortes fluctuations, comme en témoignent les modulations du cycle solaire au cours des derniers millénaires. La notion d'intermittence renvoie généralement à l'apparition aléatoire de bouffées chaotiques qui viennent interrompre des phases laminaires présentant une activité réduite. Sous certaines conditions, des fluctuations stochastiques peuvent être à l'origine de l'apparition de l'intermittence dite *on-off*, observée entre autres dans des modèles de champ moyen et parfois suggérée comme modèle de la variabilité à long terme de l'activité magnétique solaire (Schmitt *et al.* 1996). Nous étudions l'apparition de l'intermittence *on-off* dans un modèle simple de dynamos de Couette sphérique engendrées par l'écoulement entre deux sphères concentriques en contrarotation.

Dans un second temps, nous montrerons comment les interactions non linéaires entre modes de différentes parités peuvent conduire à différents types de modulations temporelles de l'activité magnétique, par l'étude de modèles d'intérieur stellaire analogues à ceux du chapitre précédent. Cette analyse présente, en outre, l'avantage de rendre compte de la localisation hémisphérique du champ magnétique.

4.1 *On-off* : notion de bruit multiplicatif

La plupart des phénomènes naturels ont nécessairement lieu dans un environnement en présence de bruit, que l'on qualifie de multiplicatif lorsque l'effet des fluctuations dépend de l'état du système. Dans l'instabilité dynamo, par exemple, l'effet des fluctuations turbulentes de l'écoulement est proportionnel à l'amplitude du champ magnétique. Une telle situation se retrouve aussi dans d'autres contextes, comme dans certaines réactions chimiques impliquant plusieurs espèces.

Proche du seuil d'instabilité, un système soumis à un bruit multiplicatif peut présenter un type particulier d'intermittence qui se manifeste sous la forme de bouffées. On distingue alors des périodes d'intense activité où l'amplitude du mode instable croît exponentiellement, et des phases de repos. Les séries temporelles présentent donc une alternance entre des phases d'amplitude très faible (phases *off*) et des phases de forte amplitude (phases *on*), d'où le nom d'intermittence *on-off* donné à ce phénomène par une équipe qui étudiait la dynamique de deux systèmes chaotiques couplés (Platt *et al.* 1993).

4.1.1 Un modèle simple

L'exemple canonique (Aumaître *et al.* 2005) qui reproduit un tel comportement part de la forme normale d'une bifurcation fourche supercritique et est donné par

$$\dot{X} = [a + \zeta(t)]\,X - X^3\,, \tag{4.1}$$

où a représente l'écart au seuil et où ζ est en général un bruit blanc gaussien, de moyenne nulle et de corrélation $\langle\zeta(t)\zeta(t')\rangle = 2D\delta(t-t')$ [1]. Le taux de croissance instantané $a+\zeta(t)$ étant aléatoire, il peut prendre des valeurs négatives et faire décroître l'amplitude du mode instable avant qu'elle ne croisse à nouveau.

Lorsque le terme X est très petit, on peut négliger le terme non linéaire et écrire

$$\dot{Y} = a + \zeta(t)\,, \quad \text{avec} \quad Y = \ln(X)\,, \tag{4.2}$$

soit

$$\ln(X(t)) = \ln(X(0)) + at + \int_0^t \zeta(t')\,\mathrm{d}t'\,. \tag{4.3}$$

La variable $\ln(X)$ suit donc une marche aléatoire durant les phases *off*, avec un biais a. En moyenne, $\langle\ln(X)\rangle$ tend vers $-\infty$ si a est négatif et croît si a est positif, jusqu'à ce que les non linéarités entrent en jeu et assurent la saturation. Le cas $a=0$ correspond donc au seuil d'instabilité de la solution nulle en présence de bruit. Ces caractéristiques sont illustrés figure 4.1.

---

[1] Les crochets $\langle\ \rangle$ désignent la moyenne sur des réalisations du bruit.

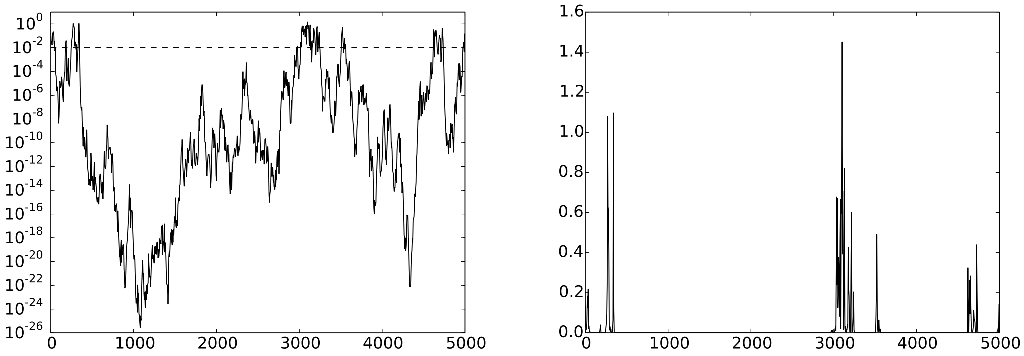

Figure 4.1 – Série temporelle de $X(t)$ solution de l'équation (4.1). On identifie à gauche que $\ln(X)$ décrit une marche aléatoire avec un faible biais vers les valeurs positives et une saturation par les effets non linéaires pour des valeurs proches de l'unité. Les parties de la courbe situées au-dessous d'un seuil X_0 matérialisé par une ligne pointillée horizontale dans la figure en semilog apparaissent à droite comme quasiment nulles en représentation linéaire.

4.1.2 Propriétés caractéristiques

Densité de probabilité

Le calcul de la densité de probabilité (PDF) se fonde sur l'équation de Fokker-Planck associée à l'équation de Langevin (4.1), interprétée au sens de Stratonovitch. La difficulté provient du sens à donner à l'intégrale $\int c(x(t'))\zeta(t')\,\mathrm{d}t'$ lorsque l'on considère l'équation de Langevin

$$\dot{x} = A(x) + c(x)\zeta(t)\,. \tag{4.4}$$

Stratonovitch (1963) a établi l'équivalence avec l'équation de Fokker-Planck pour la PDF $P(x,t)$

$$\frac{\partial P(x,t)}{\partial t} = -\frac{\partial}{\partial x}\left[A(x) + \frac{1}{2}c(x)c'(x)\right]P(x,t) + \frac{1}{2}\frac{\partial^2}{\partial x^2}\left[c^2(x)P(x,t)\right]. \tag{4.5}$$

L'interprétation de Stratonovitch revient à remplacer le cœfficient $c(x)$ par sa moyenne sur un domaine d'intégration infinitésimal

$$x(t+dt) - x(t) = \int_t^{t+dt} A(x(t'))\,\mathrm{d}t' + c\left(\frac{x(t) + x(t+dt)}{2}\right)\int_t^{t+dt} \zeta(t')\,\mathrm{d}t'. \tag{4.6}$$

Elle est souvent utilisée en physique car elle permet de continuer à manipuler les équations avec les règles de calcul usuelles[2].

---

[2] Ce n'est plus le cas avec l'interprétation d'Itô.

Dans notre cas, on peut calculer la solution stationnaire de l'équation de Fokker-Planck qui, pour a positif, s'avère être de la forme (Schenzle & Brand 1979)

$$P(X) \propto X^{(2a/D)-1} e^{-X^2/D}. \tag{4.7}$$

Si $2a > D$, les valeurs les plus probables sont $X_\mathrm{p} = \pm\sqrt{a - D/2}$. Loin du seuil, le caractère intermittent disparaît et X fluctue autour de sa valeur déterministe $\sqrt{a}$. En revanche, pour $2a \leq D$, la PDF diverge quand $X \to 0$, ce qui témoigne de la prépondérance de longues phases *off* où la variable X prend des valeurs proches de zéro. Au seuil, $2a/D \ll 1$, on retiendra le comportement caractéristique de la PDF en loi puissance. La coupure exponentielle pour les grandes valeurs de X vient des non linéarités.

Distribution des phases *off*

Sur la figure 4.1, on constate qu'on peut définir une phase *off* comme une période durant laquelle $X < X_0$, où X_0 est une valeur seuil arbitraire raisonnablement choisie. À partir de l'analogie avec la marche aléatoire (justement établie pour les phases *off*), on en déduit que la durée T_off d'une phase *off* peut être vue comme un temps de retour d'un mouvement brownien biaisé. Ding & Yang (1995) creusent l'analogie entre marche aléatoire et intermittence *on-off*. On montre ainsi que la distribution des durées des phases *off* suit une loi puissance $P(T_\mathrm{off}) \sim T_\mathrm{off}^{-3/2}$ (Heagy *et al.* 1994). Cette caractéristique présente en outre une certaine universalité puisqu'elle reste valable pour d'autres types de bruit.

Linéarité des moments

Dans la limite où l'écart au seuil tend vers zéro, les statistiques des moments présentent une dépendance particulière en fonction de l'écart au seuil, $\langle X^n \rangle \propto a$. Ce résultat se déduit de l'expression de la PDF $P(X) \sim X^{(2a/D)-1}$ en introduisant une coupure X_m pour les grandes valeurs de X. Physiquement, on peut considérer que les phases *off* ne contribuent pas aux moments et que seules les phases *on* vont être significatives. Soit C_n la valeur de moyenne de X^n durant une phase *on*, une estimation de $\langle X^n \rangle$ est alors donnée par

$$\langle X^n \rangle = \frac{\langle T_\mathrm{on} \rangle C_n}{\langle T_\mathrm{on} \rangle + \langle T_\mathrm{off} \rangle}. \tag{4.8}$$

Lorsque l'écart au seuil tend vers zéro, la durée des phases *off* diverge en $1/a$, ce qui redonne la linéarité des moments. Proche du seuil, le système entre donc dans les phases *on* avec une fréquence proportionnelle à a, mais la durée et les valeurs atteintes pendant les bursts sont indépendantes de l'écart au seuil.

4.1.3 Influence du spectre du bruit

Contrairement à ce que l'on pourrait penser, des simulations réalisées avec différents types de bruit (par exemple, bruit coloré, ou bien variable chaotique solution d'un système d'équations déterministe) ont montré que l'intermittence *on-off* n'est pas contrôlée par l'amplitude du bruit, mais par sa composante à fréquence nulle (Aumaître *et al.* 2006, Pétrélis 2011). L'équation (4.2) montre que l'intermittence *on-off* résulte de la compétition entre l'écart au seuil et le terme de bruit. Pour $0 < a \ll 1$, les phases de décroissance sont permises si l'inégalité

$$aT + \int_0^T \zeta(t)\,\mathrm{d}t \leq 0 \tag{4.9}$$

est vérifiée sur d'assez longues périodes T. L'intégrale $\int_0^T \zeta(t)\,\mathrm{d}t/T$ est alors dominée par la composante du bruit à fréquence nulle. Ce résultat est en lien avec le théorème de Wiener-Khintchine qui établit un lien entre l'intégrale de la fonction d'autocorrélation du bruit et sa densité spectrale. Lorsque la valeur du bruit à fréquence nulle est trop petite devant l'écart au seuil, l'inégalité (4.9) est de moins en moins probable et l'intermittence *on-off* disparaît.

4.1.4 Bilan

Les propriétés caractéristiques de l'intermittence *on-off* sont donc surtout contrôlées par les phases où la variable est de petite amplitude, lesquelles présentent une analogie intéressante avec une marche aléatoire légèrement biaisée. L'intermittence *on-off* permet ainsi d'étudier les taux de croissance et de décroissance près du seuil d'une instabilité en présence de bruit. Malgré sa simplicité, le modèle que nous avons présenté est susceptible de fournir des informations sur l'écart au seuil. En effet, la distribution en loi puissance de la PDF ou encore le scaling linéaire des moments (grandeurs qu'il est possible de déterminer à partir de signaux temporels) permettent, en théorie, de tirer une estimation directe de la distance par rapport au seuil. Il s'agit bien souvent d'une information cruciale, comme, par exemple, dans les expériences de dynamos (Sweet *et al.* 2001).

4.2 Spherical Couette dynamos

4.2.1 Context and motivations

Dynamo action, i.e. the self-amplification of a magnetic field by the flow of an electrically conducting fluid, is considered to be the main mechanism for the generation of magnetic fields in the universe for a variety of systems, including planets, stars, and galaxies (Dormy & Soward 2007). Dynamo action is an instability by which a conducting fluid transfers part of its kinetic energy to magnetic energy.

In experiments, it is rather difficult to achieve a regime of self-excited dynamo action. The low value of the magnetic Prandtl number of liquid metals requires the injection of a sufficiently high mechanical power, and thus generates turbulent flows, before reaching the dynamo threshold. Dynamo action was first observed experimentally only in 2001, in Karlsruhe (Stieglitz & Müller 2001) and Riga (Gailitis *et al.* 2001), and then in 2007 with a von Kármán swirling flow of liquid sodium (Monchaux *et al.* 2007).

In parallel with these approaches, numerical simulations have been carried out to model either laboratory experiments or astrophysical systems, for which the spherical geometry is relevant. We investigate spherical Couette flow and focus on the characteristics of the magnetic field close to the dynamo onset. We observe a series of short bursts of the magnetic energy separated by low-energy phases. This intermittent behavior, also known as on-off intermittency or blowout bifurcation, is usually interpreted as the effect of a multiplicative noise acting on a bifurcating system (Fujisaka & Yamada 1986, Platt *et al.* 1993).

On-off intermittency has so far never been observed in dynamo experiments, except in the case of an externally amplified magnetic field (Verhille *et al.* 2010). In contrast, it has been reported in a small number of numerical simulations (Sweet *et al.* 2001, Leprovost *et al.* 2006, Alexakis & Ponty 2008), all relying on a flow in a periodic geometry produced by a periodic analytic forcing. Here we investigate the influence of a realistic choice of boundary conditions on this phenomenon.

4.2.2 Governing equations

The spherical Couette flow geometry consists of two concentric spheres in differential rotation: the outer sphere, of radius r_o, is rotating around the vertical axis $\mathbf{e}_z$ with an angular velocity Ω, and the solid inner sphere, of radius r_i, is rotating at velocity $\Omega + \Delta\Omega$ around an axis that can make an angle θ with $\mathbf{e}_z$. The aspect ratio $\chi = r_\mathrm{i}/r_\mathrm{o}$ is set to 0.35 to mimic that of Earth's liquid core. The spherical shell in between the two spheres is filled with an incompressible conducting fluid of kinematic viscosity ν, electrical conductivity σ, and density ρ. Its magnetic permeability μ_0 is that of vacuum. The magnetic diffusivity η is defined as $\eta = 1/(\mu_0\sigma)$.

We describe the problem in the reference frame rotating with the outer sphere. This introduces two extra terms in the governing equations: the Coriolis force and the centrifugal acceleration. The latter can be rewritten in the form $\frac{1}{2}\nabla\left(\Omega^2 s^2\right)$, where s denotes the distance to the axis of rotation. This term is a gradient and can be added to the pressure term which acts as a Lagrange multiplier to enforce the solenoidal condition on the velocity field. To establish the set of equations for this system, we rely on the same non-dimensional form as Guervilly & Cardin (2010): the velocity $\mathbf{u}$ is scaled by $r_\mathrm{i}\Delta\Omega$, the magnetic field $\mathbf{B}$ by $\sqrt{\rho\mu_0 r_\mathrm{i} r_\mathrm{o}\left(\Omega+\Delta\Omega\right)\Delta\Omega}$, and the length scale by r_o. The Navier-Stokes equation governing the fluid velocity $\mathbf{u}$ then takes the form

$$\frac{\partial \mathbf{u}}{\partial t}+(\mathbf{u}\cdot\nabla)\,\mathbf{u}+\frac{2}{\mathrm{ERe}}\left(\mathbf{e}_z\times\mathbf{u}\right)=-\frac{1}{\mathrm{Re}}\nabla\Pi+\frac{1}{\mathrm{Re}}\nabla^2\mathbf{u}+\frac{1}{\mathrm{Re}}\left(\frac{1}{\mathrm{E}}+\frac{\mathrm{Re}}{\chi}\right)(\nabla\times\mathbf{B})\times\mathbf{B}, \quad (4.10)$$

and the induction equation for the magnetic field $\mathbf{B}$,

$$\frac{\partial \mathbf{B}}{\partial t}=\nabla\times(\mathbf{u}\times\mathbf{B})+\frac{1}{\mathrm{Rm}}\nabla^2\mathbf{B}. \quad (4.11)$$

Both fields are solenoidal

$$\nabla\cdot\mathbf{u}=0, \qquad \nabla\cdot\mathbf{B}=0. \quad (4.12)$$

The dimensionless parameters are the Ekman number $\mathrm{E}=\nu/\left(\Omega r_\mathrm{o}^2\right)$, the Reynolds number $\mathrm{Re}=\left(r_\mathrm{o} r_\mathrm{i}\Delta\Omega\right)/\nu$, the magnetic Prandtl number $\mathrm{Pm}=\nu/\eta$, and the magnetic Reynolds number $\mathrm{Rm}=\mathrm{RePm}$. The potential Π includes all gradient terms (the pressure term as well as the centrifugal effect introduced above). The Reynolds number varies with the rotation rate of the inner sphere, while the Ekman number is inversely proportional to the rotation rate of the outer sphere. When the latter is at rest, the Ekman number tends toward infinity and the Coriolis term in the Navier-Stokes equation vanishes. In our simulations, the Ekman number is set to 10^{-3}. This moderate value yields a moderate computing time.

We impose no slip boundary conditions for the velocity field on both spheres. Magnetic boundary conditions are of three types. The first one can only be applied to the inner sphere, as it implies a meshing of the bounding solid domain. The inner sphere can be a conductor with the same electric and magnetic properties as the fluid. In that case the magnetic diffusion equation is discretized and solved in the solid conductor (we refer to this set of boundary conditions as “conducting”). The outer sphere as well as the inner sphere can be electrical insulators. In that case the magnetic field is continuous across the boundary and matches a potential field, decaying away from the boundary. The spherical harmonic expansion allows an explicit and local expression for these boundary conditions (we refer to these boundary conditions as “insulating”). In addition, the use of high-magnetic-permeability boundary conditions may enhance dynamo action (Gissinger *et al.* 2008). Therefore, we also used boundary conditions which enforce the magnetic field to be normal to the boundary. This is equivalent to assuming that the medium on the other side of the boundary has an infinitely larger permeability[3] (we refer to these boundary conditions as “ferromagnetic”). The different configurations investigated in this study are summarized in Table 4.1.

---

[3] Jump conditions at a boundary between media of different magnetic permeabilities are given

Table 4.1 – The three different configurations of magnetic boundary conditions used in this study.

	Inner Sphere	Outer Sphere
B.C.1	Conducting	Insulating
B.C.2	Insulating	Insulating
B.C.3	Ferromagnetic	Ferromagnetic

We integrated our system with PARODY, a parallel code which has been benchmarked against other international codes. The vector fields are transformed into scalars using the poloidal-toroidal decomposition. This expansion on a solenoidal basis enforces the constraints (4.12). The equations are then discretized in the radial direction with a finite-difference scheme on a stretched grid. On each concentric sphere, variables are expanded using a spherical harmonic basis (i.e., generalized Legendre polynomials in latitude and a Fourier basis in longitude). The coefficients of the expansion are identified with their degree l and order m. The simulations were performed using from 150 to 216 points in the radial direction, and the spherical harmonic decomposition is truncated at $(l_{\max}, m_{\max}) = (70, 20)$. We observe for both spectra a decrease of more than two orders of magnitude over

---

by

$$\mathbf{B}\cdot\mathbf{n}|_1 = \mathbf{B}\cdot\mathbf{n}|_2\,, \tag{4.13a}$$

$$\mathbf{B}\times\mathbf{n}|_1 = \frac{\mu_1}{\mu_2}\mathbf{B}\times\mathbf{n}|_2\,, \tag{4.13b}$$

where subscripts 1 and 2 denote the two different regions and **n** is normal to the boundary. Expressed in terms of poloidal and toroidal components (cf. decomposition (2.61)) for a spherical boundary at radius r_0, they become

$$B_{\mathrm{P}}^1(r_0) = B_{\mathrm{P}}^2(r_0)\,, \tag{4.14a}$$

$$B_{\mathrm{T}}^1(r_0) = \frac{\mu_1}{\mu_2}B_{\mathrm{T}}^2(r_0)\,, \tag{4.14b}$$

$$\frac{1}{r_0}\frac{\partial\left(rB_{\mathrm{P}}^1\right)}{\partial r}\bigg|_{r_0} = \frac{\mu_1}{\mu_2}\frac{1}{r_0}\frac{\partial\left(rB_{\mathrm{P}}^2\right)}{\partial r}\bigg|_{r_0}\,. \tag{4.14c}$$

In an experiment, a ferromagnetic sphere will have a magnetic permeability much larger than the fluid permeability (set to μ_0), and one can therefore take the limit for a medium with infinite permeability, which leads to

$$B_{\mathrm{T}}(r_0) = 0\,, \tag{4.15a}$$

$$\frac{\partial B_{\mathrm{P}}}{\partial r}\bigg|_{r_0} + \frac{1}{r_0}B_{\mathrm{P}}(r_0) = 0\,. \tag{4.15b}$$

the range of l and m. This provides an empirical validation of convergence. We checked on a few critical cases that the results are not affected when the resolution is increased to $l_{\max} = 100$.

Let us define the non-dimensional kinetic and magnetic energy densities as

$$E_k = \frac{1}{V_s} \int_{V_s} \mathbf{u}^2 \, \mathrm{d}\mathbf{x}, \tag{4.16}$$

$$E_b = \frac{1}{V_s} \frac{1}{\mathrm{Re}} \left(\frac{1}{\mathrm{E}} + \frac{\mathrm{Re}}{\chi} \right) \int_{V_s} \mathbf{B}^2 \, \mathrm{d}\mathbf{x}, \tag{4.17}$$

in which the unit of energy density is $\rho \, (r_i \, \Delta\Omega)^2$. In the above expressions, V_s refers to the volume of the spherical shell. In addition, we also investigate the symmetry of the flow and the symmetry of the magnetic field with respect to the equatorial plane. To that end, we define the contributions to the energy densities corresponding to the symmetric and antisymmetric components of the velocity (respectively E_k^S and E_k^A) and magnetic field (respectively E_D and E_Q). The symmetric and antisymmetric contributions to the kinetic energy density respectively correspond to the flows

$$\mathbf{u}_S(x, y, z) = \tfrac{1}{2} \left[\mathbf{u}(x, y, z) + \mathbf{u}(x, y, -z) \right], \tag{4.18}$$

$$\mathbf{u}_A(x, y, z) = \tfrac{1}{2} \left[\mathbf{u}(x, y, z) - \mathbf{u}(x, y, -z) \right]. \tag{4.19}$$

In contrast, the symmetries are reversed for the magnetic field. This comes from the fact that the magnetic field is a pseudovector (i.e, the curl of a vector). Then,

$$\mathbf{B}_S(x, y, z) = \tfrac{1}{2} \left[\mathbf{B}(x, y, z) - \mathbf{B}(x, y, -z) \right], \tag{4.20}$$

$$\mathbf{B}_A(x, y, z) = \tfrac{1}{2} \left[\mathbf{B}(x, y, z) + \mathbf{B}(x, y, -z) \right]. \tag{4.21}$$

According to our definition, the dipolar component is symmetric.

4.2.3 Direct numerical simulations

As shown by Guervilly & Cardin (2010), contra-rotation is more efficient than co-rotation for dynamo action. In order to introduce more control over the system, we let the angle θ between the axes of rotation of both spheres take any value in $[0, \pi]$. Contrary to our expectations, we do not significantly lower the dynamo threshold with the inclination of the rotation axis of the inner sphere. In fact, for $\theta = \pi/2$, the fluid is mainly in co-rotation with the outer sphere, and dragged only by a thin layer on the inner sphere, which is not sufficient to trigger dynamo action. In our parameter regime, the best configuration seems to remain $\theta = \pi$, when the two spheres are in contra-rotation. We therefore keep this parameter fixed in the rest of the study.

Role of boundary conditions

Let us first investigate the dynamo transition in this setup at fixed magnetic Prandtl number Pm = 0.2, using the Reynolds number as the controlling parameter. With a conducting inner sphere and an insulating outer sphere, we find a critical magnetic Reynolds number $\mathrm{Rm_c} \in [291.0; 292.0]$, which is in good agreement with Guervilly & Cardin (2010). Above the dynamo onset, the magnetic field displays an intermittent behavior characterized by series of short bursts of the magnetic energy separated by low energy phases (see Fig. 4.2). When the distance to the threshold increases, bursts become more and more frequent and eventually intermittency disappears.

Changing the boundary conditions generally leads to different thresholds for dynamo action. Using ferromagnetic boundary conditions, we find a critical magnetic Reynolds number $\mathrm{Rm_c} \in [298.6; 300.0]$. With insulating boundary conditions, the threshold becomes large and involves larger numerical resolutions. In order to maintain the hydrodynamic Reynolds number at values which involve a moderate resolution, we therefore had to increase the magnetic Prandtl number from 0.2 to 0.4. We then obtain the dynamo onset for $\mathrm{Rm_c} \in [530.0; 534.8]$. We emphasize that we observe the same intermittent regime with all the above choices of boundary conditions as long as the magnetic Reynolds number is close enough to the onset of the instability.

For all boundary conditions, we observe that the dominant mode is predominantly of quadrupolar symmetry [the larger poloidal and toroidal modes are the $(l = 2, m = 0)$ and $(l = 1, m = 0)$ modes, respectively]. For these Reynolds numbers, the flow is predominantly equatorially symmetric ($E_k^A \ll E_k^S$).

Increasing the magnetic Prandtl number

Having assessed that the intermittent behavior of the magnetic field near onset could be observed with three different sets of boundary conditions, we restrict here our attention to simulations with ferromagnetic boundary conditions. Figure 4.3 presents the results we obtain at Pm = 2. Close to the threshold, the magnetic field still exhibits intermittency, but the nature of the process has significantly changed. There is now a clear distinction between two different regimes: phases of dynamo activity separated by phases of pure exponential decay. Both seem to alternate randomly. When the dynamo is active, the magnetic field still displays a quadrupolar symmetry. In contrast, we observe the emergence of an axial dipole during decaying phases. The change of the global symmetry of the field coincides with the change of slope in the decaying phases [see Fig. 4.3(b) and Fig. 4.4]. This change of slope is associated with a slower decay of the dipolar component over the quadrupolar mode.

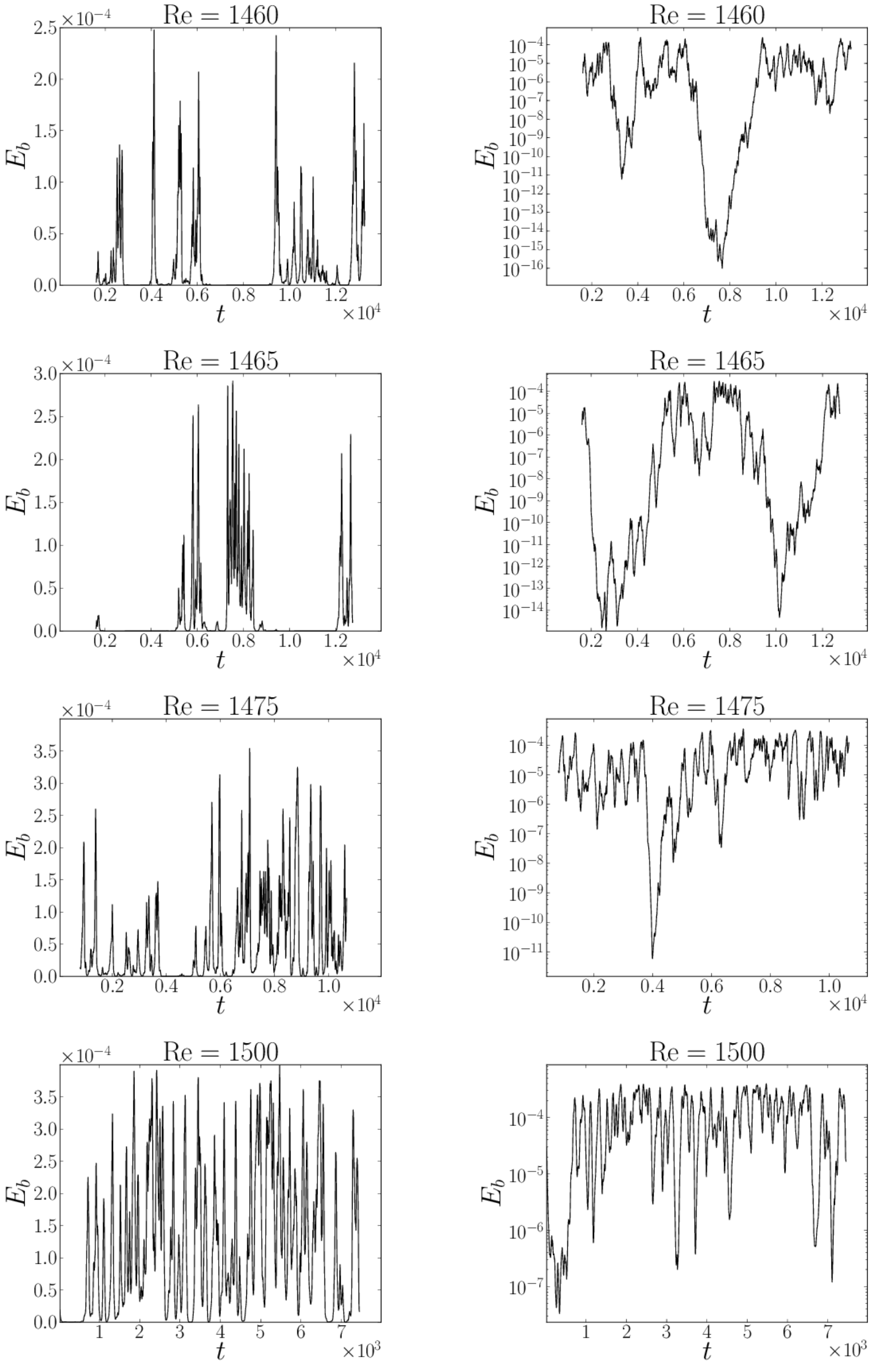

Figure 4.2 – Time evolution of the magnetic energy in linear (left) and log scale (right) for increasing Reynolds numbers at Pm = 0.2, using a conducting inner sphere (B.C.1 in Table 4.1). At lower Reynolds numbers (top), we see in linear scale the characteristic intermittent bursting. Intermittency gradually disappears at higher Reynolds numbers and the field reaches saturation.

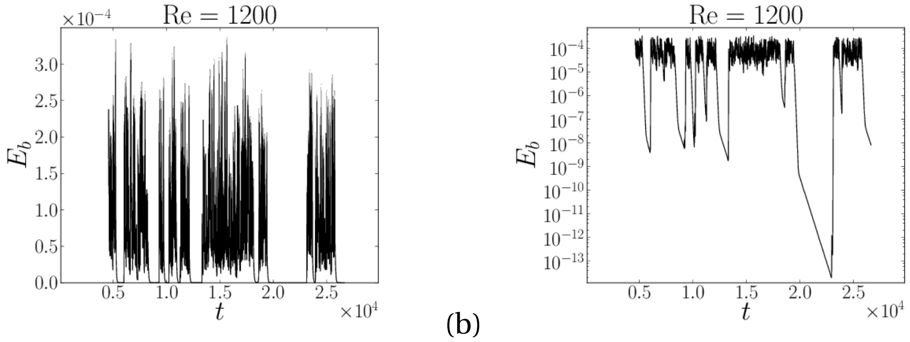

(a) (b)

Figure 4.3 – Time evolution of the magnetic energy in linear (a) and log (b) scales for Pm = 2 and Re = 1200, using ferromagnetic boundary conditions. Instead of bursts, we now observe phases of dynamo activity which seem to randomly alternate with phases of exponential decay. The latter are no longer chaotic and are instead characterized by two different decay rates.

Figure 4.4 – Time series of the symmetric (dashed line) and antisymmetric (solid line) part of the magnetic energy. We focus on one of the decaying phases presented in Fig. 4.3. The decaying phase is characterized by a change of the dominant symmetry, as we can see on the visualizations of the magnetic field lines. The color insets respectively correspond to snapshots in the quadrupolar phase (left) and dipolar phase (right).

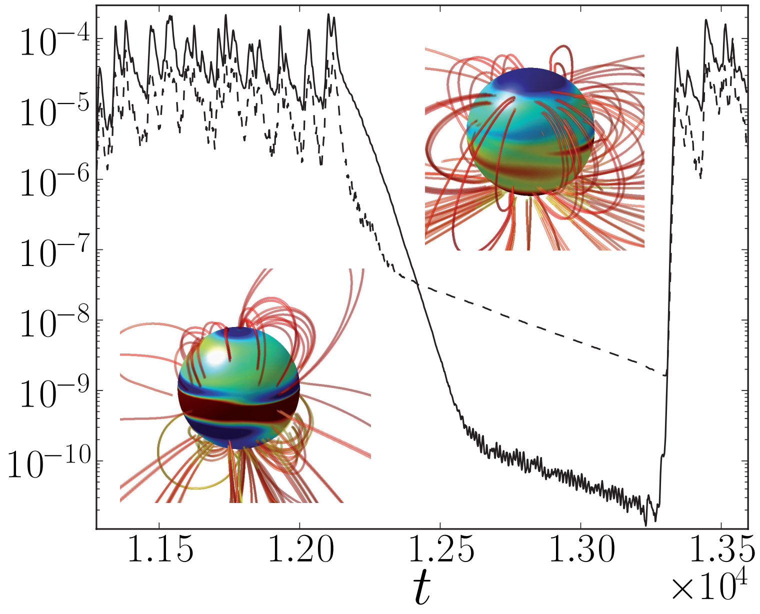

4.2.4 Discussion

Canonical model for on-off intermittency

The simplest model that exhibits on-off intermittency is (Aumaître *et al.* 2005)

$$\dot{X} = [a + \zeta(t)]\, X - X^3 , \tag{4.22}$$

where a is the distance to the threshold, and ζ a Gaussian white noise of zero mean value and amplitude D, defined as $\langle\zeta(t)\zeta(t')\rangle = D\delta(t-t')$ where $\langle\rangle$ indicates the average over realizations (ensemble average). In the absence of noise, the system undergoes a supercritical pitchfork bifurcation at $a = 0$. If a is sufficiently small, the fluctuations lead to on-off intermittency, with bursts ($a+\zeta > 0$) followed by decays ($a+\zeta < 0$). During the off phases, one can neglect nonlinearities and write $\dot{Y} = a + \zeta(t)$, with $Y = \ln(X)$. Thus, $\ln(X)$ should follow a random walk, with a small positive bias. Since solutions of Eq. (4.22) mimic solutions of the magnetohydrodynamics equations we observe in Fig. 4.2, we further investigate some properties of the model. (i) Equation (4.22) leads to a stationary probability density function (PDF) of the form (Stratonovitch 1963)

$$P(X) \propto X^{(2a/D)-1} e^{-X^2/D} , \tag{4.23}$$

which diverges at the origin for $0 \leqslant s = (2a/D) - 1 < 1$. (ii) In addition, all the moments of X must follow a linear scaling with a. (iii) Finally, another characteristic of this model is that the distribution of the duration of the off phases T_{off} follows a power law behavior, $P(T_{\text{off}}) \sim T_{\text{off}}^{-\alpha}$, with $\alpha = -3/2$. To compare these predictions to our results, we rely as Alexakis & Ponty (2008) on the magnetic energy density as a global measure of the magnetic field strength.

Predictions and results

Figure 4.5 shows the PDFs of the magnetic energy for a set of simulations at different Reynolds numbers. At low Rm, the PDF is characterized by a linear scaling on a log-log plot. The cutoff at low energies is not predicted by the theory, which considers the limit $E_b \to 0$. For Rm > 310, the magnetic energy fluctuates around a mean value and the PDF no longer scales as a power law. We see in Fig. 4.6 that the coefficient s is proportional to the distance to the threshold. Examples of the fit of the exponent s are presented in Fig. 4.7. The values of the coefficient are mainly affected by the range over which the data are fitted. Thus we select a range as large as possible. We then randomly sample this range with half-size sub-intervals. We then compute the mean slope and its standard deviation (represented in Fig. 4.6 with error bars).

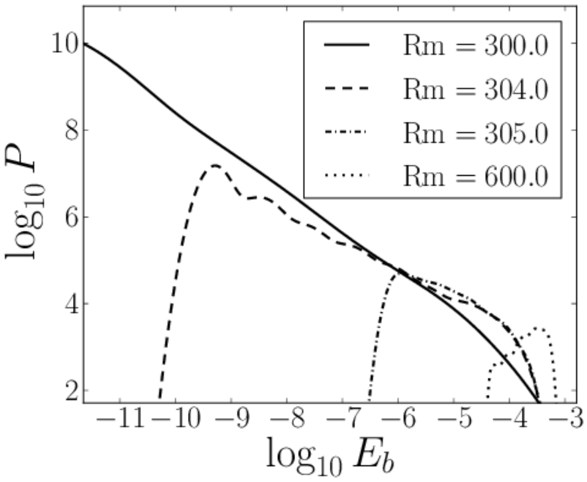

Figure 4.5 – Estimates of the probability density functions. Statistics are done from time series of the magnetic energy obtained with ferromagnetic boundary conditions, for Pm = 0.2.

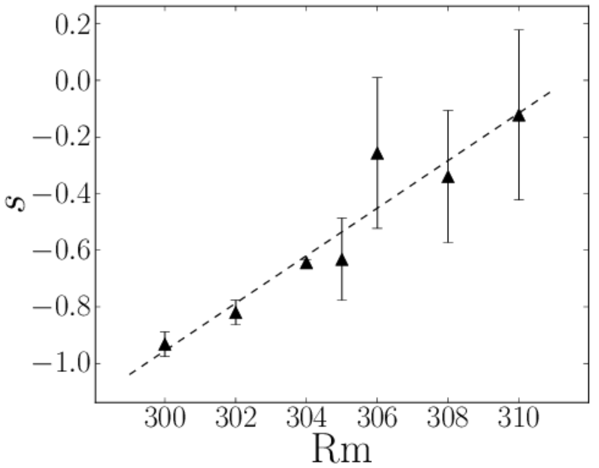

Figure 4.6 – Fit of the coefficient $s = (2a/D) - 1$, taking into account the linear domain of the PDFs in the intermittent regime only. Statistics are done from time series of the magnetic energy obtained with ferromagnetic boundary conditions, for Pm = 0.2.

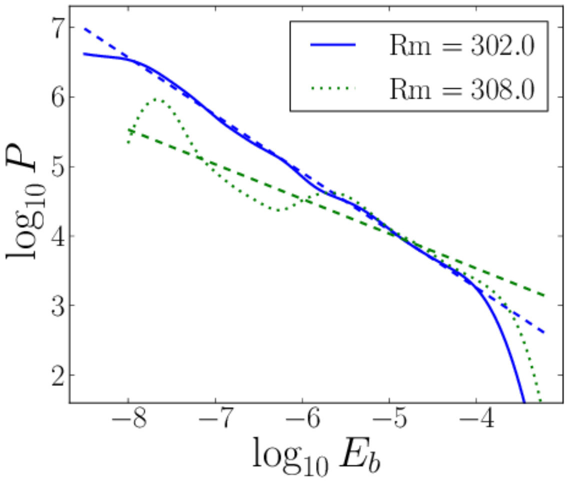

Figure 4.7 – Examples of the fit (dashed lines) of the probability density functions (solid and dotted lines). Statistics are done from time series of the magnetic energy obtained with ferromagnetic boundary conditions, for Pm = 0.2.

We then investigate the linearity of the moments. Figure 4.8 shows our results for the first and second moments of the magnetic energy. We see that the mean magnetic energy grows linearly as a function of the magnetic Reynolds number. The second moments seem to follow the same linear trend, but only at the lower values of the magnetic Reynolds number. Deviations at larger values of Rm are expected, as this description is only valid in the limit $\mathrm{Rm} \to \mathrm{Rm_c}$. The duration t_I of the time series used to compute these values ranges from $3.2\,10^3$ to $1.4\,10^4$ U.T. (values are presented in Table 4.2). These integration times are quite significant for a fully three dimensional set of partial differential equations but are necessarily short compared to the ones usually used with simplified models such as Eq. (4.22). To quantify the uncertainty associated with the moment values, we sampled the integration time with sub-intervals randomly chosen. We then computed the moments on the full interval (symbols in Fig. 4.8) and the standard deviation on the sub-intervals (reported as error bars). The sub-intervals can be set from $t_I/4$ to $t_I/10$ without affecting these estimates.

Finally, we also tested the distribution of the duration time of the off phases. A definitive validation would require longer simulations, in order to have a significant number of off phases. For this reason, we can not rely on the simulations immediately above the threshold. Despite these short-comings, an illustrative case is presented in Fig. 4.9. Numerical values are given in Table 4.3.

To conclude, we emphasize that the predictions of the model are consistent with the three-dimensional simulations, and thus confirm the on-off hypothesis for the observed intermittency at low magnetic Prandtl number.

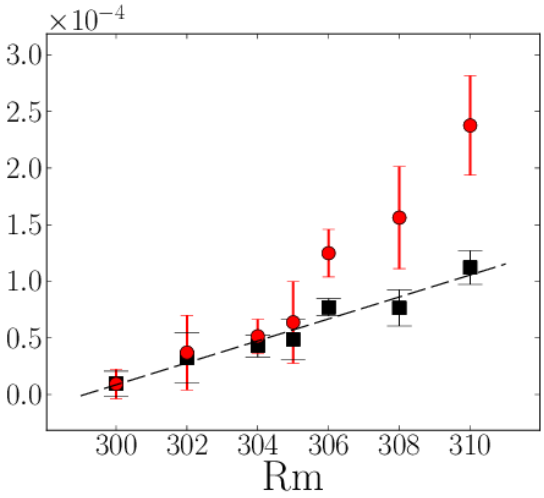

Figure 4.8 – Moments of the magnetic energy as function of the magnetic Reynolds number. Black squares represent the mean. The dashed line fits these data points with an error about 10% on the slope coefficient. The second moments (red circles) have been rescaled to match with the mean at $\mathrm{Rm} = 300$.

Table 4.2 – Duration of the time series used to compute the moments of the magnetic energy. The integration time t_I is presented in units of $(\chi\Delta\Omega)^{-1}$ (t_I) and in units of the magnetic diffusion time r_0^2/η (t_I/Rm).

Rm	t_I	t_I/Rm
300	$1{,}40 \times 10^4$	46,7
302	$9{,}06 \times 10^3$	30,0
304	$9{,}05 \times 10^3$	29,8
305	$3{,}33 \times 10^3$	10,9
306	$7{,}58 \times 10^3$	24,8
308	$3{,}20 \times 10^3$	10,4
310	$5{,}46 \times 10^3$	17,6

Table 4.3 – Estimate of the exponent α of the PDF of the duration of the off phases for different threshold values and different ranges over which the fit is done. The standard error on the estimate of α is about 1%. Range values correspond to $\log_{10} T_{\mathrm{off}}$ [x axis in Fig. 4.9(b)].

Threshold	Range		
	[1.7 ; 3]	[2.0 ; 3]	[2.1 ; 3]
$1{,}1 \times 10^{-4}$	-1.30	-1.48	-1.51
$1{,}0 \times 10^{-4}$	-1.35	-1.48	-1.50
$7{,}5 \times 10^{-5}$	-1.40	-1.41	-1.40
$5{,}0 \times 10^{-5}$	-1.48	-1.52	-1.51
$3{,}5 \times 10^{-5}$	-1.51	-1.60	-1.65

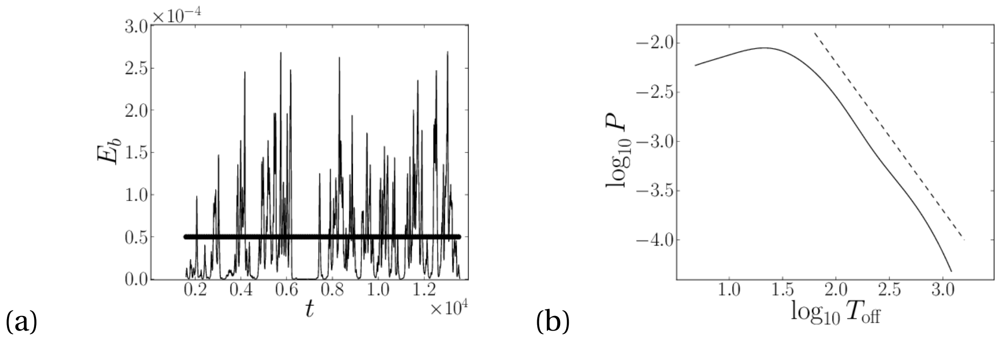

Figure 4.9 – Distribution of the duration of the off phases for a simulation performed at Pm = 0.2 and Re = 1470, with conducting boundary conditions. We define an off phase by a magnetic energy below a threshold value (horizontal black line). The PDF (b) decay is close to a power law with the expected −3/2 value for the exponent (dashed line).

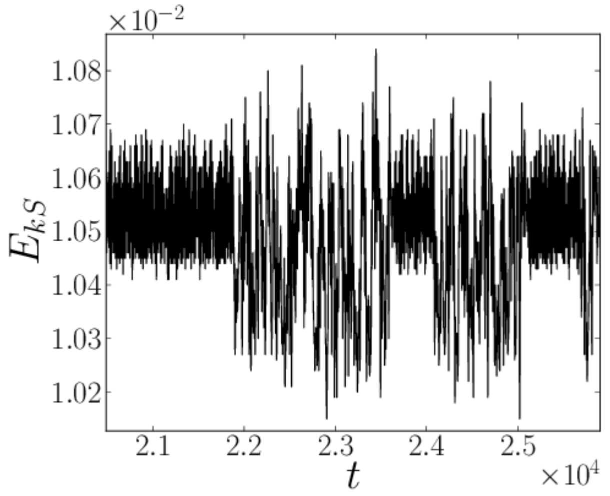

Figure 4.10 – Time evolution of the symmetric part of the kinetic energy E_k^S at Re = 1200 in a purely hydrodynamic simulation. Intermittent transitions between “laminar” and more turbulent phases are clearly visible.

Simulations at higher magnetic Prandtl number

The simulations we performed at Pm = 2 exhibit a peculiar behavior of the magnetic field. This can be better understood by examining the dynamics of the flow. Indeed, we also carried out purely hydrodynamic simulations at Re = 1200 and observed intermittent transitions between two states. This kind of intermittent behavior of the flow was not reported in Guervilly & Cardin (2010), but has been observed experimentally (Zimmerman *et al.* 2011). One state is characterized by larger fluctuations of the energy as we can see in Fig. 4.10. In addition, the analysis of the energy spectra reveals that the $m = 3$ modes dominate over the $m = 2$ modes during the “laminar” phases, whereas both are of the same order during the “turbulent” phases. Duration of the “turbulent” phases tends to increase gradually

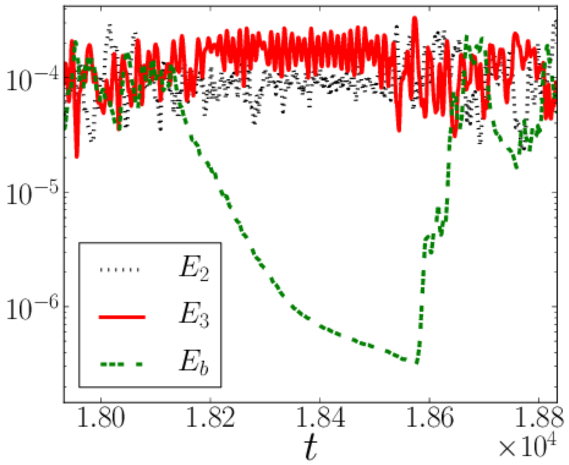

Figure 4.11 – Time series at Re = 1200 and Pm = 2 of the total magnetic energy E_b (dashed green line) and the kinetic energies E_2 (dotted black line) and E_3 (solid red line) for the $m = 2$ and $m = 3$ modes, respectively. When the latter becomes larger than the former, the dynamo is no longer sustained and the magnetic energy exponentially decays.

with the increase of the Reynolds number, so that the intermittent behavior of the flow eventually disappears and is thus no longer present in the simulations at higher Reynolds number in which we have identified on-off intermittency.

Dynamo action is inhibited during the “laminar” phases (when the $m = 3$ modes dominate), which highlights the mechanism which leads to the peculiar behavior of the magnetic field, as we can see in Fig. 4.11. In contrast, “turbulent” phases favor dynamo action, and one must wait a change in the flow to see the restart of dynamo action after a phase of decay. Moreover, in a full magnetohydrodynamics simulation, we can artificially suppress the $m = 3$ modes of the velocity field by setting them equal to zero at each time step. We check that it is sufficient to suppress intermittency of the flow. Then, we observe that the phases of exponential decay are also suppressed and the dynamo is no longer intermittent.

Despite the fact that on-off intermittency has so far never been observed in dynamo experiments, we showed that the phenomenon can appear in numerical simulations of dynamo action using realistic boundary conditions. We identified in several cases the predicted behavior of the PDF of the magnetic energy, linear scaling of the moments, and distribution of the duration of the off phases. In addition, we tested these properties for three different boundary conditions (conducting inner core with insulating outer sphere, insulating or ferromagnetic spheres). Finally, we pointed out a different kind of intermittency due to hydrodynamic transitions that appears at lower Reynolds numbers.

To explain the absence of on-off intermittency in the experiments, several reasons have already been invoked (Pétrélis *et al.* 2007). One explanation could be the imperfectness of the bifurcation (due for instance to Earth’s ambient magnetic field). Since it has been shown that low-frequency noise controls on-off intermittency (Aumaître *et al.* 2005), another possible explanation could be that the low-frequency fluctuations are too small. However, the lack of experimental observations of on-off intermittency remains an open question and needs further investigations.

4.3 Dynamos stellaires : symétries et modulations

4.3.1 Contexte

De nombreux modèles de champ moyen reproduisent en partie les caractéristiques du cycle solaire (Charbonneau 2010) dont les modulations temporelles pourraient être de nature stochastique (Schmitt *et al.* 1996, Choudhuri & Karak 2012) ou chaotique, étant donné le caractère intrinsèquement non-linéaire du système (Dormy & Soward 2007, ch. 6). Une approche complémentaire consiste à dériver des modèles de basse dimension contraints par les symétries du système ; cela permet ainsi d'établir le caractère générique de la dynamique tout en s'affranchissant des problèmes liés à la modélisation des effets de champ moyen (Weiss 2011). Ces approches combinées ont permis d'identifier deux classes de modulations, le type 1 étant caractérisé par des changements de parité sans modulation d'amplitude, et le type 2 par des modulations d'amplitude sans changement de parité (Knobloch *et al.* 1998). En outre, les interactions entre modes de différentes parités conduisent aisément à des champs magnétiques fortement localisés dont il existe plusieurs exemples observationnels (Sokoloff & Nesme-Ribes 1994, Langlais & Quesnel 2008) et expérimentaux (Gallet *et al.* 2012). Nous confrontons ces résultats à la dynamique du champ magnétique obtenu par simulations numériques directes d'un écoulement convectif dans une coquille sphérique en rotation.

Pour mener cette étude, le système d'équations (2.49)–(2.51) a été intégré entre 5 et 60 temps de diffusion magnétique avec la version anélastique du code PARODY, dans un régime de paramètres tel que $\mathrm{E} = 10^{-4}$, $\mathrm{Pr} = 1$, $\mathrm{Pm} = 1$, $\chi = 0{,}35$, $n = 2$ et $N_\varrho = 0{,}5$, ce qui correspond à une faible stratification. Dans ces conditions, le Rayleigh critique pour le seuil linéaire de convection vaut $\mathrm{Ra_c} = 3{,}34 \times 10^5$ (Schrinner *et al.* 2014). L'analyse des simulations repose principalement sur le calcul des énergies cinétique $E_k = 1/2 \int w^n \mathbf{v}^2 \,\mathrm{d}V$ et magnétique $E_b = \mathrm{Pm}/(2\mathrm{E}) \int \mathbf{B}^2 \,\mathrm{d}V$. Afin d'étudier les interactions entre familles de symétrie par rapport au plan équatorial, nous définissons les énergies cinétiques symétrique et antisymétrique E_k^S et E_k^A, calculées à partir des écoulements symétrique et antisymétrique. De même, on définit les énergies magnétiques symétrique E_D et antisymétrique E_Q correspondant aux symétries dipolaire et quadrupolaire.

4.3.2 Résultats

Dans cette étude, nous nous sommes concentrés sur les modulations à basse fréquence de la branche multipolaire, qui seule persiste à bas Reynolds magnétique et qui est alors dominée par un mode non axisymétrique $m = 1$ (Raynaud *et al.* 2014). Ces dynamos — pour lesquelles le vent zonal (mesuré par l'énergie cinétique toroïdale axisymétrique) joue un rôle essentiel dans la régénération du champ magnétique toroïdal par effet Ω (Schrinner *et al.* 2012) — apparaissent suite à une bifurcation de Hopf donnant naissance à des solutions oscillantes qui peuvent, en théorie, être de symétrie dipolaire ou quadrupolaire (Tobias 2002). Ces solutions sont souvent interprétées commes des ondes de Parker dont la période est de l'ordre de 0,1 temps de diffusion magnétique. Proche du seuil dynamo[4] ($\mathrm{Ra} = 1.4 \times 10^6$), nous observons une nouvelle forme de bistabilité entre solutions de symétrie dipolaire ou quadrupolaire. Les écoulements associés ne brisent pas la symétrie équatoriale et se caractérisent par un mode de convection $m = 9$ dans le cas dipolaire et $m = 8$ dans le cas quadrupolaire. D'autre part, les fluctuations de l'énergie cinétique sont plus importantes pour la solution dominée par la symétrie dipolaire. L'augmentation du nombre de Rayleigh conduit à la déstabilisation de la solution quadrupolaire et à l'apparition d'un cycle limite pouvant être décrit comme l'apparition d'une modulation de type 1 : la symétrie dominante du champ magnétique change périodiquement alors que l'énergie magnétique totale reste relativement constante. Ce cycle coexiste avec la solution de symétrie dipolaire, puis finit par perdre sa stabilité pour $\mathrm{Ra} = 1.49 \times 10^6$. L'évolution de ces différentes solutions avec l'augmentation du nombre de Rayleigh est synthétisée figure 4.12(a). En outre, lorsque les énergies magnétiques symétrique et antisymétrique sont du même ordre, le champ magnétique tend à être confiné dans un hémisphère, comme l'illustre la figure 4.12(b). Cette forte localisation du champ magnétique revient périodiquement au cours du cycle limite qui est caractérisé par l'interaction des deux familles de symétrie du champ magnétique. Comme on le voit figure 4.13(a), ce couplage s'accompagne d'une faible brisure de la symétrie équatoriale de la part de l'écoulement, en adéquation avec les conditions expérimentales propices à l'observation d'un champ magnétique localisé (Gallet *et al.* 2012). Enfin, notons que le cycle limite semble apparaître avec une période infinie dont le carré décroît linéairement avec Ra, comme le montre la figure 4.13(b). La relation $f \propto \sqrt{\mu}$ reliant la fréquence du cycle à l'écart au seuil de la bifurcation indique que ce cycle limite résulte de la collision d'un point fixe stable et d'un point fixe instable (nœud-col).

Lorsque l'on poursuit l'augmentation du nombre de Rayleigh, des modulations d'amplitude apparaissent et l'on passe progressivement d'une modulation de

---

[4] Dans ce régime de paramètres, le Rayleigh critique pour le seuil dynamo est tel que $\mathrm{Ra_d} > 10^6$.

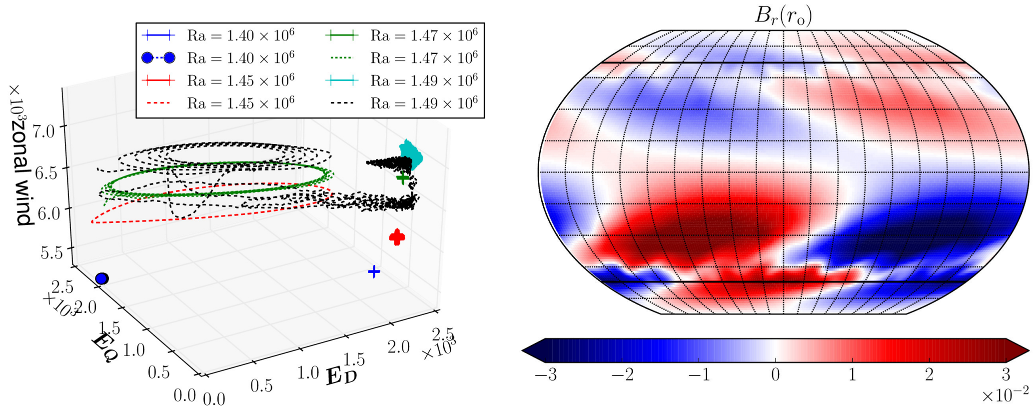

(a)

(b) $\mathrm{Ra} = 1.47 \times 10^6$

Figure 4.12 – (a) : Bistabilité et déstabilisation du cycle limite. (b) : Instantané du champ magnétique radial à la surface lorsque la symétrie dipolaire domine le cycle limite à $t = 48.74$. On note la localisation hémisphérique du champ magnétique ainsi que la domination claire du mode $m = 1$.

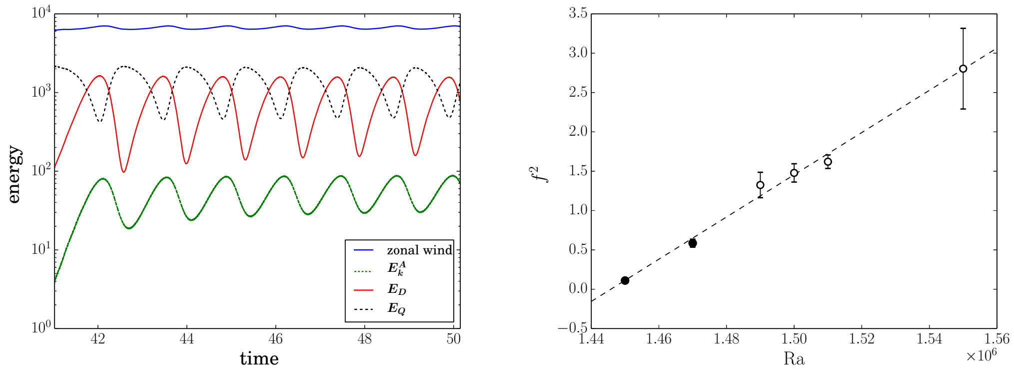

(a) $\mathrm{Ra} = 1.47 \times 10^6$

(b) $f \propto \sqrt{\mathrm{Ra} - \mathrm{Ra}_{\mathrm{SN}}}$

Figure 4.13 – (a) : Séries temporelles de différentes énergies dans le cas du cycle limite. (b) : Évolution en fonction de Ra du carré de la fréquence du cycle calculée à partir des séries temporelles de l'énergie magnétique antisymétrique. Les symboles vides indiquent que le cycle n'est plus stable. L'estimation du seuil donne la valeur $\mathrm{Ra}_{\mathrm{SN}} \sim 1.446 \times 10^6$ (pointillés). Les barres d'erreurs indiquent les écarts types.

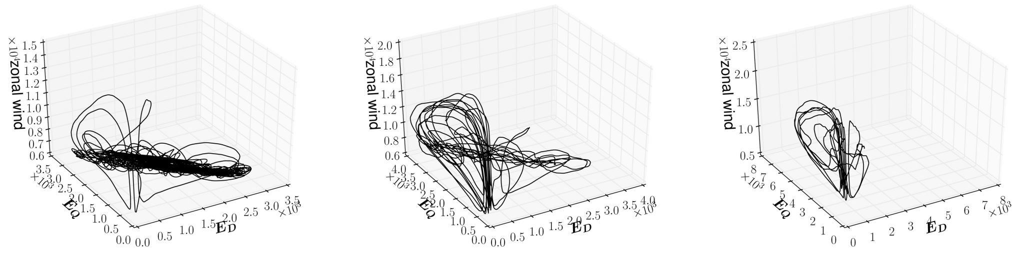

(a) Ra = 1.55×10^6 (b) Ra = 1.65×10^6 (c) Ra = 1.85×10^6

Figure 4.14 – Apparition de la modulation de type 2 avec l'augmentation de Ra.

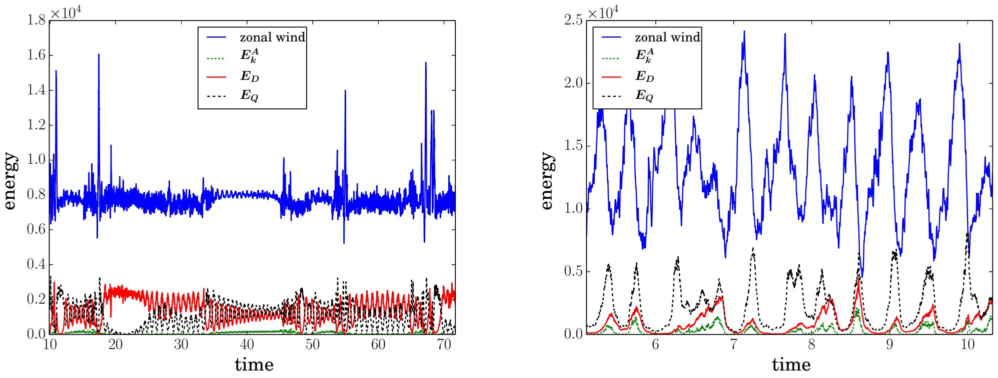

(a) Ra = 1.55×10^6 (b) Ra = 1.85×10^6

Figure 4.15 – Séries temporelles de différentes énergies dans le cas de la modulation de type 2.

type 1 à une modulation de type 2 pour laquelle le champ magnétique est alors fortement modulé en amplitude mais reste dominé par la symétrie quadrupolaire (cf. figure 4.14). La dynamo passe alors par des minimums dont la fréquence augmente avec Ra. La figure 4.15(a) illustre plus particulièrement l'apparition de la modulation d'amplitude caractérisée par la décroissance intermittente de l'énergie magnétique suivie d'une soudaine augmentation du vent zonal. Entre ces sursauts du vent zonal, les phases saturées sont caractérisées par des échanges d'énergie entre les deux familles de symétries du champ magnétique. Il est même possible de faire la distinction entre les périodes dominées par la symétrie dipolaire et celles dominées par la symétrie quadrupolaire. Le système semble alors revisiter l'ancien cycle limite, comme on peut le voir pour $t \sim 40$ sur la figure 4.15(a).

En revanche, les séries temporelles sont trop courtes pour permettre une analyse statistique des modulations d'amplitude de l'énergie magnétique illustrées figure 4.15(b). On observe que l'énergie magnétique est bien majoritairement

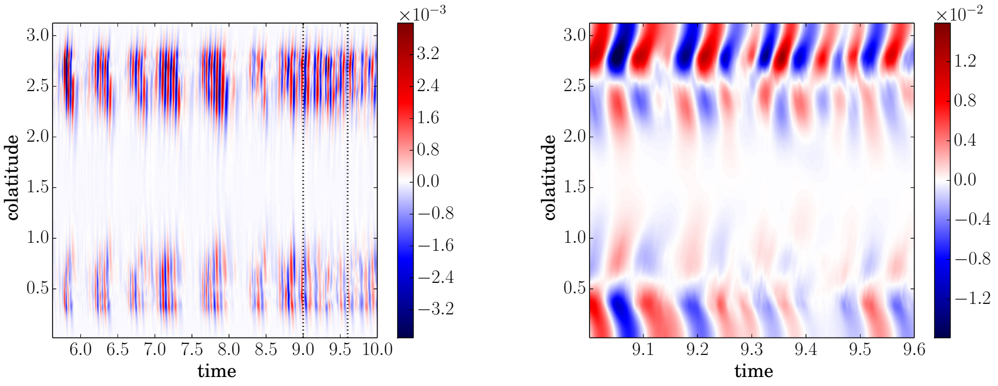

(a) $\langle B_\varphi \rangle_\varphi$ (b) $\langle B_r \rangle_\varphi$

Figure 4.16 – Diagrammes papillon obtenus pour Ra = 1.65×10^6 à partir des composantes azimutale (a) et radiale (b) du champ magnétique mesuré sous la surface et moyenné en azimut. La figure (b) correspond à la période délimitée par les lignes pointillées sur la figure (a).

dominée par sa composante antisymétrique E_Q, et que les minimums semblent parfois causés par la croissance graduelle de la composante symétrique E_D. Ce scénario pourrait rappeler une forme d'intermittence *in-out* décrite par certaines études (Moss & Brooke 2000, et références incluses). Toutefois, si la symétrie dipolaire est artificiellement annulée à un instant donné, la modulation d'amplitude persiste, mais avec un autre temps caractéristique. Par ailleurs, la durée moyenne d'une phase saturée entre deux minimums peut croître significativement suite à une augmentation de 10 % de Pr ou une diminution de 10 % de Pm. Nous avons également vérifié, à l'aide de simulations sans champ magnétique, que l'on ne se trouve pas en présence d'oscillations de relaxation du vent zonal : ces modulations ne sont donc pas d'origine purement hydrodynamique.

Enfin, notons que la coexistence des deux types de modulations se répercute sur les diagrammes papillons correspondants sous forme de motifs intéressants qui rappellent, en partie, les observations solaires. On distingue ainsi de fortes modulations d'amplitude sur la figure 4.16(a) alors que la figure 4.16(b) met en évidence un changement de symétrie du champ lors d'une phase saturée. De plus, l'activité magnétique migre préférentiellement vers les pôles à haute latitude et vers l'équateur à basse latitude.

4.3.3 Bilan

Les simulations numériques directes présentées mettent en évidence un nouveau type de bistabilité entre dynamos multipolaires de différentes symétries. Bien que dominées par un mode non axisymétrique $m = 1$, ces dynamos présentent un riche comportement dynamique ayant certains points communs avec les études précédentes reposant sur des modèles de champ moyen ou de basse dimension. Toutefois, les détails de la structure de bifurcation semblent ici plus complexes. Nous avons ainsi relié l'apparition d'une modulation de type 1 à la création d'un cycle limite suite à une bifurcation nœud-col où collisionnent un point fixe stable de symétrie quadrupolaire et un point fixe instable de symétrie dipolaire. L'écoulement brise alors faiblement la symétrie équatoriale et le couplage de modes de différentes parités s'accompagne de la localisation périodique du champ magnétique dans un hémisphère. L'augmentation du nombre de Rayleigh conduit à la déstabilisation de ce cycle limite et la dynamo entre alors progressivement dans un régime chaotique correspondant à une modulation de type 2. Ce régime est, en effet, caractérisé par l'occurrence de minimums d'énergie magnétique suivis d'une forte croissance du vent zonal. L'analyse statistique de ces minimums mérite d'être approfondie, tout comme l'influence des nombres de Prandtl thermique et magnétique sur la dynamique du système.

⁂

Chapitre 5

Conclusion

> *Que devons-nous conclure ?*
> *Rien, sinon que nous nous trouvons en présence d'un paradoxe scientifique, dont l'explication se fera, mais qui ne laisse pas d'être intéressant.*
>
> Gérard-Lescuyer (1880)

5.1 Bilan général

Nos travaux ont permis d'établir l'existence de plusieurs similarités entre modèles Boussinesq et anélastiques (cf. section 3.1). La classification binaire entre dynamos dipolaires et multipolaires peut être étendue aux modèles anélastiques. Ainsi, des champs magnétiques dipolaires de grande échelle sont obtenus si la force de Coriolis (autrement dit, l'influence de la rotation) est prépondérante par rapport à l'inertie ; le critère du nombre de Rossby local peut être généralisé aux dynamos anélastiques tant que le contraste de densité vérifie $N_\varrho \leq 2$. Ce critère reposant sur des moyennes volumiques, il semble devenir inadapté pour de plus fortes stratifications, sans que cela ne remette en question le rôle de l'inertie dans la perte de la branche dipolaire.

Nous avons cependant mis en évidence quelques différences significatives propres aux simulations anélastiques. Les configurations du champ magnétique dominées par un mode non-axisymétrique $m = 1$ s'avèrent ainsi plus courantes au sein des modèles anélastiques. On constate aussi qu'une forte stratification en densité semble pouvoir inhiber la génération de champs magnétiques dominés par un dipôle axial, en accord avec d'autres études (Gastine *et al.* 2012, Jones 2014). Il convient néanmoins de nuancer ces résultats. Une étude détaillée de modèles faiblement stratifiés nous a d'abord permis de mettre en lumière le rôle important joué par le profil de gravité (cf. section 3.2). En effet, en plus des transitions usuelles entre branches dynamos obtenues avec une distribution de masse uniforme, nous avons montré que, dès lors qu'une distribution de masse centrale est considérée, la branche dipolaire peut désormais perdre sa stabilité au profit de la branche multipolaire, à bas nombre de Rayleigh et bas nombre de Prandtl magnétique. Dans ce régime de paramètres restreint, les dynamos sont alors dominées au niveau de la sphère externe par un dipôle équatorial. L'émergence de ce mode proche du seuil dynamo peut rappeler, dans une certaine mesure, les résultats de Aubert & Wicht (2004) qui ont étudié la compétition entre les dipôles axial et équatorial pour différents facteurs de forme de la zone convective dans des modèles de géodynamo. Dans notre cas, l'apparition de ce mode semble reliée à la concentration des cellules de convection autour de la sphère interne, laquelle résulte de la dépendance en $1/r^2$ du profil de gravité. Un tel effet de filtre pourrait rester pertinent pour des stratifications modérées ($N_\varrho \leq 1{,}5$) mais n'est toutefois pas à même de rendre compte de la forte composante $m = 1$ de modèles plus stratifiés.

En outre, la rareté des dipôles axiaux dans les simulations anélastiques ne pourrait être qu'une conséquence indirecte de la stratification, comme l'indique notre étude détaillée de l'évolution du domaine de stabilité de la branche dipolaire (cf. section 3.3). Au cours de cette évolution, il est fondamental de remarquer que le nombre de Reynolds magnétique critique de la branche dipolaire évolue peu, de sorte que l'on a toujours $Rm_\mathrm{c} \sim 10^2$. En revanche, plus N_ϱ est élevé, plus la convection se développe rapidement au fur et à mesure que l'on s'écarte du seuil de convection. La conjonction de ces deux tendances va donc avoir une double conséquence sur la stabilité de la branche dipolaire : d'une part, on constate effectivement que les nombres de Rayleigh pour lesquels les dynamos dipolaires sont des solutions stables se rapprochent du Rayleigh critique de convection lorsque la stratification augmente ; d'autre part, plus la stratification est importante, plus est atteinte rapidement la limite au-delà de laquelle l'inertie cause la perte de la solution dipolaire. Il en résulte que la branche dipolaire s'étend sur une gamme de nombres de Rayleigh de moins en moins étendue lorsque la stratification croît, d'où une impression globale de rareté des dipôles axiaux dans les simulations anélastiques.

La perte de la branche dipolaire semble donc rester tributaire de l'importance de l'inertie et la restriction du domaine de stabilité des dipôles axiaux apparaît d'abord comme le reflet de l'espace de paramètres actuellement à la portée des calculateurs, et non comme le résultat d'une modification des mécanismes dynamos induite par la stratification. Plusieurs stratégies permettent d'ailleurs de maintenir un nombre de Reynolds magnétique de l'ordre de la centaine sans que l'inertie ne vienne déstabiliser la solution dipolaire. Une première option — dont le coût numérique reste relativement modérée et que nous avons pu effectivement tester — consiste à augmenter le nombre de Prandtl magnétique. Une autre option serait de diminuer le nombre d'Ekman, mais cela devient vite plus exigeant en matière de ressources numériques. Si nous abaissons la valeur du nombre d'Ekman de $\mathrm{E} = 10^{-4}$ à 3×10^{-5} en gardant $\mathrm{Pr} = 1$ et $N_\varrho = 2$, nous retrouvons la bistabilité que nous avions perdue à $\mathrm{E} = 10^{-4}$. Nous avons, en effet, trois exemples de cas bistables pour $\mathrm{Pm} = 1$ à $\mathrm{Ra}/\mathrm{Ra_c} = 2{,}6$ et pour $\mathrm{Pm} \in \{1, 2\}$ à $\mathrm{Ra}/\mathrm{Ra_c} = 2{,}9$. À l'instar de Jones (2014), il n'est donc pas déraisonnable de conjecturer que les solutions dipolaires persistent sur un plus grand domaine de paramètres pour des valeurs plus basses du nombre d'Ekman, actuellement trop coûteuses à simuler. Dans un premier temps, la vérification d'une telle assertion requiert une exploration plus dense ainsi qu'une analyse plus détaillée des dynamos que nous pourrons obtenir à $\mathrm{E} = 3 \times 10^{-5}$.

Enfin, nous avons également étudié la dynamique temporelle de différentes dynamos (cf. section 4). Cela nous a d'abord permis d'observer un comportement d'intermittence *on-off* proche du seuil d'un modèle de dynamo de Couette sphérique, réaliste d'un point de vue expérimental. Nous avons aussi relié les modulations basse fréquence de dynamos convectives à deux types de comportements établis pour des systèmes de champ moyen. Nous avons notamment identifié l'existence d'une modulation de parité conduisant à la localisation périodique du champ magnétique dans un hémisphère, ainsi que l'apparition chaotique de minimums d'énergie magnétique. Cette modulation d'amplitude rappelle, du moins en partie, les variations de l'activité magnétique solaire. L'étude de la structure de bifurcation confirme que les interactions entre modes de différentes symétries par rapport au plan équatorial peuvent jouer un rôle fondamental dans la dynamique du champ magnétique, en accord avec des résultats de l'expérience VKS (Pétrélis & Fauve 2008, Gallet *et al.* 2012).

5.2 Perspectives

L'une des principales difficultés reste de relier ces études théoriques aux observations. À ce sujet, les lois d'échelle proposées pour les modèles Boussinesq (Christensen & Aubert 2006, Christensen 2010) semblent rester valables : l'intensité du champ magnétique peut donc être directement reliée à un nombre de Rayleigh modifié Ra_Q (cf. section 3.4). Ces relations, revisitées depuis pour des modèles de géodynamo (Davidson 2013, 2014, Oruba & Dormy 2014), n'ont toutefois pas un caractère prédictif au sens strict puisqu'elles ne dépendent pas exclusivement des paramètres de contrôle du système. De plus, leur généralité n'est pas forcément à même de mettre en évidence d'éventuels changements au niveau des mécanismes de génération du champ magnétique. En ce sens, il serait intéressant de tester les derniers développements théoriques proposés pour des modèles de géodynamo sur notre base de données de modèles stellaires.

Remarquons toutefois que la bistabilité entre les branches dynamos qui est observée dans les modèles numériques n'est pas sans rappeler certaines observations. En effet, l'étude spectropolarimétrique d'étoiles naines de type M a révélé l'existence de deux catégories distinctes de configurations magnétiques : champs magnétiques dipolaires intenses et champs magnétiques essentiellement non-axisymétriques de plus faible intensité. De plus, ces différentes configurations peuvent être observées pour des objets relativement semblables (Morin *et al.* 2010). À la suite des études précédentes (Schrinner *et al.* 2012, Gastine *et al.* 2013), nous avons montré que le comportement bistable des modèles numériques anélastiques reste une manière d'appréhender la diversité des champs magnétiques stellaires des étoiles naines de type M. Dans cette perspective, on peut noter qu'un changement de la topologie magnétique globale au niveau d'une étoile n'a encore jamais été observé. D'autres mécanismes ont également été évoqués pour expliquer cette bistabilité (Morin *et al.* 2011). Plus généralement, des observations couvrant de longues périodes apparaissent donc essentielles afin de tester la pertinence des études théoriques dont il reste difficile de tirer des observables. Shulyak *et al.* (2015) ont proposé une stratégie pour faire le lien entre les résultats théoriques et observationnels qui repose principalement sur les modes de grande échelle $m = 0$ et $m = 1$ symétriques ou antisymétriques par rapport au plan équatorial. Ces modes peuvent effectivement gouverner la dynamique basse fréquence du champ magnétique, comme nous avons pu le montrer pour nos modèles.

Gardons aussi à l'esprit que les modèles considérés ici restent relativement rudimentaires. Certaines études introduisent par exemple une conductivité variable en rayon (Duarte *et al.* 2013, Yadav *et al.* 2013b) ; d'autres essaient spécifiquement de modéliser un intérieur planétaire semblable à celui de Jupiter (Gastine *et al.* 2014, Jones 2014). Néanmoins, la prise en compte de ces complexités supplémentaires n'a révélé, jusqu'à présent, aucune incompatibilité directe avec les comportements génériques que nous avons tenté d'établir pour des modèles plus simples. À ce titre, une analyse en termes de champ moyen des simulations numériques pourrait donner un aperçu plus approfondi des mécanismes dynamos qui sous-tendent la génération du champ magnétique dans ce type de modèles (Schrinner *et al.* 2007, Schrinner 2011).

Enfin, au-delà d'une complexification directe des modèles anélastiques, il serait intéressant de développer une approximation qui permette de filtrer les ondes sonores tout en évitant certains écueils de l'approximation anélastique (Calkins *et al.* 2015). Afin de comparer différentes approximations du système compressible existantes, nous avons développé plusieurs codes 2D en géométrie cartésienne, qui ont par ailleurs servi à tester de nouveaux algorithmes d'advection développés par Alexandre Cameron (cf. annexe C.1). Nous mentionnons également les travaux de Toby Wood qui a établi un nouveau modèle hydrodynamique reprenant le système pseudo-incompressible proposé par Durran (1989) — équivalent au système anélastique si l'on considère un état de référence stratifié adiabatiquement. La dérivation de ces équations peut être obtenue en utilisant les techniques de la mécanique analytique (Salmon 1988, Vasil *et al.* 2013), toute la difficulté étant ensuite d'incorporer la diffusion thermique de manière cohérente. Le système pseudo-incompressible permet de s'affranchir de l'hypothèse d'un état de référence stratifié adiabatiquement qui, bien que relativement appropriée pour l'étude des zones convectives stellaires, n'en reste pas moins contraignante et inadaptée pour beaucoup d'autres systèmes. L'approximation pseudo-incompressible pourrait ainsi être utile, par exemple, pour l'étude de la dynamique des zones radiatives.

⁂

Annexe A

Validation du code

Nous donnons ici les résultats numériques obtenus avec PARODY pour la reproduction des trois cas tests pour le système anélastique proposés par Jones *et al.* (2011).

Table A.1 – Benchmark hydrodynamique.
($\mathrm{E} = 10^{-3}$, $N_\varrho = 5$, $\chi = 0.35$, $\mathrm{Ra} = 3.52 \times 10^5$, $\mathrm{Pr} = 1$, $n = 2$)

Code	PARODY	Leeds
K.E.	81.85	81.86
Zonal K.E.	9.388	9.377
Meridional K.E.	0.02198	0.02202
Luminosity	4.170	4.199
v_ϕ at $v_r = 0$	0.8618	0.8618
S at $u_r = 0$	0.9334	0.9330
Resolution	288 × 192 × 384	128 × 192 × 384
Timestep	5×10^{-6}	2.5×10^{-6}

Table A.2 – Benchmark dynamo stationnaire.
($\mathrm{E} = 2 \times 10^{-3}$, $N_\varrho = 3$, $\chi = 0.35$, $\mathrm{Ra} = 8.00 \times 10^4$, $\mathrm{Pr} = 1$, $\mathrm{Pm} = 50$, $n = 2$)

Code	PARODY	Leeds
K.E.	4.189×10^5	4.194×10^5
Zonal K.E.	5.993×10^4	6.018×10^4
Meridional K.E.	52.98	53.02
M.E.	3.216×10^5	3.202×10^5
Zonal M.E.	2.424×10^5	2.412×10^5
Meridional M.E.	1.704×10^5	1.697×10^4
Luminosity	11.48	11.50
v_ϕ at $v_r = 0$	-91.84	-91.78
B_θ at $v_r = 0$	±0.0343	±0.03395
S at $u_r = 0$	0.7864	0.7865
Resolution	288 × 126 × 252	128 × 144 × 252
Timestep	5×10^{-7}	10^{-6}

Table A.3 – Benchmark dynamo non stationnaire.
($\mathrm{E} = 5 \times 10^{-5}$, $N_\varrho = 3$, $\chi = 0.35$, $\mathrm{Ra} = 2.50 \times 10^7$, $\mathrm{Pr} = 2$, $\mathrm{Pm} = 2$, $n = 2$)

Code	PARODY	Leeds
K.E.	2.33×10^5	2.32×10^5
Zonal K.E.	1.38×10^4	1.36×10^4
Meridional K.E.	111	105
M.E.	2.41×10^5	2.42×10^5
Zonal M.E.	9.35×10^3	9.45×10^3
Meridional M.E.	2.10×10^4	2.13×10^4
Luminosity	42.4	42.5
Resolution	288 × 255 × 510	96 × 288 × 576
Timestep	5×10^{-7}	3×10^{-6}

Annexe B

Publications

B.1 *Intermittency in spherical Couette dynamos*

Raynaud, R. & Dormy, E., 2013, *Phys. Rev. E*, **87**, 033011.

Liens de téléchargement :
- journals.aps.org/pre/abstract/10.1103/PhysRevE.87.033011
- arxiv.org/abs/1304.6212
- hal.archives-ouvertes.fr/hal-01121376v1

PHYSICAL REVIEW E **87**, 033011 (2013)

Intermittency in spherical Couette dynamos

Raphaël Raynaud[1,2,*] and Emmanuel Dormy[1,3,†]
[1]*MAG (LRA), École Normale Supérieure, 24 rue Lhomond, 75252 Paris Cedex 05, France*
[2]*LERMA, CNRS UMR 8112, Paris, France*
[3]*IPGP, CNRS UMR 7154, Paris, France*

(Received 18 December 2012; revised manuscript received 22 February 2013; published 18 March 2013)

We investigate dynamo action in three-dimensional numerical simulations of turbulent spherical Couette flows. Close to the onset of dynamo action, the magnetic field exhibits an intermittent behavior, characterized by a series of short bursts of the magnetic energy separated by low-energy phases. We show that this behavior corresponds to the so-called on-off intermittency. This behavior is here reported for dynamo action with realistic boundary conditions. We investigate the role of magnetic boundary conditions in this phenomenon.

DOI: 10.1103/PhysRevE.87.033011 PACS number(s): 47.35.Tv, 47.65.−d, 47.27.E−

I. INTRODUCTION

First suggested by Joseph Larmor in 1919, dynamo action, i.e. the self-amplification of a magnetic field by the flow of an electrically conducting fluid, is considered to be the main mechanism for the generation of magnetic fields in the universe for a variety of systems, including planets, stars, and galaxies [1]. Dynamo action is an instability by which a conducting fluid transfers part of its kinetic energy to magnetic energy.

In experiments, it is rather difficult to achieve a regime of self-excited dynamo action. The low value of the magnetic Prandtl number of liquid metals requires the injection of a sufficiently high mechanical power, and thus generates turbulent flows, before reaching the dynamo threshold. Dynamo action was first observed experimentally only in 2001, in Karlsruhe [2] and Riga [3], and then in 2007 with a von Kármán swirling flow of liquid sodium [4].

In parallel with these approaches, numerical simulations have been carried out to model either laboratory experiments or astrophysical systems for which the spherical geometry is relevant. We investigate spherical Couette flow and focus on the characteristics of the magnetic field close to the dynamo onset. We observe a series of short bursts of the magnetic energy separated by low-energy phases. This intermittent behavior, also known as on-off intermittency or blowout bifurcation, is usually interpreted as the effect of a multiplicative noise acting on a bifurcating system [5,6].

On-off intermittency has so far never been observed in dynamo experiments, except in the case of an externally amplified magnetic field [7]. In contrast, it has been reported in a small number of numerical simulations [8–10], all relying on a flow in a periodic geometry produced by a periodic analytic forcing. Here we investigate the influence of a realistic choice of boundary conditions on this phenomenon.

II. GOVERNING EQUATIONS

The spherical Couette flow geometry consists of two concentric spheres in differential rotation: the outer sphere, of radius r_o, is rotating around the vertical axis $\mathbf{e}_z$ with an angular velocity Ω, and the solid inner sphere, of radius r_i, is rotating at velocity $\Omega + \Delta\Omega$ around an axis that can make an angle θ with $\mathbf{e}_z$. The aspect ratio $\chi = r_i/r_o$ is set to 0.35 to mimic that of Earth's liquid core. The spherical shell in between the two spheres is filled with an incompressible conducting fluid of kinematic viscosity ν, electrical conductivity σ, and density ρ. Its magnetic permeability μ_0 is that of a vacuum. The magnetic diffusivity η is defined as $\eta = 1/(\mu_0\sigma)$.

We describe the problem in the reference frame rotating with the outer sphere. This introduces two extra terms in the governing equations: the Coriolis force and the centrifugal acceleration. The latter can be rewritten in the form $\frac{1}{2}\boldsymbol{\nabla}(\Omega^2 s^2)$, where s denotes the distance to the axis of rotation. This term is a gradient and can be added to the pressure term which acts as a Lagrange multiplier to enforce the solenoidal condition on the velocity field. To establish the set of equations for this system, we rely on the same nondimensional form as in [11]: the velocity $\mathbf{u}$ is scaled by $r_i\Delta\Omega$, the magnetic field $\mathbf{B}$ by $\sqrt{\rho\mu_0 r_i r_o(\Omega+\Delta\Omega)\Delta\Omega}$, and the length scale by r_o. The Navier-Stokes equation governing the fluid velocity $\mathbf{u}$ then takes the form

$$\frac{\partial \mathbf{u}}{\partial t} + (\mathbf{u}\cdot\boldsymbol{\nabla})\mathbf{u} + \frac{2}{E\,\mathrm{Re}}(\mathbf{e}_z\times\mathbf{u}) = -\frac{1}{\mathrm{Re}}\boldsymbol{\nabla}\Pi + \frac{1}{\mathrm{Re}}\nabla^2\mathbf{u} + \frac{1}{\mathrm{Re}}\left(\frac{1}{E}+\frac{\mathrm{Re}}{\chi}\right)(\boldsymbol{\nabla}\times\mathbf{B})\times\mathbf{B}, \tag{1}$$

and the induction equation for the magnetic field $\mathbf{B}$,

$$\frac{\partial \mathbf{B}}{\partial t} = \boldsymbol{\nabla}\times(\mathbf{u}\times\mathbf{B}) + \frac{1}{\mathrm{Rm}}\nabla^2\mathbf{B}. \tag{2}$$

Both fields are solenoidal

$$\boldsymbol{\nabla}\cdot\mathbf{u} = 0, \quad \boldsymbol{\nabla}\cdot\mathbf{B} = 0. \tag{3}$$

The dimensionless parameters are the Ekman number $E = \nu/(\Omega r_o^2)$, the Reynolds number $\mathrm{Re} = (r_o r_i \Delta\Omega)/\nu$, the magnetic Prandtl number $P_m = \nu/\eta$, and the magnetic Reynolds number $\mathrm{Rm} = \mathrm{Re}P_m$. The potential Π includes all gradient terms (the pressure term as well as the centrifugal effect introduced above). The Reynolds number varies with the rotation rate of the inner sphere, while the Ekman number is inversely proportional to the rotation rate of the outer sphere. When the latter is at rest, the Ekman number tends toward

---

[*] raphael.raynaud@ens.fr
[†] dormy@phys.ens.fr

TABLE I. The three different configurations of magnetic boundary conditions used in this study.

	Inner sphere	Outer sphere
B.C.1	Conducting	Insulating
B.C.2	Insulating	Insulating
B.C.3	Ferromagnetic	Ferromagnetic

infinity and the Coriolis term in the Navier-Stokes equation vanishes. In our simulations, the Ekman number is set to 10^{-3}. This moderate value yields a moderate computing time.

We impose no slip boundary conditions for the velocity field on both spheres. Magnetic boundary conditions are of three types. The first one can only be applied to the inner sphere, as it implies a meshing of the bounding solid domain. The inner sphere can be a conductor with the same electric and magnetic properties as the fluid. In that case the magnetic diffusion equation is discretized and solved in the solid conductor (we refer to this set of boundary conditions as "conducting"). The outer sphere as well as the inner sphere can be electrical insulators. In that case the magnetic field is continuous across the boundary and matches a potential field, decaying away from the boundary. The spherical harmonic expansion allows an explicit and local expression for these boundary conditions (we refer to these boundary conditions as "insulating"). In addition, the use of high-magnetic-permeability boundary conditions may enhance dynamo action [12]. Therefore, we also used boundary conditions which enforce the magnetic field to be normal to the boundary. This is equivalent to assuming that the medium on the other side of the boundary has an infinitely larger permeability (we refer to these boundary conditions as "ferromagnetic"). The different configurations investigated in this study are summarized in Table I.

We integrated our system with PARODY [13], a parallel code which has been benchmarked against other international codes. The vector fields are transformed into scalars using the poloidal-toroidal decomposition. This expansion on a solenoidal basis enforces the constraints (3). The equations are then discretized in the radial direction with a finite-difference scheme on a stretched grid. On each concentric sphere, variables are expanded using a spherical harmonic basis (i.e., generalized Legendre polynomials in latitude and a Fourier basis in longitude). The coefficients of the expansion are identified with their degree l and order m. The simulations were performed using from 150 to 216 points in the radial direction, and the spherical harmonic decomposition is truncated at $(l_{\max},m_{\max}) = (70,20)$. We observe for both spectra a decrease of more than two orders of magnitude over the range of l and m. This provides an empirical validation of convergence. We checked on a few critical cases that the results are not affected when the resolution is increased to $l_{\max} = 100$.

Let us define the nondimensional kinetic and magnetic energy densities as

$$E_k = \frac{1}{V_s}\int_{V_s} \mathbf{u}^2 d\mathbf{x}, \tag{4}$$

$$E_b = \frac{1}{V_s}\frac{1}{\mathrm{Re}}\left(\frac{1}{E}+\frac{\mathrm{Re}}{\chi}\right)\int_{V_s} \mathbf{B}^2 d\mathbf{x}, \tag{5}$$

in which the unit of energy density is $\rho(r_i\,\Delta\Omega)^2$. In the above expressions, V_s refers to the volume of the spherical shell. In addition, we also investigate the symmetry of the flow and the symmetry of the magnetic field with respect to the equatorial plane. To that end, we define the contributions to the energy densities corresponding to the symmetric and antisymmetric components of the velocity (respectively, E_{kS} and E_{kA}) and magnetic field (respectively, E_{bS} and E_{bA}). The symmetric and antisymmetric contributions to the kinetic energy density, respectively, correspond to the flows

$$\mathbf{u}_S(x,y,z) = \tfrac{1}{2}[\mathbf{u}(x,y,z)+\mathbf{u}(x,y,-z)], \tag{6}$$

$$\mathbf{u}_A(x,y,z) = \tfrac{1}{2}[\mathbf{u}(x,y,z)-\mathbf{u}(x,y,-z)]. \tag{7}$$

In contrast, the symmetries are reversed for the magnetic field. This comes from the fact that the magnetic field is a pseudovector (i.e., the curl of a vector). Then,

$$\mathbf{B}_S(x,y,z) = \tfrac{1}{2}[\mathbf{B}(x,y,z)-\mathbf{B}(x,y,-z)], \tag{8}$$

$$\mathbf{B}_A(x,y,z) = \tfrac{1}{2}[\mathbf{B}(x,y,z)+\mathbf{B}(x,y,-z)]. \tag{9}$$

According to our definition, the dipolar component is symmetric.

III. DIRECT NUMERICAL SIMULATIONS

As shown by [11], contrarotation is more efficient than corotation for dynamo action. In order to introduce more control over the system, we let the angle θ between the axes of rotation of both spheres take any value in $[0,\pi]$. Contrary to our expectations, we do not significantly lower the dynamo threshold with the inclination of the rotation axis of the inner sphere. In fact, for $\theta = \pi/2$, the fluid is mainly in corotation with the outer sphere, and dragged only by a thin layer on the inner sphere, which is not sufficient to trigger dynamo action. In our parameter regime, the best configuration seems to remain $\theta = \pi$, when the two spheres are in contrarotation. We therefore keep this parameter fixed in the rest of the study.

A. Role of boundary conditions

Let us first investigate the dynamo transition in this setup at fixed magnetic Prandtl number $P_m = 0.2$, using the Reynolds number as the controlling parameter. With a conducting inner sphere and an insulating outer sphere, we find a critical magnetic Reynolds number $\mathrm{Rm_c} \in [291.0;292.0]$, which is in good agreement with [11]. Above the dynamo onset, the magnetic field displays an intermittent behavior characterized by series of short bursts of the magnetic energy separated by low-energy phases (see Fig. 1). When the distance to the threshold increases, bursts become more and more frequent and eventually intermittency disappears.

Changing the boundary conditions generally leads to different thresholds for dynamo action. Using ferromagnetic boundary conditions, we find a critical magnetic Reynolds number $\mathrm{Rm_c} \in [298.6;300.0]$. With insulating boundary conditions, the threshold becomes large and involves larger numerical

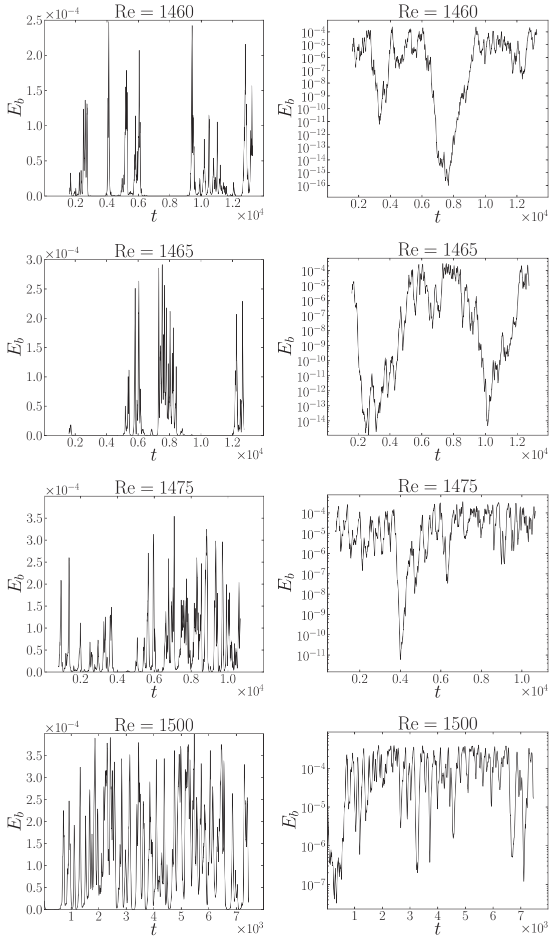

FIG. 1. Time evolution of the magnetic energy in linear (left) and log scale (right) for increasing Reynolds numbers at $P_m = 0.2$, using a conducting inner sphere (B.C.1 in Table I). At lower Reynolds numbers (top), we see in linear scale the characteristic intermittent bursting. Intermittency gradually disappears at higher Reynolds numbers and the field reaches saturation.

resolutions. In order to maintain the hydrodynamic Reynolds number at values which involve a moderate resolution, we therefore had to increase the magnetic Prandtl number from 0.2 to 0.4. We then obtain the dynamo onset for $\mathrm{Rm_c} \in [530.0; 534.8]$. We emphasize that we observe the same intermittent regime with all the above choices of boundary conditions as long as the magnetic Reynolds number is close enough to the onset of the instability.

For all boundary conditions, we observe that the dominant mode is predominantly of quadrupolar symmetry [the larger poloidal and toroidal modes are the $(l = 2, m = 0)$ and $(l = 1, m = 0)$ modes, respectively]. For these Reynolds numbers, the flow is predominantly equatorially symmetric ($E_{kA} \ll E_{kS}$).

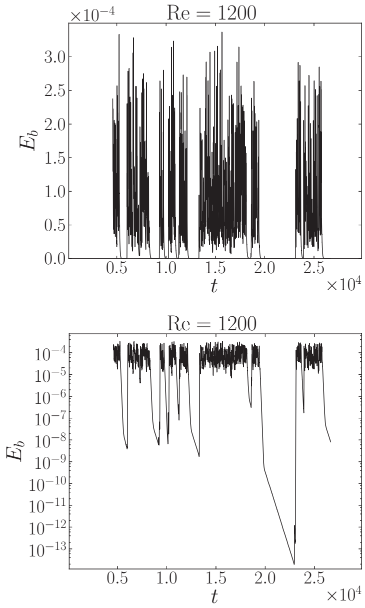

FIG. 2. Time evolution of the magnetic energy in linear and log scales for $P_m = 2$ and Re = 1200, using ferromagnetic boundary conditions. Instead of bursts, we now observe phases of dynamo activity which seem to randomly alternate with phases of exponential decay. The latter are no longer chaotic and are instead characterized by two different decay rates.

B. Increasing the magnetic Prandtl number

Having assessed that the intermittent behavior of the magnetic field near onset could be observed with three different sets of boundary conditions, we restrict here our attention to simulations with ferromagnetic boundary conditions. Figure 2 presents the results we obtain at $P_m = 2$. Close to the threshold, the magnetic field still exhibits intermittency, but the nature of the process has significantly changed. There is now a clear distinction between two different regimes: phases of dynamo activity separated by phases of pure exponential decay. Both seem to alternate randomly. When the dynamo is active, the magnetic field still displays a quadrupolar symmetry. In contrast, we observe the emergence of an axial dipole during decaying phases. The change of the global symmetry of the field coincides with the change of slope in the decaying phases [see Fig. 2 (bottom) and Fig. 3]. This change of slope is associated with a slower decay of the dipolar component over the quadrupolar mode.

IV. DISCUSSION

A. Canonical model for on-off intermittency

The simplest model that exhibits on-off intermittency is [14]

$$\dot{X} = [a + \zeta(t)]X - X^3, \qquad (10)$$

where a is the distance to the threshold, and ζ a Gaussian white noise of zero mean value and amplitude D, defined

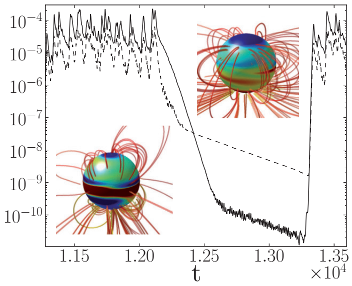

FIG. 3. (Color online) Time evolution of the symmetric (dashed line) and antisymmetric (solid line) part of the magnetic energy. We focus on one of the decaying phases presented in Fig. 2. The decaying phase is characterized by a change of the dominant symmetry, as we can see on the visualizations of the magnetic field lines. The color insets correspond to snapshots in the quadrupolar phase (left) and dipolar phase (right).

as $\langle\zeta(t)\zeta(t')\rangle = D\delta(t-t')$ where $\langle\rangle$ indicates the average over realizations (ensemble average). In the absence of noise, the system undergoes a supercritical pitchfork bifurcation at $a = 0$. If a is sufficiently small, the fluctuations lead to on-off intermittency, with bursts $(a + \zeta > 0)$ followed by decays $(a + \zeta < 0)$. During the off phases, one can neglect nonlinearities and write $\dot{Y} = a + \zeta(t)$, with $Y = \ln(X)$. Thus, $\ln(X)$ should follow a random walk, with a small positive bias. Since solutions of Eq. (10) mimic solutions of the magnetohydrodynamics equations we observe in Fig. 1, we further investigate some properties of the model. (i) Equation (10) leads to a stationary probability density function (PDF) of the form [15]

$$P(X) \propto X^{(2a/D)-1} e^{-X^2/D}, \tag{11}$$

which diverges at the origin for $0 \leqslant s = (2a/D) - 1 < 1$. (ii) In addition, all the moments of X must follow a linear scaling with a. (iii) Finally, another characteristic of this model is that the distribution of the duration of the off phases T_{off} follows a power-law behavior, $P(T_{\mathrm{off}}) \sim T_{\mathrm{off}}^{-\alpha}$, with $\alpha = -3/2$. To compare these predictions to our results, we rely as in [10] on the magnetic energy density as a global measure of the magnetic field strength.

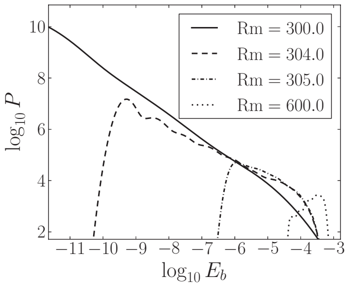

FIG. 4. Estimates of the probability density functions. Statistics are done from time series of the magnetic energy obtained with ferromagnetic boundary conditions, for $P_m = 0.2$.

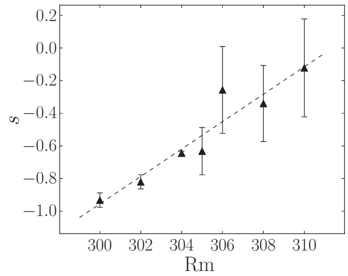

FIG. 5. Fit of the coefficient $s = (2a/D) - 1$, taking into account the linear domain of the PDFs in the intermittent regime only. Statistics are done from time series of the magnetic energy obtained with ferromagnetic boundary conditions, for $P_m = 0.2$.

B. Predictions and results

Figure 4 shows the PDFs of the magnetic energy for a set of simulations at different Reynolds numbers. At low Rm, the PDF is characterized by a linear scaling on a log-log plot. The cutoff at low energies is not predicted by the theory, which considers the limit $E_{\mathrm{b}} \to 0$. For Rm > 310, the magnetic energy fluctuates around a mean value and the PDF no longer scales as a power law. We see in Fig. 5 that the coefficient s is proportional to the distance to the threshold. Examples of the fit of the exponent s are presented in Fig. 6. The values of the coefficient are mainly affected by the range over which the data are fitted. Thus we select a range as large as possible. We then randomly sample this range with half-size subintervals. We then compute the mean slope and its standard deviation (represented in Fig. 5 with error bars).

We then investigate the linearity of the moments. Figure 7 shows our results for the first and second moments of the magnetic energy. We see that the mean magnetic energy grows linearly as a function of the magnetic Reynolds number. The second moments seem to follow the same linear trend, but only at the lower values of the magnetic Reynolds number. Deviations at larger values of Rm are expected, as this description is only valid in the limit $\mathrm{Rm} \to \mathrm{Rm}_{\mathrm{c}}$. The duration t_I of the time series used to compute these values ranges from 3.2×10^3 to 1.4×10^4 U.T. (values are presented in

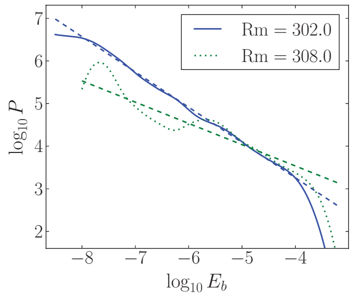

FIG. 6. (Color online) Examples of the fit (dashed lines) of the probability density functions (solid and dotted lines). Statistics are done from time series of the magnetic energy obtained with ferromagnetic boundary conditions, for $P_m = 0.2$.

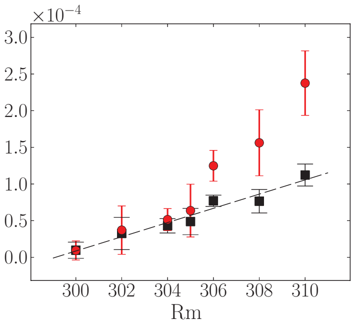

FIG. 7. (Color online) Moments of the magnetic energy as function of the magnetic Reynolds number. Black squares represent the mean. The dashed line fits these data points with an error about 10% on the slope coefficient. The second moments (red circles) have been rescaled to match with the mean at Rm = 300.

Table II). These integration times are quite significant for a fully three-dimensional set of partial differential equations but are necessarily short compared to the ones usually used with simplified models such as Eq. (10). To quantify the uncertainty associated with the moment values, we sampled the integration time with subintervals randomly chosen. We then computed the moments on the full interval (symbols in Fig. 7) and the standard deviation on the subintervals (reported as error bars). The subintervals can be set from $t_I/4$ to $t_I/10$ without affecting these estimates.

Finally, we also tested the distribution of the duration time of the off phases. A definitive validation would require longer simulations in order to have a significant number of off phases. For this reason, we cannot rely on the simulations immediately above the threshold. Despite these shortcomings, an illustrative case is presented in Fig. 8. Numerical values are given in Table III.

To conclude, we emphasize that the predictions of the model are consistent with the three-dimensional simulations and thus confirm the on-off hypothesis for the observed intermittency at low magnetic Prandtl number.

C. Simulations at higher magnetic Prandtl number

The simulations we performed at $P_m = 2$ exhibit a peculiar behavior of the magnetic field. This can be better understood by examining the dynamics of the flow. Indeed, we also carried out purely hydrodynamic simulations at Re = 1200 and observed intermittent transitions between two states. This kind of intermittent behavior of the flow was not reported in [11], but has been observed experimentally [16]. One state is characterized by larger fluctuations of the energy as we can see in Fig. 9. In addition, the analysis of the energy spectra reveals that the $m = 3$ modes dominate over the $m = 2$ modes during the "laminar" phases, whereas both are of the same order during the "turbulent" phases. Duration of the turbulent phases tends to increase gradually with the increase of the Reynolds number, so that the intermittent behavior of the flow eventually disappears and is thus no longer present in the simulations at higher Reynolds number in which we have identified on-off intermittency.

TABLE II. Duration of the time series used to compute the moments of the magnetic energy. The integration time t_I is presented in units of $(\chi\,\Delta\Omega)^{-1}$ (t_I) and in units of the magnetic diffusion time r_o^2/η (t_I/Rm).

Rm	t_I	t_I/Rm
300	1.40×10^4	46.7
302	9.06×10^3	30.0
304	9.05×10^3	29.8
305	3.33×10^3	10.9
306	7.58×10^3	24.8
308	3.20×10^3	10.4
310	5.46×10^3	17.6

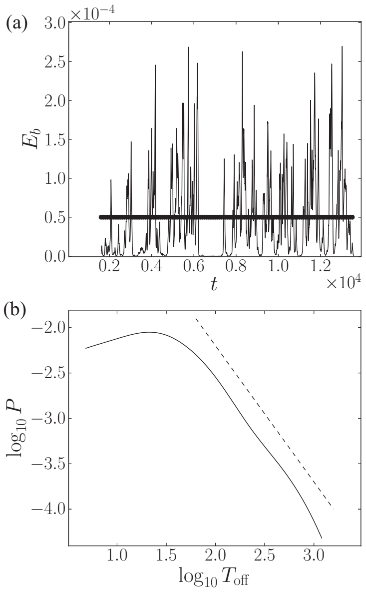

FIG. 8. Distribution of the duration of the off phases for a simulation performed at $P_m = 0.2$ and Re = 1470, with conducting boundary conditions. We define an off phase by a magnetic energy below a threshold value (indicated here by the horizontal black line). The PDF (b) decay is close to a power law with the expected $-3/2$ value for the exponent (dashed line).

TABLE III. Estimate of the exponent α of the PDF of the duration of the off phases for different threshold values and different ranges over which the fit is done. The standard error on the estimate of α is about 1%. Range values correspond to $\log_{10} T_{\rm off}$ [x axis in Fig. 8(b)].

Threshold Range	[1.7; 3]	[2.0; 3]	[2.1; 3]
1.1×10^{-4}	−1.30	−1.48	−1.51
1.0×10^{-4}	−1.35	−1.48	−1.50
7.5×10^{-5}	−1.40	−1.41	−1.40
5.0×10^{-5}	−1.48	−1.52	−1.51
3.5×10^{-5}	−1.51	−1.60	−1.65

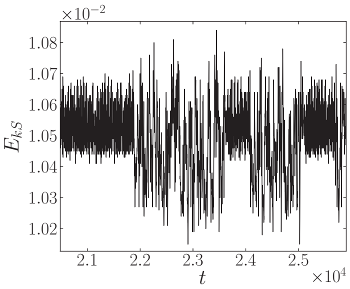

FIG. 9. Time evolution of the symmetric part of the kinetic energy E_{kS} at Re = 1200 in a purely hydrodynamic simulation. Intermittent transitions between laminar and more turbulent phases are clearly visible.

Dynamo action is inhibited during the laminar phases (when the $m = 3$ modes dominate), which highlights the mechanism which leads to the peculiar behavior of the magnetic field, as we can see in Fig. 10. In contrast, turbulent phases favor dynamo action, and one must wait a change in the flow to see the restart of dynamo action after a phase of decay. Moreover, in a full magnetohydrodynamics simulation, we can artificially suppress the $m = 3$ modes of the velocity field by setting them equal to zero at each time step. We check that it is sufficient to suppress intermittency of the flow. Then we observe that the phases of exponential decay are also suppressed and the dynamo is no longer intermittent.

V. CONCLUSION

Despite the fact that on-off intermittency has so far never been observed in dynamo experiments, we showed that the phenomenon can appear in numerical simulations of dynamo action using realistic boundary conditions. We identified in several cases the predicted behavior of the PDF of the magnetic energy, linear scaling of the moments, and distribution of the duration of the off phases. In addition, we tested these properties for three different boundary conditions (conducting inner core with insulating outer sphere, insulating or ferromagnetic spheres). Finally, we pointed out a different kind of intermittency due to hydrodynamic transitions that appears at lower Reynolds numbers.

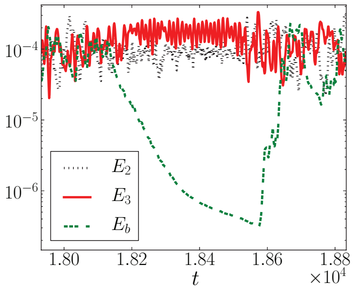

FIG. 10. (Color online) Time evolution at Re = 1200 and $P_m = 2$ of the total magnetic energy E_b (dashed green line) and the kinetic energies E_2 (dotted black line) and E_3 (solid red line) for the $m = 2$ and $m = 3$ modes, respectively. When the latter becomes larger than the former, the dynamo is no longer sustained and the magnetic energy exponentially decays.

To explain the absence of on-off intermittency in experiments, several reasons have already been invoked [17]. One explanation could be the imperfectness of the bifurcation (due for instance to Earth's ambient magnetic field). Since it has been shown that low-frequency noise controls on-off intermittency [14], another possible explanation could be that the low-frequency fluctuations are too small. However, the lack of experimental observations of on-off intermittency remains an open question and needs further investigation.

ACKNOWLEDGMENTS

The numerical simulations were carried out at CEMAG, CINES, and MESOPSL. We thank S. Fauve, F. Pétrélis, and M. Schrinner for fruitful discussions and comments. We are most grateful to C. Gissinger for technical assistance.

[1] *Mathematical Aspects of Natural Dynamos*, edited by E. Dormy and A. M. Soward (CRC, Boca Raton, FL, 2007).
[2] R. Stieglitz and U. Müller, Phys. Fluids **13**, 561 (2001).
[3] A. Gailitis, O. Lielausis, E. Platacis, S. Dement'ev, A. Cifersons, G. Gerbeth, T. Gundrum, F. Stefani, M. Christen, and G. Will, Phys. Rev. Lett. **86**, 3024 (2001).
[4] R. Monchaux, M. Berhanu, M. Bourgoin, M. Moulin, P. Odier, J.-F. Pinton, R. Volk, S. Fauve, N. Mordant, F. Pétrélis, A. Chiffaudel, F. Daviaud, B. Dubrulle, C. Gasquet, L. Marié, and F. Ravelet, Phys. Rev. Lett. **98**, 044502 (2007).
[5] H. Fujisaka and T. Yamada, Prog. Theor. Phys. **75**, 1087 (1986).
[6] N. Platt, E. A. Spiegel, and C. Tresser, Phys. Rev. Lett. **70**, 279 (1993).
[7] G. Verhille, N. Plihon, G. Fanjat, R. Volk, M. Bourgoin, and J.-F. Pinton, Geophys. Astrophys. Fluid Dyn. **104**, 189 (2010).
[8] D. Sweet, E. Ott, J. M. Finn, T. M. Antonsen, and D. P. Lathrop, Phys. Rev. E **63**, 066211 (2001).
[9] N. Leprovost, B. Dubrulle, and F. Plunian, Magnetohydrodynamics **42**, 131 (2006).
[10] A. Alexakis and Y. Ponty, Phys. Rev. E **77**, 056308 (2008).
[11] C. Guervilly and P. Cardin, Geophys. Astrophys. Fluid Dyn. **104**, 221 (2010).
[12] C. Gissinger, A. Iskakov, S. Fauve, and E. Dormy, Europhys. Lett. **82**, 29001 (2008).
[13] E. Dormy, P. Cardin, and D. Jault, Earth Planet. Sci. Lett. **160**, 15 (1998).
[14] S. Aumaître, F. Pétrélis, and K. Mallick, Phys. Rev. Lett. **95**, 064101 (2005).
[15] R. L. Stratonovitch, *Topics in the Theory of Random Noise* (Gordon and Breach, New York, 1963).
[16] D. S. Zimmerman, S. A. Triana, and D. P. Lathrop, Phys. Fluids **23**, 065104 (2011).
[17] F. Pétrélis, N. Mordant, and S. Fauve, Geophys. Astrophys. Fluid Dyn. **101**, 289 (2007).

B.2 *Topology and field strength in spherical, anelastic dynamo simulations*

Schrinner, M., Petitdemange, L., Raynaud, R. & Dormy, E., 2014, *Astronomy and Astrophysics*, **564**, A78.

Liens de téléchargement :
- www.aanda.org/articles/aa/abs/2014/04/aa22801-13/aa22801-13.html
- arxiv.org/abs/1312.7364
- hal.archives-ouvertes.fr/hal-01122251v1

A&A 564, A78 (2014)
DOI: 10.1051/0004-6361/201322801
© ESO 2014

Astronomy & Astrophysics

Topology and field strength in spherical, anelastic dynamo simulations[⋆]

M. Schrinner[⋆⋆], L. Petitdemange, R. Raynaud, and E. Dormy

MAG (ENS/IPGP), LRA/LERMA, Département de Physique, École Normale Supérieure, 24 rue Lhomond, 75252 Paris Cedex 5, France
e-mail: `martin@schrinner.eu`

Received 4 October 2013 / Accepted 30 December 2013

ABSTRACT

Context. Numerical modelling of convection driven dynamos in the Boussinesq approximation revealed fundamental characteristics of the dynamo-generated magnetic fields and the fluid flow. Because these results were obtained for an incompressible fluid of constant density, their validity for gas planets and stars remains to be assessed. A common approach is to take some density stratification into account with the so-called anelastic approximation.

Aims. The validity of previous results obtained in the Boussinesq approximation is tested for anelastic models. We point out and explain specific differences between both types of models, in particular, with respect to the field geometry and the field strength, but we also compare scaling laws for the velocity amplitude, the magnetic dissipation time, and the convective heat flux.

Methods. Our investigation is based on a systematic parameter study of spherical dynamo models in the anelastic approximation. We make use of a recently developed numerical solver and provide results for the test cases of the anelastic dynamo benchmark.

Results. The dichotomy of dipolar and multipolar dynamos identified in Boussinesq simulations is also present in our sample of anelastic models. Dipolar models require that the typical length scale of convection is an order of magnitude larger than the Rossby radius. However, the distinction between both classes of models is somewhat less explicit than in previous studies. This is mainly due to two reasons: we found a number of models with a considerable equatorial dipole contribution and an intermediate overall dipole field strength. Furthermore, a large density stratification may hamper the generation of dipole dominated magnetic fields. Previously proposed scaling laws, such as those for the field strength, are similarly applicable to anelastic models. It is not clear, however, if this consistency necessarily implies similar dynamo processes in both settings.

Key words. convection – magnetohydrodynamics (MHD) – dynamo – methods: numerical – stars: magnetic field

1. Introduction

Magnetic fields of low-mass stars and planets are maintained by currents resulting from the motion of a conducting fluid (or gas) in their interiors. Because the magnetic field acts back on the flow via the Lorentz force, the hydrodynamic dynamo problem is intrinsically non-linear. Moreover, a sufficiently complex flow and magnetic field geometry has to be assumed in order to enable dynamo action. Further complications result from tiny diffusivities, such as small kinematic viscosities, which introduce small dynamic length scales compared to stellar or planetary radii. Thus, self-consistent simulations of natural dynamos are not only three-dimensional, but a vast range of spatial and temporal scales has to be resolved. These difficulties prevented a direct numerical treatment of the dynamo problem for a significant time. Only for the past 20 years, increasing computer power made global, direct numerical simulations feasible, in particular for the geodynamo problem (e.g., Glatzmaier & Roberts 1995; Kageyama & Sato 1997; Kuang & Bloxham 1997; Christensen et al. 1998; Sarson et al. 1998; Katayama et al. 1999; Buffett 2000; Dormy et al. 2000); for an early cylindrical annulus model of the geodynamo see Busse (1975). In these simulations, an incompressible conducting fluid was considered, and the Boussinesq approximation was applied. Intensive and systematic parameter studies revealed fundamental properties of these models related to their field and flow topologies, their field strength, their velocity amplitudes, their advective heat transport, or their time dependence (e.g. Christensen et al. 1999; Grote et al. 2000; Kutzner & Christensen 2002; Busse & Simitev 2006; Christensen & Aubert 2006; Sreenivasan & Jones 2006; Busse & Simitev 2010; Hori et al. 2010; Landeau & Aubert 2011; Schrinner et al. 2012; Yadav et al. 2013a). The simplifying assumption of constant density in Boussinesq models, however, is probably not justified for gas planets or stars, in which the density typically varies over many scale heights. An alternative approach, which takes compressibility into account, is the so-called anelastic approximation (Ogura & Phillips 1962; Gough 1969; Gilman & Glatzmaier 1981). In anelastic models, the density varies with radius, but its time derivative is neglected in the continuity equation and the mass flux is solenoidal (e.g., Glatzmaier 1984; Braginsky & Roberts 1995; Lantz & Fan 1999; Miesch et al. 2000; Brun et al. 2004; Browning et al. 2004). Consequently, fast travelling sound waves are filtered out and, compared to fully compressible models, larger time steps in the discretisation scheme may be reached. In this article, we carry out a systematic parameter study of global dynamo simulations in the anelastic approximation guided by well known results of Boussinesq models. In this way, we intend to point out specific differences between anelastic and Boussinesq models and assess the validity of previous findings obtained in the Boussinesq approximation. A similar approach was followed by Gastine et al. (2012) and Yadav et al. (2013b). We compare our

---

[⋆] Appendices B and C are available in electronic form at http://www.aanda.org

[⋆⋆] *Present address:* Universität Göttingen, Institut für Astrophysik, Friedrich-Hundt-Platz 1, 37077 Göttingen, Germany results with their findings and discuss some differences we obtained for our varied sample of models. The conditions for the generation of large-scale, dipolar fields (Sect. 3) and the test of the flux-based scaling law for the magnetic field strength (Sect. 4), originally proposed by Christensen & Aubert (2006) for Boussinesq models, are revisited . We argue that the typical length scale of convection relative to the Rossby radius is of crucial importance for the resulting field topology (see also Schrinner et al. 2012) and show that larger magnetic Prandtl numbers are required to obtain dipolar solutions with increasing density contrast. Furthermore, the flux-based scaling laws derived for Boussinesq models seem to hold in the anelastic approximation as well. However, because of their general validity, the flux-based scaling laws might not be appropriate to distinguish between different conditions for magnetic field generation.

The paper is organised as follows: Sect. 2 introduces the anelastic models considered here and the recently developed numerical solver; results for a numerical benchmark are given in Appendix A. In Sect. 3, we present new evidence of the existence of a class of dynamos dominated by an axial dipole and a class of models with a more variable magnetic field geometry. Various scaling laws originally derived for Boussinesq models are tested and discussed in Sect. 4, and we give some conclusions in Sect. 5.

2. Dynamo calculations

2.1. The anelastic approximation

Convection of a gas or a compressible fluid in the interior of planets and stars takes place on a vast range of spatial and temporal scales. Sound waves excited in convection zones, for example, have very short oscillation periods compared to the turnover time of convection or the magnetic diffusion time relevant for the generation of magnetic fields. Thus, extremely small timesteps would be required to resolve these waves in numerical dynamo models. To avoid this problem, simplifications of the governing equations are often applied. The anelastic approximation used in this study advantageously filters out sound waves (Ogura & Phillips 1962; Gough 1969; Gilman & Glatzmaier 1981); it is motivated by the idea that the superadiabatic temperature gradient driving convection in planetary or stellar convection zones is tiny. The thermodynamic variables are then decomposed into the sum of (close to adiabatic) reference values, denoted here by an overbar, and perturbations, denoted by a prime,

$$\varrho = \overline{\varrho} + \varrho', \quad T = \overline{T} + T', \quad P = \overline{P} + P'. \tag{1}$$

Subsequently, the anelastic equations result from the "thermodynamic linearization" around the reference state. It should be stressed that a number of different formulations of the anelastic problem can be found in the literature (e.g., Glatzmaier 1984; Braginsky & Roberts 1995; Lantz & Fan 1999; Miesch et al. 2000; Brun et al. 2004; Rogers & Glatzmaier 2005; Jones & Kuzanyan 2009; Alboussière & Ricard 2013). We follow here the approach introduced by Lantz & Fan (1999) and Braginsky & Roberts (1995), also known as LBR-approximation. They noticed that the only relevant thermodynamic variable in the equation of motion is the entropy, if the reference state is assumed to be close to adiabatic. Further advantages of the LBR-equations over others are that they give a mathematically consistent, asymptotic limit of the full, general equations (Jones et al. 2011) and guarantee the conservation of energy (Brown et al. 2012). Moreover, the LBR-equations were used to formulate anelastic dynamo benchmarks (Jones et al. 2011). The presentation of the equations given here follows the benchmark paper and Jones et al. (2009).

2.2. Basic assumptions

We consider a perfect, electrically conducting gas in a rotating spherical shell with an inner boundary at $r = r_{\rm i}$ and an outer boundary at $r = r_{\rm o}$. The aspect ratio of the shell is then defined by $\chi = r_{\rm i}/r_{\rm o}$. Convection in our simulations is driven by an imposed entropy difference, Δs, between the inner and the outer boundary. As discussed above, Δs is assumed to be small. This implies small convective velocities compared to the speed of sound. For consistency, we also require that the Alfvén velocity of the magnetic field is small. Moreover, the kinematic viscosity ν, the thermal diffusivity κ, and the magnetic diffusivity η are constants throughout in this paper. Following Jones et al. (2011), we represent the heat flux in our models in terms of the entropy gradient instead of the temperature gradient. This assumption relies on wide-spread ideas about turbulent mixing (Braginsky & Roberts 1995) but does not follow from first principles. Applying this simplification allows us to consider the entropy as the only relevant thermodynamic variable in the formulation of the anelastic problem.

2.3. The reference state

The reference state of our models is a solution of the hydrostatic equations for an adiabatic atmosphere. Moreover, the centrifugal acceleration is neglected and we assume that gravity varies radially, $\boldsymbol{g} = -GM\hat{\boldsymbol{r}}/r^2$, with G being the gravitational constant and M the central mass of the star or the planet. This admits a polytropic solution for the reference atmosphere,

$$\overline{P} = P_{\rm c}\, w^{n+1}, \quad \overline{\varrho} = \varrho_{\rm c}\, w^{n}, \quad \overline{T} = T_{\rm c}\, w, \quad w = c_0 + \frac{c_1 d}{r}, \tag{2}$$

with the polytropic index n and $d = r_{\rm o} - r_{\rm i}$. We note that n defines the value of the adiabatic exponent γ, or the ratio of specific heats c_p/c_v via $\gamma = (n+1)/n$. The values $P_{\rm c}$, $\varrho_{\rm c}$, and $T_{\rm c}$ are taken midway between the inner and the outer boundary and serve as units for the reference-state variables. Moreover, the constants c_0 and c_1 in (2) are defined as

$$c_0 = \frac{2w_0 - \chi - 1}{1 - \chi}, \quad c_1 = \frac{(1+\chi)(1 - w_{\rm o})}{(1-\chi)^2}, \tag{3}$$

with

$$w_0 = \frac{\chi + 1}{\chi \exp(N_\varrho/n) + 1}, \quad w_{\rm i} = \frac{1 + \chi - w_{\rm o}}{\chi}, \tag{4}$$

and $N_\varrho = \ln(\varrho_{\rm i}/\varrho_{\rm o})$, where $\varrho_{\rm i}$ and $\varrho_{\rm o}$ denote the reference state density at the inner and outer boundary, respectively. We emphasise again that convection in our models is not driven by the reference state, or by the choice of a particular polytropic index n, but by an imposed entropy difference Δs between the boundaries.

2.4. The non-dimensional equations

The use of non-dimensional equations minimizes the number of free parameters and is a prerequisite for a systematic parameter study. We choose the shell width d as the fundamental length scale of our models, time is measured in units of d^2/η, and Δs is the unit of entropy. The magnetic field is then measured in units of $\sqrt{\Omega \varrho_{\rm c} \mu \eta}$, where Ω is the rotation rate and μ the magnetic permeability. Finally, our dynamo models are solutions for the velocity $\boldsymbol{v}$, the magnetic field $\boldsymbol{B}$, and the entropy s of the following, non-dimensional equations,

$$\begin{aligned}\frac{\partial \boldsymbol{v}}{\partial t}+\boldsymbol{v}\cdot\nabla\boldsymbol{v} &= Pm\left[-\frac{1}{E}\nabla\frac{P'}{w^n}+\frac{\mathrm{Pm}}{Pr}Ra\frac{s}{r^2}\hat{\boldsymbol{r}}-\frac{2}{E}\hat{\boldsymbol{z}}\times\boldsymbol{v}\right.\\ &\qquad\left.+\boldsymbol{F}_\nu+\frac{1}{E\,w^n}(\nabla\times\boldsymbol{B})\times\boldsymbol{B}\right], &(5)\\ \frac{\partial\boldsymbol{B}}{\partial t} &= \nabla\times(\boldsymbol{v}\times\boldsymbol{B})+\nabla^2\boldsymbol{B}, &(6)\\ \frac{\partial s}{\partial t}+\boldsymbol{v}\cdot\nabla s &= w^{-n-1}\frac{\mathrm{Pm}}{Pr}\nabla\cdot\left(w^{n+1}\,\nabla s\right)\\ &\qquad+\frac{Di}{w}\left[E^{-1}w^{-n}(\nabla\times\boldsymbol{B})^2+Q_\nu\right], &(7)\\ \nabla\cdot(w^n\boldsymbol{v}) &= 0, &(8)\\ \nabla\cdot\boldsymbol{B} &= 0. &(9)\end{aligned}$$

In (5), we used the viscous force $\boldsymbol{F}_\nu = w^{-n}\nabla\boldsymbol{S}$ with the rate of strain tensor

$$S_{ij} = 2w^n\left(e_{ij}-\frac{1}{3}\delta_{ij}\nabla\cdot\boldsymbol{v}\right),\quad e_{ij}=\frac{1}{2}\left(\frac{\partial v_i}{\partial x_j}+\frac{\partial v_j}{\partial x_i}\right). \tag{10}$$

Moreover, the dissipation parameter Di and the viscous heating Q_ν in (7) are given by

$$Di = \frac{c_1 Pr}{\mathrm{Pm}Ra}, \tag{11}$$

and

$$Q_\nu = 2\left[e_{ij}e_{ij}-\frac{1}{3}(\nabla\cdot\boldsymbol{v})^2\right]. \tag{12}$$

The system of Eqs. (5)–(9) is governed by a number of dimensionless parameters. These are the Rayleigh number Ra, the Ekman number E, the Prandtl number Pr, and the magnetic Prandtl number Pm. With the aspect ratio χ, the polytropic index n, and the number of density scale heights N_ϱ defining the reference state, our models are therefore fully determined by seven dimensionless parameters:

$$\begin{aligned} Ra &= \frac{GMd\Delta s}{\nu\kappa c_p},\quad Pr=\frac{\nu}{\kappa},\quad \mathrm{Pm}=\frac{\nu}{\eta},\quad E=\frac{\nu}{\Omega d^2},\\ N_\varrho &= \ln\left(\frac{\varrho_i}{\varrho_o}\right),\quad n,\quad \chi=\frac{r_i}{r_o}. &(13)\end{aligned}$$

Following Jones et al. (2009), we also considered a linearized form of Eqs. (5) and (7) to calculate some critical Rayleigh numbers for the onset of convection. These are listed in Table B.1.

2.5. Boundary conditions

The mechanical boundary conditions are impenetrable and stress free on both boundaries,

$$v_r = \frac{\partial}{\partial r}\left(\frac{v_\theta}{r}\right)=\frac{\partial}{\partial r}\left(\frac{v_\phi}{r}\right)=0 \qquad \text{on} \quad r=r_i \quad \text{and} \quad r=r_o. \tag{14}$$

Furthermore, the magnetic field matches a potential field outside the fluid shell. The choice of these boundary conditions requires that the total angular momentum is conserved (Jones et al. 2011). Finally, the entropy is fixed on the inner and the outer boundary with

$$s=\Delta s \qquad \text{on} \quad r=r_i \quad \text{and} \quad s=0 \qquad \text{on} \quad r=r_o. \tag{15}$$

2.6. Output parameters

We use a number of non-dimensional output parameters to characterize our numerical dynamo models. These are mostly based on the kinetic and magnetic energy densities,

$$E_k = \frac{1}{2\,V}\int_V w^n\boldsymbol{v}^2\,\mathrm{d}v \;\text{ and }\quad E_m=\frac{1}{2\,V}\frac{\mathrm{Pm}}{E}\int_V\boldsymbol{B}^2\,\mathrm{d}v, \tag{16}$$

where the integrals are taken over the volume of the fluid shell V. A non-dimensional measure for the velocity amplitude is then the magnetic Reynolds number, $Rm = \sqrt{2E_k}$, or the Rossby number, $Ro = \sqrt{2E_k}E/\mathrm{Pm}$. To distinguish models with different field geometries, it turned out to be useful to introduce also a local Rossby number, $Ro_\ell = Ro_c\,\ell_c/\pi$. Here, ℓ_c stands for the mean harmonic degree of the velocity component $\boldsymbol{v}_c$ from which the mean zonal flow has been subtracted (Schrinner et al. 2012),

$$\ell_c = \sum_\ell \ell\frac{\langle w^n\,(\boldsymbol{v}_c)_\ell\cdot(\boldsymbol{v}_c)_\ell\rangle}{\langle w^n\,\boldsymbol{v}_c\cdot\boldsymbol{v}_c\rangle}. \tag{17}$$

The brackets in (17) denote an average over time and radii. Also, Ro_c is adapted consistently and stands for the Rossby number based on the kinetic energy density without the contribution from the mean zonal flow. The definition of Ro_ℓ given here is different from Christensen & Aubert (2006), as it is not based on the total velocity and tries to avoid any dependence on the mean zonal flow.

The amplitude of the average magnetic field in our simulations is measured in terms of the Lorentz number, $Lo = \sqrt{2E_m}E/P\mathrm{m}$, which was previously used to derive a power law for the field strength in Boussinesq simulations (Christensen & Aubert 2006). The topology of the field is characterized by the relative dipole field strength, f_{dip}, defined as the time-average ratio on the outer shell boundary of the dipole field strength to the total field strength.

The total amount of heat transported in and out of the fluid shell relative to the conductive heat flux is quantified by the Nusselt number,

$$\begin{aligned} Nu_{\mathrm{bot}} &= -\frac{(\exp(N_\varrho)-1)w_i r_i^2}{4\pi n c_1}\int_{S_i}\frac{\partial s}{\partial r}\sin\theta\,\mathrm{d}\theta\mathrm{d}\phi, &(18)\\ Nu_{\mathrm{top}} &= -\frac{(1-\exp(-N_\varrho))w_o r_o^2}{4\pi n c_1}\int_{S_o}\frac{\partial s}{\partial r}\sin\theta\,\mathrm{d}\theta\mathrm{d}\phi. &(19)\end{aligned}$$

The integrals are taken here over the spherical surface at radius r_i and radius r_o, respectively. For a steady equilibrium state, Nu_{bot} and Nu_{top} are identical if time averaged. For later use, we also define a Nusselt number based on the advective heat flux alone,

$$Nu^\star = (Nu_{\mathrm{bot}}-1)\frac{E}{Pr}, \tag{20}$$

and accordingly a quantity usually referred as the flux based Rayleigh number,

$$Ra_Q = (Nu_{\mathrm{bot}}-1)\,\frac{Ra\,E^3}{r_o^2\,Pr^2}. \tag{21}$$

The energy balance plays a crucial role in the classical derivation of scaling laws for the saturation level of the magnetic field. In particular, the fraction of ohmic to total dissipation, $f_{\mathrm{ohm}} = D/P$, is introduced because it determines the available power used for the magnetic field generation. In an equilibrium state, the total dissipation equals the power released by buoyancy,

$$P = \frac{Ra\,E^3}{Pr\,Pm}\int_V w^n\,v_r\,s\,\mathrm{d}v, \tag{22}$$

and the ohmic dissipation is given by

$$D = \left(\frac{E}{Pm}\right)^2 \int_V (\nabla \times \boldsymbol{B})^2 \, dv. \qquad (23)$$

In (22) and (23), we scaled P and D by $\varrho_c \Omega^3 d^5$.

2.7. Equation for a tracer field

For some of our models, we calculated the evolution of a magnetic tracer field simultaneously with (5)−(9),

$$\frac{\partial \boldsymbol{B}_{\mathrm{Tr}}}{\partial t} = \nabla \times (\boldsymbol{v} \times \boldsymbol{B}_{\mathrm{Tr}}) + \nabla^2 \boldsymbol{B}_{\mathrm{Tr}}. \qquad (24)$$

In the above equation, $\boldsymbol{B}_{\mathrm{Tr}}$ is a passive vector field, which was advanced at each time step kinematically with the quenched velocity field, but $\boldsymbol{B}_{\mathrm{Tr}}$ did not contribute to the Lorentz force (Cattaneo & Tobias 2009; Tilgner & Brandenburg 2008; Schrinner et al. 2010). Schrinner et al. (2010) found that $\boldsymbol{B}_{\mathrm{Tr}}$ grows exponentially for multipolar dynamos but stays stable for models dominated by a dipole field. The stability of $\boldsymbol{B}_{\mathrm{Tr}}$ also serves in this study to distinguish between different classes of dynamos (Schrinner et al. 2012).

2.8. Numerical implementation

The numerical solver used to compute solutions of Eqs. (5)−(9) is a recently developed anelastic version of PaRoDy (Dormy et al. 1998 and further developments). The code uses a poloidal-toroidal expansion and a pseudo-spectral spherical harmonic expansion. The numerical method is similar in these aspects to the one originally introduced in Glatzmaier (1984). The radial discretisation, however, is based on finite differences on a stretched grid (allowing for a parallelization by a radial domain decomposition). Moreover, the pressure term has been eliminated by taking twice the curl of the momentum equation. The anelastic benchmark results obtained with PaRoDy are presented in Appendix A.

3. Field topology

3.1. Dipolar and multipolar dynamos

Parameter studies for Boussinesq simulations revealed two distinct classes of dynamo models. They can be distinguished by their field geometry and are therefore referred to as "dipolar" and "multipolar" models (Kutzner & Christensen 2002; Christensen & Aubert 2006). The spatial variability of multipolar dynamos is a direct consequence of dynamo action in a turbulent environment and has to be expected. The class of dipolar dynamos, however, is more peculiar. Schrinner et al. (2011b) showed that these models are single-mode dynamos, that is, except for the fundamental mode, all more structured magnetic eigenmodes are highly damped. The single-mode property leads to further characteristic differences between both classes of dynamos apart from their different field geometries. Whereas the dipole axis is stable for models with a dominant axial dipole field, multipolar models show frequent polarity reversals (Kutzner & Christensen 2002) or oscillations (Goudard & Dormy 2008; Schrinner et al. 2012). A third fundamental difference between dipolar and multipolar models is related to their saturation mechanism. If a magnetic tracer field is advanced kinematically with the self-consistent, quenched velocity field stemming from the full dynamo simulation, the tracer field grows exponentially for multipolar but not for dipolar models. Dipolar dynamos are "kinematically stable" and in this numerical experiment, the tracer field becomes aligned with the actual, self-consistent magnetic field after some initial transition period (Schrinner et al. 2010). Finally, dipolar and multipolar dynamos follow slightly different scaling laws for the magnetic field (Christensen 2010; Schrinner et al. 2012; Yadav et al. 2013a). This aspect is further discussed in Sect. 4.1.

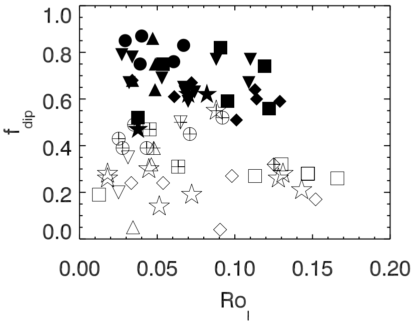

Fig. 1. Relative dipole field-strength versus the local Rossby number for our sample of models. Filled symbols stand for dipolar, open symbols for multipolar dynamos. The symbol shape indicates the number of density scale heights: $N_\varrho = 0.5$: circle; $N_\varrho = 1$: upward triangle; $N_\varrho = 1.5$: downward triangle; $N_\varrho = 2$: diamond; $N_\varrho = 2.5$: square; $N_\varrho = 3, 3.5, 4$: star. A cross inscribed in some open symbols means that the field of these models exhibits a strong equatorial dipole component.

Christensen & Aubert (2006) proposed a criterion based on a local Rossby number to separate dipolar from multipolar dynamos. We adopt this criterion in a slightly altered form (Schrinner et al. 2012). It says that dipolar dynamos may be found if the typical length scale of convection, ℓ, is at least an order of magnitude larger than the Rossby radius, or, $Ro_\ell = v/(\Omega\ell) < 0.12$ (in which v is a typical rms velocity). Our criterion is different from Christensen & Aubert (2006), and entirely based on convection and not influenced by the mean zonal flow. This helped to generalize the Rossby number rule to models with different aspect ratios and mechanical boundary conditions (Schrinner et al. 2012). Moreover, our reinterpretation assumes that the magnetic field is generated only by convection and therefore explains why the Rossby number criterion is not applicable to models for which differential rotation plays an essential role.

Figure 1 shows the relative dipole field strength versus the local Rossby number for all anelastic models considered here. Gastine et al. (2012) presented a similar plot but with f_{dip} based on the magnetic energy density instead of the field strength. This leads to considerably lower values of f_{dip} for multipolar dynamos. As for Boussinesq simulations, only multipolar models are found for $Ro_\ell > 0.12$ (Christensen & Aubert 2006), and the multipolar branch extends into the dipolar regime in the form of a bistable region, where both solutions are possible, depending on the initial conditions (Schrinner et al. 2012). However, in contrast to comparable parameter studies of Boussinesq models (Christensen & Aubert 2006; Schrinner et al. 2012), dipolar and multipolar dynamos are hardly distinguishable from each other in terms of their relative dipole field strength. Contrary to previous results, models with an intermediate dipolarity ($f_{\mathrm{dip}} \approx 0.5$) lead to a fairly smooth transition of f_{dip} in Fig. 1. These are in particular those models with a high equatorial dipole contribution denoted by a cross that is inscribed in the plotting symbol. Because the dipole field strength alone is not conclusive

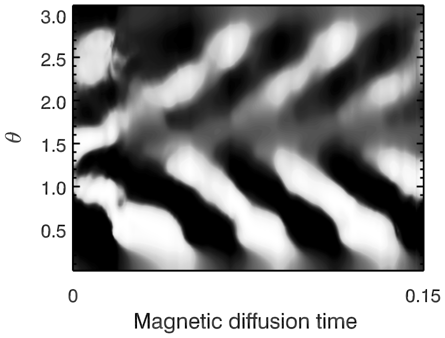

Fig. 2. Contour plot of the azimuthally averaged radial magnetic field of model3m versus time and colatitude. The contour plot was normalised by the maximum absolute value at each time step. The grey-scale coding ranges from −1, white, to +1, black.

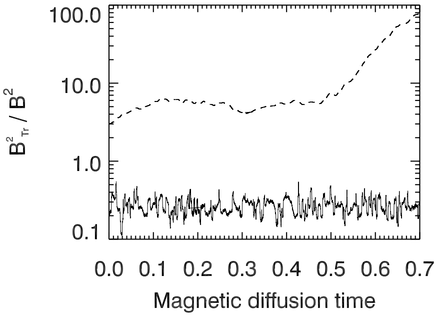

Fig. 3. Evolution of the energy of the tracer field normalised by the energy of the actual magnetic field for model2m (dashed line) and model54d (solid line).

to classify our models in Fig. 1, their time-dependence, their kinematic stability, and their scaling behaviour (see Sect. 4.1) were additionally considered to assign them to one of both classes.

As in the case of Boussinesq simulations, only multipolar models were found to exhibit polarity reversals or oscillatory dynamo solutions. An example of a coherent dynamo wave for model3m ($N_\varrho = 3$) is given in Fig. 2. The period of these oscillatory dynamo modes and the poleward propagation direction of the resulting wave can be surprisingly well explained by Parker's plane layer formalism (Parker 1955; Busse & Simitev 2006; Goudard & Dormy 2008; Schrinner et al. 2011a; Gastine et al. 2012). However, the recent claim that dynamo waves could migrate towards the equator if there is a considerable density stratification (Käpylä et al. 2013) was not confirmed by our simulations.

Moreover, we tested 13 arbitrarily chosen models (see the caption of Table C.1) for kinematic stability and found the dipolar models to be kinematically stable, whereas all multipolar models considered exhibited at least periods of instability. Figure 3 shows as an example the evolution of the kinematically advanced tracer field for model2m and model54d. For the first, the tracer field grows exponentially but it stays stable for the latter although it has been permanently perturbed during the simulation.

A transition from the dipolar to the multipolar regime can be triggered by a decrease in the rotation rate or the dynamical length scale (possibly associated with a change in the aspect ratio), or an increase in the velocity amplitude. These three quantities influence the local Rossby number directly. In Fig. 4, we show that a transition towards the multipolar regime may also be forced by increasing N_ϱ. A higher density stratification with all the other parameters fixed causes smaller length scales and larger velocity amplitudes. This leads to an increase of Ro_ℓ and to a decrease of $f_{\rm dip}$ at $Ro_\ell \approx 0.12$ in Fig. 4.

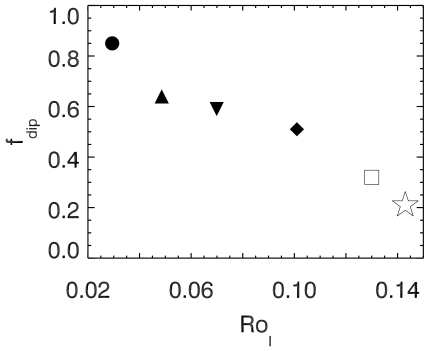

Fig. 4. Relative dipole field strength versus Ro_ℓ for a sequence of models with $E = 3 \times 10^{-4}$, $Ra = 4Ra_c$, Pm = 3, and $Pr = 1$. The meaning of the symbols is defined in the caption of Fig. 1.

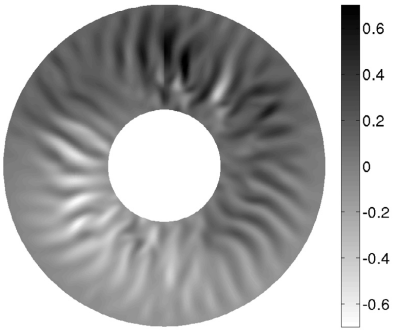

Fig. 5. Contour plot (equatorial cut) of the radial magnetic field of model2m at a given time.

3.2. Equatorial dipole

An example of a model strongly influenced by an equatorial dipole mode is presented in Fig. 5. A strong mean zonal flow often present in these models seems to be in conflict with the generation of non-axisymmetric fields. Figure 6 demonstrates that the strong equatorial dipole mode of model5m is indeed maintained and rebuilt by the columnar convection and damped by the differential rotation. In Fig. 6 the mean zonal kinetic energy normalised by an arbitrary value (dotted line) and the ratio of the axisymmetric magnetic energy to the total magnetic energy (solid line) are displayed. The action of the mean zonal flow, or more precisely the differential rotation, tends to damp non-axisymmetric components of the magnetic field. Thus, a burst of the mean zonal kinetic energy is followed by a maximum of the axisymmetric and a dip in the non-axisymmetric magnetic energy. Subsequently, the mean zonal flow is quenched by the

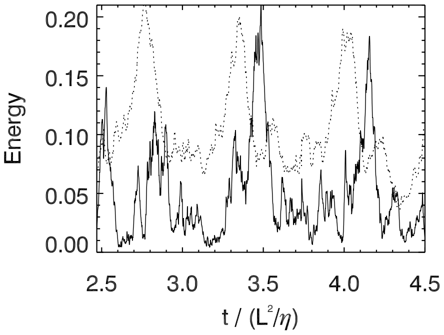

Fig. 6. Dotted line: axisymmetric kinetic energy of model5m normalised by an arbitrary value. Solid line: ratio of axisymmetric to total magnetic energy.

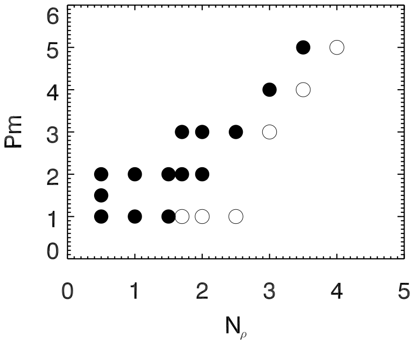

Fig. 7. Magnetic Prandtl number versus N_ϱ for models with $E = 10^{-4}$ and $Pr = 1$ and variable Rayleigh numbers. Filled circles stand for parameters for which dipolar solutions were obtained.

axisymmetric field, the axisymmetric field decays and the non-axisymmetric field is rebuilt. The interaction between the mean zonal flow and the magnetic field observed in this model is still fairly weak, although the mean zonal flow contributes already 58% to the total kinetic energy. Therefore, the magnetic field of model5m stays on average highly non-axisymmetric. We note that this is very different from the Sun, for instance, where probably an even more efficient differential rotation causes a predominantly axisymmetric large-scale magnetic field (Charbonneau 2010), but also non-axisymmetric stellar magnetic fields were reported (Donati & Landstreet 2009).

3.3. Discussion

The fundamental cause of the high dipolarity of dynamo models in the low Rossby number regime is an outstanding question. Schrinner et al. (2012) argued that cylindrical convection in a spherical fluid domain leads to a characteristic pattern of the axisymmetric toroidal field for Boussinesq models, which eventually results in the clear preference of only one, dipolar eigenmode. The argument relies on the idea that a line of fluid elements moving towards the outer spherical boundary has to shorten and causes a converging flow towards the equatorial plane. The toroidal field is then advected and markedly shaped by this flow component (see also Olson et al. 1999). This advection process could be rigorously identified and quantified as a strong γ-effect in a corresponding mean-field description (Schrinner et al. 2007, 2012). In addition, the recent finding that the dichotomy of dipolar and multipolar dynamos seems to be absent in convective dynamo simulations in Cartesian geometry (Tilgner 2012) is consistent with this argument and points again to the significance of the underlying symmetry constraints.

What has been said above about Boussinesq models largely applies to anelastic models, too. However, geometrical constraints are somewhat relaxed for a compressible fluid. Therefore, compressibility might damp the advection of the mean toroidal field towards the equatorial plane (γ-effect), and we hypothesize that this results in at least two specific differences.

First, depending on the density contrast applied, it is more difficult to obtain dipolar solutions for anelastic models than for Boussinesq ones, even if $Ro_\ell < 0.12$. However, unlike Gastine et al. (2012), we did not find that dipolar solutions become impossible if N_ϱ exceeds a certain threshold. Instead, we observe that for a given N_ϱ, Ekman and Prandtl number, there seems to exist a critical magnetic Prandtl number for dipolar dynamos. For $E = 10^{-4}$, $Pr = 1$, and $N_\varrho \geq 1.5$, we found $Pm_{\rm crit} = 2N_\varrho - 2$, as apparent from Fig. 7. We emphasize again that the results of Fig. 7 depend of course on E and Pr; the data of our numerical study indicate that decreasing E and increasing Pr is favorable to dipolar dynamo models.

Second, magnetic field configurations dominated by an equatorial dipole seem to be more easily realized in anelastic than in Boussinesq simulations. For the latter, only a few examples under very specific conditions were reported (Aubert & Wicht 2004; Gissinger et al. 2012). The preference of non-axisymmetric modes is well known from dynamo models based on columnar convection (e.g. Ruediger 1980; Tilgner 1997), it is also the case of the Karlsruhe dynamo experiment (Müller & Stieglitz 2002). This agrees with our reasoning on the importance of the γ-effect in the axial dipole generation mechanisms (see also Schrinner et al. 2012). Indeed, the γ-effect vanishes in the above examples, as the geometrical constraints are relaxed.

4. Scaling laws

Because of computational limitations, very small length scales and time scales associated with extreme parameter values that are relevant for planets and stars cannot be resolved in global direct numerical dynamo simulations. Therefore, numerical models are in general not directly comparable to planetary or stellar dynamos. Instead, scaling laws, in particular for the field strength, have been derived from theory and simulations and then extrapolated to realistic parameter regimes (see Christensen 2010, and references therein).

Subsequently, their predictions may be compared with planetary or stellar magnetic-field data obtained from observations (Christensen et al. 2009; Christensen 2010; Davidson 2013). By this consistency test, scaling laws may provide some evidence about the reliability of numerical dynamo models.

Moreover, different scaling laws typically represent different force balances or dynamo mechanisms, and their investigation might enable us to better distinguish between different types of dynamo models. It is this second aspect in particular, which is of interest in the following. We adopt here the approach by Christensen & Aubert (2006) and derive scaling laws for the field strength, the velocity, the magnetic dissipation time, and the convective heat transport and compare them with previous results from Boussinesq simulations. A similar study was recently published by Yadav et al. (2013b) based on a somewhat different sample of models. Similarities and differences with their findings are discussed.

Most of the proposed scaling laws are independent of diffusivities, which are thought to be negligible under astrophysical conditions (Christensen 2010). However, present global dynamo simulations run in parameter regimes where diffusivities still influence the overall dynamics and weak dependencies on the magnetic Prandtl number seem to persist in purely empirically derived scalings (Christensen & Tilgner 2004; Christensen & Aubert 2006; Christensen 2010; Yadav et al. 2013a; Stelzer & Jackson 2013). In this study we do not attempt to resolve this secondary dependence on Pm because the magnetic Prandtl number varies only between 1 and 5 in our sample of models.

4.1. Magnetic field scaling

The magnetic field strength measured in terms of the Lorentz number scales with the available energy flux to the power of approximately 1/3. For the dipolar dynamos of our sample we find

$$\frac{Lo}{f_{\mathrm{ohm}}^{1/2}} \simeq 1.58\, Ra_Q^{0.35}, \tag{25}$$

and for the multipolar models,

$$\frac{Lo}{f_{\mathrm{ohm}}^{1/2}} \simeq 1.19\, Ra_Q^{0.34}. \tag{26}$$

Except for somewhat larger exponential prefactors, this is in good agreement with previous results from Boussinesq simulations (Christensen 2010; Schrinner et al. 2012; Yadav et al. 2013a) and very similar to the magnetic field scaling given by Yadav et al. (2013b). Unlike Yadav et al. (2013b), we note, however, that we scale the Lorentz number with the flux-based Rayleigh number Ra_Q and not directly with the power released by buoyancy forces. Of course, both should be closely related to each other. The same remark applies for the velocity scaling discussed below.

Models on the multipolar branch exhibit lower field strengths compared to their dipolar counterparts. This is not only apparent by the smaller prefactor in the multipolar scaling, but also the dynamo efficiency f_{ohm} for multipolar models is systematically lower than for the corresponding dipolar ones. The latter indicates that the bistable behaviour for models at $Ro_\ell \leq 0.12$ is caused by different dynamo mechanisms. This was already seen in Boussinesq simulations (Schrinner et al. 2012) and later confirmed by Gastine et al. (2012) for anelastic models.

Apart from a few exceptions, the shift between the two scalings in Fig. 8 may serve to separate dipolar from multipolar dynamos. In agreement with Yadav et al. (2013b), we obtained several models with dipole field strengths up to $f_{\mathrm{dip}} \approx 0.5$, which, nevertheless, clearly follow the multipolar scaling and belong to the multipolar class of dynamos.

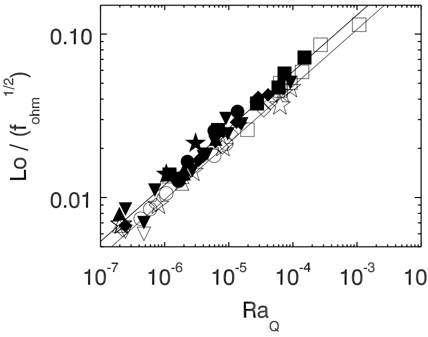

Fig. 8. Lorentz number compensated by f_{ohm} versus the flux-based Rayleigh number for our sample of models. Filled symbols correspond to dipolar models, open symbols are multipolar models and the symbol shape indicates N_ρ as explained in the caption of Fig. 1.

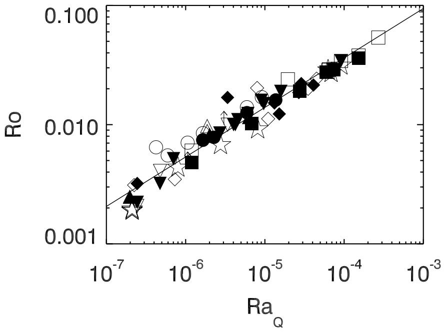

Fig. 9. Rossby number versus the flux-based Rayleigh number for our sample of models.

4.2. Velocity scaling

There is an ongoing discussion about the velocity scaling in dynamo models (Christensen 2010; Davidson 2013; Yadav et al. 2013b). It is probably not surprising that the velocity measured in terms of the Rossby number scales with the flux based Rayleigh number, but the correct exponent and its theoretical justification is debated. The lower bound is set by the assumption of a balance between inertia and buoyancy forces (mixing length balance), which leads to an exponent of 1/3 (Christensen 2010). If, however, the predominant force balance is assumed to be between the Lorentz force, the buoyancy, and the Coriolis force (MAC-balance) the exponent is closer to 1/2 (Christensen 2010; Davidson 2013). As most previous studies (Christensen & Aubert 2006; Christensen 2010; Yadav et al. 2013a; Stelzer & Jackson 2013; Yadav et al. 2013b), we obtained an exponent in between these two values for our sample of models,

$$Ro = 1.66\, Ra_Q^{0.42}. \tag{27}$$

The scatter in Fig. 9 is considerable, but the standard error is of the same order as for Boussinesq models with stress-free mechanical boundary conditions (Yadav et al. 2013a). Compressible effects do not seem to deteriorate the scaling.

However, as in Yadav et al. (2013b), we are not able to distinguish between dipolar and multipolar models in our velocity scaling, which is contrary to what has been previously reported by Yadav et al. (2013a) for Boussinesq models.

4.3. Scaling of Ohmic dissipation time

The scaling of magnetic dissipation time,

$$\tau_{\mathrm{diss}} = E_{\mathrm{M}}/D = \ell_B^2/\eta, \tag{28}$$

is used to evaluate the characteristic length scale ℓ_B of the magnetic field. Christensen & Tilgner (2004) originally identified a

Table 1. Scaling laws for anelastic and Boussinesq models.

Scaling	Anelastic			Boussinesq		
	c	x	σ	c	x	σ
$Lo/f_{\rm ohm}^{1/2} = c\,Ra_Q^x$	1.58	0.35	0.017	1.08	0.37	0.017
Multipolar branch	1.19	0.34	0.067	0.65	0.35	0.006
$Ro = c\,Ra_Q^x$	1.66	0.42	0.025	0.73^a	0.39^a	0.013^a
				1.79^b	0.44^b	0.010^b
$\tau_{\rm diss} = c\,Ro^{-x}$	0.75	0.76	0.024	–	0.8	–
$Nu = c\,Ra_Q^x$	0.25	0.59	0.032	0.06	0.52	0.004

Notes. Results for Boussinesq models were taken from Yadav et al. (2013a; see also Schrinner et al. 2012). Yadav et al. (2013a) distinguished between dipolar and multipolar dynamos for their Rossby number scaling, whereas we derived a single power law for both classes of dynamo models. [(a)] Dipolar models. [(b)] Multipolar models.

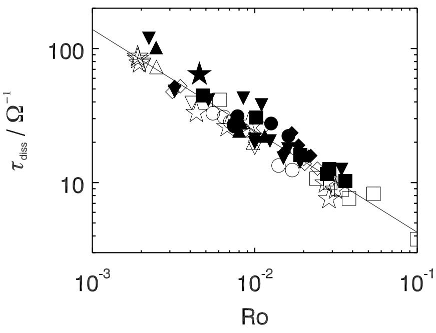

Fig. 10. Ohmic dissipation time versus Rossby number for all models considered in this study.

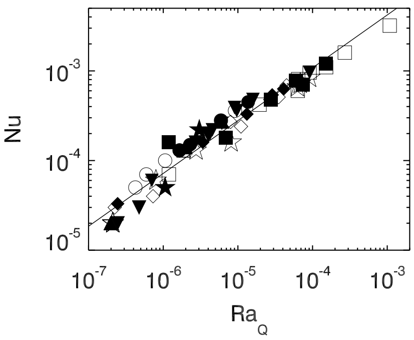

Fig. 11. Nusselt number versus the flux-based Rayleigh number for our sample of models.

linear dependence of $\tau_{\rm diss}$ on the inverse Rossby number provided that time is measured in units of Ω^{-1}. Their finding was supported by dipole-dominated Boussinesq models with no-slip mechanical boundary conditions and the evaluation of the Ohmic dissipation time in the Karlsruhe dynamo experiment. The best fit for our data points in Fig. 10, however, gives an exponent with a significantly lower absolute value,

$$\tau_{\rm diss} = 0.75\,Ro^{-0.76}. \tag{29}$$

An almost identical result was found by Yadav et al. (2013b) from their somewhat more diverse and scattered data set. Apparently, the application of stress-free boundary conditions and possibly the compressible effects flatten the slope of $\tau_{\rm diss}$ as a function of the Rossby number. Moreover, it would seem plausible that $\tau_{\rm diss}$ followed different scaling relations for dipolar and multipolar models. Indeed, the dissipation time for bistable pairs is systematically larger for dipolar than for multipolar models. However, separate least square fits for all dipolar and all multipolar models of our sample lead to very similar results.

4.4. Nusselt number scaling

The convective heat transport in dynamo models is very sensitive to rotation and depends on the magnetic field, boundary conditions, or the geometry of the fluid domain to a much lower degree (Christensen 2002; Christensen & Aubert 2006; Aurnou 2007; Schmitz & Tilgner 2009; Busse & Simitev 2011; Gastine & Wicht 2012; Yadav et al. 2013a; Stelzer & Jackson 2013). The power law for the Nusselt number inferred from Fig. 11,

$$Nu^\star = 0.25\,Ra_Q^{0.59}, \tag{30}$$

is consistent with previous results and also confirms this finding for anelastic dynamo models; the exponent of 0.59 is very close to the value of 5/9 established by the above mentioned references. However, the scaling is somewhat more scattered than for Boussinesq models (Yadav et al. 2013a). We excluded in a test all models for which convection is only marginaly above the onset ($Nu^\star < 2$), but this reselection of models did not improve the quality of the fit.

4.5. Discussion

In an overall view, the scaling relations for Boussinesq and anelastic models are very similar (see Table 1). Beyond that, there is no obvious effect of compressibility on the scaling results and they might be even considered as consistent irrespective of the density stratification of the underlying models (Yadav et al. 2013b). However, the reason for the good agreement could be that the flux-based scaling laws are insensitive to different physical conditions. Using the example of the magnetic field scaling, we argue in the following that differences in the dynamo processes might not be visible in the scaling relation, and some caution is needed in generalizing results from Boussinesq simulations.

If the magnetic energy density follows a simple power law in terms of the convective energy flux, an exponent of 2/3 is already required for dimensional reasons (e.g., Christensen 2010). Moreover, the flux-based scaling law for the magnetic field is composed of the scalings for the velocity and the magnetic dissipation time. By definition, we have $E_{\rm M} \sim f_{\rm ohm}\,\tau_{\rm diss}\,P$, and with

$Ro \sim P^{\alpha}$ and $\tau_{\text{diss}} \sim Ro^{\beta}$, we find $E_{\text{M}} \sim f_{\text{ohm}}\, P\, P^{\alpha\beta}$. Dimensional arguments require $\alpha\beta = -1/3$, which establishes relations (25) and (26). Whereas the exponent in the flux-based scaling law for the magnetic field is fix, α and β are to some extend variable and may change according to the specific physical conditions. This reflects the outcome of more and more extended parameter studies: The exponent of $1/3$ in the magnetic-field scaling is reliably reproduced, but the values for α and β seem to be less certain and are under debate.

In addition, scaling relations (25) and (26) require that the field strength, measured by Lo, is compensated by the square root of f_{ohm} (interpreted as dynamo efficiency in Schrinner 2013). However, f_{ohm} is probably a complicated function of several control parameters and might depend strongly on the specific physical conditions. The often made assumption that $f_{\text{ohm}} \rightarrow 1$ for $Pm \ll 1$ (e.g. Davidson 2013) is probably too simple. For example, Schrinner (2013) recently demonstrated that f_{ohm} in dynamo models might depend strongly on the rotation rate. The dynamo efficiency dropped by two orders of magnitude as the rotation rate of these models was decreased. A further counterexample could be the solar dynamo. Independent estimates result in $f_{\text{ohm}} \sim O(10^{-3})$, (Schrinner 2013; Rempel 2006) although the magnetic Prandtl number is thought to be much smaller than one in the solar interior.[1] In other words, the flux based scaling laws probably do not distinguish between different types of dynamos because differences in the field strength are absorbed by changes in f_{ohm}.

5. Conclusions

Our study revealed a number of similarities between Boussinesq and anelastic dynamo models. The dichotomy between dipolar and multipolar models seems to extend to anelastic models, and the flux-based scaling laws originally proposed for Boussineq models appear to hold similarly for models in the anelastic approximation. Thus, large scale, dipolar magnetic fields for both types of models can only be produced if rotation is important (as measured by the local Rossby number), and the magnetic field strength is directly related to the energy flux via (25) and (26) (see Fig. 8).

However, we also pointed out some significant differences between Boussinesq and anelastic dynamo simulations. Magnetic field configurations with a significant equatorial dipole contribution are less typical for Boussinesq than for anelastic models. Moreover, a large density stratification in anelastic models may inhibit the generation of magnetic fields dominated by an axial dipole. The above claimed consistency of the scalings for Boussinesq and anelastic simulations partly relies on the very general formulation of the flux-based scaling laws and does not necessarily imply similar dynamo processes. We also stress that the assumption of a radially varying conductivity may introduce additional effects, which were not examined here. Whereas Yadav et al. (2013b) obtained very similar scaling laws for models with variable conductivities, Duarte et al. (2013) reported that the field topology of some models depends on the radial conductivity profile. A mean-field analysis (Schrinner et al. 2007; Schrinner 2011) of numerical dynamo models in the anelastic approximation might give more detailed insight in relevant dynamo processes and is envisaged for a future study.

Acknowledgements. M.S. is grateful for financial support from the DFG fellowship SCHR 1299/1-1. Computations were performed at CINES, CEMAG, and GWDG computing centres. Moreover, this work was granted access to the HPC resources of MesoPSL financed by the Région Ile de France and the project Equip@Meso (reference ANR-10-EQPX-29-01) of the programme Investissements d'Avenir supervised by the Agence Nationale pour la Recherche.

Appendix A: Benchmark results

Table A.1. Hydrodynamic benchmark ($E = 10^{-3}$, $N_{\varrho} = 5$, $\chi = 0.35$, $Ra = 3.52 \times 10^{5}$, $Pr = 1$, $n = 2$).

Code	PaRoDy	Leeds
K.E.	81.85	81.86
Zonal K.E.	9.388	9.377
Meridional K.E.	0.02198	0.02202
Luminosity	4.170	4.199
v_{ϕ} at $v_r = 0$	0.8618	0.8618
S at $u_r = 0$	0.9334	0.9330
Resolution	288 × 192 × 384	128 × 192 × 384
Timestep	5×10^{-6}	2.5×10^{-6}

Table A.2. Steady dynamo benchmark ($E = 2 \times 10^{-3}$, $N_{\varrho} = 3$, $\chi = 0.35$, $Ra = 8.00 \times 10^{4}$, $Pr = 1$, $P\text{m} = 50$, $n = 2$).

Code	PaRoDy	Leeds
K.E.	4.189×10^{6}	4.194×10^{5}
Zonal K.E.	5.993×10^{4}	6.018×10^{4}
Meridional K.E.	52.98	53.02
M.E.	3.216×10^{5}	3.202×10^{5}
Zonal M.E.	2.424×10^{5}	2.412×10^{5}
Meridional M.E.	1.704×10^{5}	1.697×10^{4}
Luminosity	11.48	11.50
v_{ϕ} at $v_r = 0$	–91.84	–91.78
B_{θ} at $v_r = 0$	±0.0343	±0.03395
S at $u_r = 0$	0.7864	0.7865
Resolution	288 × 126 × 252	128 × 144 × 252
Timestep	5×10^{-7}	10^{-6}

Table A.3. Unsteady dynamo benchmark ($E = 5 \times 10^{-5}$, $N_{\varrho} = 3$, $\chi = 0.35$, $Ra = 2.50 \times 10^{7}$, $Pr = 2$, $P\text{m} = 2$, $n = 2$).

Code	PaRoDy	Leeds
K.E.	2.33×10^{5}	2.32×10^{5}
Zonal K.E.	1.38×10^{4}	1.36×10^{4}
Meridional K.E.	111	105
M.E.	2.41×10^{5}	2.42×10^{5}
Zonal M.E.	9.35×10^{3}	9.45×10^{3}
Meridional M.E.	2.10×10^{4}	2.13×10^{4}
Luminosity	42.4	42.5
Resolution	288 × 255 × 510	96 × 288 × 576
Timestep	5×10^{-7}	3×10^{-6}

---

[1] In Schrinner (2013), a wrong mean solar density has been used to estimate f_{ohm} which lead to $f_{\text{ohm}} \approx 10^{-2}$. We correct this error here.

References

Alboussière, T., & Ricard, Y. 2013, J. Fluid Mech., 725, 1
Aubert, J., & Wicht, J. 2004, Earth Planetary Sci. Lett., 221, 409
Aurnou, J. M. 2007, Geophys. Astrophys. Fluid Dyn., 101, 327
Braginsky, S. I., & Roberts, P. H. 1995, Geophysical and Astrophysical Fluid Dynamics, 79, 1
Brown, B. P., Vasil, G. M., & Zweibel, E. G. 2012, ApJ, 756, 109
Browning, M. K., Brun, A. S., & Toomre, J. 2004, ApJ, 601, 512
Brun, A. S., Miesch, M. S., & Toomre, J. 2004, ApJ, 614, 1073
Buffett, B. A. 2000, Science, 288, 2007
Busse, F. H. 1975, Geophys. J. Int., 42, 437
Busse, F. H., & Simitev, R. D. 2006, Geophys. Astrophys. Fluid Dyn., 100, 341
Busse, F. H., & Simitev, R. D. 2010, in Turbulence in the Atmosphere and Oceans, IUTAM Bookseries (Springer), 28, 181
Busse, F., & Simitev, R. 2011, Geophys. Astrophys. Fluid Dyn., 105, 234
Cattaneo, F., & Tobias, S. M. 2009, J. Fluid Mech., 621, 205
Charbonneau, P. 2010, Liv. Rev. Sol. Phys., 7
Christensen, U. R. 2002, J. Fluid Mech., 470, 115
Christensen, U. R. 2010, Space Sci. Rev., 152, 565
Christensen, U. R., & Aubert, J. 2006, Geophy. J. Int., 166, 97
Christensen, U. R., & Tilgner, A. 2004, Nature, 429, 169
Christensen, U., Olson, P., & Glatzmaier, G. A. 1998, Geophys. Res. Lett., 25, 1565
Christensen, U., Olson, P., & Glatzmaier, G. A. 1999, Geophys. J. Int., 138, 393
Christensen, U. R., Holzwarth, V., & Reiners, A. 2009, Nature, 457, 167
Davidson, P. A. 2013, Geophys. J. Int., 195, 67
Donati, J.-F., & Landstreet, J. D. 2009, ARA&A, 47, 333
Dormy, E., Cardin, P., & Jault, D. 1998, Earth Planet. Sci. Lett., 160, 15
Dormy, E., Valet, J.-P., & Courtillot, V. 2000, Geochem. Geophys. Geosyst., 1, 1037
Duarte, L. D. V., Gastine, T., & Wicht, J. 2013, Phys. Earth Planet. Inter., 222, 22
Gastine, T., & Wicht, J. 2012, Icarus, 219, 428
Gastine, T., Duarte, L., & Wicht, J. 2012, A&A, 546, A19
Gilman, P. A., & Glatzmaier, G. A. 1981, ApJS, 45, 335
Gissinger, C., Petitdemange, L., Schrinner, M., & Dormy, E. 2012, Phys. Rev. Lett., 108, 234501
Glatzmaier, G. A. 1984, J. Comput. Phys., 55, 461
Glatzmaier, G. A., & Roberts, P. H. 1995, Nature, 377, 203
Goudard, L., & Dormy, E. 2008, Europhys. Lett., 83, 59001
Gough, D. O. 1969, J. Atmos. Sci., 26, 448
Grote, E., Busse, F. H., & Tilgner, A. 2000, Phys. Earth Planet. Inter., 117, 259
Hori, K., Wicht, J., & Christensen, U. R. 2010, Phys. Earth Planet. Inter., 182, 85
Jones, C. A., & Kuzanyan, K. M. 2009, Icarus, 204, 227
Jones, C. A., Kuzanyan, K. M., & Mitchell, R. H. 2009, J. Fluid Mech., 634, 291
Jones, C. A., Boronski, P., Brun, A. S., et al. 2011, Icarus, 216, 120
Kageyama, A., & Sato, T. 1997, Phys. Rev. E, 55, 4617
Käpylä, P. J., Mantere, M. J., Cole, E., Warnecke, J., & Brandenburg, A. 2013, ApJ, 778, 41
Katayama, J. S., Matsushima, M., & Honkura, Y. 1999, Phys. Earth Planet. Inter., 111, 141
Kuang, W., & Bloxham, J. 1997, Nature, 389, 371
Kutzner, C., & Christensen, U. R. 2002, Phys. Earth Planet. Inter., 131, 29
Landeau, M., & Aubert, J. 2011, Phys. Earth Planet. Inter., 185, 61
Lantz, S. R., & Fan, Y. 1999, ApJS, 121, 247
Miesch, M. S., Elliott, J. R., Toomre, J., et al. 2000, ApJ, 532, 593
Müller, U., & Stieglitz, R. 2002, Nonlinear Processes in Geophysics, 9, 165
Ogura, Y., & Phillips, N. A. 1962, J. Atmos. Sci., 19, 173
Olson, P., Christensen, U. R., & Glatzmaier, G. A. 1999, J. Geophys. Res., 104, 10383
Parker, E. N. 1955, ApJ, 122, 293
Rempel, M. 2006, ApJ, 647, 662
Rogers, T. M., & Glatzmaier, G. A. 2005, ApJ, 620, 432
Ruediger, G. 1980, Astron. Nachr., 301, 181
Sarson, G. R., Jones, C. A., & Longbottom, A. W. 1998, Geophys. Astrophys. Fluid Dyn., 88, 225
Schmitz, S., & Tilgner, A. 2009, Phys. Rev. E, 80, 015305
Schrinner, M. 2011, A&A, 533, A108
Schrinner, M. 2013, MNRAS, 431, L78
Schrinner, M., Rädler, K.-H., Schmitt, D., Rheinhardt, M., & Christensen, U. R. 2007, Geophys. Astrophys. Fluid Dyn., 101, 81
Schrinner, M., Schmitt, D., Cameron, R., & Hoyng, P. 2010, Geophys. J. Int., 182, 675
Schrinner, M., Petitdemange, L., & Dormy, E. 2011a, A&A, 530, A140
Schrinner, M., Schmitt, D., & Hoyng, P. 2011b, Phys. Earth Planet. Inter., 188, 185
Schrinner, M., Petitdemange, L., & Dormy, E. 2012, ApJ, 752, 121
Sreenivasan, B., & Jones, C. A. 2006, Geophys. J. Int., 164, 467
Stelzer, Z., & Jackson, A. 2013, Geophys. J. Int., 193, 1265
Tilgner, A. 1997, Phys. Lett. A, 226, 75
Tilgner, A. 2012, Phys. Rev. Lett., 109, 248501
Tilgner, A., & Brandenburg, A. 2008, MNRAS, 391, 1477
Yadav, R. K., Gastine, T., & Christensen, U. R. 2013a, Icarus, 225, 185
Yadav, R. K., Gastine, T., Christensen, U. R., & Duarte, L. D. V. 2013b, ApJ, 774, 6

Pages 11 to 13 are available in the electronic edition of the journal at `http://www.aanda.org`

Appendix B: Critical Rayleigh numbers for the onset of convection

Table B.1. Overview of the critical Rayleigh numbers and the corresponding critical azimuthal wavenumbers for the onset of convection determined, as explained in Jones et al. (2009).

E	Pr	N_ϱ	χ	Ra_c	m_c
3×10^{-5}	1	2.0	0.35	6.79×10^{6}	24
1×10^{-4}	1	0.5	0.35	3.34×10^{5}	10
1×10^{-4}	1	1.0	0.35	5.67×10^{5}	12
1×10^{-4}	1	1.5	0.35	9.25×10^{5}	14
1×10^{-4}	1	1.7	0.35	1.09×10^{6}	15
1×10^{-4}	1	2.0	0.35	1.43×10^{6}	16
1×10^{-4}	1	2.5	0.35	2.18×10^{6}	19
1×10^{-4}	1	3.0	0.35	3.02×10^{6}	29
1×10^{-4}	1	3.5	0.35	3.62×10^{6}	37
1×10^{-4}	1	4.0	0.35	4.09×10^{6}	43
1×10^{-4}	2	3.0	0.35	7.48×10^{6}	33
1×10^{-4}	1	2.0	0.55	5.35×10^{6}	42
3×10^{-4}	1	0.5	0.35	9.66×10^{4}	7
3×10^{-4}	1	1.0	0.35	1.52×10^{5}	9
3×10^{-4}	1	1.5	0.35	2.32×10^{5}	10
3×10^{-4}	1	2.0	0.35	3.51×10^{5}	12
3×10^{-4}	1	2.5	0.35	5.19×10^{5}	14
3×10^{-4}	1	3.0	0.35	7.12×10^{5}	19
3×10^{-4}	1	3.5	0.35	8.71×10^{5}	25
3×10^{-4}	1	2.0	0.45	6.83×10^{5}	18
3×10^{-4}	1	2.0	0.55	1.26×10^{6}	28
3×10^{-4}	2	3.0	0.35	8.90×10^{5}	22
1×10^{-3}	1	2.0	0.35	7.70×10^{4}	8
2×10^{-3}	1	2.5	0.35	4.60×10^{4}	7

Appendix C: Numerical models

Table C.1. Overview of the simulations carried out, ordered with respect to their local Rossby number.

Model	E	Ra	Pm	Pr	χ	N_ϱ	Ro_ℓ	Rm	Lo	$f_{\rm dip}$	$f_{\rm ohm}$	Nu
1m	1×10^{-4}	5.00×10^{6}	2.0	2	0.35	3.0	1.54×10^{-2}	34	1.10×10^{-3}	0.07	0.05	1.3
2m	1×10^{-4}	5.00×10^{6}	3.0	2	0.35	3.0	1.69×10^{-2}	57	2.06×10^{-3}	0.55	0.09	1.4
3m	1×10^{-4}	5.00×10^{6}	4.0	2	0.35	3.0	1.80×10^{-2}	78	2.35×10^{-3}	0.26	0.12	1.4
4m	1×10^{-4}	5.00×10^{6}	5.0	2	0.35	3.0	1.80×10^{-2}	95	2.21×10^{-3}	0.28	0.11	1.4
5m	1×10^{-4}	2.00×10^{6}	1.0	1	0.35	0.5	2.52×10^{-2}	65	2.16×10^{-3}	0.43	0.08	1.5
6d	2×10^{-3}	8.00×10^{4}	50	1	0.35	3.0	2.71×10^{-2}	240	8.38×10^{-3}	0.83	0.01	1.1
7d	5×10^{-5}	1.50×10^{7}	2.0	1	0.35	1.5	2.72×10^{-2}	128	3.89×10^{-3}	0.79	0.31	1.6
7m	5×10^{-5}	1.50×10^{7}	2.0	1	0.35	1.5	2.51×10^{-2}	164	2.84×10^{-3}	0.20	0.22	1.6
8m	1×10^{-4}	2.00×10^{6}	1.5	1	0.35	0.5	2.77×10^{-2}	83	3.08×10^{-3}	0.39	0.13	1.7
9d	3×10^{-4}	4.00×10^{5}	3.0	1	0.35	0.5	2.94×10^{-2}	78	8.78×10^{-3}	0.85	0.28	1.5
10d	1×10^{-4}	7.64×10^{5}	2.0	1	0.60	1.5	3.19×10^{-2}	44	2.89×10^{-3}	0.78	0.14	1.2
10m	1×10^{-4}	7.64×10^{5}	2.0	1	0.60	1.5	3.12×10^{-2}	42	2.03×10^{-3}	0.35	0.11	1.2
11d	1×10^{-4}	2.78×10^{6}	2.0	1	0.35	1.5	3.39×10^{-2}	104	5.72×10^{-3}	0.78	0.26	1.6
12d	3×10^{-5}	1.96×10^{7}	2.0	1	0.35	2.0	3.39×10^{-2}	213	3.87×10^{-3}	0.68	0.32	2.1
12m	3×10^{-5}	1.96×10^{7}	2.0	1	0.35	2.0	3.33×10^{-2}	207	3.02×10^{-3}	0.24	0.23	2.0
13d	1×10^{-4}	6.14×10^{6}	2.0	1	0.60	1.0	3.41×10^{-2}	49	2.75×10^{-3}	0.68	0.12	1.2
13m	1×10^{-4}	6.14×10^{6}	2.0	1	0.60	1.0	3.44×10^{-2}	49	2.32×10^{-3}	0.05	0.12	1.2
14m	1×10^{-4}	2.50×10^{6}	1.5	1	0.35	0.5	3.51×10^{-2}	106	4.59×10^{-3}	0.49	0.19	2.0
15d	1×10^{-4}	4.01×10^{6}	3.0	1	0.35	2.5	3.76×10^{-2}	144	6.74×10^{-3}	0.52	0.24	1.7
15m	1×10^{-4}	$4,01\times10^{6}$	3.0	1	0.35	2.5	4.51×10^{-2}	182	6.48×10^{-3}	0.47	0.23	1.7
16d	1×10^{-4}	$5,00\times10^{6}$	4.0	1	0.35	3.0	3.76×10^{-2}	182	6.64×10^{-3}	0.47	0.23	1.5
17d	1×10^{-4}	3.00×10^{6}	2.0	1	0.35	0.5	3.90×10^{-2}	148	8.15×10^{-3}	0.75	0.37	2.3
18d	1×10^{-4}	3.01×10^{6}	1.5	1	0.35	0.5	4.00×10^{-2}	112	7.83×10^{-3}	0.87	0.35	2.3
18m	1×10^{-4}	3.01×10^{6}	1.5	1	0.35	0.5	4.32×10^{-2}	127	6.09×10^{-3}	0.39	0.23	2.3
19m	5×10^{-5}	2.52×10^{7}	2.0	2	0.35	3.0	4.46×10^{-2}	176	4.62×10^{-3}	0.30	0.26	3.4
20d	1×10^{-4}	3.40×10^{6}	1.0	1	0.35	1.0	4.71×10^{-2}	80	8.55×10^{-3}	0.86	0.37	2.4
20m	1×10^{-4}	3.40×10^{6}	1.0	1	0.35	1.0	4.62×10^{-2}	97	5.93×10^{-3}	0.32	0.24	2.3
21d	3×10^{-4}	6.08×10^{5}	3.0	1	0.35	1.0	4.86×10^{-2}	115	1.27×10^{-2}	0.64	0.31	1.9
22d	1×10^{-4}	3.40×10^{6}	1.5	1	0.35	1.0	4.88×10^{-2}	124	8.76×10^{-3}	0.75	0.35	2.4
22m	1×10^{-4}	3.40×10^{6}	1.5	1	0.35	1.0	4.78×10^{-2}	132	6.62×10^{-3}	0.39	0.25	2.3
23m	1×10^{-4}	1.00×10^{7}	3.0	2	0.35	3.0	5.13×10^{-2}	203	6.26×10^{-3}	0.14	0.19	3.6
24d	1×10^{-4}	4.00×10^{6}	2.0	1	0.35	1.5	5.30×10^{-2}	170	8.37×10^{-3}	0.69	0.33	2.6
25d	3×10^{-4}	1.00×10^{6}	3.0	1	0.35	2.5	5.36×10^{-2}	226	1.17×10^{-2}	0.75	0.21	1.6
26m	1×10^{-4}	1.14×10^{7}	2.0	1	0.60	2.0	5.38×10^{-2}	70	3.41×10^{-3}	0.24	0.14	1.4
27m	1×10^{-4}	1.00×10^{7}	3.0	2	0.35	3.0	5.46×10^{-2}	205	6.24×10^{-3}	0.21	0.19	3.6
28d	3×10^{-4}	8.00×10^{5}	3.0	1	0.35	0.5	6.06×10^{-2}	161	2.14×10^{-2}	0.76	0.41	2.5
29d	1×10^{-4}	5.00×10^{6}	3.0	1	0.35	2.0	6.10×10^{-2}	270	1.00×10^{-2}	0.61	0.36	2.6
30m	1×10^{-4}	5.00×10^{6}	1.0	1	0.35	1.7	6.50×10^{-2}	100	8.06×10^{-3}	0.5	0.26	2.6
31d	1×10^{-4}	5.00×10^{6}	1.0	1	0.35	0.5	6.70×10^{-2}	126	1.41×10^{-2}	0.83	0.48	3.8
31m	1×10^{-4}	5.00×10^{6}	1.0	1	0.35	0.5	7.10×10^{-2}	140	1.05×10^{-2}	0.45	0.34	3.8
32d	1×10^{-4}	5.00×10^{6}	2.0	1	0.35	1.5	6.70×10^{-2}	220	1.16×10^{-2}	0.65	0.40	3.2
33d	1×10^{-4}	5.00×10^{6}	3.0	1	0.35	1.7	6.70×10^{-2}	300	1.08×10^{-2}	0.63	0.37	2.9
34d	1×10^{-4}	5.00×10^{6}	2.0	1	0.35	1.7	6.80×10^{-2}	200	1.07×10^{-2}	0.67	0.35	3.0
35d	3×10^{-4}	6.08×10^{5}	3.0	1	0.35	1.5	6.99×10^{-2}	160	1.78×10^{-2}	0.59	0.34	2.3
36d	1×10^{-4}	8.00×10^{6}	4.0	1	0.35	3.0	7.00×10^{-2}	380	1.41×10^{-2}	0.62	0.40	2.9
37d	3×10^{-4}	1.05×10^{6}	3.0	1	0.35	2.0	7.21×10^{-2}	152	1.60×10^{-2}	0.67	0.31	2.1
38m	1×10^{-4}	1.20×10^{7}	5.0	1	0.35	4.0	7.22×10^{-2}	458	1.15×10^{-2}	0.19	0.32	2.6
39d	1×10^{-4}	5.55×10^{6}	2.0	1	0.35	1.5	7.40×10^{-2}	247	1.52×10^{-2}	0.63	0.49	3.6
40d	1×10^{-4}	6.00×10^{6}	1.0	1	0.35	0.5	8.00×10^{-2}	150	1.64×10^{-2}	0.82	0.49	4.7
41d	1×10^{-4}	1.00×10^{7}	5.0	1	0.35	3.5	8.20×10^{-2}	500	1.23×10^{-2}	0.63	0.33	3.2
42d	1×10^{-4}	6.50×10^{6}	1.0	1	0.35	1.5	8.80×10^{-2}	150	1.64×10^{-2}	0.77	0.45	4.6
43d	1×10^{-4}	7.00×10^{6}	2.0	1	0.35	2.0	8.80×10^{-2}	280	1.64×10^{-2}	0.66	0.46	4.3
44m	1×10^{-4}	7.00×10^{6}	1.0	1	0.35	2.0	9.05×10^{-2}	140	1.18×10^{-2}	0.04	0.34	3.7
45d	1×10^{-3}	2.50×10^{5}	3.0	1	0.35	2.5	9.07×10^{-2}	87	2.76×10^{-2}	0.82	0.23	1.7
45m	1×10^{-3}	2.50×10^{5}	3.0	1	0.35	2.5	6.35×10^{-2}	86	2.17×10^{-2}	0.31	0.19	1.6
46m	1×10^{-4}	6.00×10^{6}	1.0	1	0.35	0.5	9.20×10^{-2}	170	1.26×10^{-2}	0.52	0.35	4.6
47d	3×10^{-4}	1.50×10^{6}	3.0	1	0.35	2.5	9.35×10^{-2}	191	2.29×10^{-2}	0.59	0.37	2.6

Notes. In case of bistable pairs, the local Rossby number of the dipolar model was considered to create the sequence. Kinematic stability: out of the 13 models tested, the kinematically stable are model16d, model37d, model45d, model54d, model55d, and model56d, and the kinematically unstable are model2m, model5m, model8m, model14m, model18m, model65m, and model66m. Models with a considerable equatorial dipole field are model2m, model5m, model8m, model14m, model18m, model22m, model27m, model30m, model31m, model45m, model46m, and model56m.

Table C.1. continued.

Model	E	Ra	Pm	Pr	χ	N_ϱ	Ro_ℓ	Rm	Lo	$f_{\rm dip}$	$f_{\rm ohm}$	Nu
47m	3×10^{-4}	1.50×10^{6}	3.0	1	0.35	2.5	8.67×10^{-2}	234	1.67×10^{-2}	0.39	0.22	2.2
48m	3×10^{-4}	2.52×10^{6}	3.0	1	0.55	2.0	9.81×10^{-2}	112	1.12×10^{-2}	0.27	0.21	1.8
49d	3×10^{-4}	1.40×10^{6}	3.0	1	0.35	2.0	1.01×10^{-1}	221	2.47×10^{-2}	0.51	0.36	2.8
50d	3×10^{-4}	1.50×10^{6}	3.0	1	0.35	1.5	1.09×10^{-1}	265	3.18×10^{-2}	0.67	0.45	3.7
51d	1×10^{-4}	8.00×10^{6}	1.0	1	0.35	1.5	1.10×10^{-1}	190	1.97×10^{-2}	0.77	0.49	5.8
52d	1×10^{-4}	1.52×10^{7}	3.0	1	0.55	2.0	1.13×10^{-1}	369	2.10×10^{-2}	0.64	0.54	4.3
53d	3×10^{-4}	2.05×10^{6}	3.0	1	0.45	2.0	1.14×10^{-1}	186	2.27×10^{-2}	0.60	0.35	2.6
54d	1×10^{-3}	3.00×10^{5}	3.0	1	0.35	2.5	1.19×10^{-1}	108	4.14×10^{-2}	0.74	0.33	2.2
54m	1×10^{-3}	3.00×10^{5}	3.0	1	0.35	2.5	1.13×10^{-1}	114	2.97×10^{-2}	0.27	0.28	2.1
55d	3×10^{-4}	2.00×10^{6}	3.0	1	0.35	2.5	1.22×10^{-1}	277	2.91×10^{-2}	0.56	0.38	3.6
56d	3×10^{-4}	2.39×10^{6}	3.0	1	0.45	2.0	1.29×10^{-1}	215	2.73×10^{-2}	0.59	0.42	3.1
56m	3×10^{-4}	2.39×10^{6}	3.0	1	0.45	2.0	1.25×10^{-1}	243	2.05×10^{-2}	0.32	0.29	3.3
57m	3×10^{-4}	2.08×10^{6}	3.0	1	0.35	2.5	1.30×10^{-1}	291	2.71×10^{-2}	0.32	0.36	3.7
58m	3×10^{-4}	2.50×10^{6}	3.0	1	0.35	3.0	1.28×10^{-1}	272	2.58×10^{-2}	0.26	0.35	3.4
59m	3×10^{-4}	5.00×10^{5}	2.0	2	0.35	3.0	1.34×10^{-1}	191	1.98×10^{-2}	0.28	0.29	5.4
60m	3×10^{-4}	3.50×10^{6}	3.0	1	0.35	3.5	1.41×10^{-1}	294	2.58×10^{-2}	0.17	0.34	3.6
61m	3×10^{-4}	2.85×10^{6}	3.0	1	0.35	3.0	1.43×10^{-1}	314	2.79×10^{-2}	0.21	0.36	3.8
62m	3×10^{-4}	2.50×10^{6}	3.0	1	0.35	2.5	1.47×10^{-1}	342	3.15×10^{-2}	0.28	0.39	4.2
63m	1×10^{-4}	1.10×10^{7}	1.0	1	0.35	2.5	1.50×10^{-1}	240	1.58×10^{-2}	0.28	0.37	5.2
64m	3×10^{-4}	3.78×10^{6}	3.0	1	0.55	2.0	1.52×10^{-1}	200	1.92×10^{-2}	0.17	0.31	2.7
65m	1×10^{-3}	4.00×10^{5}	3.0	1	0.35	2.5	1.66×10^{-1}	162	4.39×10^{-2}	0.26	0.26	2.6
66m	2×10^{-3}	2.00×10^{5}	3.0	1	0.35	2.5	2.18×10^{-1}	150	4.66×10^{-2}	0.19	0.17	2.6

B.3 *Influence of the mass distribution on the magnetic field topology*

Raynaud, R., Petitdemange, L. & Dormy, E., 2014, *Astronomy and Astrophysics*, **567**, A107.

Liens de téléchargement :
— www.aanda.org/articles/aa/abs/2014/07/aa23902-14/aa23902-14.html
— arxiv.org/abs/1406.4743
— hal.archives-ouvertes.fr/hal-01122419v1

A&A 567, A107 (2014)
DOI: 10.1051/0004-6361/201423902

Astronomy & Astrophysics

Influence of the mass distribution on the magnetic field topology★

R. Raynaud[1,2], L. Petitdemange[1,2], and E. Dormy[1,3]

[1] MAG (ENS/IPGP), LRA, Département de Physique, École normale supérieure, 24 rue Lhomond, 75252 Paris Cedex 5, France
e-mail: `raphael.raynaud@ens.fr;ludovic@lra.ens.fr;dormy@phys.ens.fr`
[2] LERMA, CNRS UMR 8112, 75005 Paris, France
[3] IPGP, CNRS UMR 7154, 75005 Paris, France

Received 28 March 2014 / Accepted 16 June 2014

ABSTRACT

Context. Three-dimensional spherical dynamo simulations carried out within the framework of the anelastic approximation have revealed that the established distinction between dipolar and multipolar dynamos tends to be less clear than it was in Boussinesq studies. This result was first interpreted as a direct consequence of the existence of a larger number of models with a high equatorial dipole contribution, together with an intermediate dipole field strength. However, this finding has not been clearly related to specific changes that would have been introduced by the use of the anelastic approximation.
Aims. In this paper, we primarily focus on the effects of choosing a different mass distribution. Indeed, it is likely to have as large consequences as taking a stratified reference state into account would, especially when comparing our results to previous Boussinesq studies.
Methods. Our investigation is based on a systematic parameter study of weakly stratified anelastic dynamo models.
Results. We show that the tendencies highlighted in previous anelastic dynamo simulations are already present in the Boussinesq limit. Thus they cannot be systematically related to anelastic effects. Actually, a central mass distribution can result in changes in the magnetic field topology that are mainly due to the concentration of convective cells close to the inner sphere.

Key words. dynamo – magnetohydrodynamics – magnetic fields – stars: magnetic field

1. Introduction

Dynamo action, i.e. the self-amplification of a magnetic field by the flow of an electrically conducting fluid, is considered to be the main mechanism for generating magnetic fields in the universe for a variety of systems, including planets, stars, and galaxies (e.g. Dormy & Soward 2007). Dynamo action is an instability by which a conducting fluid transfers part of its kinetic energy to magnetic energy. Because of the difficulty simulating turbulent fluid motions, one must resort to some approximations to model the fluid flow, whose convective motions are assumed to be driven by the temperature difference between a hot inner core and a cooler outer surface. A strong simplification can be achieved when applying the Boussinesq approximation (Boussinesq 1903), which performs well in so far as variations in pressure scarcely affect the density of the fluid. However, in essence, this approximation will not be adequate for describing convection in highly stratified systems, such as stars or gas giants. A common approach to overcoming this difficulty is then to use the anelastic approximation, which allows for a reference density profile while filtering out sound waves for faster numerical integration. This approximation was first developed to study atmospheric convection (Ogura & Phillips 1962; Gough 1969). It has then been used to model convection in the Earth core or in stars and is found in the literature under slightly different formulations (Gilman & Glatzmaier 1981; Braginsky & Roberts 1995; Lantz & Fan 1999; Anufriev et al. 2005; Berkoff et al. 2010; Jones et al. 2011; Alboussière & Ricard 2013). Nevertheless, the starting point in the anelastic approximation is always to consider convection as a perturbation of a stratified reference state that is assumed to be close to adiabatic.

Observations of low mass stars have revealed very different magnetic field topologies from small scale fields to large scale dipolar fields (Donati & Landstreet 2009; Morin et al. 2010), and highlight possible correlations between differential rotation and magnetic field topologies (Reinhold et al. 2013). Boussinesq models partly reproduce this diversity (Busse & Simitev 2006; Morin et al. 2011; Sasaki et al. 2011; Schrinner et al. 2012). Moreover, the dichotomy between dipolar and "non-dipolar" (or multipolar) dynamos seems to hold for anelastic models (Gastine et al. 2012; Yadav et al. 2013b). However, we show in Schrinner et al. (2014) that this distinction may somewhat be less clear than it was with Boussinesq models. Indeed, in a systematic parameter study we found a large number of models with both a high equatorial dipole contribution and an intermediate dipole field strength. Only a few examples of equatorial dipoles have been reported from Boussinesq spherical dynamo simulations (Aubert & Wicht 2004; Gissinger et al. 2012). At the same time, observations have shown that for some planets, such as Uranus or Neptune, the dipole axis can make an angle up to $\pi/2$ with respect to the rotation axis, owing to a significant contribution from the equatorial dipole (Jones 2011).

★ Appendices are available in electronic form at
`http://www.aanda.org`

In this paper, we aim to clarify the reasons likely for the emergence of an equatorial dipole contribution when measuring the dipole field strength at the surface of numerical models. Since our approach closely follows previous methodology for studying the link with Boussinesq results, we decided to focus in more detail on one important change that comes with the anelastic approximation as formulated in Jones et al. (2011), assuming that all mass is concentrated inside the inner sphere to determine the gravity profile. In contrast, as proposed by the Boussinesq dynamo benchmark Christensen et al. (2001), it was common for geodynamo studies to assume that the density is homogeneously distributed. This leads to different gravity profiles, the first being proportional to $1/r^2$, whereas the second is proportional to r. According to Duarte et al. (2013), Gastine et al. (2012) show that both gravity profiles lead to very similar results. Contrary to this statement, we show that the choice of the gravity profile may have strong consequences on the dynamo-generated field topology. We briefly recall the anelastic equations in Sect. 2 before presenting our results in Sect. 3. In Appendix A, we give the fit coefficients obtained for the scalings of the magnetic and velocity fields and the convective heat flux. A summary of the numerical simulations carried out is given in Appendix B.

2. Governing equations

2.1. The non-dimensional anelastic equations

We rely on the LBR-formulation, named after Lantz & Fan (1999) and Braginsky & Roberts (1995), as it is used in the dynamo benchmarks proposed by Jones et al. (2011). It guarantees the energy conservation, unlike other formulations (see Brown et al. 2012). A more detailed presentation of the equations can be found in our preceding paper Schrinner et al. (2014).

Let us consider a spherical shell of width d and aspect ratio χ, rotating about the z axis at angular velocity $\boldsymbol{\Omega}$ and filled with a perfect, electrically conducting gas with kinematic viscosity ν, thermal diffusivity κ, specific heat c_p, and magnetic diffusivity η (all assumed to be constant). In contrast to the usual Boussinesq framework, convection is driven by an imposed entropy difference Δs between the inner and the outer boundaries, and the gravity is given by $\boldsymbol{g} = -GM\hat{\boldsymbol{r}}/r^2$ where G is the gravitational constant and M the central mass, assuming that the bulk of the mass is concentrated inside the inner sphere.

The reference state is given by the polytropic equilibrium solution of the anelastic system

$$\overline{P} = P_\mathrm{c}\, w^{n+1}, \quad \overline{\varrho} = \varrho_\mathrm{c}\, w^n, \quad \overline{T} = T_\mathrm{c}\, w, \quad w = c_0 + \frac{c_1 d}{r}, \tag{1}$$

$$c_0 = \frac{2w_0 - \chi - 1}{1-\chi}, \quad c_1 = \frac{(1+\chi)(1-w_\mathrm{o})}{(1-\chi)^2}, \tag{2}$$

with

$$w_0 = \frac{\chi + 1}{\chi \exp(N_\varrho/n) + 1}, \quad w_\mathrm{i} = \frac{1+\chi-w_\mathrm{o}}{\chi}. \tag{3}$$

In the above expressions, n is the polytropic index and N_ϱ the number of density scale heights, defined by $N_\varrho = \ln(\varrho_\mathrm{i}/\varrho_\mathrm{o})$, where ϱ_i and ϱ_o denote the reference state density at the inner and outer boundaries, respectively. The values P_c, ϱ_c, and T_c are the reference-state density, pressure, and temperature midway between the inner and outer boundaries, and serve as units for these variables.

We adopt the same non-dimensional form as Jones et al. (2011): length is scaled by the shell width d, time by the magnetic diffusion time d^2/η, and entropy by the imposed entropy difference Δs. The magnetic field is measured in units of $\sqrt{\Omega\varrho_\mathrm{c}\mu\eta}$ where μ is the magnetic permeability. Then, the equations governing the system are

$$\frac{\partial \boldsymbol{v}}{\partial t} + \boldsymbol{v}\cdot\nabla\boldsymbol{v} = Pm\Big[-\frac{1}{E}\nabla\frac{P'}{w^n} + \frac{Pm}{Pr}Ra\frac{s}{r^2}\hat{\boldsymbol{r}} - \frac{2}{E}\,\hat{\boldsymbol{z}}\times\boldsymbol{v} + \boldsymbol{F}_\nu + \frac{1}{E\,w^n}(\nabla\times\boldsymbol{B})\times\boldsymbol{B}\Big], \tag{4}$$

$$\frac{\partial \boldsymbol{B}}{\partial t} = \nabla\times(\boldsymbol{v}\times\boldsymbol{B}) + \nabla^2\boldsymbol{B}, \tag{5}$$

$$\frac{\partial s}{\partial t} + \boldsymbol{v}\cdot\nabla s = w^{-n-1}\frac{Pm}{Pr}\nabla\cdot\left(w^{n+1}\,\nabla s\right) + \frac{Di}{w}\left[E^{-1}w^{-n}(\nabla\times\boldsymbol{B})^2 + Q_\nu\right], \tag{6}$$

$$\nabla\cdot(w^n\boldsymbol{v}) = 0\,, \tag{7}$$

$$\nabla\cdot\boldsymbol{B} = 0. \tag{8}$$

The viscous force $\boldsymbol{F}_\nu$ in (4) is given by $\boldsymbol{F}_\nu = w^{-n}\nabla\boldsymbol{S}$, where $\boldsymbol{S}$ is the rate of strain tensor

$$S_{ij} = 2w^n\left(e_{ij} - \frac{1}{3}\delta_{ij}\nabla\cdot\boldsymbol{v}\right), \quad e_{ij} = \frac{1}{2}\left(\frac{\partial v_\mathrm{i}}{\partial x_j} + \frac{\partial v_j}{\partial x_\mathrm{i}}\right)\cdot \tag{9}$$

Moreover, the expressions of the dissipation parameter Di and the viscous heating Q_ν in (6) are

$$Di = \frac{c_1 Pr}{PmRa}, \tag{10}$$

and

$$Q_\nu = 2\left[e_{ij}e_{ij} - \frac{1}{3}(\nabla\cdot\boldsymbol{v})^2\right]\cdot \tag{11}$$

The boundary conditions are the following. We impose stress free boundary conditions for the velocity field at both the inner and the outer sphere, the magnetic field matches a potential field inside and outside the fluid shell, and the entropy is fixed at the inner and outer boundaries.

The system of Eqs. (4)–(8) involves seven control parameters, namely the Rayleigh number $Ra = GMd\Delta s/(\nu\kappa c_p)$, the Ekman number $E = \nu/(\Omega d^2)$, the Prandtl number $Pr = \nu/\kappa$, and the magnetic Prandtl number $Pm = \nu/\eta$, together with the aspect ratio χ, the polytropic index n, and the number of density scale heights N_ϱ that define the reference state. In this study, we restrict our investigation of the parameter space keeping $E = 10^{-4}$, $Pr = 1$, $\chi = 0.35$, and $n = 2$ for all simulations. Furthermore, to differentiate the effects related to the change in gravity profile from those related to the anelastic approximation, we decided to perform low N_ϱ simulations so that we can assume that stratification no longer influences the dynamo process. In practice, we chose $N_\varrho = 0.1$, which means that the density contrast between the inner and outer spheres is only 1.1, and the simulations are thus very close to the Boussinesq limit. To further ensure the lack of stratification effects, we also checked in a few cases that the results do not differ from purely Boussinesq simulations.

We have integrated our system at least on one magnetic diffusion time with the anelastic version of (Dormy et al. (1998) and further developments), which reproduces the anelastic dynamo benchmarks (see Schrinner et al. 2014). The vector fields are transformed into scalars using the poloidal-toroidal decomposition. The equations are then discretized in the radial direction with a finite-difference scheme; on each concentric sphere, variables are expanded using a spherical harmonic basis. The coefficients of the expansion are identified with their degree ℓ and order m. Typical resolutions use from 256 to 288 points in the radial direction and a spectral decomposition truncated at $80 \leq \ell_\mathrm{max} \sim m_\mathrm{max} \leq 116$.

2.2. Diagnostic parameters

The quantities used to analyse our simulations first rely on the kinetic and magnetic energy densities E_k and E_m,

$$E_\mathrm{k} = \frac{1}{2\,V}\int_V w^n \boldsymbol{v}^2\,\mathrm{d}v \quad \text{and} \quad E_\mathrm{m} = \frac{1}{2\,V}\frac{Pm}{E}\int_V \boldsymbol{B}^2\,\mathrm{d}v. \qquad (12)$$

We define the corresponding Rossby number $Ro = \sqrt{2E_\mathrm{k}}E/Pm$ and Lorentz number $Lo = \sqrt{2E_\mathrm{m}}E/Pm$. The latter is a non-dimensional measure of the magnetic field amplitude, while the former is a non-dimensional measure of the velocity field amplitude. A measure of the mean zonal flow is the zonal Rossby number Ro_z, whose definition is based on the averaged toroidal axisymmetric kinetic energy density. To distinguish between dipolar and multipolar dynamo regimes, we know from Boussinesq results that it is useful to measure the balance between inertia and Coriolis force, which can be approximated in terms of a local Rossby number $Ro_\ell = Ro_\mathrm{c}\,\ell_\mathrm{c}/\pi$, which depends on the characteristic length scale of the flow rather than on the shell thickness (Christensen & Aubert 2006; Olson & Christensen 2006; Schrinner et al. 2012). Again, we emphasize that our definition of the local Rossby number tries to avoid any dependence on the mean zonal flow and thus differs from the original definition introduced by Christensen & Aubert (2006)(see Schrinner et al. 2012, App. A for a discussion). Our typical convective length scale is based on the mean harmonic degree ℓ_c of the velocity component $\boldsymbol{v}_\mathrm{c}$ from which the mean zonal flow has been subtracted,

$$\ell_\mathrm{c} = \sum_\ell \ell\,\frac{\langle w^n\,(\boldsymbol{v}_\mathrm{c})_\ell \cdot (\boldsymbol{v}_\mathrm{c})_\ell\rangle}{\langle w^n\,\boldsymbol{v}_\mathrm{c}\cdot\boldsymbol{v}_\mathrm{c}\rangle}. \qquad (13)$$

Where the brackets denote an average of time and radii. Consistently, the contribution of the mean zonal flow is removed for calculating Ro_c.

The dipolarity of the magnetic field is characterized by the relative dipole field strength, f_dip, originally defined as the time-average ratio on the outer shell boundary S_o of the dipole field strength to the total field strength,

$$f_\mathrm{dip} = \left\langle \sqrt{\frac{\int_{S_o} {\boldsymbol{B}^2}_{\ell=1}^{m=\{0,1\}}\,\sin\theta\,\mathrm{d}\theta\,\mathrm{d}\phi}{\int_{S_o} \boldsymbol{B}^2\,\sin\theta\,\mathrm{d}\theta\,\mathrm{d}\phi}} \right\rangle_t. \qquad (14)$$

We also define a relative *axial* dipole field strength filtering out non-axisymmetric contributions

$$f_{\mathrm{dip}_\mathrm{ax}} = \left\langle \sqrt{\frac{\int_{S_o} {\boldsymbol{B}^2}_{\ell=1}^{m=0}\,\sin\theta\,\mathrm{d}\theta\,\mathrm{d}\phi}{\int_{S_o} \boldsymbol{B}^2\,\sin\theta\,\mathrm{d}\theta\,\mathrm{d}\phi}} \right\rangle_t. \qquad (15)$$

This definition of $f_{\mathrm{dip}_\mathrm{ax}}$ is similar to the relative dipole field strength used by Gastine et al. (2012), except for the square root, which explains the lower values for the dipolarity found in Gastine et al. (2012).

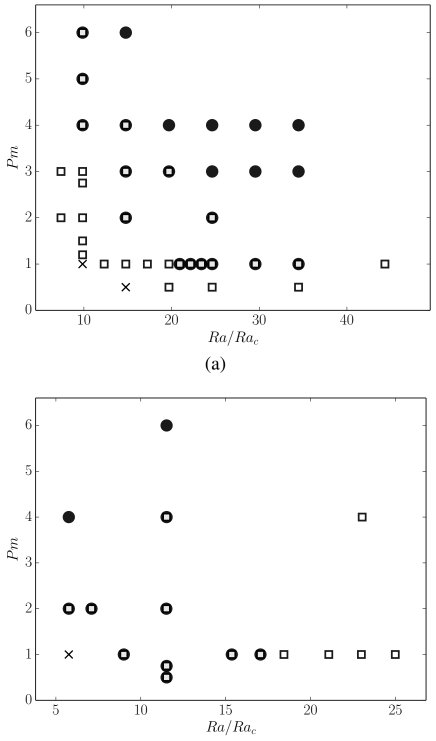

(a)

(b)

Fig. 1. Dipolar (black circles) and multipolar (white squares) dynamos as a function of Ra/Ra_c and Pm, for a central mass **a)** and a uniform mass distribution **b)**. Crosses indicate the absence of a self-sustained dynamo.

To further characterize the topology of the magnetic field, we introduce a time-averaged measure of the departure from a pure equatorial dipole solution

$$\theta = \frac{2}{\pi}\left\langle \sqrt{\left(\Theta(t) - \frac{\pi}{2}\right)^2} \right\rangle_t, \qquad (16)$$

where Θ is the tilt angle of the dipole axis. A low value of θ indicates that the tilt angle of the dipole fluctuates close to $\Theta = \pi/2$.

3. Results

3.1. Bifurcations between dynamo branches

In our simulations we recover the two distinct dynamo regimes observed with both Boussinesq (Kutzner & Christensen 2002; Christensen & Aubert 2006; Schrinner et al. 2012; Yadav et al. 2013a) and anelastic models (Gastine et al. 2012; Schrinner et al. 2014). These are characterized by different magnetic field configurations: dipolar dynamos are dominated by a strong axial dipole component, whereas "non-dipolar" dynamos usually present a more complex geometry with higher spatial and temporal variability. The branches are easily identified by continuing simulations performed with other parameters, for which the dipolar/multipolar characteristic was previously established. Figure 1a shows the regime diagram we obtained, as a function of the Rayleigh and magnetic Prandtl numbers. For comparison,

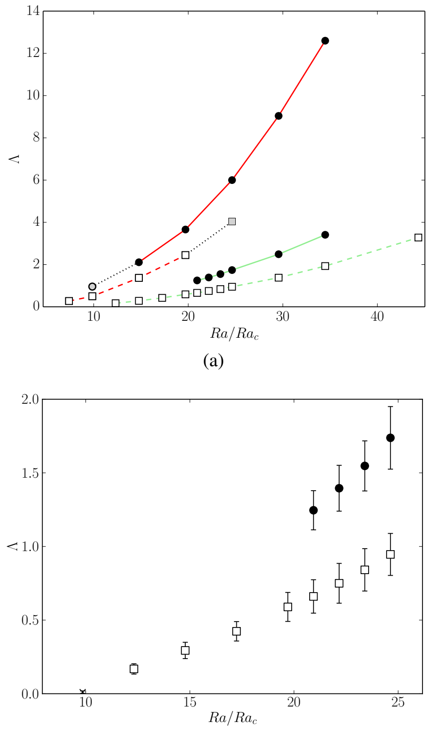

(a)

(b)

Fig. 2. a) Elsasser number Λ as a function of Ra/Ra_c, for $Pm = 1$ (green) and $Pm = 3$ (red). The meaning of the symbol shapes is defined in the caption of Fig. 1. A grey marker indicates that the solution loses its stability. **b)** Detail of the bifurcation close to the dynamo threshold for $Pm = 1$. Error bars represent the standard deviations.

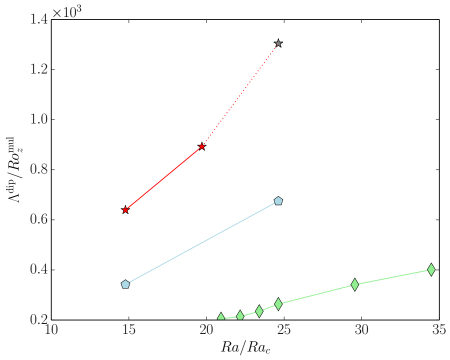

Fig. 3. $\Lambda^{\rm dip}/Ro_z^{\rm mul}$ as a function of Ra/Ra_c, for $Pm = 1$ (green diamonds), $Pm = 2$ (blue pentagons) and $Pm = 3$ (red stars). The point marked with the grey star has been computed with the model corresponding to the grey square in Fig. 2.

we use the data from Schrinner et al. (2012) and show in Fig. 1b the same regime diagram obtained for Boussinesq models with a uniform mass distribution. For $Pm = 1$, the transition from the dipolar to the multipolar branch can be triggered by an increase in Ra. In that case, the transition is due to the increasing role of inertia as revealed by Ro_ℓ. Alternatively, the transition from multipolar to dipolar dynamo can be triggered by increasing Pm. Then, the multipolar branch is lost when the saturated amplitude of the mean zonal flow becomes too small to prevent the growth of the dipolar solution (see Schrinner et al. 2012). It is worth noting that the two branches overlap for a restricted parameter range for which dipolar and multipolar dynamos may coexist. In that case, the observed solution strongly depends of the initial magnetic field, so we tested both weak and strong field initial conditions for all our models to delimit the extent of the bi-stable zone with greater accuracy. Actually, multipolar dynamos are favoured by the stronger zonal wind that may develop with stress-free boundary conditions, allowing for this hysteretic transition (Schrinner et al. 2012). Finally, we see that the dynamo threshold is lower for multipolar models, which allows the multipolar branch to extend below the dipolar branch at low Rayleigh and magnetic Prandtl numbers. We see in Fig. 1b that this is different from Boussinesq models with a uniform mass distribution.

To investigate the different transitions between the different dynamo branches, we plot the Elsasser number $\Lambda = B^2_{\rm rms}/(\Omega\varrho_c\mu\eta)$ in Fig. 2a (related to the Lorentz number by $\Lambda = Lo^2 Pm/E$) as a function of the distance to the threshold for models at $Pm = 1$ and $Pm = 3$. We see in Fig. 2b that the bifurcation for multipolar branch is supercritical. When decreasing the Rayleigh number, the dipolar branch loses its stability for $Ra/Ra_c \sim 20$, when the magnetic field strength becomes too weak.

For higher magnetic Prandtl numbers, the bifurcation of the multipolar branch still seems to be supercritical. Interestingly, one notes in Fig. 2a for $Pm = 3$ that the multipolar branch loses its stability when increasing the Rayleigh number. A physical explanation for this behaviour is that the mean zonal flow does not grow fast enough as the field strength increases, and the dynamo switches to the dipolar solution. This simple physical scenario can be illustrated by comparing the variation in the field strength of the dipolar branch, as measured by $\Lambda^{\rm dip}$, and the zonal shear of the multipolar branch, as measured by $Ro_z^{\rm mul}$. Indeed, we see in Fig. 3 that the higher the magnetic Prandtl number, the faster the growth of the ratio between $\Lambda^{\rm dip}$ and $Ro_z^{\rm mul}$. This explains why the multipolar branch destabilizes at large forcing for larger Pm ($Pm = 3$, red dashed line in Fig. 2a), while it remains stable at smaller Pm ($Pm = 1$, dashed green line in Fig. 2a). Because of computational limitations, we were not able to find for $Pm > 1$ the Rayleigh numbers for which the dipolar branch should disappear.

3.2. Equatorial dipole

Schrinner et al. (2014) show that dipolar and multipolar dynamos in anelastic simulations were no longer distinguishable from each other in terms of $f_{\rm dip}$, contrary to Boussinesq models. This smoother transition has been attributed to the presence of dynamos with a high equatorial dipole contribution, which leads to intermediate values for $f_{\rm dip}$. However, Fig. 4a shows that this tendency already exits at low N_ϱ, and thus cannot be accounted for only in terms of anelastic effects. Furthermore, when the equatorial dipole component is removed to compute the relative dipole field strength, we recover a more abrupt transition, as we can see in Fig. 4b which shows the relative axial dipole field strength $f_{\rm dip_{ax}}$. Dipolar dynamos are left unchanged by this new definition, whereas multipolar dynamos of intermediate dipolarity are no longer observed, which confirms that the increase

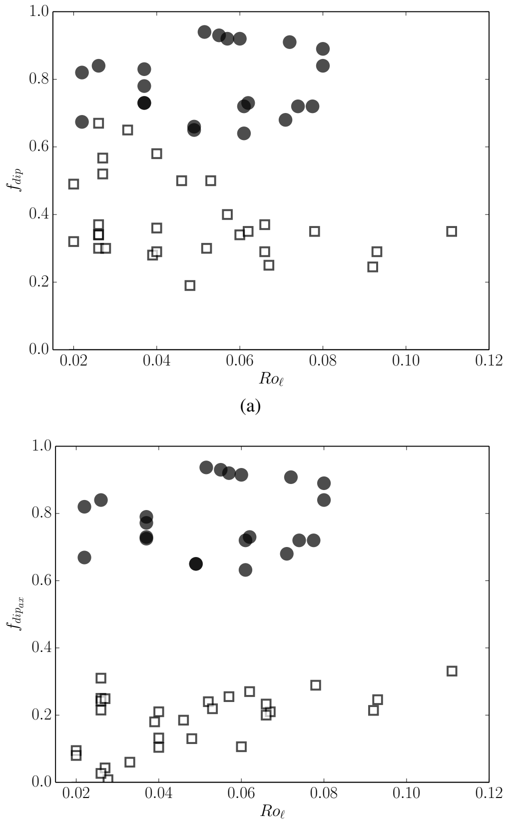

(a)

(b)

Fig. 4. **a)** Relative dipole field strength f_{dip} versus local Rossby number. **b)** Relative axial dipole field strength $f_{\mathrm{dip_{ax}}}$ versus local Rossby number. The meaning of the symbol shapes is defined in the caption of Fig. 1.

in f_{dip} is due to a significant equatorial dipole component. The quantity $f_{\mathrm{dip_{ax}}}$ therefore provides a robust criterion to distinguish the dipolar and the multipolar branches.

To further characterize the emergence of multipolar dynamos with a significant equatorial dipole contribution, we plot the values of the modified tilt angle θ in the parameter space in Fig. 5a. Low values of θ are characteristic of an equatorial dipole on the surface of the outer sphere and they appear to be preferably localized close to the dynamo threshold of the multipolar branch, at low Rayleigh and magnetic Prandtl numbers. In our case, dynamos with a stronger equatorial dipole component belong to the class of multipolar dynamos, but since they are always close to the threshold, fewer modes are likely to be excited. As the Rayleigh number or the magnetic Prandtl number is increased, the dipole axis is not stable anymore but fluctuates in the interval $[0, \pi]$, which is typical of polarity reversals for multipolar dynamos (Kutzner & Christensen 2002). This evolution is illustrated in Fig. 5b for dynamos at $Pm = 1$. For this subset of models, we computed the percentage of the non-axisymmetric magnetic energy density with respect to the total magnetic energy density E_{m} and saw that it tends to increase from 85%

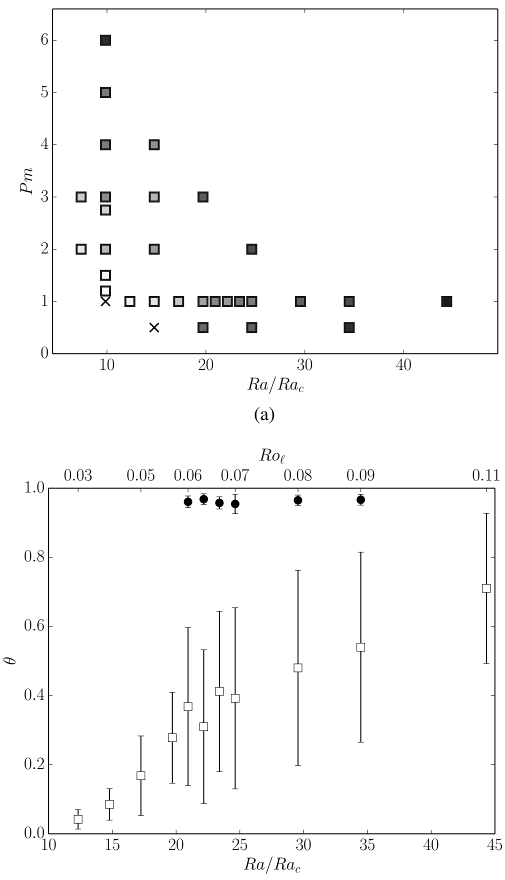

(a)

(b)

Fig. 5. **a)** Evolution of the modified tilt angle θ defined by Eq. (16) for multipolar dynamos as a function of Ra/Ra_{c} and Pm. Colour scale ranges from white ($\theta = 0$) to black ($\theta = 0.7$). **b)** θ as a function of Ra/Ra_{c} for $Pm = 1$. Upper x axis corresponds to the values of Ro_ℓ for the multipolar branch. The meaning of the symbol shapes is defined in the caption of Fig. 1. Error bars represent the standard deviations.

on average for multipolar dynamos up to 93% as the Rayleigh number is decreased.

Part of the changes reported in Schrinner et al. (2014) about anelastic dynamos simulations do not seem to come from the stratified reference density profile, but from the choice of a gravity profile proportional to $1/r^2$. This profile differs from the gravity profile proportional to r that was used for Boussinesq simulations and is actually the only significant difference between previous studies and our low N_ϱ simulations. As a consequence, convection cells form and stay closer to the inner sphere, as we can see in Fig. 6. We compare here equatorial cuts of the radial component of the velocity for both choices of gravity profile. This strong difference in the flow reflects on the localization of the active dynamo regions, as we can see in the corresponding cuts of the radial component of the magnetic field in Fig. 7. With a gravity profile proportional to $1/r^2$, the magnetic field is mainly generated close to the inner sphere where the convection cells

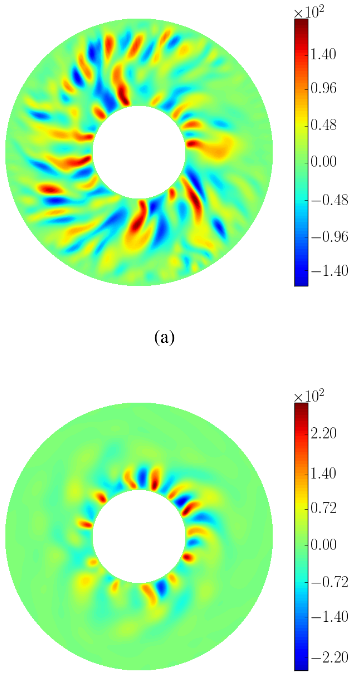

(a)

(b)

Fig. 6. Equatorial cross-section of the radial component of the velocity, with $E = 10^{-4}$, $Pr = 1$. **a)** $g \propto r$ and $Ra/Ra_c = 9.0$, $Pm = 1$. **b)** $g \propto 1/r^2$ and $Ra/Ra_c = 9.9$, $Pm = 1.2$.

form. Consequently, our measure of the dipole field strength $f_{\rm dip}$ at the surface of the outer sphere appears to be biased, since it will essentially be sensitive to the less diffusive large scale modes. This filter effect is likely to be responsible for the increase in $f_{\rm dip}$ we reported in some anelastic dynamo models. However, for higher density stratification $N_\varrho = 3$ and Prandtl numbers $Pr = 2$ and $Pm = 4$, Schrinner et al. (2014) identify equatorial dipole dynamos with a $m = 1$ component that is not localized on the outer sphere and for which the present mechanism will not be relevant.

4. Conclusion

In this paper, we focussed on very weakly stratified anelastic dynamo models with a central mass distribution. We investigated the bifurcations between the dipolar and multipolar dynamo branches and recovered in parts the behaviour that has been observed for Boussinesq models with a uniform mass distribution. In addition, we show that the dipolar branch can now lose its stability and switch to the multipolar branch at low Rayleigh and magnetic Prandtl numbers. The multipolar dynamos that are observed in this restricted parameter regime usually present a stronger equatorial dipole component at the surface of the outer sphere. When increasing the Rayleigh number at higher Pm, it seems that the mean zonal flow does not grow fast enough to maintain the multipolar solution, and we identified several cases where the multipolar branch switches to the dipolar solution.

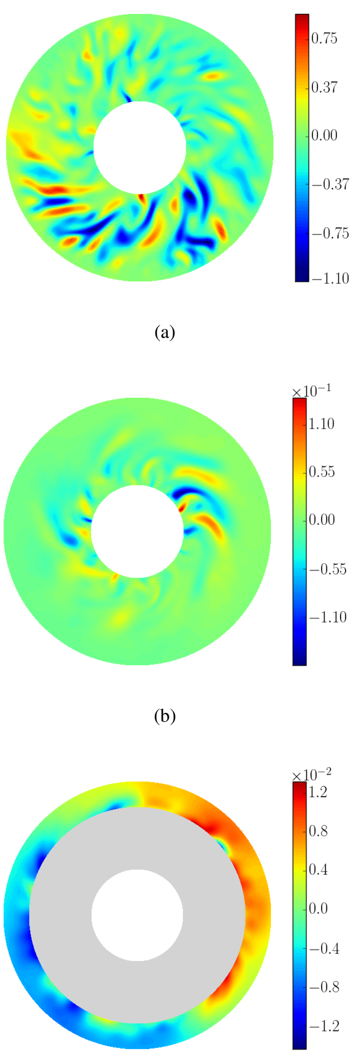

(a)

(b)

(c)

Fig. 7. Equatorial cross-section of the radial component of the magnetic field,with $E = 10^{-4}$, $Pr = 1$. **a)** $g \propto r$ and $Ra/Ra_c = 9.0$, $Pm = 1$. **b)**, **c)** $g \propto 1/r^2$ and $Ra/Ra_c = 9.9$, $Pm = 1.2$. Colour in panel **c)** has been rescaled to highlight the emergence of a $m = 1$ mode at the outer sphere.

This study has shed interesting light on the recent systematic parameter study of spherical anelastic dynamo models started by Schrinner et al. (2014). Focussing on weakly stratified dynamo models, we showed that magnetic field configurations with a significant equatorial dipole contribution can already be observed in the Boussinesq limit. In the parameter regime we investigate, our study reveals that the choice of gravity profile has a strong influence on the fluid flow and thus on the dynamo generated magnetic field, depending whether one considers a uniform or a central mass distribution. In the parameter space, we showed that multipolar dynamos with a significant equatorial dipole contribution are preferably observed close to the dynamo threshold. This is reminiscent of the results of Aubert & Wicht (2004), who studied the competition between axial and equatorial dipolar dynamos when varying the aspect ratio of the spherical shell in geodynamo models.

However, the filter effect we highlight here focusses on the topology of the magnetic field at the outer surface of the models. As a consequence, it will not be able to explain the stronger equatorial dipole component for all models in Schrinner et al. (2014). Independently, Cole et al. (2014) also report the discovery of an azimuthal dynamo wave of a $m = 1$ mode in numerical simulations corresponding to higher density stratification. Their Coriolis number plays a similar role to the inverse of our local Rossby number. Upper x axis of Fig. 5b shows that equatorial dipole configurations are favoured with the decrease in Ro_ℓ.

Observational results from photometry (Hackman et al. 2013) and spectropolarimetry (Kochukhov et al. 2013) of rapidly rotating cool active stars reveal that the surface magnetic field of these objects can be highly non-axisymmetric. Further investigation of direct numerical simulations is therefore required to better understand the influence of the Prandtl number and the density stratification on the magnetic field topology.

Acknowledgements. This work was granted access to the HPC resources of MesoPSL financed by the Région Ile-de-France and the project Equip@Meso (reference ANR-10-EQPX-29-01) of the programme Investissements d'Avenir supervised by the French Agence Nationale pour la Recherche. Numerical simulations were also carried out at CEMAG and TGCC computing centres (GENCI project x2013046698). L. P. acknowledges financial support from "Programme National de Physique Stellaire" (PNPS) of CNRS/INSU, France.

References

Alboussière, T., & Ricard, Y. 2013, J. Fluid Mech., 725, 1
Anufriev, A. P., Jones, C. A., & Soward, A. M. 2005, Phys. Earth Planet. Inter., 152, 163
Aubert, J., & Wicht, J. 2004, Earth Planet. Sci. Lett., 221, 409
Berkoff, N. A., Kersale, E., & Tobias, S. M. 2010, Geophys. Astrophys. Fluid Dyn., 104, 545
Boussinesq, J. 1903, Théorie analytique de la chaleur, Vol. 2 (Gauthier-Villars)
Braginsky, S. I., & Roberts, P. H. 1995, Geophys. Astrophys. Fluid Dyn., 79, 1
Brown, B. P., Vasil, G. M., & Zweibel, E. G. 2012, ApJ, 756, 109
Busse, F. H., & Simitev, R. D. 2006, Geophys. Astrophys. Fluid Dyn., 100, 341
Christensen, U. R., & Aubert, J. 2006, Geophys. J. Int., 166, 97
Christensen, U. R., Aubert, J., Cardin, P., et al. 2001, Phys. Earth Planet. Inter., 128, 25
Cole, E., Käpylä, P. J., Mantere, M. J., & Brandenburg, A. 2014, ApJ, 780, L22
Donati, J.-F., & Landstreet, J. D. 2009, ARA&A, 47, 333
Dormy, E., Cardin, P., & Jault, D. 1998, Earth Planet. Sci. Lett., 160, 15
Dormy, E., & Soward, A. M. 2007, Mathematical aspects of natural dynamos (CRC Press/Taylor & Francis)
Duarte, L. D. V., Gastine, T., & Wicht, J. 2013, Phys. Earth Planet. Inter., 222, 22
Gastine, T., Duarte, L., & Wicht, J. 2012, A&A, 546, A19
Gilman, P. A., & Glatzmaier, G. A. 1981, ApJS, 45, 335
Gissinger, C., Petitdemange, L., Schrinner, M., & Dormy, E. 2012, Phys. Rev. Lett., 108, 234501
Gough, D. O. 1969, J. Atmos. Sci., 26, 448
Hackman, T., Pelt, J., Mantere, M. J., et al. 2013, A&A, 553, A40
Jones, C. A. 2011, Ann. Rev. Fluid Mech., 43, 583
Jones, C. A., Boronski, P., Brun, A. S., et al. 2011, Icarus, 216, 120
Kochukhov, O., Mantere, M. J., Hackman, T., & Ilyin, I. 2013, A&A, 550, A84
Kutzner, C., & Christensen, U. R. 2002, Phys. Earth Planet. Inter., 131, 29
Lantz, S. R., & Fan, Y. 1999, ApJS, 121, 247
Morin, J., Donati, J.-F., Petit, P., et al. 2010, MNRAS, 407, 2269
Morin, J., Dormy, E., Schrinner, M., & Donati, J.-F. 2011, MNRAS, 418, L133
Ogura, Y., & Phillips, N. A. 1962, J. Atmos. Sci., 19, 173
Olson, P., & Christensen, U. R. 2006, Earth Planet. Sci. Lett., 250, 561
Reinhold, T., Reiners, A., & Basri, G. 2013, A&A, 560, A4
Sasaki, Y., Takehiro, S.-i., Kuramoto, K., & Hayashi, Y.-Y. 2011, Phys. Earth Planet. Inter., 188, 203
Schrinner, M., Petitdemange, L., & Dormy, E. 2012, ApJ, 752, 121
Schrinner, M., Petitdemange, L., Raynaud, R., & Dormy, E. 2014, A&A, 564, A78
Stelzer, Z., & Jackson, A. 2013, Geophys. J. Int., 193, 1265
Yadav, R. K., Gastine, T., & Christensen, U. R. 2013a, Icarus, 225, 185
Yadav, R. K., Gastine, T., Christensen, U. R., & Duarte, L. D. V. 2013b, ApJ, 774, 6

Pages 8 to 9 are available in the electronic edition of the journal at `http://www.aanda.org`

Appendix A: Scaling laws

Table A.1. Summary of the coefficients obtained for the different scaling laws, with their standard error from the linear regression.

Scaling	α	β	χ_{rel}
$Lo/\sqrt{f_{\mathrm{ohm}}}$			
Multipolar	0.29 ± 0.01	-0.52 ± 0.1	0.06
Dipolar	0.32 ± 0.02	-0.08 ± 0.2	0.06
Ro	0.39 ± 0.01	0.35 ± 0.2	0.1
$Nu^{\star}$	0.58 ± 0.003	-1.16 ± 0.04	0.03

For our samples of models we compute the usual scaling laws that have been derived for the magnetic and velocity fields and the convective heat flux (Christensen & Aubert 2006; Yadav et al. 2013a; Stelzer & Jackson 2013; Yadav et al. 2013b). As in Schrinner et al. (2014), we do not attempt to solve any secondary dependence on Pm because we do not vary this parameter on a wide enough range. We transform our problem to a linear one by taking the logarithm and look for a law of the form $\ln \hat{y} = \beta + \alpha \ln x$. To quantify the misfit between data and fitted values, we follow Christensen & Aubert (2006) and compute the relative misfit

$$\chi_{\mathrm{rel}} = \sqrt{\frac{1}{n}\sum_{i=1}^{n}\left(\frac{y_{\mathrm{i}} - \hat{y}_{\mathrm{i}}}{y_{\mathrm{i}}}\right)^2}, \qquad (\mathrm{A.1})$$

where $\hat{y}_{\mathrm{i}}$ stands for predicted values, y_{i} for measured values, and n is the number of data. Our results are summarized in Table A.1 and compared with those found in Schrinner et al. (2014) and Yadav et al. (2013a) in Table A.2. We did not find significant differences between the anelastic scalings and the scaling we obtained in the Boussinesq limit with the same mass distribution. The coefficients we obtained seem closer on average to the coefficients obtained by Yadav et al. (2013a) with Boussinesq models with a uniform mass distribution. However, it is not possible to deduce from our data set any influence of N_ϱ on the different coefficients of the scaling laws. In our models, the Nusselt number evaluated at the surface of the inner sphere S_i is defined by

$$Nu_{\mathrm{bot}} = -\frac{(\exp(N_\varrho) - 1) w_{\mathrm{i}} r_{\mathrm{i}}^2}{4\pi n c_1} \int_{S_i} \frac{\partial s}{\partial r} \sin\theta \, \mathrm{d}\theta \, \mathrm{d}\phi, \qquad (\mathrm{A.2})$$

which enables a flux based Rayleigh number to be defined,

$$Ra_Q = Nu^{\star} \frac{Ra\, E^2}{r_o^2\, Pr} \quad \text{with} \quad Nu^{\star} = (Nu_{\mathrm{bot}} - 1)\frac{E}{Pr}, \qquad (\mathrm{A.3})$$

which is used in derivating scaling laws, together with the fraction of ohmic to total dissipation f_{ohm}.

Table A.2. Comparison between the different scaling laws obtained with different dynamo models.

Scaling	RPD		SPRD		YGC	
	c	x	c	x	c	x
g	$1/r^2$		$1/r^2$		r	
N_ϱ	≤ 0.1		$\in [0.5, 4]$		0	
$Lo/\sqrt{f_{\mathrm{ohm}}} = c\, Ra_Q^x$						
Multipolar	0.59	0.29	1.19	0.34	0.65	0.35
Dipolar	0.92	0.32	1.58	0.35	1.08	0.37
$Ro = c\, Ra_Q^x$	1.42	0.39	1.66	0.42	1.79^a	0.44^a
					0.73^b	0.39^b
$Nu^{\star} = c\, Ra_Q^x$	0.31	0.58	0.25	0.59	0.06	0.52

Notes. RPD refers to the present study, SPRD to Schrinner et al. (2014), and YGC to Yadav et al. (2013a), respectively. Yadav et al. (2013a) distinguished between dipolar and multipolar dynamos for their Rossby number scaling, whereas we derived a single power law for both classes of dynamo models. [(a)] Multipolar models. [(b)] Dipolar models.

Appendix B: Numerical models

Table B.1. Overview of the simulations carried out with $E = 10^{-4}$, $Pr = 1$, $\chi = 0.35$, $n = 2$, and $N_\varrho = 0.1$.

Model	Ra	Pm	Ro	Ro_ℓ	ℓ_c	Lo	Nu	f_{dip}	$f_{dip_{ax}}$	f_{ohm}
1m	1.50×10^6	2.00	3.6×10^{-3}	2.0×10^{-2}	1.8×10^1	2.1×10^{-3}	1.4	4.9×10^{-1}	8.0×10^{-2}	8.0×10^{-2}
2m	1.50×10^6	3.00	3.8×10^{-3}	2.0×10^{-2}	1.6×10^1	3.0×10^{-3}	1.5	3.2×10^{-1}	9.5×10^{-2}	1.5×10^{-1}
3m	2.00×10^6	1.20	6.8×10^{-3}	2.6×10^{-2}	1.7×10^1	2.5×10^{-3}	1.7	6.7×10^{-1}	2.7×10^{-2}	8.1×10^{-2}
4m	2.00×10^6	1.50	6.2×10^{-3}	2.7×10^{-2}	1.7×10^1	3.1×10^{-3}	1.7	5.7×10^{-1}	4.3×10^{-2}	1.3×10^{-1}
5m	2.00×10^6	2.00	5.1×10^{-3}	2.7×10^{-2}	1.7×10^1	3.6×10^{-3}	1.8	5.2×10^{-1}	2.5×10^{-1}	1.7×10^{-1}
6m	2.00×10^6	2.75	5.2×10^{-3}	2.8×10^{-2}	1.7×10^1	4.0×10^{-3}	1.8	3.0×10^{-1}	8.0×10^{-3}	2.1×10^{-1}
7m	2.00×10^6	2.90	5.2×10^{-3}	2.3×10^{-2}	1.6×10^1	4.1×10^{-3}	1.8	6.4×10^{-1}	1.3×10^{-1}	1.9×10^{-1}
8m	2.00×10^6	3.00	5.9×10^{-3}	2.6×10^{-2}	1.6×10^1	4.1×10^{-3}	1.8	3.7×10^{-1}	2.4×10^{-1}	1.9×10^{-1}
9m	2.00×10^6	4.00	5.6×10^{-3}	2.6×10^{-2}	1.6×10^1	4.5×10^{-3}	1.8	3.0×10^{-1}	2.1×10^{-1}	2.2×10^{-1}
9d	2.00×10^6	4.00	5.3×10^{-3}	2.2×10^{-2}	1.4×10^1	6.6×10^{-3}	1.7	8.2×10^{-1}	8.2×10^{-1}	4.0×10^{-1}
10m	2.00×10^6	5.00	5.5×10^{-3}	2.6×10^{-2}	1.6×10^1	4.7×10^{-3}	1.8	3.4×10^{-1}	2.5×10^{-1}	2.3×10^{-1}
10d	2.00×10^6	5.00	5.3×10^{-3}	2.6×10^{-2}	1.4×10^1	6.6×10^{-3}	1.8	8.4×10^{-1}	8.4×10^{-1}	3.9×10^{-1}
11m	2.00×10^6	6.00	5.4×10^{-3}	2.6×10^{-2}	1.6×10^1	4.8×10^{-3}	1.8	3.4×10^{-1}	3.1×10^{-1}	2.5×10^{-1}
11d	2.00×10^6	6.00	5.7×10^{-3}	2.2×10^{-2}	1.3×10^1	9.0×10^{-3}	1.9	6.7×10^{-1}	6.7×10^{-1}	4.9×10^{-1}
12m	2.50×10^6	1.00	8.0×10^{-3}	3.3×10^{-2}	1.6×10^1	4.1×10^{-3}	2.0	6.5×10^{-1}	6.0×10^{-2}	1.8×10^{-1}
13m	3.00×10^6	1.00	7.8×10^{-3}	4.0×10^{-2}	1.6×10^1	5.3×10^{-3}	2.3	5.8×10^{-1}	1.0×10^{-1}	2.2×10^{-1}
14m	3.00×10^6	2.00	8.9×10^{-3}	4.0×10^{-2}	1.6×10^1	6.4×10^{-3}	2.4	3.6×10^{-1}	2.1×10^{-1}	2.6×10^{-1}
14d	3.00×10^6	2.00	7.4×10^{-3}	3.7×10^{-2}	1.5×10^1	8.1×10^{-3}	2.4	8.3×10^{-1}	7.9×10^{-1}	3.9×10^{-1}
15m	3.00×10^6	3.00	8.7×10^{-3}	4.0×10^{-2}	1.6×10^1	6.8×10^{-3}	2.5	2.9×10^{-1}	1.3×10^{-1}	2.8×10^{-1}
15d	3.00×10^6	3.00	7.5×10^{-3}	3.7×10^{-2}	1.6×10^1	8.4×10^{-3}	2.3	7.8×10^{-1}	7.7×10^{-1}	4.0×10^{-1}
16m	3.00×10^6	4.00	8.2×10^{-3}	3.9×10^{-2}	1.6×10^1	7.2×10^{-3}	2.4	2.8×10^{-1}	1.8×10^{-1}	3.1×10^{-1}
16d	3.00×10^6	4.00	7.5×10^{-3}	3.7×10^{-2}	1.6×10^1	8.7×10^{-3}	2.4	7.3×10^{-1}	7.2×10^{-1}	4.0×10^{-1}
17d	3.00×10^6	6.00	7.8×10^{-3}	3.7×10^{-2}	1.5×10^1	9.2×10^{-3}	2.5	7.3×10^{-1}	7.3×10^{-1}	4.0×10^{-1}
18m	3.50×10^6	1.00	9.1×10^{-3}	4.6×10^{-2}	1.6×10^1	6.5×10^{-3}	2.6	5.0×10^{-1}	1.8×10^{-1}	2.5×10^{-1}
19m	4.00×10^6	0.50	1.7×10^{-2}	4.8×10^{-2}	1.6×10^1	4.9×10^{-3}	2.7	1.9×10^{-1}	1.3×10^{-1}	1.9×10^{-1}
20m	4.00×10^6	1.00	1.0×10^{-2}	5.3×10^{-2}	1.6×10^1	7.7×10^{-3}	3.0	5.0×10^{-1}	2.2×10^{-1}	3.1×10^{-1}
21m	4.00×10^6	3.00	1.1×10^{-2}	5.2×10^{-2}	1.6×10^1	9.0×10^{-3}	3.1	3.0×10^{-1}	2.4×10^{-1}	3.4×10^{-1}
21d	4.00×10^6	3.00	1.0×10^{-2}	4.9×10^{-2}	1.6×10^1	1.1×10^{-2}	3.1	6.5×10^{-1}	6.5×10^{-1}	4.2×10^{-1}
22d	4.00×10^6	4.00	1.0×10^{-2}	4.9×10^{-2}	1.5×10^1	1.2×10^{-2}	3.1	6.6×10^{-1}	6.5×10^{-1}	4.3×10^{-1}
23m	4.25×10^6	1.00	1.1×10^{-2}	5.7×10^{-2}	1.6×10^1	8.1×10^{-3}	3.2	4.0×10^{-1}	2.6×10^{-1}	2.8×10^{-1}
23d	4.25×10^6	1.00	1.0×10^{-2}	5.1×10^{-2}	1.6×10^1	1.1×10^{-2}	3.2	9.4×10^{-1}	9.4×10^{-1}	4.4×10^{-1}
24m	4.50×10^6	1.00	1.2×10^{-2}	6.0×10^{-2}	1.6×10^1	8.7×10^{-3}	3.4	3.4×10^{-1}	1.1×10^{-1}	3.0×10^{-1}
24d	4.50×10^6	1.00	1.1×10^{-2}	5.5×10^{-2}	1.6×10^1	1.2×10^{-2}	3.4	9.3×10^{-1}	9.3×10^{-1}	4.4×10^{-1}
25m	4.75×10^6	1.00	1.2×10^{-2}	6.2×10^{-2}	1.6×10^1	9.2×10^{-3}	3.6	3.5×10^{-1}	2.7×10^{-1}	3.0×10^{-1}
25d	4.75×10^6	1.00	1.2×10^{-2}	5.7×10^{-2}	1.5×10^1	1.2×10^{-2}	3.6	9.2×10^{-1}	9.2×10^{-1}	4.5×10^{-1}
26m	5.00×10^6	0.50	1.7×10^{-2}	6.6×10^{-2}	1.6×10^1	8.1×10^{-3}	3.7	2.9×10^{-1}	2.0×10^{-1}	2.5×10^{-1}
27m	5.00×10^6	1.00	1.3×10^{-2}	6.6×10^{-2}	1.6×10^1	9.7×10^{-3}	3.8	3.7×10^{-1}	2.3×10^{-1}	3.2×10^{-1}
28d	5.00×10^6	1.00	1.2×10^{-2}	6.0×10^{-2}	1.5×10^1	1.3×10^{-2}	3.8	9.2×10^{-1}	9.2×10^{-1}	4.6×10^{-1}
29m	5.00×10^6	2.00	1.4×10^{-2}	6.7×10^{-2}	1.6×10^1	1.1×10^{-2}	3.9	2.5×10^{-1}	2.1×10^{-1}	3.6×10^{-1}
30d	5.00×10^6	2.00	1.2×10^{-2}	6.1×10^{-2}	1.6×10^1	1.4×10^{-2}	3.9	7.2×10^{-1}	7.2×10^{-1}	4.6×10^{-1}
31d	5.00×10^6	3.00	1.2×10^{-2}	6.1×10^{-2}	1.6×10^1	1.4×10^{-2}	3.9	6.4×10^{-1}	6.3×10^{-1}	4.6×10^{-1}
32d	5.00×10^6	4.00	1.3×10^{-2}	6.2×10^{-2}	1.6×10^1	1.4×10^{-2}	4.1	7.3×10^{-1}	7.3×10^{-1}	4.3×10^{-1}
33m	6.00×10^6	1.00	1.5×10^{-2}	7.8×10^{-2}	1.6×10^1	1.2×10^{-2}	4.5	3.5×10^{-1}	2.9×10^{-1}	3.4×10^{-1}
34d	6.00×10^6	1.00	1.5×10^{-2}	7.2×10^{-2}	1.5×10^1	1.6×10^{-2}	4.6	9.1×10^{-1}	9.1×10^{-1}	4.9×10^{-1}
35d	6.00×10^6	3.00	1.4×10^{-2}	7.1×10^{-2}	1.6×10^1	1.7×10^{-2}	4.7	6.8×10^{-1}	6.8×10^{-1}	4.8×10^{-1}
36d	6.00×10^6	4.00	1.5×10^{-2}	7.4×10^{-2}	1.6×10^1	1.8×10^{-2}	4.9	7.2×10^{-1}	7.2×10^{-1}	4.7×10^{-1}
37m	7.00×10^6	0.50	1.8×10^{-2}	9.2×10^{-2}	1.6×10^1	1.2×10^{-2}	5.2	2.4×10^{-1}	2.1×10^{-1}	3.7×10^{-1}
38m	7.00×10^6	1.00	2.0×10^{-2}	9.3×10^{-2}	1.6×10^1	1.4×10^{-2}	5.5	2.9×10^{-1}	2.5×10^{-1}	3.7×10^{-1}
38d	7.00×10^6	1.00	1.7×10^{-2}	8.0×10^{-2}	1.5×10^1	1.8×10^{-2}	5.2	8.9×10^{-1}	8.9×10^{-1}	5.2×10^{-1}
39d	7.00×10^6	3.00	1.6×10^{-2}	7.7×10^{-2}	1.5×10^1	2.0×10^{-2}	5.4	7.2×10^{-1}	7.2×10^{-1}	5.2×10^{-1}
40d	7.00×10^6	4.00	1.7×10^{-2}	8.0×10^{-2}	1.6×10^1	2.1×10^{-2}	5.4	8.4×10^{-1}	8.4×10^{-1}	5.0×10^{-1}
41m	9.00×10^6	1.00	2.4×10^{-2}	1.1×10^{-1}	1.5×10^1	1.8×10^{-2}	6.8	3.5×10^{-1}	3.3×10^{-1}	4.1×10^{-1}

Notes. The critical Rayleigh number for the onset of convection is $Ra_c = 2.03 \times 10^5$, and the corresponding critical azimuthal wavenumber $m_c = 8$.

B.4 *Dipolar dynamos in stratified systems*

Raynaud, R., Petitdemange, L. & Dormy, E., 2015, *Monthly Notices of the RAS*, **448**, 2055-2065.

Liens de téléchargement :
- mnras.oxfordjournals.org/content/448/3/2055.short
- arxiv.org/abs/1503.00165v2
- hal.archives-ouvertes.fr/hal-01122919v1

Monthly Notices of the ROYAL ASTRONOMICAL SOCIETY
MNRAS **448,** 2055–2065 (2015) doi:10.1093/mnras/stv122

Dipolar dynamos in stratified systems

R. Raynaud,[1,2★] L. Petitdemange[1,2] and E. Dormy[1,3]

[1]*MAG (ENS/IPGP), LRA, Département de Physique, École normale supérieure, 24 rue Lhomond, F-75252 Paris Cedex 5, France*
[2]*LERMA, Observatoire de Paris, PSL Research University, CNRS, UMR 8112, F-75014 Paris, France*
[3]*IPGP, CNRS UMR 7154, F-75005 Paris, France*

Accepted 2015 January 15. Received 2015 January 15; in original form 2014 December 9

ABSTRACT

Observations of low-mass stars reveal a variety of magnetic field topologies ranging from large-scale, axial dipoles to more complex magnetic fields. At the same time, three-dimensional spherical simulations of convectively driven dynamos reproduce a similar diversity, which is commonly obtained either with Boussinesq models or with more realistic models based on the anelastic approximation, which take into account the variation of the density with depth throughout the convection zone. Nevertheless, a conclusion from different anelastic studies is that dipolar solutions seem more difficult to obtain as soon as substantial stratifications are considered. In this paper, we aim at clarifying this point by investigating in more detail the influence of the density stratification on dipolar dynamos. To that end, we rely on a systematic parameter study that allows us to clearly follow the evolution of the stability domain of the dipolar branch as the density stratification is increased. The impact of the density stratification both on the dynamo onset and the dipole collapse is discussed and compared to previous Boussinesq results. Furthermore, our study indicates that the loss of the dipolar branch does not ensue from a specific modification of the dynamo mechanisms related to the background stratification, but could instead result from a bias as our observations naturally favour a certain domain in the parameter space characterized by moderate values of the Ekman number, owing to current computational limitations. Moreover, we also show that the critical magnetic Reynolds number of the dipolar branch is scarcely modified by the increase of the density stratification, which provides an important insight into the global understanding of the impact of the density stratification on the stability domain of the dipolar dynamo branch.

Key words: convection – dynamo – MHD – stars: magnetic field.

1 INTRODUCTION

Observations of low-mass stars reveal very different magnetic field topologies, ranging from small-scale fields to large-scale dipolar fields, and the last advances in spectropolarimetry should enable one to improve the understanding of the magnetic fields of solar-type stars (Donati & Landstreet 2009; Morin et al. 2010). Among the three suggestions advanced by Larmor to explain the generation of such magnetic fields (Larmor 1919), it is now the consensus that their decay is prevented by the action of self-excited dynamos induced by the turbulent motions that occur in stellar interiors. More often, these motions are assumed to be driven by convection, owing to the temperature difference between the inner core and the cooler surface. In dynamo theory, this partial transfer of the kinetic energy of a conducting fluid into magnetic energy is an instability process: above a certain threshold, electrical currents start to be amplified by the fluid flow, so that a magnetic field can be sustained against the resistive decay due to ohmic dissipation.

After Glatzmaier & Roberts (1995), numerical modelling of self-consistent dynamos underwent considerable development (in contrast with the small number of successful experimental studies). However, despite the continuous increase of computer power, direct numerical simulations still face the difficulty to resolve a vast range of spatial and temporal scales when attempting to simulate a three-dimensional turbulent flow on a magnetic diffusion timescale. As a simplification, one usually resorts to some convective approximations, and most of the early studies were relying on the Boussinesq approximation, which performs well as long as variations in pressure hardly affect the density of the fluid. However, this assumption is not valid to describe convection in large stratified systems such as stars or gas giants, in which the density typically varies over many scaleheights between the top and bottom of the convection zone. This limitation of the Boussinesq approximation

---

★ E-mail: raphael.raynaud@ens.fr

Published by Oxford University Press on behalf of the Royal Astronomical Society

is basically what motivated the use of the anelastic approximation, originally developed to study atmospheric convection (Ogura & Phillips 1962; Gough 1969), to model convection in the Earth core and stellar interiors. Indeed, if we assume that the overall system remains close to an adiabatically stratified reference state at marginal stability so that convective motions can be treated as small perturbations (which in turns implies that typical velocities remain small compare to the speed of sound), then the anelastic approximation allows us to take some stratification into account while filtering out sound waves for faster numerical integration. This approximation can be found in the literature under slightly different formulations (Gilman & Glatzmaier 1981; Braginsky & Roberts 1995; Lantz & Fan 1999; Anufriev, Jones & Soward 2005; Berkoff, Kersale & Tobias 2010; Jones et al. 2011; Alboussière & Ricard 2013), which are in part compared in Brown, Vasil & Zweibel (2012).

Just as in Boussinesq models (Christensen & Aubert 2006; Schrinner, Petitdemange & Dormy 2012; Yadav et al. 2013), magnetic fields obtained in anelastic simulations (Gastine, Duarte & Wicht 2012; Duarte, Gastine & Wicht 2013; Schrinner et al. 2014) fall into two categories: dipolar dynamos, dominated by a large-scale axial dipole component, and multipolar dynamos, characterized by a more complex field topology with higher spatial and temporal variability. However, these studies identified several differences specific to anelastic dynamos. For instance, dipolar solutions seem more difficult to obtain as the density stratification is increased (Gastine et al. 2012; Jones 2014). We found in Schrinner et al. (2014) that for a given N_ϱ, E and Pr, there seems to exist a critical magnetic $\mathrm{Pm_c}$ below which the dipolar solution is not stable, and the higher the density stratification, the higher this critical magnetic Prandtl number. Furthermore, multipolar dynamos with a magnetic field configuration dominated by an equatorial dipole seem more easily realized with anelastic models than with Boussinesq models. However, we show in Raynaud, Petitdemange & Dormy (2014) that this characteristic also stands for weakly stratified models, since it is actually related to the use of different mass distributions. Indeed, the gravity profile may strongly influence the localisation of the convective cells, depending on whether one considers a homogeneous ($g \propto r$) or a central mass ($g \propto 1/r^2$) distribution: as opposed to the former, the latter results in the concentration of the convective cells close to the inner sphere, which favours the emergence of a less diffusive large-scale $m = 1$ mode at the outer surface of the model.

Our last study of weakly stratified models with a central mass distribution naturally constitutes an appropriate reference basis from which a detailed understanding of the role of the density stratification in anelastic dynamo models can be achieved. In this paper, we will primarily focus on dipolar dynamos. We aim at clarifying apparent contradictions between previous anelastic studies by investigating in more detail the evolution of the stability domain of the dipolar branch when increasing the density stratification. To that end, we rely on a systematic parameter study consisting of 119 three-dimensional, self-consistent dynamo models obtained by direct numerical simulations. As opposed to previous studies that were focusing on Jupiter's magnetic field (Duarte et al. 2013; Gastine et al. 2014; Jones 2014), we do not consider here more realistic models to reproduce a particular observation, but instead try to understand systematic and general tendencies in anelastic models, as a function of the physical control parameters. The anelastic equations are recalled in Section 2 and we present our results in Section 3. The complete list of numerical simulations performed for this study is given in Table A1 (see Appendix A).

2 EQUATIONS AND METHODS

Following Jones et al. (2011), we rely on the LBR formulation of the anelastic approximation (Lantz & Fan 1999; Braginsky & Roberts 1995). Actually, both the model and the numerical methods used here are the same as in Schrinner et al. (2014) and Raynaud et al. (2014) but we briefly recall them for completeness. We consider a spherical shell of width d and aspect ratio χ, rotating about the z-axis at angular velocity $\boldsymbol{\Omega}$ and filled with a perfect, electrically conducting gas with kinematic viscosity ν, thermal diffusivity κ, specific heat c_p and magnetic diffusivity η (all assumed to be constant). Convection is driven by an imposed entropy difference Δs between the inner and the outer boundaries, and the gravity is given by $\boldsymbol{g} = -GM\hat{\boldsymbol{r}}/r^2$, where G is the gravitational constant and M the central mass.

The reference state is given by the polytropic equilibrium solution of the anelastic system

$$\overline{P} = P_c\, w^{n+1}, \quad \overline{\varrho} = \varrho_c\, w^n, \quad \overline{T} = T_c\, w, \quad w = c_0 + \frac{c_1 d}{r}, \tag{1}$$

$$c_0 = \frac{2w_0 - \chi - 1}{1-\chi}, \quad c_1 = \frac{(1+\chi)(1-w_o)}{(1-\chi)^2}, \tag{2}$$

with

$$w_0 = \frac{\chi + 1}{\chi\, \exp(N_\varrho/n) + 1}, \quad w_i = \frac{1+\chi-w_o}{\chi}. \tag{3}$$

In the above expressions, n is the polytropic index and $N_\varrho = \ln(\varrho_i/\varrho_o)$ the number of density scaleheights. The values P_c, ϱ_c and T_c are the reference-state density, pressure and temperature mid-way between the inner and outer boundaries, and serve as units for these variables.

Length is scaled by the shell width d, time by the magnetic diffusion time d^2/η and entropy by the imposed entropy difference Δs. The magnetic field is measured in units of $\sqrt{\Omega\varrho_c\mu\eta}$, where μ is the magnetic permeability. Then, the equations governing the system are

$$\frac{\partial \boldsymbol{v}}{\partial t} + (\boldsymbol{v}\cdot\nabla)\,\boldsymbol{v} = \mathrm{Pm}\left[-\frac{1}{E}\nabla\frac{P'}{w^n} + \frac{\mathrm{Pm}}{\mathrm{Pr}}\mathrm{Ra}\frac{s}{r^2}\hat{\boldsymbol{r}} - \frac{2}{E}\hat{\boldsymbol{z}}\times\boldsymbol{v} \right.$$
$$\left. + \boldsymbol{F}_\nu + \frac{1}{E\,w^n}(\nabla\times\boldsymbol{B})\times\boldsymbol{B}\right], \tag{4}$$

$$\frac{\partial \boldsymbol{B}}{\partial t} = \nabla\times(\boldsymbol{v}\times\boldsymbol{B}) + \nabla^2\boldsymbol{B}\,, \tag{5}$$

$$\frac{\partial s}{\partial t} + \boldsymbol{v}\cdot\nabla s = w^{-n-1}\frac{\mathrm{Pm}}{\mathrm{Pr}}\nabla\cdot\left(w^{n+1}\,\nabla s\right)$$
$$+ \frac{\mathrm{Di}}{w}\left[E^{-1}w^{-n}(\nabla\times\boldsymbol{B})^2 + Q_\nu\right], \tag{6}$$

$$\nabla\cdot\left(w^n\boldsymbol{v}\right) = 0\,, \tag{7}$$

$$\nabla\cdot\boldsymbol{B} = 0\,. \tag{8}$$

The viscous force $\boldsymbol{F}_\nu$ in equation (4) is given by $\boldsymbol{F}_\nu = w^{-n}\nabla\boldsymbol{S}$, where $\boldsymbol{S}$ is the rate of strain tensor

$$S_{ij} = 2w^n\left(e_{ij} - \frac{1}{3}\delta_{ij}\nabla\cdot\boldsymbol{v}\right), \quad e_{ij} = \frac{1}{2}\left(\frac{\partial v_i}{\partial x_j} + \frac{\partial v_j}{\partial x_i}\right). \tag{9}$$

Moreover, the expressions of the dissipation parameter Di and the viscous heating Q_ν in equation (6) are

$$\mathrm{Di} = \frac{c_1 \mathrm{Pr}}{\mathrm{PmRa}}\,, \tag{10}$$

and

$$Q_\nu = 2\left[e_{ij}e_{ij} - \frac{1}{3}(\nabla\cdot\boldsymbol{v})^2\right]. \tag{11}$$

We impose stress-free boundary conditions for the velocity field at both the inner and the outer spheres, the magnetic field matches a potential field inside and outside the fluid shell, and the entropy is fixed at the inner and outer boundaries. Besides, both weak and strong field initial conditions have been tested for all models, since the system may exhibit hysteretic transitions between dynamo branches when stress-free boundary conditions are used.

The system of equations (4)–(8) involves seven control parameters, namely the Rayleigh number $\mathrm{Ra} = GMd\Delta s/(\nu\kappa c_p)$, the Ekman number $E = \nu/(\Omega d^2)$, the Prandtl number $\mathrm{Pr} = \nu/\kappa$ and the magnetic Prandtl number $\mathrm{Pm} = \nu/\eta$, together with the aspect ratio χ, the polytropic index n and the number of density scaleheights N_ϱ that define the reference state. We choose $E = 10^{-4}$, $\mathrm{Pr} = 1$ and $n = 2$. Different from Gastine et al. (2012), we also kept the central gravity profile and the aspect ratio $\chi = 0.35$ fixed for all simulations, but varied the magnetic Prandtl number, which turns out to be a key point to understand the partial divergence of our conclusions.

The equations are integrated in average for one magnetic diffusion time with the anelastic version of PARODY (Dormy, Cardin & Jault 1998; Schrinner et al. 2014).[1] The vector fields are transformed into scalars using the poloidal–toroidal decomposition. The equations are then discretized in the radial direction with a finite-difference scheme; on each concentric sphere, variables are expanded using a spherical harmonic basis. The coefficients of the expansion are identified with their degree ℓ and order m. Typical resolutions are 288 points in the radial direction (up to 320 points). The spectral decomposition is truncated at a hundred modes (up to $\ell_{\max} \sim m_{\max} \leq 128$), in order to observe for both spectra a decrease of more than two orders of magnitude over the range of l and m. The highest resolutions are required for the models with the highest density stratification ($N_\varrho = 3$).

The amplitudes of the velocity and the magnetic fields are measured in terms of the Rossby number $\mathrm{Ro} = \sqrt{2E_\mathrm{k}}E/\mathrm{Pm}$ and Lorentz number $\mathrm{Lo} = \sqrt{2E_\mathrm{m}}E/\mathrm{Pm}$, where E_k and E_m are the energy densities integrated over the fluid shell,

$$E_\mathrm{k} = \frac{1}{2}\frac{1}{V}\int_V w^n \boldsymbol{v}^2\,\mathrm{d}v \quad \text{and} \quad E_\mathrm{m} = \frac{1}{2}\frac{1}{V}\frac{\mathrm{Pm}}{E}\int_V \boldsymbol{B}^2\,\mathrm{d}v\,. \tag{12}$$

Likewise, the measure of the mean zonal flow is given by the zonal Rossby number Ro_z based on the averaged toroidal axisymmetric kinetic energy.

We also define a local Rossby number $\mathrm{Ro}_\ell = \mathrm{Ro}_c\,\ell_c/\pi$ based on the mean harmonic degree ℓ_c of the velocity component $\boldsymbol{v}_c$ from which the mean zonal flow has been subtracted (Schrinner et al. 2012, 2014),

$$\ell_c = \sum_\ell \ell\,\frac{\langle\, w^n\,(\boldsymbol{v}_c)_\ell\cdot(\boldsymbol{v}_c)_\ell\rangle}{\langle w^n\,\boldsymbol{v}_c\cdot\boldsymbol{v}_c\rangle}\,, \tag{13}$$

where the brackets denote an average over time and radii. The contribution of the mean zonal flow is removed for calculating Ro_c.

Furthermore, as the stratification is increased, it turns out that it is useful to examine the variations with depth of the local Rossby number, defined in such a way that $\mathrm{Ro}_\ell = \int_{r_i}^{r_o}\mathrm{Ro}_\ell(r)r^2\,\mathrm{d}r$. We found that it is more suitable to slightly adapt our initial definition and investigate the radial dependence of $\mathrm{Ro}_\ell^\star(r)$, which differs from $\mathrm{Ro}_\ell(r)$ in so far as the velocity is not weighted by the reference density profile w^n. We also checked that, in our range of N_ϱ, both estimates of a characteristic velocity do not make a qualitative difference on the volume-averaged quantities. For instance, the difference between the values of the magnetic Reynolds number $\mathrm{Rm} = \mathrm{RoPm}/E$ is about 1 per cent at $N_\varrho = 0.5$. Of course, it increases with N_ϱ: energy-based estimates lead to lower values about 7 and 10 per cent for $N_\varrho = 2.0$ and 2.5, respectively. However, this does not change our conclusions, and that is why we do not adapt our definition for volume-averaged quantities.

3 RESULTS

3.1 Bistability

Fig. 1 shows the distribution of dipolar and multipolar dynamos in the parameter space ($\mathrm{Ra}/\mathrm{Ra}_\mathrm{c}$, Pm) (left-hand panels), together with the corresponding dipolarities (right-hand panels), for increasing density stratifications from top to bottom. One can see that several examples of bistable pairs are displayed. Bistability is commonly known for Boussinesq and anelastic models, and is related to the use of stress-free boundary conditions that allows for the growth of stronger zonal winds (Sasaki et al. 2011; Gastine et al. 2012; Schrinner et al. 2012). For $N_\varrho = 0.5$, the regime diagram in Fig. 1(a) does not qualitatively differ from what we can observe in the Boussinesq regime. As we found in Raynaud et al. (2014), the multipolar branch undergoes a supercritical bifurcation as Ra is increased, whereas the dipolar one still loses its stability in favour of the multipolar branch at low Rayleigh and magnetic Prandtl numbers. When increasing the density contrast N_ϱ to 1.5, one can note in Fig. 1(c) that the overlap between the two branches shrinks. At $N_\varrho = 2$, we do not observe a bistable case. More generally, for all models of our sample with a density stratification $N_\varrho \geq 2$, the saturated field of the dynamo is not anymore sensitive to the amplitude of the initial magnetic field. To understand this evolution from Boussinesq models to anelastic models with moderate stratification ($N_\varrho \leq 1.5$), it is worth stressing that the transition process from the multipolar to the dipolar branch triggered by the increase of Pm still applies to our sample of models (see Schrinner et al. 2012). Fig. 2(a) illustrates on a few cases the progressive merging of the multipolar branch which is indeed lost when its zonal Rossby number becomes comparable to the zonal Rossby number of the dipolar branch. For a given Rayleigh number, the fact that the mean zonal flow of the multipolar branch decreases with Pm (and eventually becomes too small to prevent the growth of the axial dipole) is actually the limiting factor of the upper extent of the multipolar branch in the left-hand panels of Fig. 1. This also emphasizes the essential role played by differential rotation in the dynamo mechanism of the multipolar branch, often accounted for in terms of Ω-effect.

Interestingly, the zonal Rossby number for multipolar dynamos substantially decreases between $N_\varrho = 0.5$ and 1.5 (see the blue and red squares in Fig. 2a), while it remains of the same order for dipolar dynamos. Hence, the available range of Pm for the multipolar solution is reduced, which therefore explains the relative shrinking of the bistable region when comparing Figs 1(a) and (c). The simplest argument to understand this downtrend is given by the comparison of the x-axis in Fig. 1, which reveals that the

---

[1] The integration times range from 0.63 to 5.2 magnetic diffusion times (for the models `101m` and `004m`, respectively).

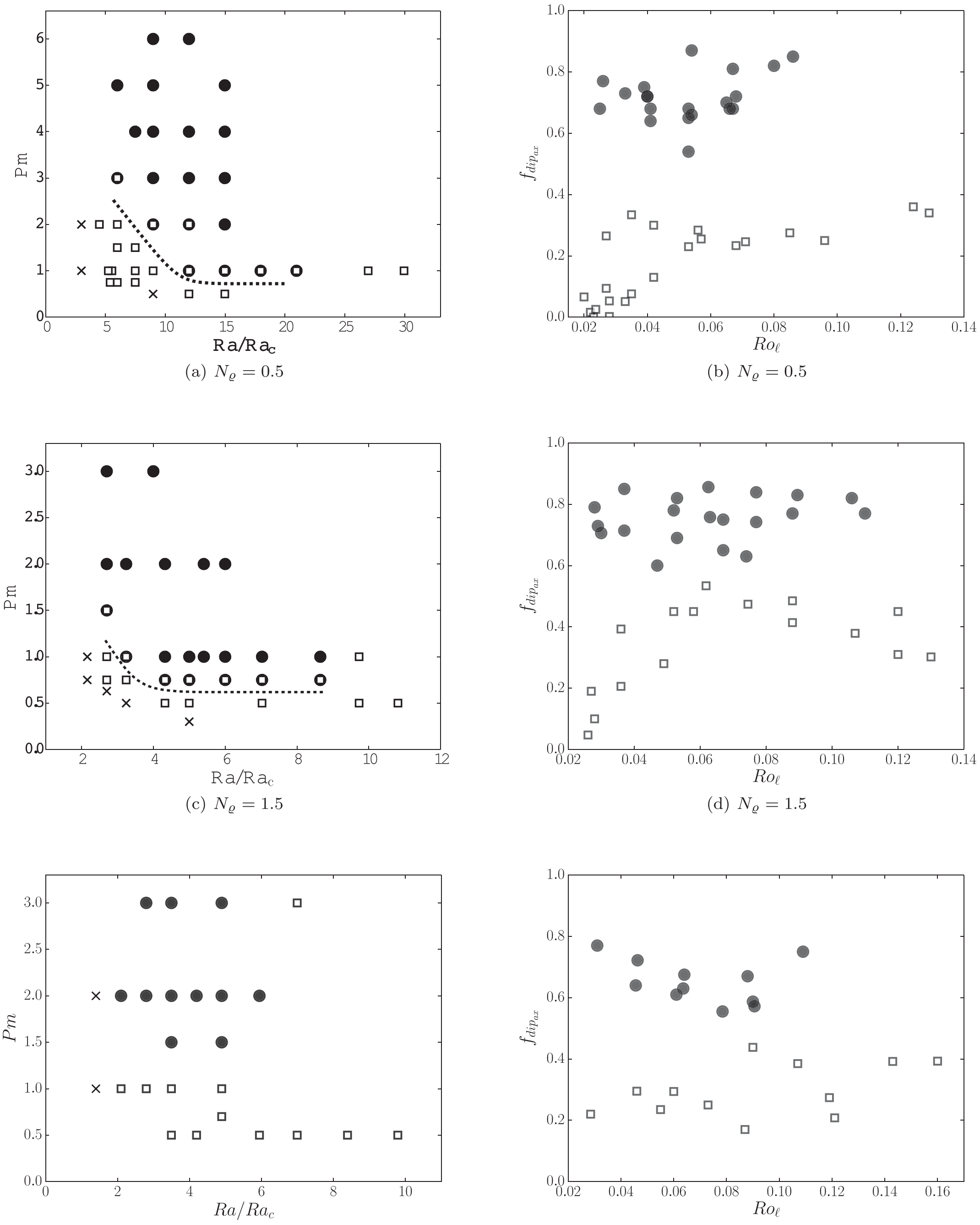

(a) $N_\varrho = 0.5$

(b) $N_\varrho = 0.5$

(c) $N_\varrho = 1.5$

(d) $N_\varrho = 1.5$

(e) $N_\varrho = 2.0$

(f) $N_\varrho = 2.0$

Figure 1. Left: dipolar (black circles) and multipolar (white squares) dynamos as a function of Ra/Ra$_c$ and Pm, for $N_\varrho = 0.5$ (a), $N_\varrho = 1.5$ (c) and $N_\varrho = 2.0$ (e). A cross indicates the absence of a self-sustained dynamo. Right: the relative axial dipole field strength $f_{\mathrm{dip_{ax}}}$ versus the local Rossby number for $N_\varrho = 0.5$ (b), $N_\varrho = 1.5$ (d) and $N_\varrho = 2.0$ (f).

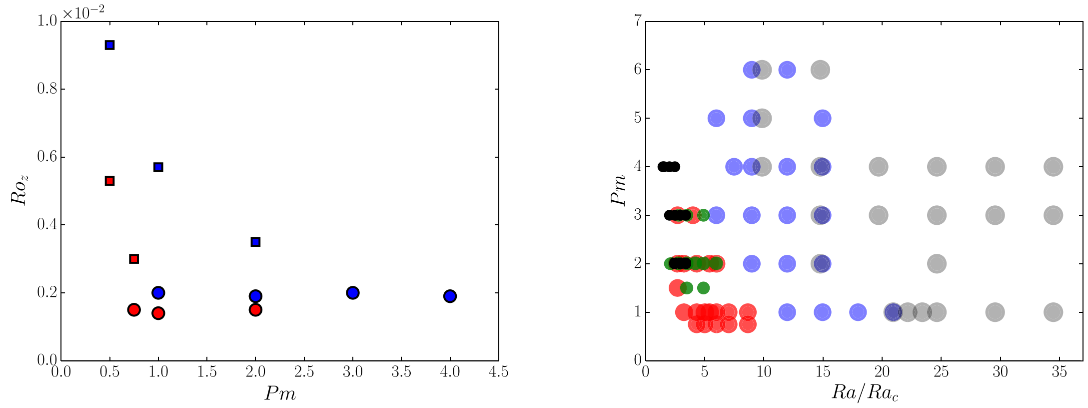

(a) (b)

Figure 2. (a) Evolution of the zonal Rossby number as a function of Pm for a dynamo model with Ra = 4×10^6, at $N_\varrho = 0.5$ (blue) and $N_\varrho = 1.5$ (red). Circles (squares) stand for dipolar (multipolar) dynamos. (b) Dipolar dynamos in the parameter space (Ra/Ra$_c$, Pm), for increasing density stratifications: $N_\varrho = 0.1$ (grey), $N_\varrho = 0.5$ (blue) $N_\varrho = 1.5$ (red), $N_\varrho = 2.0$ (green) and $N_\varrho = 2.5$ (black).

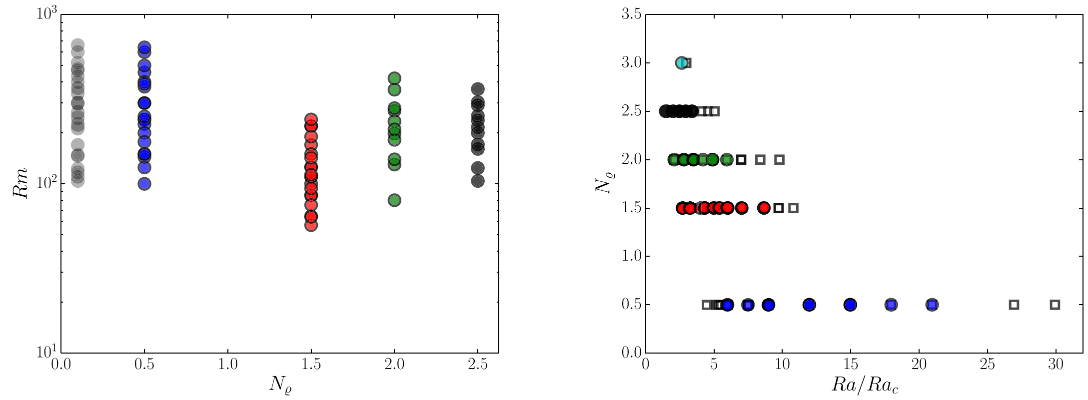

(a) (b)

Figure 3. (a) Magnetic Reynolds number as a function of N_ϱ for dipolar dynamos. (b) Our sample of dipolar (circles) and multipolar (squares) dynamos in the parameter space (Ra/Ra$_c$, N_ϱ).

dynamo onset moves closer to the onset of convection when the density stratification is increased, as mentioned by Gastine et al. (2012). Indeed, despite changing the value of N_ϱ, we found that the Rayleigh numbers we had to consider always stay of the order of 10^6. At the same time, the critical Rayleigh number for the linear onset of convection monotonically increases with N_ϱ. From table B.1 in Schrinner et al. (2014), we have in our case the following values of 3.34×10^5, 9.25×10^5 and finally 1.43×10^6 for the sequence of density stratifications $N_\varrho = 0.5$, 1.5 and 2.0, respectively.

3.2 Dipole onset

The density stratification strongly impacts on the stability domain of the dipolar branch, as we clearly see in Fig. 2(b). In this figure, we included data from Raynaud et al. (2014) in order to better highlight the differences with Boussinesq simulations. For moderate values of N_ϱ at a fixed Pm, the critical value of Ra/Ra$_c$ at which it is possible to sustain a dipolar dynamo rapidly falls off (up to a factor of 4 if we consider the line Pm = 1). However, this tendency hardly persists once we reach Ra/Ra$_c \sim 5$ for $N_\varrho = 1.5$, and the further increase of N_ϱ mainly affects the critical magnetic Prandtl number Pm$_c$ below which it is not possible to sustain a dipolar dynamo. In our sample of models, the increase of Pm$_c$ becomes effective for $N_\varrho \geq 2$, but we already reported it as a general tendency in Schrinner et al. (2014). Fig. 1(c) enables us to conclude that $0.5 < \mathrm{Pm}_c \leq 0.75$ for $N_\varrho = 1.5$, whereas from Fig. 1(e), it is clear that $\mathrm{Pm}_c > 1$ for $N_\varrho = 2$.

The fact that dipolar dynamos are found closer to the convection threshold as N_ϱ increases can be more or less readily understood if one notices that, despite the increase of the density stratification, the critical magnetic Reynolds number Rm$_c$ of the dipolar branch does not significantly vary, but stays in first approximation of the order of 10^2, as shown in Fig. 3(a). Then, if we take this as a necessary condition to obtain a dipolar solution, and given the fact that for a constant value of Ra/Ra$_c$ the flow amplitude increases with N_ϱ (Gastine et al. 2012), it explains why the dipolar branch can be found closer to the onset of convection when the stratification increases.

However, we will see in the next subsection that, as N_ϱ is further increased, not only does the dipolar branch occur closer to the onset of convection, but also higher magnetic Prandtl numbers have to be considered to maintain a sufficiently high Rm while preventing the collapse of the dipole.

3.3 Dipole collapse

Another striking feature that arises when investigating the stability domain of the dipolar branch is that the range of Rayleigh numbers over which it extends becomes smaller and smaller as N_ϱ is increased. This is clearly visible in Fig. 3(b) that shows for different N_ϱ the transition from the dipolar to the multipolar branch resulting from the increase of Ra. In other words, at this moderate value of the Ekman number, dipolar dynamos are confined in a narrower and narrower window of Rayleigh numbers, which explains why dipolar solutions may seem more difficult to obtain at higher N_ϱ, despite comparable critical magnetic Reynolds numbers. As for the modification of the dynamo onset, this can be related to the fact that for a given value of $\mathrm{Ra}/\mathrm{Ra_c}$, the Rossby number Ro increases with N_ϱ.[2] The transition from a dipolar to a multipolar solution triggered by an increase of Ra is related to the fact that inertia becomes significant in the force balance. We know from Christensen & Aubert (2006) that this transition can be measured by a local Rossby number Ro_ℓ based on a characteristic length-scale of the flow. We find that the collapse of the dipole still occurs for $\mathrm{Ro}_\ell \sim 0.1$ when $N_\varrho \leq 2$, which is consistent with the results in Gastine et al. (2012). This is illustrated by Figs 1(b), (d) and (f) which show the relative axial dipole field strength $f_{\mathrm{dip_{ax}}}$ computed at the outer sphere, as a function of Ro_ℓ. In Fig. 1(b), the very low values of $f_{\mathrm{dip_{ax}}}$ at low Ro_ℓ are characteristics of multipolar dynamos dominated by an equatorial dipole component. We showed in Raynaud et al. (2014) that this magnetic configuration arises close to the dynamo onset and when convective cells are localized close to the inner sphere. However, we know from hydrodynamic studies that the convection cells move towards the outer shell when the stratification is increased (Jones, Kuzanyan & Mitchell 2009; Gastine & Wicht 2012), which explains why this feature tends to disappear in Figs 1(d) and (f). Besides, we see in Fig. 4 that the values of $f_{\mathrm{dip_{ax}}}$ tend to decrease with N_ϱ, which is also clear if we focus for instance on the dipolar branch in Fig. 1(f) for which $f_{\mathrm{dip_{ax}}} < 0.8$. As expected, this indicates that the small magnetic scales at the outer surface are favoured with the increase of the stratification. This is also clearly confirmed by the comparison of the radial magnetic fields at the outer surface of the model, as shown in the left-hand panels of Figs 5 and 6. Finally, we also report the existence of multipolar dynamos whose dipolarity displays strong variations in time. This leads to averaged values of $f_{\mathrm{dip_{ax}}} \sim 0.5$, as one can notice in Fig. 1(d). These dynamos usually exhibit a relatively strong axial dipole component which undergoes reversals during which the value of $f_{\mathrm{dip_{ax}}}$ decreases drastically. Duarte et al. (2013) also reported similar behaviour for dynamo models with a variable electrical conductivity.

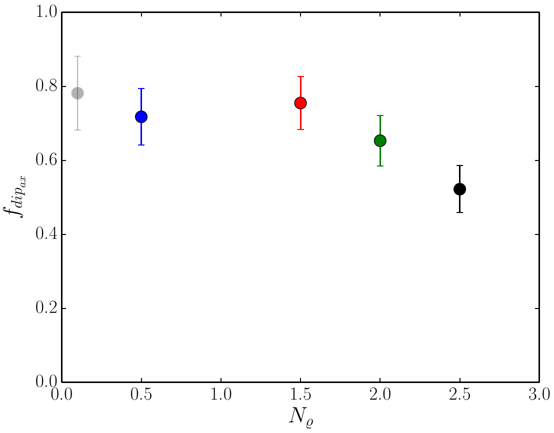

Figure 4. Average values of $f_{\mathrm{dip_{ax}}}$ for dipolar dynamos as a function of N_ϱ. Error bars represent the standard deviation. The average is done with 11 models for $N_\varrho = 2.5$.

For $N_\varrho > 2.0$, we found that the dipole collapse tends to occur at values of Ro_ℓ lower than 0.1. However, it is likely that a volume-averaged quantity becomes less relevant when applied to models with a substantial stratification. For instance, we see in Figs 5(b) and 6(b) that the smaller structures that develop at $N_\varrho = 2.5$ are confined close to the outer boundary, whereas there are no significant differences in the radial flow at mid-depth. Thus, we also examined the radial dependence of the different components of the local Rossby number $\mathrm{Ro}_l^\star$, which is computed as the product of two terms: a convective Rossby number based on the velocity field $\boldsymbol{v}_c$ from which the mean zonal flow has been subtracted (see Fig. 7a) and a characteristic length-scale based on the mean harmonic degree of $\boldsymbol{v}_c$ (see Fig. 7b). We find that the monotonicity of $\mathrm{Ro}_l^\star$ changes as N_ϱ is increased. Indeed, for low stratifications, $\mathrm{Ro}_l^\star(r)$ mainly decreases with radius, whereas for $N_\varrho \geq 2.5$ it becomes an increasing function of r that steepens slightly close to the outer surface. Fig. 7(c) shows the evolution of $\mathrm{Ro}_l^\star(r)$ for increasing Rayleigh numbers up to the loss of the dipolar solution, at $N_\varrho = 2.5$ and 3.0. When the transition to the multipolar branch is reached, we see that $\mathrm{Ro}_\ell^\star$ tends to increase faster close to the outer surface, while the volume-averaged value can stay below the critical value of 0.1. Thus, it seems that inertia still causes the collapse of the dipolar branch, despite the fact that the usual local Rossby number criterion is not appropriate to separate the two dynamo branches for significant density stratifications.

3.4 Dynamo mechanisms

Finally, we try to investigate whether the dynamo mechanisms at work on the dipolar branch are modified when the stratification is increased. We see in Fig. 8 that the axisymmetric azimuthal magnetic field we observe at $N_\varrho = 1.5$ is strongly reminiscent of the magnetic structures that can be observed with Boussinesq models, which are usually interpreted in terms of α^2 dynamos (Olson, Christensen & Glatzmaier 1999; Schrinner et al. 2007, 2012; Schrinner, Petitdemange & Dormy 2011). Inside the tangent cylinder, the azimuthal magnetic field is mainly produced by the Ω-effect, $r\overline{\boldsymbol{B}}_r\partial\left(r^{-1}\overline{\boldsymbol{V}}_\varphi\right)/\partial r + r^{-1}\sin\theta\,\overline{\boldsymbol{B}}_\theta\partial\left(\sin\theta^{-1}\overline{\boldsymbol{V}}_\varphi\right)/\partial\theta$, which correlates inside the tangent cylinder with the axisymmetric azimuthal magnetic field, when comparing Figs 8(b) and (c). However, outside the tangent cylinder, the large part of the mean azimuthal field does not seem to be the result of the Ω-effect, and it is thus likely that the

---

[2] For instance, one can compare the models `008d`, `055d` and `083d` for which $\mathrm{Ra}/\mathrm{Ra_c} \sim 6$ and an increasing Ro of 4.8×10^{-3}, 1.3×10^{-2} and 1.8×10^{-2}, respectively, or else the models `021d`, `051d` and `096d` that have a similar Rossby number of 0.01, but for which $\mathrm{Ra}/\mathrm{Ra_c}$ is about 12, 5 and 2.9, respectively.

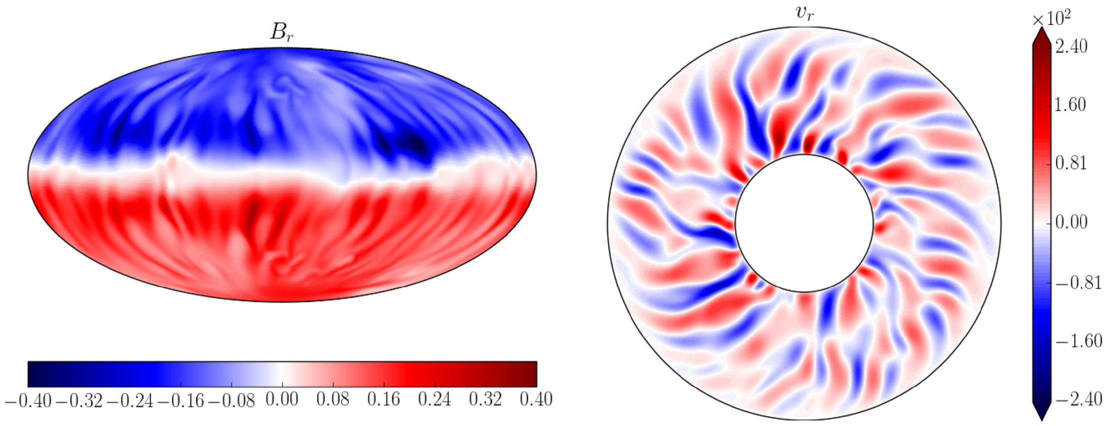

(a) $N_\varrho = 1.5$ (b) $N_\varrho = 1.5$

Figure 5. Snapshot of $B_r(r = r_o)$ (a) and equatorial cut of v_r (b) for a dipolar dynamo with $N_\varrho = 1.5$, Pm = 0.75, Ra = $4.625 \times 10^6 = 5\mathrm{Ra_c}$.

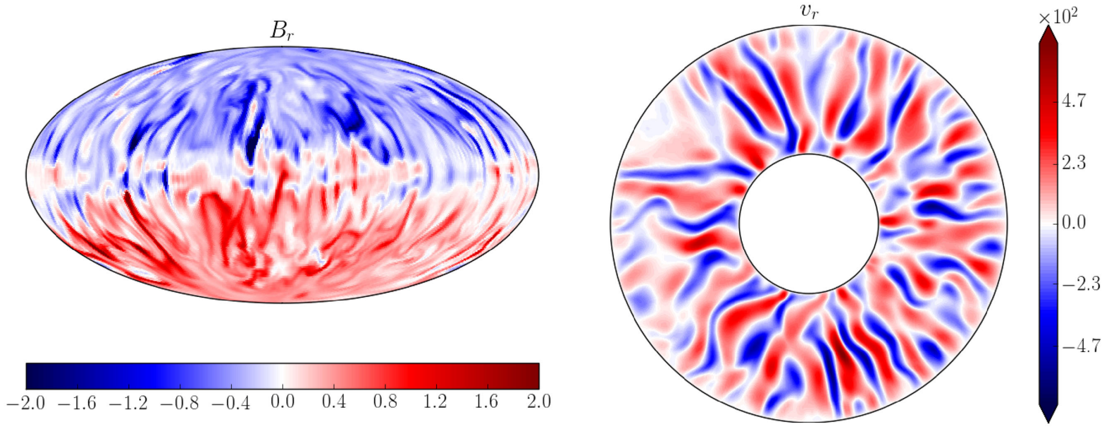

(a) $N_\varrho = 2.5$ (b) $N_\varrho = 2.5$

Figure 6. Snapshot of $B_r(r = r_o)$ (a) and equatorial cut of v_r (b) for a dipolar dynamo with $N_\varrho = 2.5$, Pm = 2, Ra = $7.40 \times 10^6 = 3.4\mathrm{Ra_c}$.

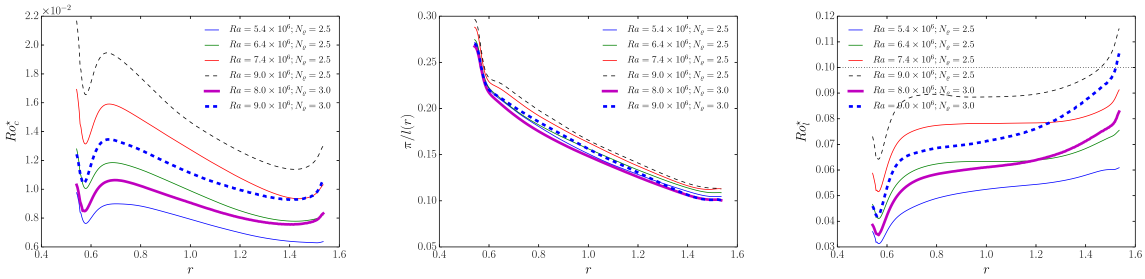

(a) (b) (c)

Figure 7. The convective Rossby number (a), the convective length-scale (b) and the local Rossby number (c) as a function of radius for dipolar (solid lines) and multipolar (dashed lines) dynamos at ($N_\varrho = 2.5$, Pm = 2) (thin lines) and ($N_\varrho = 3$, Pm = 4) (thick lines).

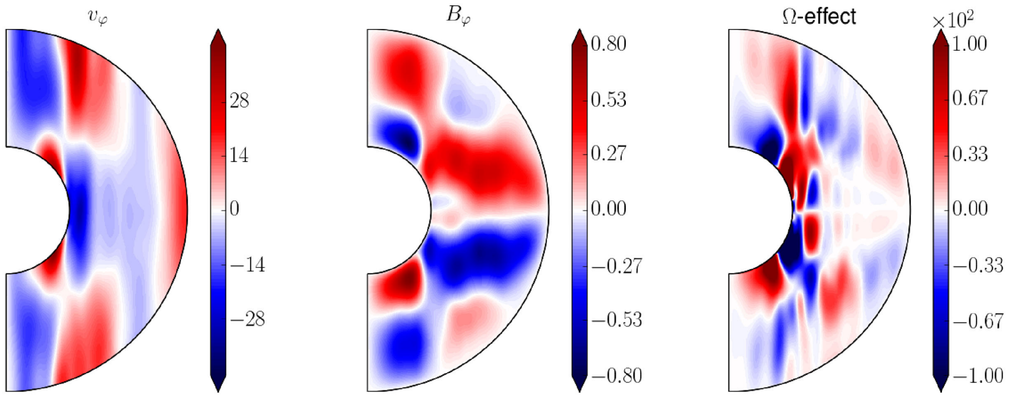

(a) $N_\varrho = 1.5$ (b) $N_\varrho = 1.5$ (c) $N_\varrho = 1.5$

Figure 8. Time-averaged axisymmetric component of the azimuthal magnetic field (top) and velocity field (bottom) for a dipolar dynamo with $N_\varrho = 1.5$, Ra = 4.625×10^6, Pm = 0.75.

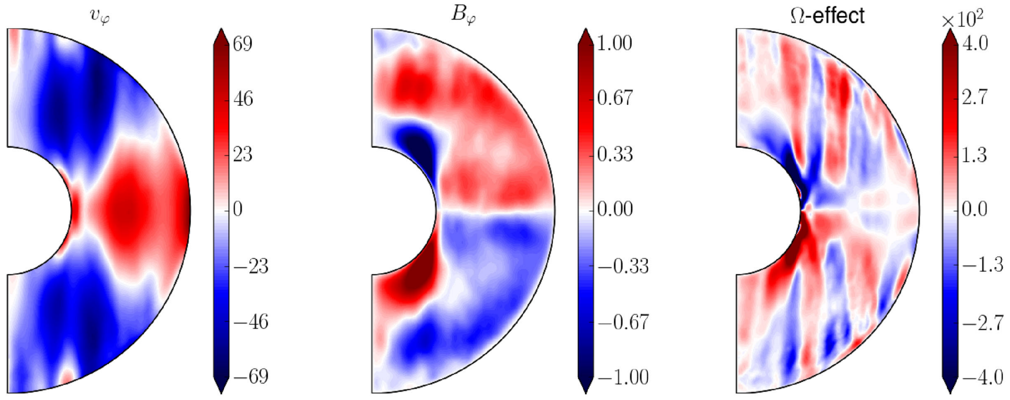

(a) $N_\varrho = 2.5$ (b) $N_\varrho = 2.5$ (c) $N_\varrho = 2.5$

Figure 9. Time-averaged axisymmetric component of the azimuthal magnetic field (top) and velocity field (bottom) for a dipolar dynamo with $N_\varrho = 2.5$, Ra = 7.40×10^6, Pm = 2.

essential regeneration of the poloidal field is achieved by α-effect, leading to the emergence of characteristic equatorial patches of opposite polarity (see e.g. Christensen 2011; Schrinner et al. 2012). We did not find in our sample of models tangible evidence that would invalidate this scenario at higher N_ϱ. For instance, at $N_\varrho = 2.5$, we see in Fig. 9 that the major differences lie in the stronger axisymmetric azimuthal velocity (compare Figs 8a and 9a). Nevertheless, the axisymmetric azimuthal magnetic field shown in Fig. 9(b) seems only modified about a colatitude $\theta \sim \pi/4$ close to the outer surface, and keeps now the same polarity in each hemisphere outside the tangent cylinder. This change can be correlated to the modifications of the axisymmetric azimuthal velocity, which in turn affect the Ω-effect (compare Figs 8c and 9c). Of course, we are for now limited to the observation of correlations, but it would be interesting to have a further insight into the dynamo mechanism in anelastic simulations using a test field method, in the spirit of the Boussinesq study by Schrinner et al. (2012).

4 CONCLUSION

With this systematic parameter study, we are able to improve our understanding of the successive modifications that are exhibited by the stability domain of the dipolar branch when increasing the density stratification in anelastic dynamo models. In general, dipolar dynamos are found closer to the onset of convection. Moreover, we show that dipole-dominated solutions can be observed even at high-density stratifications, provided high enough magnetic Prandtl numbers are considered. Besides, this study also highlights why dipolar dynamos seem more difficult to find in anelastic simulations. Indeed, this tendency is usually reported as a general statement, but here we show that this impression mainly results from the fact that the dipolar branch extends on a smaller and smaller range of Rayleigh numbers as N_ϱ is increased. However, despite the relative shrinking of the stability domain, we found that the critical magnetic Reynolds number of the dipolar branch seems scarcely modified in the overall process. At the same time, the higher N_ϱ, the faster convection will develop as we depart from the onset. In consequence, the higher N_ϱ, the faster is reached the critical Rossby number above which inertia causes the collapse of the dipole. This explains why dipolar dynamos become clearly confined in a smaller region of the parameter space. However, we stress that, in terms of magnetic Reynolds number, the dynamo threshold does not significantly increase with the density stratification in the range of N_ϱ we investigated.

In addition, this study also suggests that the scarcity of dipolar solutions for substantial density stratifications would thus rather come from the restriction of the parameter space being currently explored (because of computational limitations), rather than an intrinsic modification of the dynamo mechanisms that would be caused by the density stratification. Furthermore, if we decrease the Ekman number from $E = 10^{-4}$ to 3×10^{-5} keeping $\mathrm{Pr} = 1$, we find that we recover three examples of bistable pairs at $N_\varrho = 2$, for $\mathrm{Pm} = 1$ at $\mathrm{Ra}/\mathrm{Ra}_c = 2.6$ and for $\mathrm{Pm} \in \{1, 2\}$ at $\mathrm{Ra}/\mathrm{Ra}_c = 2.9$. Then, beyond the results of this study, and for low values of the Ekman number that are currently very expensive to simulate, it seems more likely that dipolar solutions will persist in a larger region of parameter space (see also Duarte 2014; Jones 2014).

Despite the fact that it is not straightforward to relate the output of numerical models with observations (Gastine et al. 2013), the bistability that is reported for numerical simulations can be similarly observed with real objects. For instance, in a spectropolarimetric survey done with a sample of active M dwarfs, Morin et al. (2010) report two distinct categories of magnetic topologies. They distinguish strong axisymmetric dipolar fields and weak fields with significant non-axisymmetric components, and both configurations seem to be observed on objects with similar stellar parameters. After Schrinner et al. (2012), we show that the bistable behaviour observed in numerical models could be a possible way towards a better understanding of the broad diversity of the magnetic fields of M dwarfs, and that it cannot be ruled out even when taking into account the density stratification. The understanding of the impact of the stratification on the dynamo mechanisms deserves further studies.

ACKNOWLEDGEMENTS

The authors thank Lúcia D. V. Duarte for a thoughtful review. This work was granted access to the HPC resources of MesoPSL financed by the Région Île-de-France and the project Equip@Meso (reference ANR-10-EQPX-29-01) of the programme Investissements d'Avenir supervised by the Agence Nationale pour la Recherche. Numerical simulations were also carried out at CEMAG and TGCC computing centres (GENCI project x2013046698). LP acknowledges financial support from 'Programme National de Physique Stellaire' (PNPS) of CNRS/INSU, France.

REFERENCES

Alboussière T., Ricard Y., 2013, J. Fluid Mech., 725, 1
Anufriev A. P., Jones C. A., Soward A. M., 2005, Phys. Earth Planet. Inter., 152, 163
Berkoff N. A., Kersale E., Tobias S. M., 2010, Geophys. Astrophys. Fluid Dyn., 104, 545
Braginsky S. I., Roberts P. H., 1995, Geophys. Astrophys. Fluid Dyn., 79, 1
Brown B. P., Vasil G. M., Zweibel E. G., 2012, ApJ, 756, 109
Christensen U. R., 2011, Phys. Earth Planet. Inter., 187, 157
Christensen U. R., Aubert J., 2006, Geophys. J. Int., 166, 97
Donati J.-F., Landstreet J. D., 2009, ARA&A, 47, 333
Dormy E., Cardin P., Jault D., 1998, Earth Planet. Sci. Lett., 160, 15
Duarte L., 2014, PhD thesis, Technische Universität Braunschweig
Duarte L. D. V., Gastine T., Wicht J., 2013, Phys. Earth Planet. Inter., 222, 22
Gastine T., Wicht J., 2012, Icarus, 219, 428
Gastine T., Duarte L., Wicht J., 2012, A&A, 546, A19
Gastine T., Morin J., Duarte L., Reiners A., Christensen U. R., Wicht J., 2013, A&A, 549, L5
Gastine T., Wicht J., Duarte L. D. V., Heimpel M., Becker A., 2014, Geophys. Res. Lett., 41, 5410
Gilman P. A., Glatzmaier G. A., 1981, ApJS, 45, 335
Glatzmaier G. A., Roberts P. H., 1995, Nature, 377, 203
Gough D. O., 1969, J. Atmos. Sci., 26, 448
Jones C., 2014, Icarus, 241, 148
Jones C. A., Kuzanyan K. M., Mitchell R. H., 2009, J. Fluid Mech., 634, 291
Jones C. A., Boronski P., Brun A. S., Glatzmaier G. A., Gastine T., Miesch M. S., Wicht J., 2011, Icarus, 216, 120
Lantz S. R., Fan Y., 1999, ApJS, 121, 247
Larmor J., 1919, Report of the British Association for the Advancement of Science, 87th Meeting, p. 159, available at: https://archive.org/details/cbarchive_123167_howcouldarotatingbodysuchasthe1920
Morin J., Donati J.-F., Petit P., Delfosse X., Forveille T., Jardine M. M., 2010, MNRAS, 407, 2269
Ogura Y., Phillips N. A., 1962, J. Atmos. Sci., 19, 173
Olson P., Christensen U. R., Glatzmaier G. A., 1999, J. Geophys. Res., 104, 10383
Raynaud R., Petitdemange L., Dormy E., 2014, A&A, 567, A107
Sasaki Y., Takehiro S.-i., Kuramoto K., Hayashi Y.-Y., 2011, Phys. Earth Planet. Inter., 188, 203
Schrinner M., Rädler K.-H., Schmitt D., Rheinhardt M., Christensen U. R., 2007, Geophys. Astrophys. Fluid Dyn., 101, 81
Schrinner M., Petitdemange L., Dormy E., 2011, A&A, 530, A140
Schrinner M., Petitdemange L., Dormy E., 2012, ApJ, 752, 121
Schrinner M., Petitdemange L., Raynaud R., Dormy E., 2014, A&A, 564, A78
Yadav R. K., Gastine T., Christensen U. R., Duarte L. D. V., 2013, ApJ, 774, 6

APPENDIX A: NUMERICAL MODELS

Table A1. Overview of the simulations carried out, with $E = 10^{-4}$, $\mathrm{Pr} = 1$, $\chi = 0.35$ and $n = 2$.

Model	N_ϱ	Ra	Pm	Ro	Ro_ℓ	Ro_z	Lo	$f_{\mathrm{dip_{ax}}}$
001m	0.5	1.500×10^6	2.00	3.2×10^{-3}	2.0×10^{-2}	1.8×10^{-3}	2.3×10^{-3}	6.6×10^{-2}
002m	0.5	1.750×10^6	1.00	3.7×10^{-3}	2.2×10^{-2}	2.7×10^{-3}	1.8×10^{-3}	1.6×10^{-2}
003m	0.5	1.800×10^6	0.75	3.5×10^{-3}	2.8×10^{-2}	2.8×10^{-3}	1.9×10^{-3}	2.2×10^{-3}
004m	0.5	1.850×10^6	1.00	3.9×10^{-3}	2.4×10^{-2}	4.2×10^{-3}	2.0×10^{-3}	2.5×10^{-2}
005m	0.5	2.000×10^6	0.75	4.1×10^{-3}	2.3×10^{-2}	5.2×10^{-3}	2.4×10^{-3}	9.0×10^{-5}
006m	0.5	2.000×10^6	1.50	5.5×10^{-3}	2.8×10^{-2}	3.0×10^{-3}	3.1×10^{-3}	5.3×10^{-2}
007m	0.5	2.000×10^6	2.00	5.3×10^{-3}	2.7×10^{-2}	2.0×10^{-3}	3.7×10^{-3}	9.4×10^{-2}
008m	0.5	2.000×10^6	3.00	5.1×10^{-3}	2.7×10^{-2}	1.7×10^{-3}	4.1×10^{-3}	2.7×10^{-1}
008d	0.5	2.000×10^6	3.00	4.8×10^{-3}	2.6×10^{-2}	1.0×10^{-3}	5.5×10^{-3}	7.7×10^{-1}
009d	0.5	2.000×10^6	5.00	4.8×10^{-3}	2.5×10^{-2}	1.1×10^{-3}	5.7×10^{-3}	6.8×10^{-1}
010m	0.5	2.500×10^6	0.75	7.7×10^{-3}	3.3×10^{-2}	5.2×10^{-3}	3.8×10^{-3}	5.1×10^{-2}
011m	0.5	2.500×10^6	1.00	7.2×10^{-3}	3.5×10^{-2}	3.6×10^{-3}	4.5×10^{-3}	7.6×10^{-2}
012m	0.5	2.500×10^6	1.50	7.1×10^{-3}	3.5×10^{-2}	3.1×10^{-3}	4.5×10^{-3}	3.3×10^{-1}
013d	0.5	2.500×10^6	4.00	6.0×10^{-3}	3.3×10^{-2}	1.5×10^{-3}	6.9×10^{-3}	7.3×10^{-1}
014m	0.5	3.000×10^6	1.00	8.6×10^{-3}	4.2×10^{-2}	4.0×10^{-3}	5.5×10^{-3}	1.3×10^{-1}
015m	0.5	3.000×10^6	2.00	8.2×10^{-3}	4.2×10^{-2}	2.8×10^{-3}	6.3×10^{-3}	3.0×10^{-1}
015d	0.5	3.000×10^6	2.00	7.5×10^{-3}	3.9×10^{-2}	1.7×10^{-3}	7.9×10^{-3}	7.5×10^{-1}
016d	0.5	3.000×10^6	3.00	7.5×10^{-3}	4.0×10^{-2}	1.7×10^{-3}	8.5×10^{-3}	7.2×10^{-1}
017d	0.5	3.000×10^6	4.00	7.5×10^{-3}	4.0×10^{-2}	1.7×10^{-3}	8.5×10^{-3}	7.2×10^{-1}
018d	0.5	3.000×10^6	5.00	7.5×10^{-3}	4.1×10^{-2}	1.8×10^{-3}	8.8×10^{-3}	6.8×10^{-1}
019d	0.5	3.000×10^6	6.00	7.6×10^{-3}	4.1×10^{-2}	1.9×10^{-3}	9.0×10^{-3}	6.4×10^{-1}
020m	0.5	4.000×10^6	0.50	1.3×10^{-2}	5.3×10^{-2}	9.3×10^{-3}	6.6×10^{-3}	2.3×10^{-1}
021m	0.5	4.000×10^6	1.00	1.2×10^{-2}	5.6×10^{-2}	5.7×10^{-3}	7.9×10^{-3}	2.8×10^{-1}
021d	0.5	4.000×10^6	1.00	1.0×10^{-2}	5.4×10^{-2}	2.0×10^{-3}	1.1×10^{-2}	8.7×10^{-1}
022m	0.5	4.000×10^6	2.00	1.5×10^{-2}	5.7×10^{-2}	3.5×10^{-3}	8.8×10^{-3}	2.6×10^{-1}
022d	0.5	4.000×10^6	2.00	1.0×10^{-2}	5.4×10^{-2}	1.9×10^{-3}	1.1×10^{-2}	6.6×10^{-1}
023d	0.5	4.000×10^6	3.00	1.0×10^{-2}	5.3×10^{-2}	2.0×10^{-3}	1.1×10^{-2}	6.8×10^{-1}
024d	0.5	4.000×10^6	4.00	1.0×10^{-2}	5.3×10^{-2}	1.9×10^{-3}	1.1×10^{-2}	6.5×10^{-1}
025d	0.5	4.000×10^6	6.00	1.0×10^{-2}	5.3×10^{-2}	2.2×10^{-3}	1.2×10^{-2}	5.4×10^{-1}
026m	0.5	5.000×10^6	0.50	1.5×10^{-2}	6.8×10^{-2}	8.4×10^{-3}	8.8×10^{-3}	2.3×10^{-1}
027m	0.5	5.000×10^6	1.00	1.4×10^{-2}	7.1×10^{-2}	5.5×10^{-3}	1.0×10^{-2}	2.5×10^{-1}
027d	0.5	5.000×10^6	1.00	1.3×10^{-2}	6.7×10^{-2}	2.0×10^{-3}	1.4×10^{-2}	8.1×10^{-1}
028d	0.5	5.000×10^6	2.00	1.3×10^{-2}	6.6×10^{-2}	2.2×10^{-3}	1.4×10^{-2}	6.8×10^{-1}
029d	0.5	5.000×10^6	3.00	1.3×10^{-2}	6.8×10^{-2}	2.1×10^{-3}	1.4×10^{-2}	7.2×10^{-1}
030d	0.5	5.000×10^6	4.00	1.3×10^{-2}	6.5×10^{-2}	2.5×10^{-3}	1.6×10^{-2}	7.0×10^{-1}
031d	0.5	5.000×10^6	5.00	1.3×10^{-2}	6.7×10^{-2}	2.5×10^{-3}	1.5×10^{-2}	6.8×10^{-1}
032m	0.5	6.000×10^6	1.00	1.7×10^{-2}	8.5×10^{-2}	6.3×10^{-3}	1.3×10^{-2}	2.8×10^{-1}
032d	0.5	6.000×10^6	1.00	1.5×10^{-2}	8.0×10^{-2}	2.6×10^{-3}	1.7×10^{-2}	8.2×10^{-1}
033m	0.5	7.000×10^6	1.00	2.0×10^{-2}	9.6×10^{-2}	7.4×10^{-3}	1.4×10^{-2}	2.5×10^{-1}
033d	0.5	7.000×10^6	1.00	1.8×10^{-2}	8.6×10^{-2}	3.0×10^{-3}	2.0×10^{-2}	8.5×10^{-1}
034m	0.5	9.000×10^6	1.00	2.5×10^{-2}	1.2×10^{-1}	8.2×10^{-3}	1.9×10^{-2}	3.6×10^{-1}
035m	0.5	1.000×10^7	1.00	2.7×10^{-2}	1.3×10^{-1}	8.7×10^{-3}	2.1×10^{-2}	3.4×10^{-1}
036m	1.5	2.500×10^6	0.75	3.9×10^{-3}	2.6×10^{-2}	2.9×10^{-3}	3.3×10^{-3}	4.7×10^{-2}
037m	1.5	2.500×10^6	1.00	4.5×10^{-3}	2.7×10^{-2}	2.0×10^{-3}	3.6×10^{-3}	1.9×10^{-1}
038m	1.5	2.500×10^6	1.50	4.3×10^{-3}	2.8×10^{-2}	9.2×10^{-4}	4.4×10^{-3}	1.0×10^{-1}
038d	1.5	2.500×10^6	1.50	4.3×10^{-3}	2.8×10^{-2}	8.2×10^{-4}	5.0×10^{-3}	7.9×10^{-1}
039d	1.5	2.500×10^6	2.00	4.3×10^{-3}	3.0×10^{-2}	7.7×10^{-4}	4.6×10^{-3}	7.1×10^{-1}
040d	1.5	2.500×10^6	3.00	4.2×10^{-3}	2.9×10^{-2}	8.0×10^{-4}	4.8×10^{-3}	7.3×10^{-1}
041m	1.5	3.000×10^6	0.75	5.5×10^{-3}	3.6×10^{-2}	2.9×10^{-3}	4.8×10^{-3}	2.1×10^{-1}
042m	1.5	3.000×10^6	1.00	6.0×10^{-3}	3.6×10^{-2}	2.0×10^{-3}	5.1×10^{-3}	3.9×10^{-1}
042d	1.5	3.000×10^6	1.00	5.7×10^{-3}	3.7×10^{-2}	1.1×10^{-3}	6.4×10^{-3}	8.5×10^{-1}
043d	1.5	3.000×10^6	2.00	5.5×10^{-3}	3.7×10^{-2}	1.1×10^{-3}	6.2×10^{-3}	7.1×10^{-1}
044d	1.5	3.700×10^6	3.00	7.3×10^{-3}	4.7×10^{-2}	1.4×10^{-3}	7.9×10^{-3}	6.0×10^{-1}
045m	1.5	4.000×10^6	0.50	9.5×10^{-3}	4.9×10^{-2}	5.3×10^{-3}	6.2×10^{-3}	2.8×10^{-1}
046m	1.5	4.000×10^6	0.75	8.7×10^{-3}	5.2×10^{-2}	3.0×10^{-3}	6.9×10^{-3}	4.5×10^{-1}
046d	1.5	4.000×10^6	0.75	8.5×10^{-3}	5.3×10^{-2}	1.5×10^{-3}	9.3×10^{-3}	8.2×10^{-1}
047d	1.5	4.000×10^6	1.00	8.5×10^{-3}	5.2×10^{-2}	1.4×10^{-3}	9.4×10^{-3}	7.8×10^{-1}
048d	1.5	4.000×10^6	2.00	8.5×10^{-3}	5.3×10^{-2}	1.5×10^{-3}	8.4×10^{-3}	6.9×10^{-1}
049m	1.5	4.625×10^6	0.50	9.5×10^{-3}	5.8×10^{-2}	6.0×10^{-3}	7.5×10^{-3}	4.5×10^{-1}
050m	1.5	4.625×10^6	0.75	1.0×10^{-2}	6.2×10^{-2}	3.6×10^{-3}	8.1×10^{-3}	5.3×10^{-1}

Table A1. – *continued.*

Model	N_ϱ	Ra	Pm	Ro	Ro_ℓ	Ro_z	Lo	$f_{\mathrm{dip}_{\mathrm{ax}}}$
`050d`	1.5	4.625×10^{6}	0.75	1.0×10^{-2}	6.2×10^{-2}	1.7×10^{-3}	1.1×10^{-2}	8.6×10^{-1}
`051d`	1.5	4.625×10^{6}	1.00	1.0×10^{-2}	6.3×10^{-2}	1.7×10^{-3}	1.1×10^{-2}	7.6×10^{-1}
`052d`	1.5	5.000×10^{6}	1.00	1.1×10^{-2}	6.7×10^{-2}	1.8×10^{-3}	1.2×10^{-2}	7.5×10^{-1}
`053d`	1.5	5.000×10^{6}	2.00	1.1×10^{-2}	6.7×10^{-2}	1.8×10^{-3}	1.2×10^{-2}	6.5×10^{-1}
`054m`	1.5	5.550×10^{6}	0.75	1.2×10^{-2}	7.4×10^{-2}	4.0×10^{-3}	9.9×10^{-3}	4.7×10^{-1}
`054d`	1.5	5.550×10^{6}	0.75	1.3×10^{-2}	7.7×10^{-2}	2.0×10^{-3}	1.4×10^{-2}	8.4×10^{-1}
`055d`	1.5	5.550×10^{6}	1.00	1.3×10^{-2}	7.7×10^{-2}	2.1×10^{-3}	1.3×10^{-2}	7.4×10^{-1}
`056d`	1.5	5.550×10^{6}	2.00	1.2×10^{-2}	7.4×10^{-2}	–	1.5×10^{-2}	6.3×10^{-1}
`057m`	1.5	6.500×10^{6}	0.50	1.6×10^{-2}	8.8×10^{-2}	5.5×10^{-3}	1.1×10^{-2}	4.1×10^{-1}
`058m`	1.5	6.500×10^{6}	0.75	1.5×10^{-2}	8.8×10^{-2}	4.3×10^{-3}	1.2×10^{-2}	4.8×10^{-1}
`058d`	1.5	6.500×10^{6}	0.75	1.5×10^{-2}	8.9×10^{-2}	2.4×10^{-3}	1.6×10^{-2}	8.3×10^{-1}
`059d`	1.5	6.500×10^{6}	1.00	1.5×10^{-2}	8.8×10^{-2}	2.5×10^{-3}	1.6×10^{-2}	7.7×10^{-1}
`060m`	1.5	8.000×10^{6}	0.75	1.9×10^{-2}	1.1×10^{-1}	5.4×10^{-3}	1.5×10^{-2}	3.8×10^{-1}
`060d`	1.5	8.000×10^{6}	0.75	1.9×10^{-2}	1.1×10^{-1}	3.3×10^{-3}	2.0×10^{-2}	8.2×10^{-1}
`061d`	1.5	8.000×10^{6}	1.00	1.9×10^{-2}	1.1×10^{-1}	3.0×10^{-3}	2.0×10^{-2}	7.7×10^{-1}
`062m`	1.5	9.000×10^{6}	0.50	2.2×10^{-2}	1.2×10^{-1}	6.4×10^{-3}	1.6×10^{-2}	4.5×10^{-1}
`063m`	1.5	9.000×10^{6}	1.00	2.2×10^{-2}	1.2×10^{-1}	5.1×10^{-3}	1.8×10^{-2}	3.1×10^{-1}
`064m`	1.5	1.000×10^{7}	0.50	2.5×10^{-2}	1.3×10^{-1}	8.0×10^{-3}	1.8×10^{-2}	3.0×10^{-1}
`065m`	2.0	3.000×10^{6}	1.00	4.0×10^{-3}	2.9×10^{-2}	1.8×10^{-3}	3.8×10^{-3}	2.2×10^{-1}
`066d`	2.0	3.000×10^{6}	2.00	4.0×10^{-3}	3.1×10^{-2}	5.5×10^{-4}	4.5×10^{-3}	7.7×10^{-1}
`067m`	2.0	4.000×10^{6}	1.00	6.8×10^{-3}	4.6×10^{-2}	1.7×10^{-3}	6.0×10^{-3}	2.9×10^{-1}
`068d`	2.0	4.000×10^{6}	2.00	6.5×10^{-3}	4.6×10^{-2}	1.1×10^{-3}	7.2×10^{-3}	7.2×10^{-1}
`069d`	2.0	4.000×10^{6}	3.00	6.6×10^{-3}	4.6×10^{-2}	1.1×10^{-3}	7.3×10^{-3}	6.4×10^{-1}
`070m`	2.0	5.000×10^{6}	0.50	8.3×10^{-3}	5.5×10^{-2}	5.4×10^{-3}	6.4×10^{-3}	2.3×10^{-1}
`071m`	2.0	5.000×10^{6}	1.00	9.2×10^{-3}	6.0×10^{-2}	2.1×10^{-3}	7.5×10^{-3}	2.9×10^{-1}
`072d`	2.0	5.000×10^{6}	1.50	9.3×10^{-3}	6.4×10^{-2}	1.6×10^{-3}	9.9×10^{-3}	6.8×10^{-1}
`073d`	2.0	5.000×10^{6}	2.00	9.1×10^{-3}	6.4×10^{-2}	1.7×10^{-3}	1.0×10^{-2}	6.3×10^{-1}
`074d`	2.0	5.000×10^{6}	3.00	9.0×10^{-3}	6.1×10^{-2}	1.5×10^{-3}	1.0×10^{-2}	6.1×10^{-1}
`075m`	2.0	6.000×10^{6}	0.50	1.1×10^{-2}	7.3×10^{-2}	4.1×10^{-3}	8.2×10^{-3}	2.5×10^{-1}
`076d`	2.0	6.000×10^{6}	2.00	1.2×10^{-2}	7.9×10^{-2}	2.0×10^{-3}	1.3×10^{-2}	5.6×10^{-1}
`077m`	2.0	7.000×10^{6}	0.70	1.5×10^{-2}	8.7×10^{-2}	4.0×10^{-3}	1.2×10^{-2}	1.7×10^{-1}
`078m`	2.0	7.000×10^{6}	1.00	1.4×10^{-2}	9.0×10^{-2}	3.0×10^{-3}	1.2×10^{-2}	4.4×10^{-1}
`079d`	2.0	7.000×10^{6}	1.50	1.4×10^{-2}	9.0×10^{-2}	1.9×10^{-3}	1.6×10^{-2}	5.9×10^{-1}
`080d`	2.0	7.000×10^{6}	2.00	1.4×10^{-2}	8.8×10^{-2}	1.7×10^{-3}	1.6×10^{-2}	6.7×10^{-1}
`081d`	2.0	7.000×10^{6}	3.00	1.4×10^{-2}	9.1×10^{-2}	1.9×10^{-3}	1.7×10^{-2}	5.7×10^{-1}
`082m`	2.0	8.500×10^{6}	0.50	1.8×10^{-2}	1.1×10^{-1}	4.6×10^{-3}	1.3×10^{-2}	3.9×10^{-1}
`083d`	2.0	8.500×10^{6}	2.00	1.8×10^{-2}	1.1×10^{-1}	2.9×10^{-3}	1.9×10^{-2}	7.5×10^{-1}
`084m`	2.0	1.000×10^{7}	0.50	2.2×10^{-2}	1.2×10^{-1}	7.3×10^{-3}	1.6×10^{-2}	2.7×10^{-1}
`085m`	2.0	1.000×10^{7}	3.00	2.0×10^{-2}	1.2×10^{-1}	3.9×10^{-3}	2.1×10^{-2}	2.1×10^{-1}
`086m`	2.0	1.200×10^{7}	0.50	2.6×10^{-2}	1.4×10^{-1}	8.0×10^{-3}	1.8×10^{-2}	3.9×10^{-1}
`087m`	2.0	1.400×10^{7}	0.50	3.0×10^{-2}	1.6×10^{-1}	1.0×10^{-2}	2.1×10^{-2}	3.9×10^{-1}
`088d`	2.5	3.200×10^{6}	4.00	2.6×10^{-3}	2.0×10^{-2}	3.2×10^{-4}	3.6×10^{-3}	5.2×10^{-1}
`089d`	2.5	3.400×10^{6}	4.00	3.1×10^{-3}	2.4×10^{-2}	3.7×10^{-4}	3.8×10^{-3}	6.0×10^{-1}
`090d`	2.5	4.400×10^{6}	3.00	5.7×10^{-3}	4.5×10^{-2}	8.1×10^{-4}	7.0×10^{-3}	5.5×10^{-1}
`091d`	2.5	4.400×10^{6}	4.00	5.4×10^{-3}	4.1×10^{-2}	7.5×10^{-4}	6.8×10^{-3}	5.2×10^{-1}
`092d`	2.5	5.400×10^{6}	2.00	8.0×10^{-3}	5.9×10^{-2}	1.1×10^{-3}	9.3×10^{-3}	4.0×10^{-1}
`093d`	2.5	5.400×10^{6}	3.00	7.9×10^{-3}	5.9×10^{-2}	1.1×10^{-3}	1.0×10^{-2}	5.6×10^{-1}
`094d`	2.5	5.400×10^{6}	4.00	7.6×10^{-3}	5.6×10^{-2}	1.1×10^{-3}	1.1×10^{-2}	5.0×10^{-1}
`095m`	2.5	6.400×10^{6}	1.00	9.8×10^{-3}	7.2×10^{-2}	2.0×10^{-3}	9.0×10^{-3}	1.3×10^{-1}
`096d`	2.5	6.400×10^{6}	2.00	1.0×10^{-2}	7.1×10^{-2}	1.2×10^{-3}	1.2×10^{-2}	4.3×10^{-1}
`097d`	2.5	6.400×10^{6}	3.00	9.7×10^{-3}	6.9×10^{-2}	1.3×10^{-3}	1.4×10^{-2}	5.5×10^{-1}
`098m`	2.5	7.400×10^{6}	1.00	1.2×10^{-2}	8.3×10^{-2}	2.4×10^{-3}	1.1×10^{-2}	1.5×10^{-1}
`099d`	2.5	7.400×10^{6}	2.00	1.3×10^{-2}	8.4×10^{-2}	1.8×10^{-3}	1.5×10^{-2}	6.3×10^{-1}
`100d`	2.5	7.400×10^{6}	3.00	1.2×10^{-2}	8.4×10^{-2}	1.9×10^{-3}	1.4×10^{-2}	4.8×10^{-1}
`101m`	2.5	9.000×10^{6}	2.00	1.5×10^{-2}	9.9×10^{-2}	3.6×10^{-3}	1.5×10^{-2}	1.5×10^{-1}
`102m`	2.5	1.000×10^{7}	1.00	1.8×10^{-2}	1.3×10^{-1}	4.8×10^{-3}	1.4×10^{-2}	1.2×10^{-1}
`103m`	2.5	1.100×10^{7}	1.00	2.4×10^{-2}	1.5×10^{-1}	5.8×10^{-3}	1.6×10^{-2}	1.0×10^{-1}
`104d`	3.0	8.000×10^{6}	4.00	9.2×10^{-3}	6.9×10^{-2}	1.4×10^{-3}	1.4×10^{-2}	6.0×10^{-1}
`105m`	3.0	9.000×10^{6}	4.00	1.2×10^{-2}	8.6×10^{-2}	3.0×10^{-3}	1.4×10^{-2}	3.2×10^{-1}

Annexe C

Prépublications

C.1 *Multi-linear high order semi-Lagrangian schemes for incompressible flows in Cartesian geometries*

Cameron, A., Raynaud, R. & Dormy, E., submitted to *International Journal for Numerical Methods in Fluids.*

INTERNATIONAL JOURNAL FOR NUMERICAL METHODS IN FLUIDS

Int. J. Numer. Meth. Fluids 0000; **00**:1–22

Multi-stage high order semi-Lagrangian schemes for incompressible flows in Cartesian geometries

Alexandre Cameron, Raphaël Raynaud, Emmanuel Dormy

MAG (ENS/IPGP), LRA, Département de Physique, École Normale Supérieure, Paris, France.

SUMMARY

Efficient transport algorithms are essential to the numerical resolution of incompressible fluid flow problems. Semi-Lagrangian methods are widely used in grid based methods to achieve this aim. The accuracy of the interpolation strategy then determines the properties of the scheme. We introduce a simple multi-stage procedure which can easily be used to increase the order of accuracy of a code based on multi-linear interpolations. This approach is an extension of a corrective algorithm introduced by Dupont & Liu (2003, 2007). This multi-stage procedure can be easily implemented in existing parallel codes using a domain decomposition strategy, as the communications pattern is identical to that of the multi-linear scheme. We show how a combination of a forward and backward error correction can provide a third-order accurate scheme, thus significantly reducing diffusive effects while retaining a non-dispersive leading error term.

Received . . .

KEY WORDS: Transport in fluids, Finite volumes, Finite differences, Semi-Lagrangian

---

*Correspondence to: MAG (ENS/IPGP), LRA, Département de Physique, École Normale Supérieure, 24 rue Lhomond, 75252 Paris Cedex 05, France

alexandre.cameron@ens.fr, raphael.raynaud@ens.fr, dormy@phys.ens.fr

1. INTRODUCTION

Semi-Lagrangian methods offer an efficient and widely used approach to model advection dominated problems. Initially introduced in atmospheric and weather models [1, 2], these methods are now widely used in all fields of fluid mechanics [3, 4, 5]. They have found a wide range of application in computational fluid dynamics. These methods have triggered a wide variety of schemes, including spline interpolation methods [6, 7, 8], finite element WENO algorithms [9, 10, 11] or CIP methods [12, 13]. Considerable development has also been achieved in application to hyperbolic problems (e.g. compressible hydrodynamics [14], Vlasov equation [15]) and fall out of the scope of this paper.

Semi-Lagrangian methods involve an advected field Φ, following the characteristics backward in time. The procedure requires the estimation of field values that do not lie on the computational grid. Semi-Lagrangian methods therefore rely on an interpolation of $\Phi(t - \Delta t, \mathbf{x} - \boldsymbol{u}\Delta t)$, which in general is not a known quantity on the descrete grid.

Because of their local nature, low order semi-Lagrangian methods perform remarkably well on massively parallel computers [16, 17]. Limitations occur with high-order interpolation methods. As the width of the stencil increases, the locality of the scheme is reduced and the resulting schemes require larger communications stencils. When the interpolation strategy is simple, multi-linear in the case of the CIR scheme [18], the scheme is local and the computational cost is small. If the interpolation stencil is not localized near the computational point, but near the point where the interpolated value must be reconstructed, one can show that the method is then unconditionally stable, in the case of a uniform and steady velocity field [19]. Such schemes are however prone to large inter-process communations, and are not unconditionally stable for general flows.

Dupont *et al.* [20, 21, 22] introduced two new corrective algorithms: “Forward Error Correction” (here denoted FEC) and “Backward Error Correction” (here denoted BEC). These algorithms take advantage of the reversibility of the advection equation to improve the order of most semi-Lagrangian schemes by using multiple calls of an initial advection scheme. The resulting schemes

DOI: 10.1002/fld

yield an enhanced accuracy. In that sense, they are built with a similar spirit to the predictor-corrector method [23] or the MacCormack scheme [24].

Here we introduce a new scheme following this methodology, and thus extend this approach to third order accuracy.

2. MULTI-STAGE APPROACHES

A possible strategy to increase the order of Semi-Lagrangian schemes is to use higher order interpolation formula e.g. [25]. This has the drawback of relying on a wider stencil, which requires larger communication patterns on a distributed memory computer. Another significant issue with wider stencils is the handling of boundary conditions.

Equation (1) models the advection of a passive scalar Φ by a velocity field $\boldsymbol{u}$,

$$D_t\Phi \equiv \left[\partial_t + (\boldsymbol{u}\cdot\boldsymbol{\nabla})\right]\Phi = 0\,. \tag{1}$$

The Lagrangian derivative in (1) is usually defined as the limit, following the characteristic, of

$$D_t\Phi = \lim_{\Delta t\to 0}\frac{\Phi(t,\mathbf{x}) - \Phi(t-\Delta t, \mathbf{x}-\boldsymbol{u}\Delta t)}{\Delta t}\,. \tag{2}$$

Semi-Lagrangian methods rely on this expression to discretize the advective operator $D_t\Phi$ instead of expanding the sum in a temporal term $\partial_t\Phi$ and an advective term $(\boldsymbol{u}\cdot\boldsymbol{\nabla})\Phi$, as in (1). The semi-Lagrangian discretisation of (1) therefore introduces an interpolation operator $L_{\boldsymbol{u}}\left[\Phi^n\right] = \widetilde{\Phi}^n(\mathbf{x}-\boldsymbol{u}\Delta t)$, where $\widetilde{\Phi}$ denotes the interpolated value away from the grid points.

A strategy introduced by Dupont *et al.* [20] to increase the order of a semi-Lagrangian scheme, without requiring the use of high-order interpolation formula, is based on two consecutive calls to the interpolation operator, the second call involving the reversed flow. This method is known as the "Forward Error Correction" [20]. The advantages of this procedure over the above high order schemes rely both on the accurate implementation of boundary conditions and on the limited

DOI: 10.1002/fld

communication stencil. The Forward Error Correction scheme is constructed as

$$\bar{\Phi} \equiv L_{-\boldsymbol{u}}\left[L_{\boldsymbol{u}}\left[\Phi^n\right]\right] , \tag{3}$$

$$FEC\left[\Phi^n\right] \equiv L_{\boldsymbol{u}}\left[\Phi^n\right] + \left(\Phi^n - \bar{\Phi}\right)/2 \, . \tag{4}$$

The FEC corrective algorithm has further been improved in [21, 22] using three calls to the interpolation operator for each time-step. The resulting algorithm is known as the "Backwards Error Correction" (BEC) algorithm. It is constructed using

$$BEC\left[\Phi^n\right] \equiv L_{\boldsymbol{u}}\left[\Phi^n + (\Phi^n - \bar{\Phi})/2\right] \, . \tag{5}$$

Both the FEC and the BEC algorithms suppress the leading order error term when the interpolation operator is irreversible. Both the FEC and the BEC schemes are free of numerical diffusion. However, they introduce numerical dispersive effects related to their truncation errors.

This truncation error can be advantageously used to construct a scheme free of numerical dispersion and characterized by a fourth order derivative truncation error. This is achieved for the same computational cost as the BEC scheme. A new "Combined Error Correction" (CEC) algorithm is introduced, using a linear combination of the FEC and BEC algorithms,

$$CEC\left[\Phi\right] \equiv c_F FEC\left[\Phi\right] + c_B BEC\left[\Phi\right] \, . \tag{6}$$

When the CIR scheme is used as the interpolation operator, the scheme generated by the FEC algorithm is similar, in the Eulerian framework, to the one introduced in [26]. In this case, the values of the coefficients c_F and c_B in (6) can be explicitly determined and the stability of the resulting schemes assessed. In one dimension, their expression is

$$3\,c_F = 2 - \Delta x/(|u|\Delta t) \quad \text{and} \quad c_B = 1 - c_F , \tag{7}$$

where Δt denotes the time-step and Δx the grid-step.

In one dimension of space, this scheme is strictly equivalent to the Eulerian upwind scheme. It is well known [27, 28, 29] that this scheme is stable for Courant-Friedrichs-Lewy (CFL) numbers smaller than unity and introduces diffusive errors. The spurious diffusive effects are directly related to the truncation error of the scheme.

DOI: 10.1002/fld

The generalization to d-dimension must be carried out with care. As described later, the fields can be advected one dimension at a time using a splitting technique similar to [26]. In two or three dimensions, the interpolation can be done by applying the CEC scheme on each direction separately.

3. ONE-DIMENSIONAL ALGORITHMS

In the semi-Lagrangian formalism, the advection equation can be discretized using the CIR scheme [18]. In one dimension, the CIR scheme has the same stencil as the Upwind scheme [5, 23, 28]

$$\Phi_i^{CIR} = (1-U_i)\Phi^n[i] + U_i\Phi^n[i-s_i]\,, \tag{8}$$

where $\Phi^n[i] = \Phi_i^n$ denotes the value of the passive scalar at time $n\,\Delta t$ and position $i\,\Delta x$, $s_i = \mathrm{sign}(u_i)$ the sign of the velocity and $U_i = |u_i|\Delta t/\Delta x$ the reduced velocity with u_i the velocity. A Von Neumann stability analysis shows that the scheme is strictly stable for $U \leq 1$. For a constant velocity, the modified equation takes the form

$$\Big[\partial_t\Phi + u\partial_x\Phi\Big]_{CIR} = D_{CIR}\partial_x^2\Phi + \dots \quad \text{with} \quad D_{CIR} = (1-U)\,\frac{|u|\Delta x}{2}\,. \tag{9}$$

The FEC scheme (4) is a multi-stage version of the CIR scheme. The developed expression for the FEC scheme requires the first nearest neighbors for the velocity and the second nearest neighbors for the passive scalar (see Appendix A). For a constant velocity, the expression of FEC is

$$FEC[\Phi]_i = -\tfrac{1}{2}U(1-U)\Phi^n[i+1] + (1-U^2)\Phi^n[i] + \tfrac{1}{2}U(1+U)\Phi^n[i-1]\,. \tag{10}$$

The stability analysis of (10) provides the following expression for the amplification factor

$$\xi_{FEC} = 1 - U^2 + U^2\cos(k\Delta x) - iU\sin(k\Delta x)\,. \tag{11}$$

The FEC scheme is stable for $U \leq 1$. The modified equation associated to this scheme is

$$\Big[\partial_t\Phi + u\partial_x\Phi\Big]_{FEC} = -(1-U^2)\frac{u\Delta x^2}{3!}\partial_x^3\Phi - 3(1-U^2)\frac{u^2\Delta x^2\Delta t}{4!}\partial_x^4\Phi + \dots \tag{12}$$

DOI: 10.1002/fld

The BEC scheme, presented in (5), is a modified version of the CIR scheme using $\bar{\Phi}^n$ to correct the field before the advection step. The developed expression of the BEC scheme requires the second nearest neighbors for the velocity and third nearest neighbors for the passive scalar (see Appendix A). To avoid using this long development, the simplified case of a constant velocity will be studied.

$$\begin{aligned} BEC[\Phi]_i = &- \frac{U}{2}(1-U)^2\Phi^n_{i+1} + \frac{(1-U)}{2}\left(3-(1-U)^2-2U^2\right)\Phi^n_i \\ &+ \frac{U}{2}\left(3-2(1-U)^2-U^2\right)\Phi^n_{i-1} - \frac{U^2}{2}(1-U)\Phi^n_{i-2}\,. \end{aligned} \tag{13}$$

The stability analysis on (13) leads to the following amplification factor

$$\xi_{BEC} = 1 - 2iU\sin(\tfrac{1}{2}k\Delta x)\Big[\mathrm{e}^{-\frac{1}{2}ik\Delta x}U(1+2[1-U]\sin^2(\tfrac{1}{2}k\Delta x)) + \cos(\tfrac{1}{2}k\Delta x)(1-U)\Big]\,. \tag{14}$$

It can be shown analytically that the BEC scheme is stable for $U \leq 1$. In fact, the BEC scheme is still stable for a CFL number smaller than 1.5. The truncation error analysis leads to

$$\begin{aligned} \Big[\partial_t\Phi + u\partial_x\Phi\Big]_{BEC} = &- (1-U)(1-2U)\tfrac{u\Delta x^2}{3!}\partial_x^3\Phi \\ &- 9(1-U)^2\tfrac{u^2\Delta x^2\Delta t}{4!}\partial_x^4\Phi + \ldots \end{aligned} \tag{15}$$

Simulations with Heaviside, triangle and cosine distributions advected by a constant velocity were carried out for a CFL number $U > 1$. For $U \lesssim 1.5$, the BEC scheme gives finite results consistent with the stable results collected for $U < 1$. The other schemes (CIR, FEC and CEC) diverge for $U > 1$ and the BEC scheme diverges for $U \gtrsim 1.5$. This extension of stability of the BEC scheme can be understood in the following way: for $U > 1$, the interpolation is performed with points that are not the nearest value to the reconstructed point. The contribution of the second nearest neighbors in the BEC formula results in an enhanced stability of the scheme.

The FEC and BEC schemes both have modified equations with a third order derivative truncation error. The CEC scheme, presented in (6) and (7) is a linear combination of these two schemes. The weights are computed to cancel the leading order of truncation error (see Appendix A) and generate a higher order scheme. Using the linearity of the stability analysis, the amplification

DOI: 10.1002/fld

factor is

$$\xi_{CEC} = 1 - \tfrac{2}{3}\sin(\tfrac{1}{2}k\Delta x)\Big[U\Big(3 + 2[1-U^2]\sin^2(\tfrac{1}{2}k\Delta x)\Big)\sin(\tfrac{1}{2}k\Delta x) + \Big(3 + 2U[1-U^2]\sin^2(\tfrac{1}{2}k\Delta x)\Big)i\cos(\tfrac{1}{2}k\Delta x)\Big]. \tag{16}$$

The CEC scheme is stable for $U \leq 1$. To leading order, the modified equation of the CEC scheme is

$$\Big[\partial_t\Phi + u\partial_x\Phi\Big]_{CEC} = -(1+U)(1-U)(2-U)\frac{|u|(\Delta x)^3}{4!}\partial_x^4\Phi + \dots \tag{17}$$

The essential properties of the different schemes are reported in Tab. I. The computational cost is evaluated using the number of composed interpolation operators. The complexity of the interpolation operator varies with the interpolation method used. In the case of the CIR scheme, the complexity is $\mathcal{O}(N)$ where N is the total number grid of points.

Scheme	Formula	Error	Stability	Nb of calls
CIR	$CIR\big[\Phi\big] = L_+\big[\Phi\big]$	$(1-U)\,\frac{\lvert u\rvert\Delta x}{2}\partial_x^2\Phi$	$U<1$	1
FEC	$FEC\big[\Phi\big]=L_+\big[\Phi\big] + \frac{1}{2}(\Phi-\bar{\Phi})$	$-(1-U^2)\frac{u\Delta x^2}{3!}\partial_x^3\Phi$ $-3(1-U^2)\frac{u^2\Delta x^2\Delta t}{4!}\partial_x^4\Phi$	$U<1$	2
BEC	$BEC\big[\Phi\big]=L_+\big[\Phi + \frac{1}{2}(\Phi-\bar{\Phi})\big]$	$-(1-U)(1-2U)\frac{u\Delta x^2}{3!}\partial_x^3\Phi$ $-9(1-U)^2\frac{u^2\Delta x^2\Delta t}{4!}\partial_x^4\Phi$	$U \lesssim 1.5$	3
CEC	$CEC\big[\Phi\big]=L_+\Big[\Phi + \frac{1+U}{6U}(\Phi-\bar{\Phi})\Big]$ $+\frac{1-2U}{6U}(\Phi-\bar{\Phi})$	$-(1+U)(1-U)(2-U)\frac{\lvert u\rvert(\Delta x)^3}{4!}\partial_x^4\Phi$	$U<1$	3

Table I. Comparative table of one dimension schemes.

DOI: 10.1002/fld

4. RESULTS FOR ONE-DIMENSIONAL PROBLEMS

To assess the efficiency of the schemes introduced previously, simulations with a constant velocity were performed. A one-dimensional periodic domain is considered, and the solution is advected for 10 or 100 cycles. Fig. 1, 2 and 3 show the advection of three density profiles with different regularities. Because of the Fourier properties of sine functions, the first harmonic was studied thoroughly to check that it matches the properties of the modified equation.

The first set of tests was performed using an Heaviside profile $\Phi(x,t=0) = \text{sign}\left[\sin(2\pi x/l)\right]$. This is a demanding test, as this profile is discontinuous at two cross-over positions (0 and 0.5). As time elapses, the high frequencies get damped and the profile is nearly reduced to its first harmonic. In Fig. 1, the CEC scheme is closer to the analytical solution than the other schemes by three criteria: (i) the “flatness” of its profile at the beginning of the simulation, (ii) the distance from the analytic cross-over position at all time and (iii) the phase drift of the profile at long time. These criteria may seem independent but they are all linked to the Fourier properties of the modified equation.

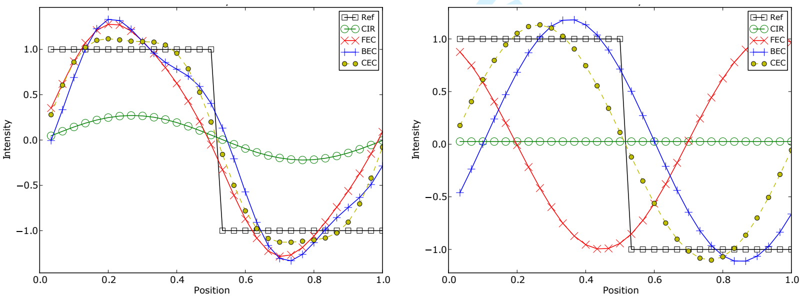

(a) 10 periods (b) 100 periods

Figure 1. One dimension advection of a Heaviside with a resolution of $N = 32$.

The second set of tests was performed using a triangular profile, $\Phi(x,t=0) = |x/l - 0.5|$. This profile is non differentiable at two cross-over position (0 and 0.5). In Fig. 2, the observations reported

DOI: 10.1002/fld

in the previous paragraph still hold for the triangular profile. As expected, the CEC scheme is closer to the analytic results in the case of a continuous but non-derivable profile.

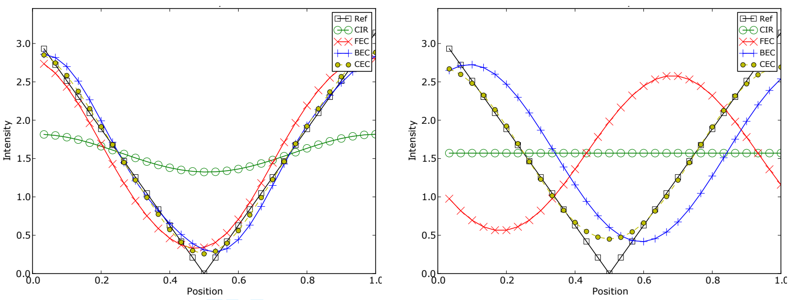

(a) 10 periods (b) 100 periods

Figure 2. One dimension advection of a triangle with a resolution of $N = 32$.

The last tests were performed using the first harmonic cosine profile, $\Phi(x, t = 0) = -\cos(2\pi x/l)$. The properties of the profile will be studied in more details in Fig. 9 and 8. In Fig. 3, the CIR scheme is so diffusive that a "corrected CIR" (green diamond line)[†] is plotted. Even though the CIR scheme is near zero in Fig. 3, the norm of its difference to the analytic profile is smaller than the FEC scheme which drifted to such an extent that it is nearly opposite to the reference profile.

[†] The corrected CIR values are equal to those of CIR multiplied by $\exp(D_{CIR}k^2t)$ where D_{CIR} is defined in (9).

DOI: 10.1002/fld

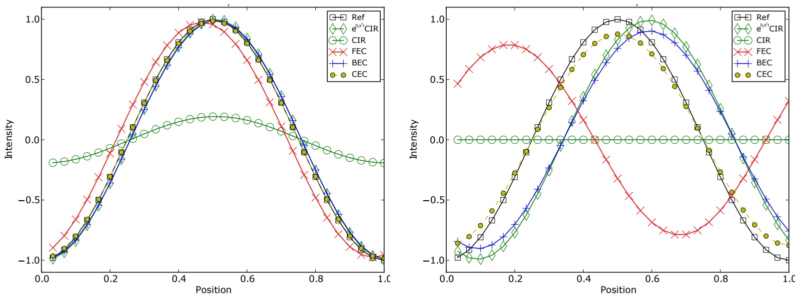

(a) 10 periods (b) 100 periods

Figure 3. One dimension advection of the cosine function with a resolution of $N = 32$.

5. MULTI-DIMENSIONAL PROBLEMS

The extension of the above procedures to multi-dimensional problems requires some care. For instance in two dimensions, the CIR scheme is

$$CIR[\Phi]_{i,j} = (1 - U^x_{i,j})(1 - U^y_{i,j})\Phi^n_{i,j} + (1 - U^x_{i,j})U^y_{i,j}\Phi^n_{i,j-s^y_{i,j}}\,, \tag{18}$$

$$+ U^x_{i,j}(1 - U^y_{i,j})\Phi^n_{i-s^x_{i,j},j} + U^x_{i,j}U^y_{i,j}\Phi^n_{i-s^x_{i,j},j-s^y_{i,j}}\,.$$

The semi-Lagrangian CIR scheme uses one more value ($\Phi[i - s^x_{i,j}][j - s^y_{i,j}]$) than the Eulerian Upwind scheme. However, the CIR scheme is very similar to the Upwind scheme with splitted directions

$$\Phi^\star_{i,j} = (1 - U^x_{i,j})\Phi^n_{i,j} + U^x_{i,j}\Phi^n[i - s^x_{i,j}][j]\,, \tag{19}$$

$$\Phi^{\star\star}_{i,j} = (1 - U^y_{i,j})\Phi^\star_{i,j} + U^y_{i,j}\Phi^\star[i][j - s^y_{i,j}]\,. \tag{20}$$

In general, there is no expression for c_F and c_B equivalent to (7) in the general case in multi-dimension. The approach introduced in the previous section can however be extended to any dimension if the scheme is splitted in directions.

DOI: 10.1002/fld

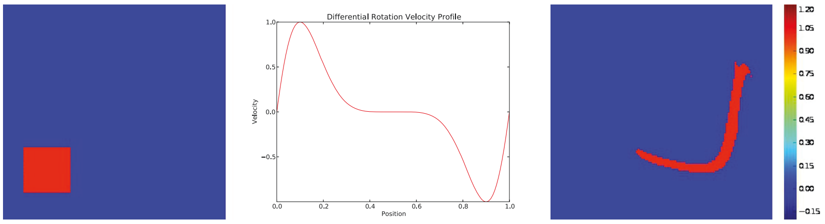

(a) Initial patch distribution (b) Velocity profile $u(x\!=\!0, y)$ or $v(x, y\!=\!0)$ (c) Pure Lagrangian advection

Figure 4. Initial condition, velocity profile and final distribution for the two-dimensional advection test case.

To illustrate applications of our strategy to higher dimensions, let us consider an advection problem in two dimensions of space. A squared patch is considered for the initial distribution of the passive scalar: one inside the square and zero outside, as presented in Fig. 4(a). The order of the schemes for regularly varying velocities should be same as the one for constant velocities. Quantitative results being difficult, only qualitative observations will be made. The following velocity field was used to test the schemes

$$u(x, y) = \frac{y}{l}\left(1 - \frac{y}{l}\right)\left(\frac{1}{2} - \frac{y}{l}\right)\left[\cos\left(2\pi\frac{y}{l}(1 - \frac{y}{l})\right) + 1\right]/(2\pi^2)\,, \tag{21}$$

$$v(x, y) = -\frac{x}{l}\left(1 - \frac{x}{l}\right)\left(\frac{1}{2} - \frac{x}{l}\right)\left[\cos\left(2\pi\frac{x}{l}(1 - \frac{x}{l})\right) + 1\right]/(2\pi^2)\,, \tag{22}$$

where l is the length of the box in both direction. In Fig. 4(b), the velocity cancels out on the edges of the box and is divergence free. With the profiles used, the patch is not transported through the walls of the box even though the simulation has periodic boundary conditions. The patch never intersects itself which makes it easier to track. To compare the results, a fully Lagrangian method was used as a reference. The time-step of this method was twenty times smaller to have more accurate results. The solution is represented in Fig. 4(c).

DOI: 10.1002/fld

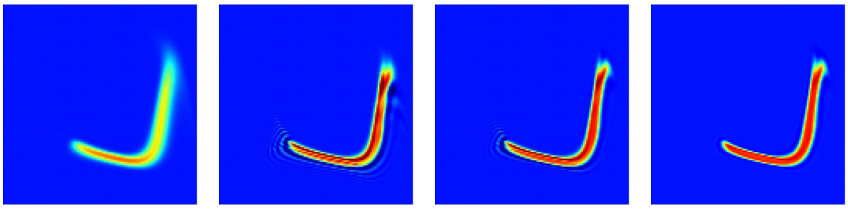

(a) CIR advection (b) FEC advection (c) BEC advection (d) CEC advection

Figure 5. Two-dimensional patch advection using the different schemes.

In Fig. 5 and 6, the analysis of the gap between a scheme and the reference solution should not only be guided by the intensity of the difference but also by the area impacted. The CIR scheme clearly introduces the largest computational error.

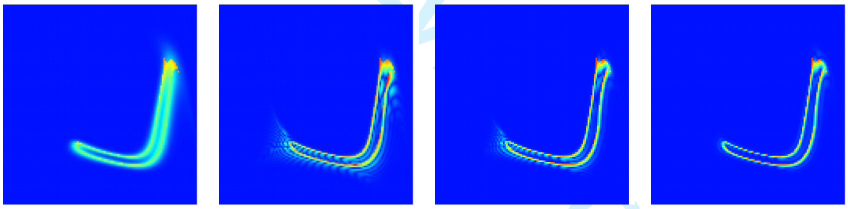

(a) CIR error. (b) FEC error. (c) BEC error. (d) CEC error.

Figure 6. Error, as measured by the difference of the numerical solutions to the reference solution obtained with pure lagrangian advection.

The perturbation of the distribution can also give an intuition of the leading error term in the modified equation. The quick oscillations at the tail of the patch in Fig. 6(b) and 6(c) can be related to the dispersive residuals of the FEC and BEC schemes. In Fig. 6(d), the CEC solution is the closest to the reference solution obtained by the pure lagrangian method. The error is of small amplitude and only impacts the edges of the patch.

DOI: 10.1002/fld

6. APPLICATION TO THERMAL CONVECTION

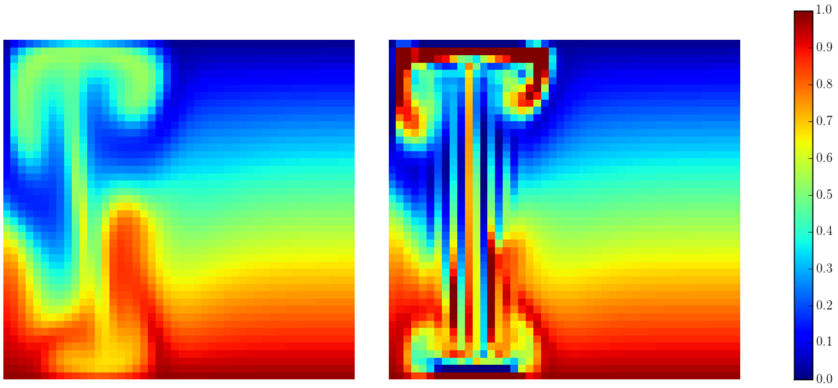

(a) CIR scheme (b) FEC scheme

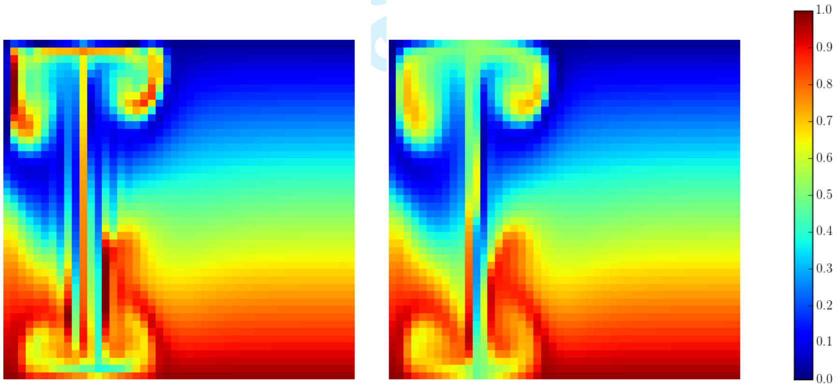

(c) BEC scheme (d) CEC scheme

Figure 7. Rayleigh-Bénard evolution of a localized thermal perturbation. The numerical resolution $N = 50^2$ is intentionally modest, in order to highlight numerical errors.

In this section, the comparison between the different advection schemes is extended to a physically more relevant case: thermal convection in a layer of fluid heated from below. This is canonical example is also known as the Rayleigh-Bénard setup. The schemes will not only be used on passive

DOI: 10.1002/fld

scalars that do not influence the velocity, but on the velocity itself and the temperature, which, in the Rayleigh-Bénard instability, modifies the velocity actively.

The system of equations describing the evolution of the velocity $\boldsymbol{u}$ and the temperature T of the fluid is solved on a two-dimensional Cartesian domain of aspect ratio $\chi = L_z/L_x = 0.5$, bounded by solid and impermeable walls. The bottom and top plates are maintained at fixed temperatures T_0 and $T_0 - \Delta T$, respectively, whereas the vertical walls are assumed to be insulating (no heat flux through the vertical boundaries). Gravity is assumed to be uniform and vertical $\boldsymbol{g} = -g\boldsymbol{e}_z$.

To retain the essential physics with a minimum complexity, the Boussinesq approximation is used to describe the fluid within the cell and assume that variations of all physical properties other than density can be ignored. Variations in density are also neglected "except in so far as they modify the action of gravity" [30]. The density ρ is assumed to be constant everywhere in the governing equations except in the buoyancy force where it is assumed to vary linearly with temperature, $\rho\,(T) = \rho_0\,(1 - \alpha\,(T - T_0))$, where α is the thermal expansion coefficient of the fluid.

The system admits the stationary diffusive solution: $\boldsymbol{u}^\star = 0$, $T^\star = T_0 - z\,\Delta T/L_z$, and $\boldsymbol{\nabla} P^\star = -g\rho\,(T^\star)\,\boldsymbol{e}_z$. Subtracting the stationary solution, choosing L_z, L_z^2/κ, and ΔT as units of length, time, and temperature, respectively, and using the temperature perturbation $\theta = T - T^\star$, the system can be written [31] as

$$\partial_t \boldsymbol{u} + (\boldsymbol{u}\cdot\boldsymbol{\nabla})\,\boldsymbol{u} = -\boldsymbol{\nabla}\Pi + \mathrm{Ra}\mathrm{Pr}\,\theta\,\boldsymbol{e}_z + \mathrm{Pr}\,\boldsymbol{\nabla}^2\boldsymbol{u}\,, \tag{23}$$

$$\partial_t \theta + (\boldsymbol{u}\cdot\boldsymbol{\nabla})\,\theta = w + \boldsymbol{\nabla}^2\theta\,, \tag{24}$$

$$\boldsymbol{\nabla}\cdot\boldsymbol{u} = 0\,, \tag{25}$$

with $w \equiv \boldsymbol{u}\cdot\boldsymbol{e}_z$ the vertical velocity. The non-dimensional control parameters are the Rayleigh number, defined by $\mathrm{Ra} = \alpha g \Delta T L_z^3/(\kappa\nu)$ and which measures the convective driving, and the Prandtl number, defined as the ratio of viscous to thermal diffusion, $\mathrm{Pr}\ = \nu/\kappa$, with ν the kinematic viscosity, κ the thermal diffusivity.

Equations (23) and (24) are discretized on a uniform grid using finite volume formula of order two in space and order one in time, with all the terms being treated explicitly. To enforce the solenoidal

DOI: 10.1002/fld

constraint (25), the pressure-correction scheme [32, 33] is used. This splitting method is composed of two steps. In the first step, a preliminary velocity field $\boldsymbol{u}^\star$ is computed by neglecting the pressure term in Navier-Stokes equation. Since this preliminary velocity field is generally not divergence-free, it is then corrected in a second step by a projection on the space of solenoidal vector fields. Given the temperature and velocity distributions at time-step n, the velocity $\boldsymbol{u}^{n+1}$ is computed by solving

$$\boldsymbol{u}^{(1)} = L\left[\boldsymbol{u}^n, \boldsymbol{u}^n\right], \tag{26}$$

$$\boldsymbol{u}^{(2)} = \boldsymbol{u}^{(1)} + \Delta t\left(\mathrm{Ra}\mathrm{Pr}\,\theta^n \boldsymbol{e}_z + \left[\boldsymbol{\nabla}^2 \boldsymbol{u}\right]^n\right), \tag{27}$$

$$\boldsymbol{\nabla}^2 \phi^n = \boldsymbol{\nabla} \cdot \boldsymbol{u}^{(2)}, \tag{28}$$

$$\boldsymbol{u}^{n+1} = \boldsymbol{u}^{(2)} - \boldsymbol{\nabla}\phi^n. \tag{29}$$

In (28), the algorithm requires to solve at each time-step a Poisson equation for the pressure. The necessary impermeability conditions for the field ϕ are found by multiplying (29) by the normal vector $\boldsymbol{n}$. Together with the velocity boundary condition, they lead to $\boldsymbol{n} \cdot \boldsymbol{\nabla}\phi^n = 0$. The boundary conditions for the velocity field are no-slip, i.e. $\boldsymbol{u} = 0$, while the temperature satisfies $\theta(z = 0) = \theta(z = 1) = 0$ on the horizontal boundaries, and $\partial_x \theta = 0$ on the vertical boundaries. Boundary conditions are imposed on the intermediate velocity field $\boldsymbol{u}^\star$ by introducing ghost points outside of the domain. In consequence, the tangential component of the actual velocity field $\boldsymbol{u}$ will not exactly satisfy the boundary conditions (the error being controlled by the time-step).

In order to develop the instability (the Rayleigh number being sufficiently large and the Prandtl number set to unity), the simulations were always started with $\boldsymbol{u} = 0$ and with a small temperature perturbation. This temperature perturbation consisted of a hot spot ($\theta = 0.1$) next to a cold spot ($\theta = -0.1$). This perturbation, localized close to the lower left corner, generates a rising and a sinking plumes. The different simulations were compared when the rising plume has reached the top boundary (after roughly a thousand iterations).

A very low resolution, $N = 50^2$, was deliberately chosen in order to highlight the numerical errors associated to the different schemes. Snapshots of the total temperature $T = T^\star + \theta$ associated with

DOI: 10.1002/fld

the thermal plume are compared on figure 7. In Fig. 7(c) and 7(b), strong ripples appear in the wake of the plumes. They are not physically relevant and are characteristics of dispersive schemes. The comparison of the plumes in Fig. 7(a) and Fig. 7(d) clearly highlights that the CEC scheme is less diffusive than the CIR scheme for practical physical applications. The CEC scheme offers an improved scheme, with significantly reduced diffusive effects, and free of the strong dispersion characterizing the FEC and BEC schemes.

7. CONCLUSION

Using the simplest semi-Lagrangian CIR scheme introduced by Courant-Isaacson-Rees, it has been demonstrated that a simple multi-stage approach can increase the order of the scheme from first to third order. The resulting scheme is, at leading order, non-dispersive. This procedure was shown to yield significant improvement on a thermal convection problem. It can easily be used to increase the order of existing codes on parallel computers, as the communication stencil is unaltered by the multi-stage approach. The communications among parallel processes are then restricted to the strict miminum (one layer of cell at each domain boundary).

The CEC algorithm, introduced here, only requires a modest increase in the computational cost and can easily be implement in existing codes. Moreover, its implementation is not limited to regular Cartesian finite differences schemes. It can be generalized to other geometries and scheme types by following two simple steps: (i) deriving the modified advection equation for the FEC and BEC schemes and (ii) combining both schemes to cancel out their leading order error.

References

1. Robert A. A stable numerical integration scheme for the primitive meteorological equations. *Atmosphere-Ocean* Mar 1981; **19**(1):35–46, doi:10.1080/07055900.1981.9649098.
2. Robert A. A semi-Lagrangian and semi-implicit numerical integration scheme for the primitive meteorological equations. *J. Meteor. Soc. Japan* 1982; **60**(1):319–325.

DOI: 10.1002/fld

3. Staniforth A, Côté J. Semi-Lagrangian Integration Schemes for Atmospheric ModelsA Review. *Mon. Wea. Rev.* Sep 1991; **119**(9):2206–2223, doi:10.1175/1520-0493(1991)119¡2206:SLISFA¿2.0.CO;2.
4. Oliveira A, Baptista AM. A comparison of integration and interpolation Eulerian-Lagrangian methods. *Int. J. Numer. Meth. Fluids* 1995; **21**(3):183–204, doi:10.1002/fld.1650210302.
5. Durran DR. *Numerical methods for wave equations in geophysical fluid dynamics*. 32, Springer, 1999.
6. Knorr G, Mond M. The representation of shock-like solutions in an Eulerian mesh. *Journal of Computational Physics* Nov 1980; **38**(2):212–226, doi:10.1016/0021-9991(80)90053-4.
7. Shoucri MM. Numerical calculations of discontinuities by shape preserving splines. *Journal of Computational Physics* Feb 1983; **49**(2):334–341, doi:10.1016/0021-9991(83)90130-4.
8. Zerroukat M, Wood N, Staniforth A. Application of the parabolic spline method (PSM) to a multi-dimensional conservative semi-Lagrangian transport scheme (SLICE). *Journal of Computational Physics* Jul 2007; **225**(1):935–948, doi:10.1016/j.jcp.2007.01.006.
9. Liu XD, Osher S, Chan T. Weighted Essentially Non-oscillatory Schemes. *Journal of Computational Physics* Nov 1994; **115**(1):200–212, doi:10.1006/jcph.1994.1187.
10. Qiu JM, Shu CW. Conservative high order semi-Lagrangian finite difference WENO methods for advection in incompressible flow. *Journal of Computational Physics* Feb 2011; **230**(4):863–889, doi:10.1016/j.jcp.2010.04.037.
11. Huang CS, Arbogast T, Qiu J. An EulerianLagrangian WENO finite volume scheme for advection problems. *Journal of Computational Physics* Jun 2012; **231**(11):4028–4052, doi:10.1016/j.jcp.2012.01.030.
12. Nakamura T, Tanaka R, Yabe T, Takizawa K. Exactly Conservative Semi-Lagrangian Scheme for Multi-dimensional Hyperbolic Equations with Directional Splitting Technique. *Journal of Computational Physics* Nov 2001; **174**(1):171–207, doi:10.1006/jcph.2001.6888.
13. Xiao F, Yabe T. Completely Conservative and Oscillationless Semi-Lagrangian Schemes for Advection Transportation. *Journal of Computational Physics* Jul 2001; **170**(2):498–522, doi:10.1006/jcph.2001.6746.
14. Lentine M, Grtarsson JT, Fedkiw R. An unconditionally stable fully conservative semi-Lagrangian method. *Journal of computational physics* 2011; **230**(8):2857–2879.
15. Sonnendrücker E, Roche J, Bertrand P, Ghizzo A. The semi-Lagrangian method for the numerical resolution of the Vlasov equation. *Journal of computational physics* 1999; **149**(2):201–220.
16. Liu Y, Liu X, Wu E. Real-time 3d fluid simulation on GPU with complex obstacles. *12th Pacific Conference on Computer Graphics and Applications, 2004. PG 2004. Proceedings*, 2004; 247–256, doi:10.1109/PCCGA.2004.1348355.
17. Wu E, Liu Y, Liu X. An improved study of real-time fluid simulation on GPU. *Comp. Anim. Virtual Worlds* 2004; **15**(3-4):139–146, doi:10.1002/cav.16.
18. Courant R, Isaacson E, Rees M. On the solution of nonlinear hyperbolic differential equations by finite differences. *Comm. Pure Appl. Math.* 1952; **5**(3):243–255, doi:10.1002/cpa.3160050303.
19. Leonard BP. Stability of explicit advection schemes. The balance point location rule. *Int. J. Numer. Meth. Fluids* Feb 2002; **38**(5):471–514, doi:10.1002/fld.189.

20. Dupont TF, Liu Y. Back and forth error compensation and correction methods for removing errors induced by uneven gradients of the level set function. *Journal of Computational Physics* 2003; **190**(1):311 – 324, doi: http://dx.doi.org/10.1016/S0021-9991(03)00276-6.
21. Dupont TF, Liu Y. Back and forth error compensation and correction methods for semi-lagrangian schemes with application to level set interface computations. *Mathematics of Computation* 2007; **76**(258):pp. 647–668.
22. Kim B, Liu Y, Llamas I, Rossignac J. Advections with significantly reduced dissipation and diffusion. *IEEE transactions on visualization and computer graphics* JAN-FEB 2007; **13**(1):135–144, doi:10.1109/TVCG.2007.3.
23. Butcher JC. *Numerical methods for ordinary differential equations*. John Wiley & Sons, 2008.
24. MacCormack R. The Effect of Viscosity in Hypervelocity Impact Cratering. *Journal of Spacecraft and Rockets* Sep 2003; **40**(5):757–763, doi:10.2514/2.6901.
25. Celledoni E, Kometa BK, Verdier O. High Order Semi-Lagrangian Methods for the Incompressible NavierStokes Equations. *J Sci Comput* Mar 2015; :1–25doi:10.1007/s10915-015-0015-6.
26. Fromm JE. A method for reducing dispersion in convective difference schemes. *Journal of Computational Physics* Oct 1968; **3**(2):176–189, doi:10.1016/0021-9991(68)90015-6.
27. Courant R, Friedrichs K, Lewy H. ber die partiellen Differenzengleichungen der mathematischen Physik. *Math. Ann.* Dec 1928; **100**(1):32–74, doi:10.1007/BF01448839.
28. Hirsch C. *Numerical Computation of Internal and External Flows: The Fundamentals of Computational Fluid Dynamics: The Fundamentals of Computational Fluid Dynamics*. Butterworth-Heinemann, 2007.
29. LeVeque RJ. *Numerical methods for conservation laws*, vol. 132. Springer, 1992.
30. Rayleigh L. Lix. on convection currents in a horizontal layer of fluid, when the higher temperature is on the under side. *Philosophical Magazine Series 6* 1916; **32**(192):529–546, doi:10.1080/14786441608635602.
31. Chandrasekhar S. *Hydrodynamic and Hydromagnetic Stability*. Dover Books on Physics Series, Dover Publications, 1961.
32. Chorin AJ. Numerical Solution of Navier-Stokes Equations. *Mathematics of Computation* 1968; **22**(104):745–&, doi:10.2307/2004575.
33. Guermond J, Minev P, Shen J. An overview of projection methods for incompressible flows. *Computer Methods in Applied Mechanics and Engineering* 2006; **195**(4447):6011 – 6045, doi: http://dx.doi.org/10.1016/j.cma.2005.10.010.

A. DEVELOPED EXPRESSIONS OF THE CORRECTIVE SCHEMES

The expressions relevant to (10) and (13) can be developed as

$$\begin{aligned} 2\,FEC[\Phi]_i = &- U_i(1-U_i)\Phi^n_{i+s_i} + (2-U_iU_i)\Phi^n_i \\ &- U_iU_{i+s_i}\Phi^n[i+s_i-s\,(i+s_i)] + U_i(1+U_{i-s_i})\Phi^n_{i-s_i}\,, \end{aligned} \tag{30}$$

$$\begin{aligned}2\,BEC[\Phi]_i = {} & (f\Phi^n)\,[i+s\,(i)] + (f\Phi^n)\,[i] + (f\Phi^n)\,[i-s\,(i)+s\,(i-s\,(i))] + \\ & (f\Phi^n)\,[i+s\,(i)-s\,(i+s\,(i))] + \\ & \Big[(f\Phi^n)\,[i-s\,(i)] + (f\Phi^n)\,[i-s\,(i)+s\,(i+s\,(i))-s\,(i-s\,(i)+s\,(i-s\,(i)))]\Big] + \\ & (f\Phi^n)\,[i-s\,(i)-s\,(i-s\,(i))]\,,\end{aligned} \tag{31}$$

where

$$f[i+s\,(i)] = -(1-U_i)U_i(1-U_{i+s(i)})\;, \tag{32}$$

$$f[i] = (1-U_i)\big[3-(1-U_i)^2\big]\;, \tag{33}$$

$$f[i-s\,(i)+s\,(i-s\,(i))] = -U_iU_{i-s(i)}(1-U_{i-s(i)+s(i-s(i))})\;, \tag{34}$$

$$f[i+s\,(i)-s\,(i+s\,(i))] = -(1-U_i)U_iU_{i+s(i)}\;, \tag{35}$$

$$f[i-s\,(i)] = U_i\big[3-\big(1-U_{i-s(i)}\big)^2\big] - (1-U_i)\big((1-U_i)U_i\big)\;, \tag{36}$$

$$f[i-s\,(i)+s\,(i+s\,(i))-s\,(i-s\,(i)+s\,(i-s\,(i)))] = -U_iU_{i-s(i)}U_{i-s(i)+s(i-s(i))}\;, \tag{37}$$

$$f[i-s\,(i)-s\,(i-s\,(i))] = -U_i(1-U_{i-s(i)})U_{i-s(i)}\;. \tag{38}$$

B. ANALYSIS OF THE MODIFIED ADVECTION EQUATION

The modified equation steming from the discretization of the advection equation has in one dimension the general form

$$\partial_t\Phi + u\,\partial_x\Phi = \sum_\alpha C_\alpha\partial_x^\alpha\Phi\,, \tag{39}$$

where the C_α prefactors come from the truncation error in the case of numeric schemes. If the CFL stability condition is met, i.e. $\Delta t \propto u^{-1}\Delta x$, with $\Delta x \propto N^{-1}$, we have

$$C_\alpha \propto N^{-\alpha+1}\,. \tag{40}$$

Going into Fourier space for spacial dimensions and Fourier-Laplace space for time,

$$\Phi(x,t) = \int \mathrm{d}k\;\mathrm{e}^{\Omega(k)t-ikx}\hat{\Phi}(k,\Omega(k)) \quad \text{where} \quad \Omega(k) = -\sigma(k) + i\omega(k)\,. \tag{41}$$

DOI: 10.1002/fld

Thus, the dispersion relation is

$$\Omega(k) = (ik)u + \sum_{\alpha} (-ik)^{\alpha} C_{\alpha} \,. \tag{42}$$

Using the decomposition introduced in (41), the decay rate and the phase drift can be expressed as

$$\sigma(k) = \sum_{p} \left(k^2\right)^{2p+2} \left(C_{4p+2} - \left(k^2\right)^{2p} C_{4p} \right) , \tag{43}$$

$$\omega(k) = k\Big(u - \sum_{p} \left((k^2)^{2p} C_{4p+1} - (k^2)^{2p+1} C_{4p+3} \right) \Big) . \tag{44}$$

The equation has strictly stable solutions if and only if $\sigma(k) > 0$. Because of their dependence on the resolution, the sequence of C_{2p} is often equivalent to its first term different from zero. The stability reduces to the criterion $C_{\alpha} > 0$ if $\alpha = 4p+2$ and $C_{\alpha} < 0$ if $\alpha = 4p$. Using the equation on ω, the phase drift can be extracted

$$\phi(k) = \omega(k) - ku = -k \sum_{p} \left((k^2)^{2p} C_{4p+1} - (k^2)^{2p+1} C_{4p+3} \right) . \tag{45}$$

It is important to note that the procedure introduced in the FEC scheme cannot be repeted recursively. In order to highlight this point let us note that for pure advection, reversing time is equivalent to reversing the velocity

$$\partial_{-t}\Phi + u\partial_x\Phi = 0 \quad \Leftrightarrow \quad \partial_t\Phi + (-u)\partial_x\Phi = 0 \quad \Leftrightarrow \quad \partial_t\Phi + u\partial_{-x}\Phi = 0 \,. \tag{46}$$

Going into Fourier space for the spacial dimension

$$\Phi(x,t) = \int \mathrm{d}k \, \mathrm{e}^{-ikx} \tilde{\Phi}(k,t) \,, \tag{47}$$

the modified advection equation can be written as

$$\partial_t \left(\ln \tilde{\Phi}\right)(k,t) = u(ik) + \sum_{\alpha} C_{\alpha} (-ik)^{\alpha} \,. \tag{48}$$

Reversing the sign of the coordinate, $x \to -x$, is equivalent to reverse the wave vector, $k \to -k$ (c.c. for a real field). In order to ensure time reversibility, the following relation should be satisfied

$$\partial_t \left(\ln \tilde{\Phi}\right)(k,t) = \partial_t \left(\ln \tilde{\Phi}\right)(-k,-t) = -\partial_t \left(\ln \tilde{\Phi}\right)(-k,t) \,. \tag{49}$$

DOI: 10.1002/fld

This last relation shows that only terms of odd derivative are reversible. The error on $\bar{\Phi}$ highlights this observation. It can be evaluated using

$$\left(\ln \tilde{\tilde{\Phi}}\right)(k,t) = \left(\ln \tilde{\Phi}\right)(k,t) + 2\Delta t \sum_p C_{2p}(ik)^{2p}. \tag{50}$$

Only terms of even order derivative modify the field and can be detected with this procedure. This property should also be true for the C_α coefficients when the velocity is reversed. In the case of the CIR scheme, the coefficients depend on the sign of the velocity. In the case of the non-ideal advection equation (39), reverting time leads to

$$\partial_t \Phi + (-u)\partial_x \Phi = \sum_p \left(C_{2p+1}(-u)\partial_x^{2p+1}\Phi - C_{2p}(-u)\partial_x^{2p}\Phi \right). \tag{51}$$

Once more, only terms of odd order derivative are reversible.

The decay rate (Fig. 8) and the phase drift (Fig. 9) were measured for different resolutions. The results are plotted as a function of the resolution on a binary log scale (lb). Fig. 8(a) and 9(a) represent the decay rate and the phase drift, respectively. As shown in (40), the prefactors of the derivative terms of the error are proportional to an integer power of the resolution, $C_\alpha \propto N^{-\alpha+1}$. The values of α are in good agreement with the error term of the modified equation. Using the theoretical value of $\alpha^{(1)}$ and $\alpha^{(2)}$, the values are rescaled to $\phi_{res} = \phi \times N^{\alpha^{(1)}-1}$ and $\sigma_{res} = \sigma \times N^{\alpha^{(2)}-1}$. Fig. 8(b) and 9(b) show that the rescaled values are nearly constant as predicted by the theory.

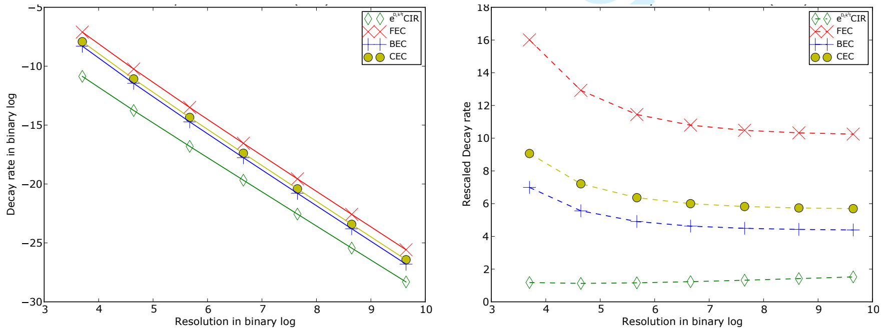

(a) Decay rate

(b) Rescaled decay rate

Figure 8. Evolution of the decay rate with the resolution in one dimension.

DOI: 10.1002/fld

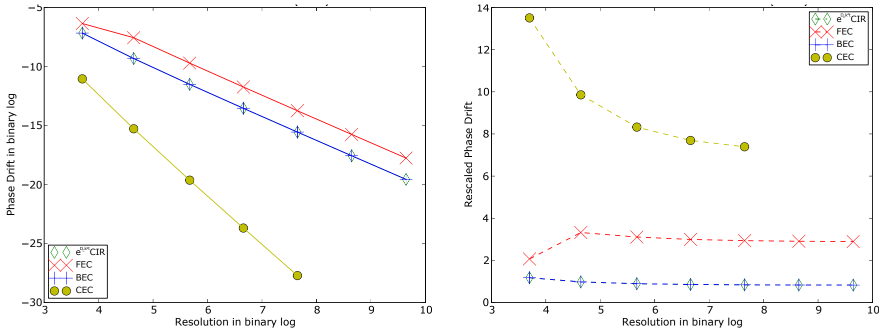

(a) Phase drift (b) Rescaled phase drift

Figure 9. Evolution of the phase drift with the resolution in one dimension.

Prepared using fldauth.cls

DOI: 10.1002/fld

C.2 *Stellar dynamos : symmetries and modulations*

Raynaud, R. & Tobias, S. M., in prep.

Under consideration for publication in J. Fluid Mech.

Stellar dynamos: symmetries and modulations

Raphaël Raynaud[1]† and Steven M. Tobias[2]‡

[1]LERMA, Observatoire de Paris, PSL Research University, CNRS, Sorbonne Universités,
UPMC Univ. Paris 06, École normale supérieure, F-75005, Paris, France
[2]Department of Applied Mathematics, University of Leeds, Leeds LS2 9JT, UK

(Received xx; revised xx; accepted xx)

Like others slowly rotating, late-type stars, the Sun displays an intermittent cyclic magnetic activity, interrupted by grand minima. Mean-field dynamo models revealed two generic types of modulation, which are in agreement with low order models based on symmetry considerations. We show that we recover in part these results when studying the long-term dynamics of convectively driven dynamos obtained with direct numerical simulations in spherical geometry, and analyse the route to intermittent amplitude modulations.

1. Introduction

Astronomical observations reveal that the Sun displays a cyclic magnetic activity with an average period of 22 yr whose amplitude is modulated on a longer time-scale of 80 yr (Gleissberg cycle). Sunspot records dating back to the 17th century indicate a period of reduced activity between 1645 and 1715, known as the Maunder minimum (Eddy 1976). This somehow anomalous behavior has been confirmed by the study of the abundances of cosmogenic isotopes ^{10}Be in polar ice and ^{14}C in tree rings that reveal 27 grand minima in the past 11 000 yr, separated by aperiodic intervals of about 200 yr (Usoskin *et al.* 2007). Moreover, the long-term monitoring of the CaII H+K flux of solar-type stars started by Wilson in 1968 provides a panel of different stellar activities. Baliunas *et al.* (1998) found that 60 % of stars in the Mont Wilson Observatory survey exhibit periodic, cyclic variations, and 25 % show irregular or aperiodic variability.

Most stellar magnetic fields are thought to be maintained again ohmic dissipation by dynamo action through the flow of an electrically conducting fluid (Moffatt 1978). Numerous mean-field dynamo models attempt to reproduce the solar cycle (Charbonneau 2010; DeRosa *et al.* 2012), whose temporal modulations could originate from stochastic fluctuations (Schmitt *et al.* 1996; Choudhuri & Karak 2012; Hazra *et al.* 2014) or deterministic chaos. However, nonlinear behaviours can be strongly dependent on mean-field modelling details, and a generic approach relies on low-order systems based on symmetry considerations (Weiss 2011). Knobloch *et al.* (1998) followed this complementary approach and distinguished parity and amplitude modulations, referred to as Type 1 and Type 2, respectively . In this paper, we aim at comparing these results to the magnetic field dynamics of convectively driven dynamos obtained with three-dimensional, direct numerical simulations.

---

† Email address for correspondence: raphael.raynaud@ens.fr
‡ Email address for correspondence: smt@maths.leeds.ac.uk

2. Governing equations

Let us consider a spherical shell of width d and aspect ratio $\chi = r_{\mathrm{i}}/r_{\mathrm{o}}$, in rotation at angular velocity $\Omega\hat{\mathbf{z}}$. We rely on the LBR anelastic approximation (Braginsky & Roberts 1995; Lantz & Fan 1999) to model a perfect gas with kinematic viscosity ν, turbulent entropy diffusivity κ, specific heat c_p and magnetic diffusivity η (all assumed to be constant). The gravity is given by $\mathbf{g} = -GM\hat{\mathbf{r}}/r^2$, where G is the gravitational constant and M the central mass. The equilibrium polytropic solution of the anelastic system defines the reference state

$$\overline{P} = P_c w^{n+1}, \quad \overline{\varrho} = \varrho_c w^n, \quad \overline{T} = T_c w, \quad w = c_0 + c_1 d/r, \tag{2.1}$$

with

$$c_0 = \frac{2w_0 - \chi - 1}{1 - \chi}, \quad c_1 = \frac{(1+\chi)(1-w_o)}{(1-\chi)^2}, \quad w_0 = \frac{\chi + 1}{\chi \exp(N_\varrho/n) + 1}\,. \tag{2.2}$$

P_c, ϱ_c and T_c are the reference-state pressure, density and temperature mid-way between the inner and outer boundaries, and serve as units for these variables. Length is scaled by d, time by d^2/η, entropy by Δs and the magnetic field by $\sqrt{\Omega\varrho_c\mu\eta}$, where μ is the magnetic permeability. Then, the governing equations are (Jones *et al.* 2011)

$$\frac{D\mathbf{v}}{Dt} = Pm\left[-\frac{1}{E}\nabla\frac{P'}{w^n} + \frac{Pm}{Pr}Ra\frac{s}{r^2}\hat{\mathbf{r}} - \frac{2}{E}\,\hat{\mathbf{z}}\times\mathbf{v} + \mathbf{F}_\nu + \frac{1}{E\,w^n}(\nabla\times\mathbf{B})\times\mathbf{B}\right], \tag{2.3}$$

$$\frac{\partial\mathbf{B}}{\partial t} = \nabla\times(\mathbf{v}\times\mathbf{B}) + \nabla^2\mathbf{B}\,, \tag{2.4}$$

$$\frac{Ds}{Dt} = w^{-n-1}\frac{Pm}{Pr}\nabla\cdot\left(w^{n+1}\,\nabla s\right) + \frac{Di}{w}\left[E^{-1}w^{-n}(\nabla\times\mathbf{B})^2 + Q_\nu\right]\,, \tag{2.5}$$

with the constraints

$$\nabla\cdot(w^n\mathbf{v}) = 0 \quad \text{and} \quad \nabla\cdot\mathbf{B} = 0\,. \tag{2.6}$$

The viscous force $\mathbf{F}_\nu$ in (2.3) is given by $\mathbf{F}_\nu = w^{-n}\nabla\mathbf{S}$, with $S_{ij} = 2w^n\left(e_{ij} - \frac{1}{3}\delta_{ij}\nabla\cdot\mathbf{v}\right)$ and $2e_{ij} = \partial_j v_i + \partial_i v_j$. The expressions of the dissipation parameter Di and the viscous heating Q_ν in (2.5) are $Di = c_1 Pr/(PmRa)$ and $Q_\nu = 2\left[e_{ij}e_{ij} - \frac{1}{3}(\nabla\cdot\mathbf{v})^2\right]$.

We impose stress-free boundary conditions for the velocity field, and the magnetic field matches a potential field inside and outside the fluid shell. The convection is driven by an imposed entropy difference Δs between the inner and the outer boundaries. The above system involves seven control parameters: the Rayleigh number $Ra = GMd\Delta s/(\nu\kappa c_p)$, the Ekman number $E = \nu/(\Omega d^2)$, the Prandtl number $Pr = \nu/\kappa$, the magnetic Prandtl number $Pm = \nu/\eta$, together with the aspect ratio χ, the polytropic index n and the number of density scale heights $N_\varrho \equiv \ln[\overline{\varrho}(r_{\mathrm{i}})/\overline{\varrho}(r_{\mathrm{o}})]$. We set $E = 10^{-4}$, $Pr = 1$, $Pm = 1$, $\chi = 0.35$, $n = 2$ and choose a relatively weak density stratification $N_\varrho = 0.5$, to limit the computational time. The critical Rayleigh for the linear onset of convection is then $Ra_{\mathrm{c}} = 3.34 \times 10^5$ (after Schrinner *et al.* 2014).

The anelastic equations are integrated between 5 and 60 magnetic diffusion times with the pseudo-spectral code PARODY (Dormy *et al.* 1998; Schrinner *et al.* 2014). We define the kinetic energy $E_k = 1/2\int w^n\mathbf{v}^2\,\mathrm{d}V$ and the magnetic energy $E_b = Pm/(2E)\int\mathbf{B}^2\,\mathrm{d}V$. To investigate the symmetry of the flow with respect to the equatorial plane, we also compute the kinetic contributions E_k^S and E_k^A, corresponding to the symmetric and antisymmetric velocity components, respectively. Likewise, the symmetric and antisymmetric magnetic energies E_b^S and E_b^A correspond to the dipolar and quadrupolar symmetries, respectively.

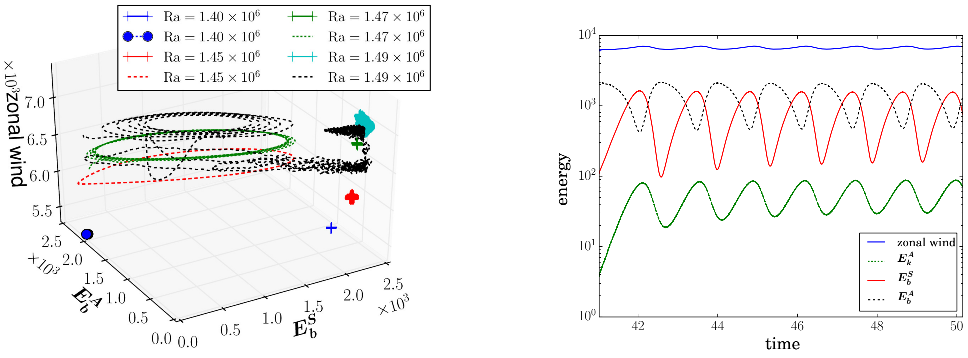

(a) (b) $Ra = 1.47 \times 10^6$

FIGURE 1. (a): Three-dimensional phase portrait showing the projection of the trajectory of the system onto the space (E_b^S, E_b^A, E_Z). (b): Energy time series for the limit cycle at $Ra = 1.47 \times 10^6$ (green dashed line in subfigure (a)).

3. Results

Systematic parameter studies established that the dichotomy between the dynamo branches reported for Boussinesq models with stress-free boundary conditions (Busse & Simitev 2006; Schrinner *et al.* 2012) extends to anelastic dynamo models (Gastine *et al.* 2012; Schrinner *et al.* 2014). In this paper, we aim to study the low frequency modulations of the dynamo waves that are characteristics of the so-called multipolar branch, which turns out to be the only one that can be sustained at low magnetic Reynolds number $Rm \sim 40$, with Rm defined by $Rm = \sqrt{2E_k/V}$, V being the volume of the fluid shell. Close to the onset of dynamo action, these dynamos take the form of oscillatory solutions characterized by a period of the order of 0.1 magnetic diffusion time. They are usually interpreted in terms of Parker waves (Parker 1955), both in the Boussinesq (Busse & Simitev 2006; Dietrich *et al.* 2013) and anelastic frameworks (Gastine *et al.* 2012), but one has to keep in mind that these results rely on crude estimates of the α-effect via the flow helicity. Following the methodology of Schrinner *et al.* (2012), we checked that the Ω-effect correlates in our models with the mean azimuthal magnetic field, which confirms the key role played by the zonal wind in the generation of the toroidal magnetic field. It is well known that the $\alpha\Omega$ dynamo instability generically sets in as a Hopf bifurcation leading to oscillatory solutions (Tobias 2002) ; however, we also mention that a test-field analysis performed on a particular dynamo model by Schrinner *et al.* (2011) revealed that the Ω-effect alone is not necessarily responsible for the cyclic behavior of the dynamo. At $Ra = 1.4 \times 10^6$, the flow does not brake the equatorial symmetry, and we expect the magnetic field to exhibit either a dipolar or quadrupolar symmetry. Depending on the choice of the initial conditions, we effectively observe a bistability between solutions of different parities, illustrated by the blue dot and the blue cross in figure 1(a). In this figure, the trajectory of the system is projected for different Rayleigh numbers onto the space spanned by the symmetric and antisymmetric magnetic energy E_b^S and E_b^A, and the zonal wind energy measured by the axisymmetric toroidal kinetic energy E_Z. We stress that the aforementioned bistability must not be confused with the hysteretic transition between the dipolar and the multipolar branches resulting from the use of stress-free boundary conditions (Schrinner *et al.* 2012). When the magnetic field is predominantly of quadrupolar symmetry, the flow is characterized by a $m = 8$ convection mode ; on the

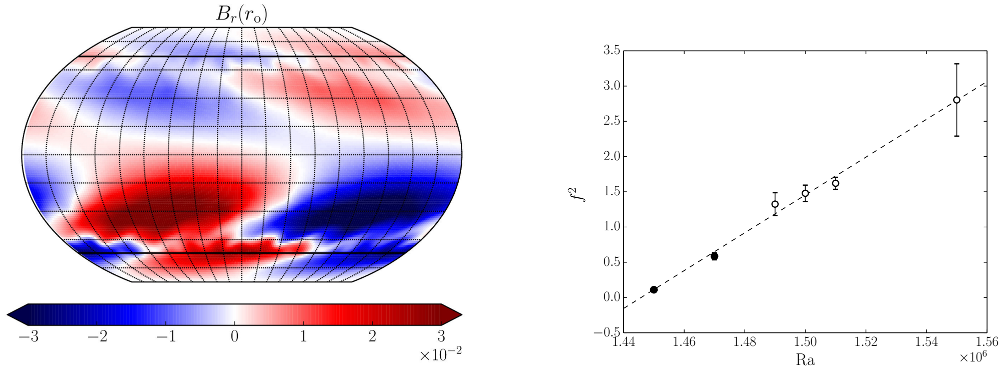

(a) $Ra = 1.47 \times 10^6$ ($t = 48.74$) (b) $f \propto \sqrt{Ra - Ra_{\rm SN}}$

FIGURE 2. (a): Snapshot of B_r at the surface of the model characterized by $Ra = 1.47 \times 10^6$. The two horizontal black lines mark the position of the tangent cylinder. (b): Linear fit of the square of the limit cycle frequencies as a function of Ra. Empty markers indicate that the cycle is not stable anymore and the error bars represent standard deviations.

other hand, when the magnetic field is predominantly dipole symmetric, the flow is then characterized by a $m = 9$ convection mode and larger fluctuations of the kinetic energy.

A first increase of the Rayleigh number from 1.40×10^6 to 1.45×10^6 leads to the destabilization of the quadrupole symmetric solution (blue dot in figure 1(a)) and the creation of a limit cycle (red dashed line), which coexists with the dipole symmetric solution (red cross). An example of the limit cycle at $Ra = 1.47 \times 10^6$ is given in figure 1(b) that shows the evolution as a function of time of the antisymmetric kinetic energy E_k^A (green dashed line), together with the symmetric and antisymmetric magnetic energies E_b^S and E_b^A (represented by the solid red and black dashed lines, respectively). This solution appears to be characterized by a tiny symmetry breaking of the flow that couples magnetic modes of different parity. Indeed, we clearly see a periodic exchange of energy between modes of dipolar and quadrupolar symmetry, which could be described as a Type 1 modulation, in reference to the terminology introduced by Knobloch *et al.* (1998). Interestingly, we also notice that the magnetic field tends to be localized in one hemisphere, when $E_b^S \sim E_b^A$, which is in agreement with the results previously reported by Grote & Busse (2000). This hemispherical localization is highlighted in figure 2(a) by a snapshot of the radial magnetic field taken at $t = 48.74$ at the surface of the same model with $Ra = 1.47 \times 10^6$. Moreover, we see that the surface magnetic field is strongly dominated by a non-axisymmetric $m = 1$ mode. This is actually characteristics of all the models considered in the present study, independently of their dominant parity. By considering almost Boussinesq models with $N_\varrho = 0.1$, Raynaud *et al.* (2014) showed that this feature is related to the choice of a gravity profile corresponding to a central mass distribution.

Finally, figure 1(a) shows that the limit cycle (dashed lines) eventually loses its stability when the Rayleigh number is further increased to 1.49×10^6 (dashed black line). For these different dynamo models, we try to estimate the frequency f of the limit cycle from the period of E_b^A time series for different Rayleigh numbers. Since this solution is only metastable for $Ra > 1.47 \times 10^6$, it is more difficult to have an exact estimate of the frequency for these models which are represented by the empty symbols in figure 2(b) with higher standard deviations at higher values of Ra. In spite of this difficulty, figure 2(b)

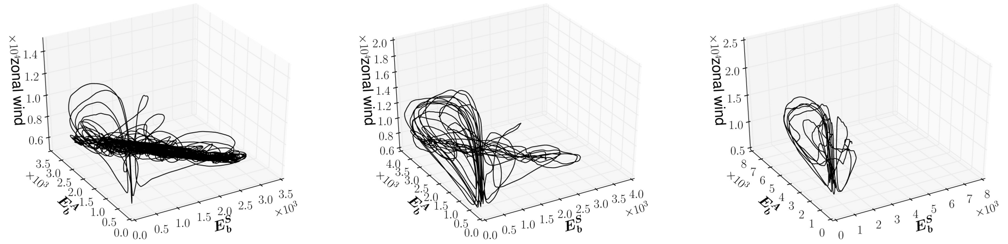

(a) $Ra = 1.55 \times 10^6$ (b) $Ra = 1.65 \times 10^6$ (c) $Ra = 1.85 \times 10^6$

FIGURE 3. Three-dimensional phase portraits showing the projection of the trajectory of the system onto the space (E_b^S, E_b^A, E_Z).

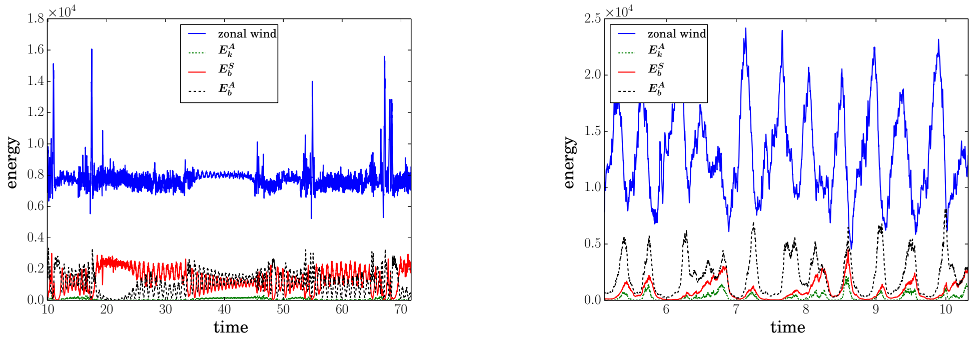

(a) $Ra = 1.55 \times 10^6$ (b) $Ra = 1.85 \times 10^6$

FIGURE 4. Energy time series.

demonstrates that f^2 tends to increase linearly as a function of Ra, which indicates that the limit cycle results from a saddle-node bifurcation. The dashed line in figure 2(b) fits the different points and gives the following estimate of the bifurcation threshold, $Ra_{\mathrm{SN}} \sim 1.446 \times 10^6$.

When the Rayleigh number is further increased, we find that the dynamics of the magnetic field progressively switches from parity to amplitude modulations, or, in other words from Type 1 to Type 2 modulation (Knobloch *et al.* 1998). This transition is particularly clear when comparing the three-dimensional phase portraits represented for increasing values of the Rayleigh number in figure 3, in which the trajectory of the system has been smoothed by applying a moving average. For $Ra = 1.55 \times 10^6$ (see figure 3(a)), the dynamics is mainly governed by the energy exchange between E_b^S and E_b^A, and we only distinguish the first signs of the Type 2 modulation through decays of the magnetic energy, always followed by an increase of the zonal wind. In contrast, we see in figure 3(c) that the system trajectory in the space (E_b^S, E_b^A, E_Z) is actually confined in the subspace where $E_b^S \leqslant E_b^A$ and characterized by the strong amplitude modulation of the zonal wind for $Ra = 1.55 \times 10^6$. The time series corresponding to the trajectories in figures 3(a) and 3(c) are shown in figures 4(a) and 4(b), respectively. Figure 4(a) reveals that the system can spend more than 10 magnetic diffusion times in a saturated phase displaying a Type 1 modulation, before the intermittent decay of the magnetic energy triggers a burst of the zonal wind. In addition, we see that the fluctuations of the kinetic energy temporarily decreases for $t \sim 40$ and that E_b^A tends to dominate over E_b^S, which is the sign that the system is revisiting the previous limit cycle solution. We used this particular time interval to compute the frequency of the limit cycle at $Ra = 1.55 \times 10^6$

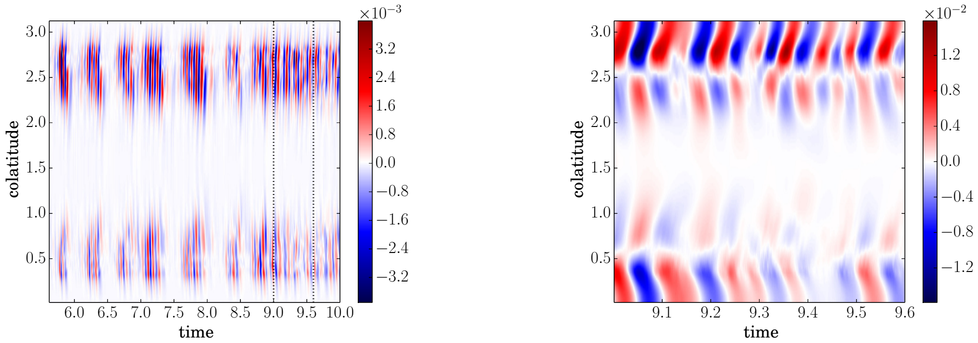

(a) $\langle B_\varphi \rangle_\varphi$ (b) $\langle B_r \rangle_\varphi$

FIGURE 5. Butterfly diagrams representing the surface axisymmetric azimuthal (a) and radial (b) components of the magnetic field at $Ra = 1.65 \times 10^6$. The time interval in subfigure (b) corresponds to the period between the vertical dashed lines in subfigure (a).

in figure 2(b). In contrast, figure 4(b) shows the strong amplitude modulation of the zonal wind observed at $Ra = 1.85 \times 10^6$. This temporal evolution is reminiscent of the relaxation oscillations that can be observed in turbulent hydrodynamic convection (Grote *et al.* 2000; Christensen 2002). In the latter case, the relaxation phenomenon originates from the fact that the columnar convection feeds the differential rotation through the action of Reynolds stresses but also tends to be disrupted by the shear due to differential rotation. This competition between the convection and the zonal wind is present in our models, since we note for instance that the Nusselt number is always minimum when the zonal wind reach its maximum. However, purely hydrodynamic simulations performed in the same parameter regime demonstrate that there is no amplitude modulation without the back-reaction of the Lorentz force. The sudden growth of the zonal wind results thus from the decrease of the magnetic field. In general, we notice that the Nusselt number is higher when the magnetic field is present, which confirms that magnetic field promotes the columnar convection and thus the heat transport by the reduction of the zonal wind, as reported by Grote *et al.* (2000).

A closer examination of the evolution of E_b^S as a function of time (red line in figure 4(b)) could suggest that minima can be caused by the gradual growth of E_b^S. A similar trend has been described by Brooke *et al.* (1998) for mean-field dynamos models, in which the grand minima were an example of in-out intermittency caused by the gradual growth and collapse of a quadrupolar component of a predominantly dipolar solution (Moss & Brooke 2000). However, we notice that the amplitude modulation does persist in our models even if the magnetic field components with dipole symmetry are artificially cancelled at a given time. During the following transient regime, the only significant difference seems to be the increase of the duration separating two bursts of the zonal wind. We also mention that the average interval between minima strongly depends of the values of the Prandtl numbers since significantly increases after increasing Pr or decreasing Pm of 10 per cent. It is then difficult to determine the causes leading to the occurence of a grand minimum, which might be related to stochastic fluctuations.

Finally, if we examine more closely the evolution of the axisymmetric magnetic field as a function of colatitude and time, we see in figure 5(a) that both Type 1 and Type 2 modulations affect the so-called butterfly diagrams in the form of interesting patterns. This diagram corresponds to the model with $Ra = 1.65 \times 10^6$ whose phase portrait is shown in figure 3(b), and for which both types of modulation are present. In addition to underline the oscillatory nature of these dynamos, these butterfly diagrams demonstrate that these modulations occur on time scales that are not comparable to the period of the dynamo wave. It is also clear that the magnetic activity appears concentrated at higher latitudes than the active latitudes displayed by the usual solar butterfly diagrams (see for instance Hathaway 2015), partly because of the much larger aspect ratio of our models (we recall that we set $\chi = 0.35$ whereas the solar convective zone has an aspect ratio closer to 0.7). Moreover, we see in figure 2(a) that the magnetic field is predominantly non-axisymmetric at low latitudes, which explains the low values displayed by the butterfly diagram close to the equator. Figure 5(a) illustrates the amplitude modulation for $t \in [6, 8]$, whereas figure 5(b) emphasizes a change of parity of the magnetic field during the following saturated phase. Interestingly, we note that the magnetic activity tends to migrate towards the poles at high latitudes, but towards the equator at lower latitudes, which recalls the results obtained in spherical wedge geometry by Käpylä *et al.* (2012).

4. Conclusion

We conclude that these dynamos display a dynamical behaviour reminiscent of the results obtained with mean-field models or low-order systems, while being dominated by a non-axisymmetric mode $m = 1$. However, the bifurcation structure is different from the one studied by Knobloch *et al.* (1998). As the Rayleigh number is increased, the Type 1 modulation results from the creation of a limit cycle by a saddle-node bifurcation between a stable and an unstable fixed point of quadrupolar and dipolar symmetry, respectively. The dynamics of the magnetic fields is then governed by the non-linear interactions between modes of different parity, which leads in addition to the periodic localization of the magnetic field in one hemisphere. This particular state has already been reported by Grote & Busse (2000), and studied in more detail by Gallet & Pétrélis (2009) for a simplified kinematic models of α^2 dynamos. Moreover, the importance of the equatorial symmetry breaking of the flow to allow for the existence of spatially localized states has also been confirmed experimentally, as reported in a study of the VKS experiment (Gallet *et al.* 2012). The analyse of the non-linear interactions between modes of different parity successfully explained the different regimes of the magnetic field reversals observed in the VKS experiment (Pétrélis & Fauve 2008) ; a simple mechanism based on this consideration has been proposed to explain the dynamics of the Earth's magnetic field (Pétrélis *et al.* 2009). The present study demonstrates that a similar framework is also pertinent to understand the dynamics of oscillatory dynamos, and thus could be relevant to explain the hemispheric magnetic configuration which has been observed on the Sun at the end of the Maunder minimum (Sokoloff & Nesme-Ribes 1994).

Furthermore, we found that the limit cycle is destabilized by the further increase of Ra, and that the dynamo progressively enters a chaotic regime characterized by the occurrence of grand minima, which are followed by bursts of the zonal wind. The statistical analysis of these minima and the understanding of the influence of Pm and Pr deserve further studies, and we stress that the usual integration times of a few magnetic diffusion times are far insufficient to unveil the rich dynamical behaviour of these dynamo models. Beyond the solar dynamo, our results may help investigating recent observational progress about the magnetism of M dwarfs with thicker convective zones (Shulyak *et al.* 2015).

This study was granted access to the HPC resources of MesoPSL financed by the Rgion Île-de-France and the project Equip@Meso (reference ANR-10-EQPX-29-01) of the programme Investissements d'Avenir supervised by the Agence Nationale pour la Recherche. Numerical simulations were also carried out at the TGCC computing center

(GENCI project x2013046698). R. Raynaud thanks E. Dormy, C. Gissinger, L. Petitdemange and F. Pétrélis for various discussions.

REFERENCES

Baliunas, S. L., Donahue, R. A., Soon, W. & Henry, G. W. 1998 Activity Cycles in Lower Main Sequence and POST Main Sequence Stars: The HK Project. *Astronomical Society of the Pacific Conference Series* **154**, 153–172.

Braginsky, S. I. & Roberts, P. H. 1995 Equations governing convection in earth's core and the geodynamo. *Geophysical and Astrophysical Fluid Dynamics* **79**, 1–97.

Brooke, J. M., Pelt, J., Tavakol, R. & Tworkowski, A. 1998 Grand minima and equatorial symmetry breaking in axisymmetric dynamo models. *Astronomy and Astrophysics* **332**, 339–352.

Busse, F. H. & Simitev, R. D. 2006 Parameter dependences of convection-driven dynamos in rotating spherical fluid shells. *Geophys. Astrophys. Fluid Dyn.* **100**, 341–361, arXiv: 0904.4293.

Charbonneau, P. 2010 Dynamo Models of the Solar Cycle. *Living Reviews in Solar Physics* **7**, 3.

Choudhuri, A. R. & Karak, B. B. 2012 Origin of Grand Minima in Sunspot Cycles. *Physical Review Letters* **109** (17), 171103.

Christensen, U. R. 2002 Zonal flow driven by strongly supercritical convection in rotating spherical shells. *Journal of Fluid Mechanics* **470**, 115–133.

DeRosa, M. L., Brun, A. S. & Hoeksema, J. T. 2012 Solar Magnetic Field Reversals and the Role of Dynamo Families. *Astrophysical Journal* **757**, 96, arXiv: 1208.1768.

Dietrich, W., Schmitt, D. & Wicht, J. 2013 Hemispherical Parker waves driven by thermal shear in planetary dynamos. *EPL (Europhysics Letters)* **104**, 49001, arXiv: 1402.0343.

Dormy, E., Cardin, P. & Jault, D. 1998 MHD flow in a slightly differentially rotating spherical shell, with conducting inner core, in a dipolar magnetic field. *Earth Planet. Sci. Lett.* **160**, 15–30.

Eddy, J. A. 1976 The Maunder Minimum. *Science* **192**, 1189–1202.

Gallet, B., Aumaître, S., Boisson, J., Daviaud, F., Dubrulle, B., Bonnefoy, N., Bourgoin, M., Odier, P., Pinton, J.-F., Plihon, N., Verhille, G., Fauve, S. & Pétrélis, F. 2012 Experimental Observation of Spatially Localized Dynamo Magnetic Fields. *Physical Review Letters* **108** (14), 144501.

Gallet, B. & Pétrélis, F. 2009 From reversing to hemispherical dynamos. *Physical Review E* **80** (3), 035302, arXiv: 0907.4428.

Gastine, T., Duarte, L. & Wicht, J. 2012 Dipolar versus multipolar dynamos: the influence of the background density stratification. *Astronomy and Astrophysics* **546**, A19, arXiv: 1208.6093.

Grote, E. & Busse, F. H. 2000 Hemispherical dynamos generated by convection in rotating spherical shells. *Physical Review E* **62**, 4457.

Grote, E., Busse, F. H. & Tilgner, A. 2000 Regular and chaotic spherical dynamos. *Physics of the Earth and Planetary Interiors* **117**, 259–272.

Hathaway, D. H. 2015 The Solar Cycle. *ArXiv e-prints* , arXiv: 1502.07020.

Hazra, S., Passos, D. & Nandy, D. 2014 A Stochastically Forced Time Delay Solar Dynamo Model: Self-consistent Recovery from a Maunder-like Grand Minimum Necessitates a Mean-field Alpha Effect. *Astrophysical Journal* **789**, 5, arXiv: 1307.5751.

Jones, C. A., Boronski, P., Brun, A. S., Glatzmaier, G. A., Gastine, T., Miesch, M. S. & Wicht, J. 2011 Anelastic convection-driven dynamo benchmarks. *Icarus* **216**, 120–135.

Käpylä, P. J., Mantere, M. J. & Brandenburg, A. 2012 Cyclic Magnetic Activity due to Turbulent Convection in Spherical Wedge Geometry. *Astrophysical Journal, Letters* **755**, L22, arXiv: 1205.4719.

Knobloch, E., Tobias, S. M. & Weiss, N. O. 1998 Modulation and symmetry changes in stellar dynamos. *Monthly Notices of the RAS* **297**, 1123–1138.

Lantz, S. R. & Fan, Y. 1999 Anelastic Magnetohydrodynamic Equations for Modeling Solar and Stellar Convection Zones. *Astrophysical Journal, Supplement* **121**, 247–264.

Moffatt, H. K. 1978 *Magnetic Field Generation in Electrically Conducting Fluids*. Cambridge University Press.

Moss, D. & Brooke, J. 2000 Towards a model for the solar dynamo. *Monthly Notices of the RAS* **315**, 521–533.

Parker, E. N. 1955 Hydromagnetic Dynamo Models. *Astrophysical Journal* **122**, 293–+.

Pétrélis, F. & Fauve, S. 2008 Chaotic dynamics of the magnetic field generated by dynamo action in a turbulent flow. *Journal of Physics Condensed Matter* **20**, 4203.

Pétrélis, F., Fauve, S., Dormy, E. & Valet, J.-P. 2009 Simple Mechanism for Reversals of Earth's Magnetic Field. *Physical Review Letters* **102** (14), 144503, arXiv: 0806.3756.

Raynaud, R., Petitdemange, L. & Dormy, E. 2014 Influence of the mass distribution on the magnetic field topology. *Astronomy and Astrophysics* **567**, A107.

Schmitt, D., Schuessler, M. & Ferriz-Mas, A. 1996 Intermittent solar activity by an on-off dynamo. *Astronomy and Astrophysics* **311**, L1–L4.

Schrinner, M., Petitdemange, L. & Dormy, E. 2011 Oscillatory dynamos and their induction mechanisms. *Astronomy and Astrophysics* **530**, A140, arXiv: 1101.1837.

Schrinner, M., Petitdemange, L. & Dormy, E. 2012 Dipole Collapse and Dynamo Waves in Global Direct Numerical Simulations. *Astrophysical Journal* **752**, 121.

Schrinner, M., Petitdemange, L., Raynaud, R. & Dormy, E. 2014 Topology and field strength in spherical, anelastic dynamo simulations. *Astronomy and Astrophysics* **564**, A78.

Shulyak, D., Sokoloff, D., Kitchatinov, L. & Moss, D. 2015 Towards understanding dynamo action in M dwarfs. *Monthly Notices of the RAS* **449**, 3471–3478, arXiv: 1503.04971.

Sokoloff, D. & Nesme-Ribes, E. 1994 The Maunder minimum: A mixed-parity dynamo mode ? *Astronomy and Astrophysics* **288**, 293–298.

Tobias, S.M. 2002 Modulation of solar and stellar dynamos. *Astronomische Nachrichten* **323** (3-4), 417–423.

Usoskin, I. G., Solanki, S. K. & Kovaltsov, G. A. 2007 Grand minima and maxima of solar activity: new observational constraints. *Astronomy and Astrophysics* **471**, 301–309.

Weiss, N. O. 2011 Chaotic behaviour in low-order models of planetary and stellar dynamos. *Geophysical and Astrophysical Fluid Dynamics* **105**, 256–272.

Annexe D

Comptes rendus de conférences

D.1 Journées de la SF2A 2014

Raynaud, R., Petitdemange, L. & Dormy, E., 2014, “Influence of the mass distribution on the magnetic field topology in spherical, anelastic dynamo simulations”, *Proceedings of the annual meeting of the French Society of Astronomy & Astrophysics.*

Liens de téléchargement :
— www.sf2a.eu/?article579
— hal.archives-ouvertes.fr/hal-01126612v1

D.2 18^{e} Rencontre du Non-Linéaire

Raynaud, R., 2015, « Dynamos stellaires : symétries et modulations », *Comptes-Rendus de la 18^{e} Rencontre du Non-Linéaire.*

Lien de téléchargement :
— nonlineaire.univ-lille1.fr/SNL/archives

Bibliographie

Abel G., 1964, *Exploration of the Universe*, Holt, Rinehart and Winston, New-York. (Cité p. 9)

Alexakis A. & Ponty Y., 2008, “Effect of the Lorentz force on on-off dynamo intermittency”, *Phys. Rev. E*, **77**(5), 056 308. [DOI], [ADS]. (Cité p. 84 et 91)

Aubert J. & Wicht J., 2004, “Axial vs. equatorial dipolar dynamo models with implications for planetary magnetic fields”, *Earth and Planetary Science Letters*, **221**, 409–419. [DOI], [ADS]. (Cité p. 54 et 104)

Aumaître S., Pétrélis F. & Mallick K., 2005, “Low-Frequency Noise Controls On-Off Intermittency of Bifurcating Systems”, *Physical Review Letters*, **95**(6), 064 101–+. [DOI], [ADS]. (Cité p. 80, 91 et 97)

Aumaître S., Mallick K. & Pétrélis F., 2006, “Effects of the Low Frequencies of Noise on On Off Intermittency”, *Journal of Statistical Physics*, **123**, 909–927. [DOI], [ADS]. (Cité p. 83)

Aurnou J. M., 2007, “Planetary core dynamics and convective heat transfer scaling”, *Geophysical and Astrophysical Fluid Dynamics*, **101**, 327–345. [DOI], [ADS]. (Cité p. 76)

Babcock H. W., 1961, “The Topology of the Sun’s Magnetic Field and the 22-year Cycle.”, *Astrophysical Journal*, **133**, 572. [DOI], [ADS]. (Cité p. 6)

Baliunas S. L., Donahue R. A., Soon W. H., Horne J. H., Frazer J., Woodard-Eklund L., Bradford M., Rao L. M., Wilson O. C., Zhang Q., Bennett W., Briggs J., Carroll S. M., Duncan D. K., Figueroa D., Lanning H. H., Misch T., Mueller J., Noyes R. W., Poppe D., Porter A. C., Robinson C. R., Russell J., Shelton J. C., Soyumer T., Vaughan A. H. & Whitney J. H., 1995, “Chromospheric variations in main-sequence stars”, *Astrophysical Journal*, **438**, 269–287. [DOI], [ADS]. (Cité p. 19)

Baliunas S. L., Donahue R. A., Soon W. & Henry G. W., 1998, “Activity Cycles in Lower Main Sequence and POST Main Sequence Stars : The HK Project”, *Astronomical Society of the Pacific Conference Series*, **154**, 153–172. [ADS]. (Cité p. 19)

Batchelor G. K., 1953, “The conditions for dynamical similarity of motions of a frictionless perfect-gas atmosphere”, *Quarterly Journal of the Royal Meteorological Society*, **79**, 224–235. [DOI], [ADS]. (Cité p. 15)

Batchelor G.K., 1967, *An Introduction to Fluid Dynamics*, Cambridge University Press, Cambridge. (Cité p. 29 et 30)

Bethe H. A., 1939, “Energy Production in Stars”, *Physical Review*, **55**, 434–456. [DOI], [ADS]. (Cité p. 16)

Boussinesq J., 1903, *Théorie analytique de la chaleur*, 2, Gauthier-Villars. [GAL]. (Cité p. 35)

Braginsky S. I. & Roberts P. H., 1995, “Equations governing convection in earth’s core and the geodynamo”, *Geophysical and Astrophysical Fluid Dynamics*, **79**, 1–97. [DOI], [ADS]. (Cité p. 26 et 32)

Braginsky S. I. & Roberts P. H., 2003, “On the theory of convection in the Earth’s core”, *Advances in Nonlinear Dynamos,The Fluid Mechanics of Astrophysics and Geophysics*, **9**. (Cité p. 32)

Braginsky S. I. & Roberts P. H., 2007, “Anelastic and Boussinesq Approximations”, *Encyclopedia of Geomagnetism and Paleomagnetism*, p. 11. (Cité p. 32)

Brown B. P., Vasil G. M. & Zweibel E. G., 2012, “Energy Conservation and Gravity Waves in Sound-proof Treatments of Stellar Interiors. Part I. Anelastic Approximations”, *Astrophysical Journal*, **756**, 109. [DOI], [ADS]. (Cité p. 33)

Brown T. M., Christensen-Dalsgaard J., Dziembowski W. A., Goode P., Gough D. O. & Morrow C. A., 1989, “Inferring the sun’s internal angular velocity from observed p-mode frequency splittings”, *Astrophysical Journal*, **343**, 526–546. [DOI], [ADS]. (Cité p. 11)

Brun A. S., Miesch M. S. & Toomre J., 2004, “Global-Scale Turbulent Convection and Magnetic Dynamo Action in the Solar Envelope”, *Astrophysical Journal*, **614**, 1073–1098. [DOI], [ADS]. (Cité p. 26)

Busse F. & Simitev R., 2011, “Remarks on some typical assumptions in dynamo theory”, *Geophysical and Astrophysical Fluid Dynamics*, **105**, 234–247. [DOI], [ADS]. (Cité p. 76)

Busse F. H. & Simitev R. D., 2006, “Parameter dependences of convection-driven dynamos in rotating spherical fluid shells”, *Geophysical and Astrophysical Fluid Dynamics*, **100**, 341–361. [DOI], [ADS]. (Cité p. 50)

Calkins M. A., Julien K. & Marti P., 2014, “Onset of rotating and non-rotating convection in compressible and anelastic ideal gases”, *Geophysical and Astrophysical Fluid Dynamics*. [DOI]. (Cité p. 34)

Calkins M. A., Julien K. & Marti P., 2015, “The breakdown of the anelastic approximation in rotating compressible convection : implications for astrophysical systems”, *Proceedings of the Royal Society of London A : Mathematical, Physical and Engineering Sciences*, **471**(2175). [DOI], [ADS]. (Cité p. 34 et 106)

Carrington R. C., 1863, *Observations of the Spots on the Sun : From November 9, 1853, to March 24, 1861, Made at Redhill*, University of Chicago Digital Preservation Collection, Williams and Norgate, London. [ADS]. (Cité p. 6 et 11)

Chabrier G. & Küker M., 2006, “Large-scale $\alpha\hat{}2$-dynamo in low-mass stars and brown dwarfs”, *Astronomy and Astrophysics*, **446**, 1027–1037. [DOI], [ADS]. (Cité p. 3)

Charbonneau P., 2010, “Dynamo Models of the Solar Cycle”, *Living Reviews in Solar Physics*, **7**, 3. [DOI], [ADS]. (Cité p. 13, 53 et 97)

Charbonneau P., 2013, *Solar and Stellar Dynamos*, Saas-Fee Advanced Course, 39, Springer-Verlag. [DOI], [ADS]. (Cité p. 3, 4, 7, 13 et 19)

Choudhuri A. R. & Karak B. B., 2012, “Origin of Grand Minima in Sunspot Cycles”, *Physical Review Letters*, **109**(17), 171103. [DOI], [ADS]. (Cité p. 8 et 97)

Christensen U. R., 2002, “Zonal flow driven by strongly supercritical convection in rotating spherical shells”, *Journal of Fluid Mechanics*, **470**, 115–133. [DOI], [ADS]. (Cité p. 76)

Christensen U. R., 2010, “Dynamo Scaling Laws and Applications to the Planets”, *Space Science Reviews*, **152**, 565–590. [DOI], [ADS]. (Cité p. 48, 71, 72, 73, 74, 75, 77 et 105)

Christensen U. R., 2011, “Geodynamo models : Tools for understanding properties of Earth’s magnetic field”, *Physics of the Earth and Planetary Interiors*, **187**, 157–169. [DOI], [ADS]. (Cité p. 70)

Christensen U. R. & Aubert J., 2006, “Scaling properties of convection-driven dynamos in rotating spherical shells and application to planetary magnetic fields”, *Geophy. J. Int.*, **166**, 97–114. [DOI], [ADS]. (Cité p. 21, 24, 48, 49, 50, 66, 72, 75, 76 et 105)

Christensen U. R. & Tilgner A., 2004, “Power requirement of the geodynamo from ohmic losses in numerical and laboratory dynamos”, *Nature*, **429**, 169–171. [DOI], [ADS]. (Cité p. 72 et 75)

Christensen U. R., Aubert J., Cardin P., Dormy E., Gibbons S., Glatzmaier G. A., Grote E., Honkura Y., Jones C., Kono M., Matsushima M., Sakuraba A., Takahashi F., Tilgner A., Wicht J. & Zhang K., 2001, “A numerical dynamo benchmark”, *Phys. Earth Planet. Inter.*, **128**, 25–34. [DOI], [ADS]. (Cité p. 55)

Christensen U. R., Holzwarth V. & Reiners A., 2009, “Energy flux determines magnetic field strength of planets and stars”, *Nature*, **457**, 167–169. [DOI], [ADS]. (Cité p. 72)

Christensen-Dalsgaard J., 2008, *Lecture Notes on Stellar Structure and Evolution*, Aarhus Universitet, sixth edn. [WEB]. (Cité p. 8 et 15)

Cohen-Tannoudji C., Dui B. & Laloe F., 1973, *Mécanique quantique*, Hermann. [ADS]. (Cité p. 40)

Constant B., 1895, *Journal intime de Benjamin Constant*, Paul Ollendorff, Paris. [GAL]. (Cité p. iii)

Davidson P. A., 2013, “Scaling laws for planetary dynamos”, *Geophysical Journal International*, **195**, 67–74. [DOI], [ADS]. (Cité p. 72, 74, 75, 78 et 105)

Davidson P. A., 2014, “The dynamics and scaling laws of planetary dynamos driven by inertial waves”, *Geophysical Journal International*, **198**, 1832–1847. [DOI], [ADS]. (Cité p. 105)

De Groot S. R. & Mazur P., 1984, *Non-Equilibrium Thermodynamics*, Dover Books on Physics, Dover Publications, New York. (Cité p. 30)

Depassier M. C. & Spiegel E. A., 1981, “The large-scale structure of compressible convection”, *Astronomical Journal*, **86**, 496–512. [DOI], [ADS]. (Cité p. 35)

Ding M. & Yang W., 1995, “Distribution of the first return time in fractional Brownian motion and its application to the study of on-off intermittency”, *Physical Review E*, **52**, 207–213. [DOI], [ADS]. (Cité p. 82)

Donati J.-F. & Landstreet J. D., 2009, “Magnetic Fields of Nondegenerate Stars”, *Annual Review of Astronomy and Astrophysics*, **47**, 333–370. [DOI], [ADS]. (Cité p. 16, 17, 18 et 53)

Dormy E., 1997, *Modélisation numérique de la dynamo terrestre*, thèse de doctorat, Institut de Physique du Globe de Paris. [WEB]. (Cité p. 1, 20, 38, 40 et 43)

Dormy E. & Soward A. M. (Eds.), 2007, *Mathematical aspects of natural dynamos*, The Fluid Mechanics of Astrophysics and Geophysics, 13, CRC Press. (Cité p. 8, 10, 20, 22, 36, 84 et 97)

Drew S. J., Jones C. A. & Zhang K., 1995, "Onset of convection in a rapidly rotating compressible fluid spherical shell", *Geophysical and Astrophysical Fluid Dynamics*, **80**, 241–254. [DOI], [ADS]. (Cité p. 26)

Duarte L. D. V., Gastine T. & Wicht J., 2013, "Anelastic dynamo models with variable electrical conductivity : An application to gas giants", *Physics of the Earth and Planetary Interiors*, **222**, 22–34. [DOI], [ADS]. (Cité p. 55, 66 et 106)

Dubois M., Berge P. & Wesfreid J., 1978, "Non Boussinesq convective structures in water near 4 °C", *Journal de Physique*, **39**(12), 1253–1257. [DOI]. (Cité p. 25)

Durran D. R., 1989, "Improving the Anelastic Approximation.", *Journal of Atmospheric Sciences*, **46**, 1453–1461. [DOI], [ADS]. (Cité p. 107)

Dziewonski A. M. & Anderson D. L., 1981, "Preliminary reference Earth model", *Physics of the Earth and Planetary Interiors*, **25**, 297–356. [DOI], [ADS]. (Cité p. 24)

Eddy J. A., 1976, "The Maunder Minimum", *Science*, **192**, 1189–1202. [DOI], [ADS]. (Cité p. 6 et 8)

Elsasser W. M., 1946, "Induction Effects in Terrestrial Magnetism Part I. Theory", *Phys. Rev.*, **69**, 106–116. [DOI]. (Cité p. 3)

Fivian M. D., Hudson H. S., Lin R. P. & Zahid H. J., 2008, "A Large Excess in Apparent Solar Oblateness Due to Surface Magnetism", *Science*, **322**, 560–562. [DOI], [ADS]. (Cité p. 25)

Fujisaka H. & Yamada T., 1986, "Stability Theory of Synchronized Motion in Coupled-Oscillator Systems. IV –Instability of Synchronized Chaos and New Intermittency–", *Progress of Theoretical Physics*, **75**, 1087–1104. [DOI], [ADS]. (Cité p. 84)

Gad-el-Hak M., 1995, "Questions in Fluid Mechanics : Stokes' Hypothesis for a Newtonian, Isotropic Fluid", *Journal of Fluids Engineering*, **177**, 3–5. [DOI]. (Cité p. 30)

Gailitis A., Lielausis O., Dement'ev S., Platacis E., Cifersons A., Gerbeth G., Gundrum T., Stefani F., Christen M., Hänel H. & Will G., 2000, "Detection of a Flow Induced Magnetic Field Eigenmode in the Riga Dynamo Facility", *Physical Review Letters*, **84**, 4365. [DOI], [ADS]. (Cité p. 20)

Gailitis A., Lielausis O., Platacis E., Dement'ev S., Cifersons A., Gerbeth G., Gundrum T., Stefani F., Christen M. & Will G., 2001, "Magnetic Field Saturation in the Riga Dynamo Experiment", *Physical Review Letters*, **86**, 3024–3027. [DOI], [ADS]. (Cité p. 84)

Galileo G., 1613, *Istoria e dimonstrazioni intorno alle macchie solari e loro accidenti comprese in tre lettere scritte all'illustrissimo signor Marco Velseri Linceo*, Giacomo Mascardi, Rome. [GAL]. (Cité p. 1)

Gallet B. & Pétrélis F., 2009, "From reversing to hemispherical dynamos", *Physical Review E*, **80**(3), 035302. [DOI], [ADS]. (Cité p. 8)

Gallet B., Aumaître S., Boisson J., Daviaud F., Dubrulle B., Bonnefoy N., Bourgoin M., Odier P., Pinton J.-F., Plihon N., Verhille G., Fauve S. & Pétrélis F., 2012, "Experimental Observation of Spatially Localized Dynamo Magnetic Fields", *Physical Review Letters*, **108**(14), 144501. [DOI], [ADS]. (Cité p. 97, 98 et 105)

Gastine T. & Wicht J., 2012, "Effects of compressibility on driving zonal flow in gas giants", *Icarus*, **219**, 428–442. [DOI], [ADS]. (Cité p. 66 et 76)

Gastine T., Duarte L. & Wicht J., 2012, "Dipolar versus multipolar dynamos : the influence of the background density stratification", *Astronomy and Astrophysics*, **546**, A19. [DOI], [ADS]. (Cité p. 48, 50, 54, 55, 63, 64, 65, 66, 74 et 103)

Gastine T., Morin J., Duarte L., Reiners A., Christensen U. R. & Wicht J., 2013, "What controls the magnetic geometry of M dwarfs ?", *Astronomy and Astrophysics*, **549**, L5. [DOI], [ADS]. (Cité p. 106)

Gastine T., Wicht J., Duarte L. D. V., Heimpel M. & Becker A., 2014, "Explaining Jupiter's magnetic field and equatorial jet dynamics", *Geophysics Research Letters*, **41**, 5410–5419. [DOI], [ADS]. (Cité p. 106)

Gérard-Lescuyer J. M. A., 1880, "Sur un paradoxe électrodynamique", *Comptes rendus hebdomadaires des séances de l'Académie des sciences*, **91**, 226–227. [GAL]. (Cité p. 103)

Gilbert W., 1600, *De Magnete, Magneticisque Corporibus, et de Magno Magnete Tellure*, Peter Short, London. (Cité p. 2)

Gilman P. A. & Glatzmaier G. A., 1981, "Compressible convection in a rotating spherical shell. I - Anelastic equations. II - A linear anelastic model. III - Analytic model for compressible vorticity waves", *Astrophysical Journal, Supplement*, **45**, 335–388. [DOI], [ADS]. (Cité p. 26)

Gissinger C., Iskakov A., Fauve S. & Dormy E., 2008, “Effect of magnetic boundary conditions on the dynamo threshold of von Kármán swirling flows”, *Europhysics Letters*, **82**, 29 001–+. [DOI], [ADS]. (Cité p. 85)

Gissinger C., Petitdemange L., Schrinner M. & Dormy E., 2012, “Bistability between Equatorial and Axial Dipoles during Magnetic Field Reversals”, *Physical Review Letters*, **108**(23), 234501. [DOI], [ADS]. (Cité p. 54)

Gizon L. & Birch A. C., 2005, “Local Helioseismology”, *Living Reviews in Solar Physics*, **2**, 6. [DOI], [ADS]. (Cité p. 11)

Glatzmaier G. A. & Roberts P. H., 1995, “A three-dimensional self-consistent computer simulation of a geomagnetic field reversal”, *Nature*, **377**, 203–209. [DOI]. (Cité p. 20)

Gleissberg W., 1939, “A long-periodic fluctuation of the sun-spot numbers”, *The Observatory*, **62**, 158–159. [ADS]. (Cité p. 6)

Gleissberg W., 1971, “The Probable Behaviour of Sunspot Cycle 21”, *Solar Physics*, **21**, 240–245. [DOI], [ADS]. (Cité p. 6)

Goudard L. & Dormy E., 2008, “Relations between the dynamo region geometry and the magnetic behavior of stars and planets”, *Europhysics Letters*, **83**, 59 001–+. [DOI], [ADS]. (Cité p. 23, 48 et 50)

Gough D. O., 1969, “The Anelastic Approximation for Thermal Convection.”, *Journal of Atmospheric Sciences*, **26**, 448–456. [DOI], [ADS]. (Cité p. 26)

Guervilly C. & Cardin P., 2010, “Numerical simulations of dynamos generated in spherical Couette flows”, *Geophysical and Astrophysical Fluid Dynamics*, **104**, 221–248. [DOI], [ADS]. (Cité p. 85, 87, 88 et 95)

Gutenberg B., 1939, *Internal Constitution of the Earth*, Physics of the earth, McGraw-Hill Book Company, Incorporated. (Cité p. 3)

Hale G. E., 1908, “On the Probable Existence of a Magnetic Field in Sun-Spots”, *Astrophysical Journal*, **28**, 315. [DOI], [ADS]. (Cité p. 2)

Hale G. E., Ellerman F., Nicholson S. B. & Joy A. H., 1919, “The Magnetic Polarity of Sun-Spots”, *Astrophysical Journal*, **49**, 153. [DOI], [ADS]. (Cité p. 2)

Hall J. C., 2008, “Stellar Chromospheric Activity”, *Living Reviews in Solar Physics*, **5**, 2. [DOI], [ADS]. (Cité p. 18)

Hathaway D. H., 2015, “The Solar Cycle”, *ArXiv e-prints*. [ADS]. (Cité p. 5)

Hazra S., Passos D. & Nandy D., 2014, “A Stochastically Forced Time Delay Solar Dynamo Model : Self-consistent Recovery from a Maunder-like Grand Minimum Necessitates a Mean-field Alpha Effect”, *Astrophysical Journal*, **789**, 5. [DOI], [ADS]. (Cité p. 8)

Heagy J. F., Platt N. & Hammel S. M., 1994, “Characterization of on-off intermittency”, *Physical Review E*, **49**, 1140–1150. [DOI], [ADS]. (Cité p. 82)

Herschel William, 1801, “Observations Tending to Investigate the Nature of the Sun, in Order to Find the Causes or Symptoms of Its Variable Emission of Light and Heat ; With Remarks on the Use That May Possibly Be Drawn from Solar Observations”, *Philosophical Transactions of the Royal Society of London*, **91**, 265–318. [DOI]. (Cité p. 27)

Howe R., 2009, “Solar Interior Rotation and its Variation”, *Living Reviews in Solar Physics*, **6**, 1. [DOI], [ADS]. (Cité p. 11)

Humboldt v. A., 1852, *Cosmos : Sketch of a Physical Description of the Universe*, vol. 3, Longman, Brown, Green, and Longmans and John Murray, London. [ADS]. Trad. Sabine, E. (Cité p. 6)

Jackson J. D., 1975, *Classical electrodynamics*, Wiley. (Cité p. 27)

Jones C. A., 2014, “A dynamo model of Jupiter’s magnetic field”, *Icarus*, **241**, 148–159. [DOI], [ADS]. (Cité p. 63, 103, 105 et 106)

Jones C. A., Kuzanyan K. M. & Mitchell R. H., 2009, “Linear theory of compressible convection in rapidly rotating spherical shells, using the anelastic approximation”, *Journal of Fluid Mechanics*, **634**, 291. [DOI], [ADS]. (Cité p. 35, 55 et 66)

Jones C. A., Boronski P., Brun A. S., Glatzmaier G. A., Gastine T., Miesch M. S. & Wicht J., 2011, “Anelastic convection-driven dynamo benchmarks”, *Icarus*, **216**, 120–135. [DOI], [ADS]. (Cité p. 26, 32, 37, 38, 55 et 109)

Kaniel S. & Kovetz A., 1967, “Schwarzschild’s Criterion for Instability”, *Physics of Fluids*, **10**, 1186–1193. [DOI], [ADS]. (Cité p. 13)

Käpylä P. J., Mantere M. J., Cole E., Warnecke J. & Brandenburg A., 2013, “Effects of Enhanced Stratification on Equatorward Dynamo Wave Propagation”, *Astrophysical Journal*, **778**, 41. [DOI], [ADS]. (Cité p. 50)

King E. M., Soderlund K. M., Christensen U. R., Wicht J. & Aurnou J. M., 2010, “Convective heat transfer in planetary dynamo models”, *Geochemistry, Geophysics, Geosystems*, **11**, Q06016. [DOI], [ADS]. (Cité p. 20)

Knobloch E., Tobias S. M. & Weiss N. O., 1998, “Modulation and symmetry changes in stellar dynamos”, *Monthly Notices of the RAS*, **297**, 1123–1138. [DOI], [ADS]. (Cité p. 97)

Korzennik S. G. & Eff-Darwich A., 2011, “The rotation rate and its evolution derived from improved mode fitting and inversion methodology”, *Journal of Physics Conference Series*, **271**(1), 012067. [DOI], [ADS]. (Cité p. 12)

Kutzner C. & Christensen U. R., 2002, “From stable dipolar towards reversing numerical dynamos”, *Physics of the Earth and Planetary Interiors*, **131**, 29–45. [DOI], [ADS]. (Cité p. 48 et 61)

Landau L. D. & Lifchitz E., 1971, *Mécanique des Fluides*, Physique théorique, 6, Éditions MIR, Moscou. Traduit du russe par E. Gloukhian. (Cité p. 13 et 29)

Langlais B. & Quesnel Y., 2008, “New perspectives on Mars’ crustal magnetic field”, *Comptes Rendus Geoscience*, **340**, 791–800. [DOI], [ADS]. (Cité p. 8 et 97)

Lantz S. R. & Fan Y., 1999, “Anelastic Magnetohydrodynamic Equations for Modeling Solar and Stellar Convection Zones”, *Astrophysical Journal, Supplement*, **121**, 247–264. [DOI], [ADS]. (Cité p. 26 et 32)

Larmor J., 1919, “How could a rotating body such as the Sun become a magnet ?”, *Report of the British Association for the Advancement of Science*, **87th Meeting**, 159–160. [ARC]. (Cité p. 3)

Le Mouël J. L. & Poirier J. P., 2013, *Une brève histoire du magnétisme : De l’aimant à la terre*, Regards, Belin. (Cité p. 1)

Lebovitz N. R., 1966, “On the Necessity of Schwarzschild’s Criterion for Stability”, *Astrophysical Journal*, **146**, 946–949. [DOI], [ADS]. (Cité p. 13)

Leprovost N., Dubrulle B. & Plunian F., 2006, “Intermittency in the homopolar disc-dynamo”, *Magnetohydrodynamics*, **42**, 131–142. [ADS]. (Cité p. 84)

Lockwood M., Harrison R. G., Woollings T. & Solanki S. K., 2010, “Are cold winters in Europe associated with low solar activity ?”, *Environmental Research Letters*, **5**(2), 024001. [DOI], [ADS]. (Cité p. 8)

Malkus W. V. R., 1964, *Boussinesq equations and convection energetics*, Geophysical Fluid Dynamics Proceedings, Woods Hole Oceanographic Institution. (Cité p. 36)

Maunder E. W., 1904, “Note on the distribution of sun-spots in heliographic latitude, 1874-1902”, *Monthly Notices of the RAS*, **64**, 747–761. [DOI], [ADS]. (Cité p. 6)

Maxwell J. C., 1865, “A Dynamical Theory of the Electromagnetic Field”, *Philosophical Transactions of the Royal Society of London*, **155**, 459–512. [DOI]. (Cité p. 27)

Miesch M. S., 2005, “Large-Scale Dynamics of the Convection Zone and Tachocline”, *Living Reviews in Solar Physics*, **2**, 1. [DOI], [ADS]. (Cité p. 11)

Moffatt H. K., 1978, *Magnetic Field Generation in Electrically Conducting Fluids*, Cambridge Monographs on Mechanics, Cambridge University Press. (Cité p. 3 et 20)

Molokov S., Moreau R. & Moffatt H. K. (Eds.), 2007, *Magnetohydrodynamics : Historical Evolution and Trends*, Springer. [ADS]. (Cité p. 20 et 47)

Monchaux R., Berhanu M., Bourgoin M., Moulin M., Odier P., Pinton J.-F., Volk R., Fauve S., Mordant N., Pétrélis F., Chiffaudel A., Daviaud F., Dubrulle B., Gasquet C., Marié L. & Ravelet F., 2007, “Generation of a Magnetic Field by Dynamo Action in a Turbulent Flow of Liquid Sodium”, *Physical Review Letters*, **98**(4), 044 502–+. [DOI], [ADS]. (Cité p. 20 et 84)

Morin J., Donati J.-F., Petit P., Delfosse X., Forveille T. & Jardine M. M., 2010, “Large-scale magnetic topologies of late M dwarfs”, *Monthly Notices of the RAS*, **407**, 2269–2286. [DOI], [ADS]. (Cité p. 106)

Morin J., Dormy E., Schrinner M. & Donati J.-F., 2011, “Weak- and strong-field dynamos : from the Earth to the stars”, *Monthly Notices of the RAS*, **418**, L133–L137. [DOI], [ADS]. (Cité p. 106)

Moss D. & Brooke J., 2000, “Towards a model for the solar dynamo”, *Monthly Notices of the RAS*, **315**, 521–533. [DOI], [ADS]. (Cité p. 101)

Müller U. & Stieglitz R., 2002, “The Karlsruhe Dynamo Experiment”, *Nonlinear Processes in Geophysics*, **9**, 165–170. [ADS]. (Cité p. 54)

Ogura Y. & Phillips N. A., 1962, “Scale Analysis of Deep and Shallow Convection in the Atmosphere.”, *Journal of Atmospheric Sciences*, **19**, 173–179. [DOI], [ADS]. (Cité p. 26)

Oláh K., Kolláth Z., Granzer T., Strassmeier K. G., Lanza A. F., Järvinen S., Korhonen H., Baliunas S. L., Soon W., Messina S. & Cutispoto G., 2009, “Multiple and changing cycles of active stars. II. Results”, *Astronomy and Astrophysics*, **501**, 703–713. [DOI], [ADS]. (Cité p. 19)

Olson P., Christensen U. R. & Glatzmaier G. A., 1999, “Numerical modeling of the geodynamo : Mechanisms of field generation and equilibration”, *Journal of Geophysics Research*, **104**, 10 383–10 404. [DOI], [ADS]. (Cité p. 54 et 70)

Oruba L. & Dormy E., 2014, “Predictive scaling laws for spherical rotating dynamos”, *Geophysical Journal International*, **198**, 828–847. [DOI], [ADS]. (Cité p. 105)

Parker E. N., 1955, “Hydromagnetic Dynamo Models.”, *Astrophysical Journal*, **122**, 293–+. [DOI], [ADS]. (Cité p. 50)

Pétrélis F., 2011, *Désordre et Instabilités*, Habilitation à diriger des recherches, Laboratoire de Physique Statistique, ENS, Paris. (Cité p. 28 et 83)

Pétrélis F. & Fauve S., 2008, “Chaotic dynamics of the magnetic field generated by dynamo action in a turbulent flow”, *Journal of Physics Condensed Matter*, **20**, 494203. [DOI], [ADS]. (Cité p. 105)

Pétrélis F., Mordant N. & Fauve S., 2007, “On the magnetic fields generated by experimental dynamos”, *Geophysical and Astrophysical Fluid Dynamics*, **101**, 289–323. [DOI], [ADS]. (Cité p. 96)

Platt N., Spiegel E. A. & Tresser C., 1993, “On-off intermittency - A mechanism for bursting”, *Physical Review Letters*, **70**, 279–282. [DOI], [ADS]. (Cité p. 80 et 84)

Poincaré H., 1885, “Sur l’équilibre d’une masse fluide animée d’un mouvement de rotation”, *Acta Mathematica*, **7**(1), 259–380. [DOI]. (Cité p. 24)

Poincaré H., 1892, “Les formes d’équilibre d’une masse fluide en rotation”, *Revue générale des sciences pures et appliquées*, **3**(23), 809–815. [GAL]. (Cité p. 24)

Ponomarenko Y. B., 1973, “Theory of the hydromagnetic generator”, *Journal of Applied Mechanics and Technical Physics*, **14**, 775–778. [DOI], [ADS]. (Cité p. 20)

Proctor M. R. E. & Gilbert A. D. (Eds.), 1994, *Lectures on Solar and Planetary Dynamos*, Publications of the Newton Institute, Cambridge University Press. [ADS]. (Cité p. 2)

Rayleigh Lord, 1916, “LIX. On convection currents in a horizontal layer of fluid, when the higher temperature is on the under side”, *Philosophical Magazine Series 6*, **32**(192), 529–546. [DOI]. (Cité p. 25 et 35)

Raynaud R., Petitdemange L. & Dormy E., 2014, “Influence of the mass distribution on the magnetic field topology”, *Astronomy and Astrophysics*, **567**, A107. [DOI], [ADS]. (Cité p. 63, 64, 66 et 98)

Reiners A., 2012, “Observations of Cool-Star Magnetic Fields”, *Living Reviews in Solar Physics*, **9**, 1. [DOI], [ADS]. (Cité p. 16 et 17)

Rempel M., 2006, “Flux-Transport Dynamos with Lorentz Force Feedback on Differential Rotation and Meridional Flow : Saturation Mechanism and Torsional Oscillations”, *Astrophysical Journal*, **647**, 662–675. [DOI], [ADS]. (Cité p. 78)

Ribes J. C. & Nesme-Ribes E., 1993, “The solar sunspot cycle in the Maunder minimum AD1645 to AD1715”, *Astronomy and Astrophysics*, **276**, 549. [ADS]. (Cité p. 13)

Rieutord M. & Rincon F., 2010, “The Sun’s Supergranulation”, *Living Reviews in Solar Physics*, **7**, 2. [DOI], [ADS]. (Cité p. 11)

Roberts G. O., 1970, “Spatially Periodic Dynamos”, *Royal Society of London Philosophical Transactions Series A*, **266**, 535–558. [DOI], [ADS]. (Cité p. 20)

Roberts P. H. & King E. M., 2013, “On the genesis of the Earth’s magnetism”, *Reports on Progress in Physics*, **76**(9), 096801. [DOI], [ADS]. (Cité p. 22)

Rogers T. M. & Glatzmaier G. A., 2005, “Penetrative Convection within the Anelastic Approximation”, *Astrophysical Journal*, **620**, 432–441. [DOI], [ADS]. (Cité p. 33)

Ruediger G., 1980, “Rapidly rotating alpha-squared dynamo models”, *Astronomische Nachrichten*, **301**, 181–187. [ADS]. (Cité p. 54)

Salmon R., 1988, “Hamiltonian fluid mechanics”, *Annual Review of Fluid Mechanics*, **20**, 225–256. [DOI], [ADS]. (Cité p. 107)

Sasaki Y., Takehiro S.-i., Kuramoto K. & Hayashi Y.-Y., 2011, “Weak-field dynamo emerging in a rotating spherical shell with stress-free top and no-slip bottom boundaries”, *Physics of the Earth and Planetary Interiors*, **188**, 203–213. [DOI], [ADS]. (Cité p. 63)

Schatzman E. L. & Praderie F., 1990, *Les Étoiles*, Savoirs actuels, InterEditions/Editions du CNRS, Paris. [ADS]. (Cité p. 8)

Schenzle A. & Brand H., 1979, “Multiplicative stochastic processes in statistical physics”, *Phys. Rev. A*, **20**, 1628–1647. [DOI]. (Cité p. 82)

Schmitt D., Schuessler M. & Ferriz-Mas A., 1996, “Intermittent solar activity by an on-off dynamo.”, *Astronomy and Astrophysics*, **311**, L1–L4. [ADS]. (Cité p. 8, 79 et 97)

Schmitz S. & Tilgner A., 2009, “Heat transport in rotating convection without Ekman layers”, *Physical Review E*, **80**(1), 015305. [DOI], [ADS]. (Cité p. 76)

Schrijver C. J., Cote J., Zwaan C. & Saar S. H., 1989, “Relations between the photospheric magnetic field and the emission from the outer atmospheres of cool stars. I - The solar CA II K line core emission”, *Astrophysical Journal*, **337**, 964–976. [DOI], [ADS]. (Cité p. 18 et 19)

Schrinner M., 2011, “Global dynamo models from direct numerical simulations and their mean-field counterparts”, *Astronomy and Astrophysics*, **533**, A108+. [DOI], [ADS]. (Cité p. 106)

Schrinner M., 2013, “Rotational threshold in global numerical dynamo simulations”, *Monthly Notices of the RAS*, **431**, L78–L82. [DOI], [ADS]. (Cité p. 78)

Schrinner M., Rädler K.-H., Schmitt D., Rheinhardt M. & Christensen U. R., 2007, “Mean-field concept and direct numerical simulations of rotating magnetoconvection and the geodynamo”, *Geophysical and Astrophysical Fluid Dynamics*, **101**, 81–116. [DOI], [ADS]. (Cité p. 54, 70 et 106)

Schrinner M., Schmitt D., Cameron R. & Hoyng P., 2010, “Saturation and time dependence of geodynamo models”, *Geophys. J. Int.*, **182**, 675–681. [DOI], [ADS]. (Cité p. 48)

Schrinner M., Petitdemange L. & Dormy E., 2011a, “Oscillatory dynamos and their induction mechanisms”, *Astronomy and Astrophysics*, **530**, A140. [DOI], [ADS]. (Cité p. 50 et 70)

Schrinner M., Schmitt D. & Hoyng P., 2011b, “Mode analysis of numerical geodynamo models”, *Physics of the Earth and Planetary Interiors*, **188**, 185–193. [DOI], [ADS]. (Cité p. 48)

Schrinner M., Petitdemange L. & Dormy E., 2012, “Dipole Collapse and Dynamo Waves in Global Direct Numerical Simulations”, *Astrophysical Journal*, **752**, 121. [DOI], [ADS]. (Cité p. 24, 48, 49, 50, 53, 54, 56, 63, 70, 71, 73, 74, 77, 98 et 106)

Schrinner M., Petitdemange L., Raynaud R. & Dormy E., 2014, “Topology and field strength in spherical, anelastic dynamo simulations”, *Astronomy and Astrophysics*, **564**, A78. [DOI], [ADS]. (Cité p. 38, 65 et 97)

Schwabe M., 1844, “Sonnenbeobachtungen im Jahre 1843. Von Herrn Hofrath Schwabe in Dessau”, *Astronomische Nachrichten*, **21**, 233. [ADS]. (Cité p. 6)

Shulyak D., Sokoloff D., Kitchatinov L. & Moss D., 2015, “Towards understanding dynamo action in M dwarfs”, *Monthly Notices of the RAS*, **449**, 3471–3478. [DOI], [ADS]. (Cité p. 106)

Simitev R. D. & Busse F. H., 2009, “Bistability and hysteresis of dipolar dynamos generated by turbulent convection in rotating spherical shells”, *EPL (Europhysics Letters)*, **85**, 19 001. [DOI], [ADS]. (Cité p. 24)

Sokoloff D. & Nesme-Ribes E., 1994, “The Maunder minimum : A mixed-parity dynamo mode ?”, *Astronomy and Astrophysics*, **288**, 293–298. [ADS]. (Cité p. 7 et 97)

Spiegel E. A. & Veronis G., 1960, “On the Boussinesq Approximation for a Compressible Fluid.”, *Astrophysical Journal*, **131**, 442. [DOI], [ADS]. (Cité p. 25)

Spiegel E. A. & Zahn J.-P., 1992, “The solar tachocline”, *Astronomy and Astrophysics*, **265**, 106–114. [ADS]. (Cité p. 13)

Spoerer G., 1889, “Mémoires et observations. Sur les différences que présentent l’hémisphère nord et l’hémisphère sud du soleil”, *Bulletin astronomique, Série I*, **6**, 60–63. [ADS], [GAL]. (Cité p. 8)

Spruit H. C., 2011, “Theories of the Solar Cycle : A Critical View”, *ArXiv e-prints*. [ADS]. (Cité p. 21 et 23)

Stelzer Z. & Jackson A., 2013, “Extracting scaling laws from numerical dynamo models”, *Geophysical Journal International*, **193**, 1265–1276. [DOI], [ADS]. (Cité p. 72, 75 et 76)

Stieglitz R. & Müller U., 2001, “Experimental demonstration of a homogeneous two-scale dynamo”, *Physics of Fluids*, **13**, 561–564. [DOI], [ADS]. (Cité p. 20 et 84)

Stratonovitch R. L., 1963, *Topics in the Theory of Random Noise*, Gordon & Breach. (Cité p. 81 et 91)

Sweet David, Ott Edward, Finn John M., Antonsen Thomas M. & Lathrop Daniel P., 2001, “Blowout bifurcations and the onset of magnetic activity in turbulent dynamos”, *Phys. Rev. E*, **63**, 066 211. [DOI]. (Cité p. 83 et 84)

Thom R., 1983, *Paraboles et catastrophes*, Champs sciences, Flammarion. (Cité p. 79)

Thomas J. T. & Weiss N. O., 2008, *Sunspots and starspots*, Cambridge Astrophysics Series, Cambridge University Press. (Cité p. 4 et 10)

Tilgner A., 1997, “A kinematic dynamo with a small scale velocity field”, *Physics Letters A*, **226**, 75–79. [DOI], [ADS]. (Cité p. 54)

Tilgner A., 2012, “Transitions in Rapidly Rotating Convection Driven Dynamos”, *Physical Review Letters*, **109**(24), 248501. [DOI], [ADS]. (Cité p. 54)

Tobias S. M., 2002, “Modulation of solar and stellar dynamos”, *Astronomische Nachrichten*, **323**, 417–423. [DOI], [ADS]. (Cité p. 98)

Tritton D. J., 1988, *Physical Fluid Dynamics*, Oxford Science Publications, Clarendon Pres, Oxford, second edn. (Cité p. 29)

Usoskin I. G., Solanki S. K. & Kovaltsov G. A., 2007, “Grand minima and maxima of solar activity : new observational constraints”, *Astronomy and Astrophysics*, **471**, 301–309. [DOI], [ADS]. (Cité p. 8)

Vasil G. M., Lecoanet D., Brown B. P., Wood T. S. & Zweibel E. G., 2013, “Energy Conservation and Gravity Waves in Sound-proof Treatments of Stellar Interiors. II. Lagrangian Constrained Analysis”, *Astrophysical Journal*, **773**, 169. [DOI], [ADS]. (Cité p. 107)

Verhille G., Plihon N., Fanjat G., Volk R., Bourgoin M. & Pinton J.-F., 2010, “Large-scale fluctuations and dynamics of the Bullard-von Kármán dynamo”, *Geophysical and Astrophysical Fluid Dynamics*, **104**, 189–205. [DOI], [ADS]. (Cité p. 84)

Weiss N. O., 2011, “Chaotic behaviour in low-order models of planetary and stellar dynamos”, *Geophysical and Astrophysical Fluid Dynamics*, **105**, 256–272. [DOI], [ADS]. (Cité p. 8 et 97)

Wilson O. C., 1978, “Chromospheric variations in main-sequence stars”, *Astrophysical Journal*, **226**, 379–396. [DOI], [ADS]. (Cité p. 18)

Yadav R. K., Gastine T. & Christensen U. R., 2013a, “Scaling laws in spherical shell dynamos with free-slip boundaries”, *Icarus*, **225**, 185–193. [DOI], [ADS]. (Cité p. 48, 72, 74, 75, 76 et 77)

Yadav R. K., Gastine T., Christensen U. R. & Duarte L. D. V., 2013b, “Consistent scaling laws in anelastic spherical shell dynamos”, *The Astrophysical Journal*, **774**(1), 6. [DOI], [ADS]. (Cité p. 72, 74, 75, 76, 77 et 106)

Zeeman P., 1897, “On the Influence of Magnetism on the Nature of the Light Emitted by a Substance.”, *Astrophysical Journal*, **5**, 332. [DOI], [ADS]. (Cité p. 1)

Zimmerman D. S., Triana S. A. & Lathrop D. P., 2011, “Bi-stability in turbulent, rotating spherical Couette flow”, *Physics of Fluids*, **23**(6), 065 104. [DOI], [ADS]. (Cité p. 95)